TECHNISCHE
UNIVERSITÄT
WIEN

HABILITATIONSSCHRIFT

Development of Advanced Characterization Techniques in Transmission Electron Microscopy

Dr. Stefan Löffler

USTEM, TU Wien
Wiedner Hauptstraße 8-10/E057-02, 1040 Wien

Wien, Juni 2022

Contents

I. Real-space Mapping of Electronic States 5

Disclaimer

Apart from original text and data, this thesis includes several published works. These are used under one of the following licenses and policies (as stated in the respective papers' title pages):

- The Creative Commons Attribution license (CC-BY);
- The Creative Commons Attribution Non-Commercial license (CC-BY-NC);
- The Elsevier sharing policy, i.e., the permission to embed published journal articles in theses [1];
- The Oxford University Press author's "right to include the article in full or in part in a thesis or dissertation, provided that this is not published commercially" [2].

Introduction

Our surrounding is governed by the microscopic world in many ways. On the one hand, atomic arrangements and the interaction between electrons naturally give rise to macroscopic properties such as electric, optic and magnetic properties of materials. On the other hand, technological advancements lead to ever increasing miniaturization to the point where transistors or magnetically stored data bits often measure only a few atoms in diameter. Moreover, many global challenges revolving around energy efficiency and energy storage could potentially be solved by nanotechnology. Consequently, studying, understanding and shaping materials on the nanometer scale is of the utmost importance.

However, due to the diffraction limit in combination with the wavelength of visible light, conventional optical microscopy does not provide sufficient spatial resolution to study features below $\approx 100\,\mathrm{nm}$. Therefore, other imaging techniques and instruments were developed. One of those was the transmission electron microscope (TEM) as first described by Knoll and Ruska in 1932 [3]. Owing to the very short de Broglie wavelength of fast electrons ($\lambda \approx 2.5\,\mathrm{pm}$ for electrons accelerated by $V = 200\,\mathrm{kV}$ to $v \approx 0.7c$), the theoretical spatial resolution limit lies well below the Bohr radius.

Unfortunately, this theoretical spatial resolution given by the diffraction limit was far beyond the experimental reality for a long time. Aberrations, in particular the spherical aberration, drastically limited the usable opening angles (to the order of a few mrad); poor coherence of the electorn beam and low electronic stability made matters worse. Consequently, the achievable spatial resolution was rather in the nanometer than in the picometer regime. In 1959, Richard Feynman said: “It would be very easy to make an analysis of any complicated chemical substance; all one would have to do would be to look at it and see where the atoms are. The only trouble is that the electron microscope is one hundred times too poor.” [4]

A lot of progress has been made since then, both in terms of the optical performance and in terms of beam coherence, brightness and stability. A very nice overview of important historical events in the development of electron microscopy until the early 2000s can be found in [5]. A particularly notable milestone was the invention of the aberration corrector [6, 7], which paved the way for sub-Å spatial resolution. The latest generation of aberration correctors already allows for a spatial resolution close to[1] 15λ [9].

In order to go beyond simple imaging, a wide variety of analytical instrumentation and detectors was developed as well, giving rise to a multitude of techniques includ-

---

[1] λ is the electron wavelength. Typical values in a TEM are somewhere between $8.59\,\mathrm{pm}$ at $20\,\mathrm{kV}$ acceleration voltage and $1.97\,\mathrm{pm}$ at $300\,\mathrm{kV}$ [8].

ing electron energy-loss spectrometry (EELS), energy-dispersive X-ray spectroscopy (EDX), Auger spectroscopy, cathodo-luminescence (CL), and interferometry.

With ever improving instrumentation and the development of new detectors comes the need for advances in methodology and characterization techniques. While at low magnification, it may be justified to interpret an electron micrograph in first approximation as simply a shadow image of the sample akin to an optical transmission microscopic image, such an interpretation soon breaks down at high magnifications as used for atomic resolution imaging. At this scale, the image formation has to be treated as a quantum mechanical scattering process of (relativistic) electrons[2]. Similarly, special scattering geometries can be chosen to, for example, visualize point defects in a crystal lattice. Again, the required setup as well as the methods to analyze and quantify the results go far beyond what is needed for a "simple shadow image". A similar situation arises when looking at analytical techniques such as EELS.

In EELS, the energy of the electron beam after passing through the sample is analyzed, typically by a sector magnet. The resulting energy spectrum provides information about which transitions are possible in a specific sample region. In the context of so-called core-losses (i.e., transitions from a tightly bound "inner shell" electron to above the Fermi energy) the energies of these transitions are characteristic for the chemical element participating in the inelastic interaction. Thus, mapping transition energies over the sample produces chemical maps.

However, a closer look at the energy spectrum reveals much more information in the fine structure of the excitation edges than "just the chemical composition". The shape of the fine structure is influenced by many factors including the local surrounding (i.e., the crystal field), the valence state, and the spin state of the atom. Thus, mapping the details of the fine structure can reveal localized information about these properties. As above, exploiting the full potential of the wealth of data available with modern instruments requires advanced methodology to properly design, simulate and analyze experiments.

Therefore, my research work is dedicated towards the development of advanced characterization techniques in TEM. This encompasses both the advancement of existing techniques as well as the development of entirely new approaches.

This thesis is composed of 12 selected (peer-reviewed) papers focusing on the development of advanced characterization techniques in TEM, to which I have contributed significantly and which had a profound impact on their respective field. A full list of all my scientific publications can be found, e.g., via my ORCID 0000-0003-0080-2495. Each paper in this thesis is represented by its own, consecutively numbered chapter to ease cross-referencing and discoverability. The chapters, in turn, are grouped thematically into four parts (numbered with roman numerals), each of which starts with a short introduction into the respective research topic, and are ordered chronologically in each part. While each part discusses a separate technique, later parts typically

---

[2] Depending on the acceleration voltage and the accuracy level required, either the classical Schrödinger equation, a relativistically corrected Schrödinger equation, or the Dirac equation have to be be used.

build upon previous ones.

The first two parts include progress on two related topics, namely the mapping and characterization of electronic states of the target. Part I — which is a continuation and advancement of my PhD work — deals with the real-space mapping of electronic transitions at and beyond atomic resolution (colloquially referred to as “orbital mapping”). It includes the first proof-of-principle experiments showing that a mapping of individual electronic states inside a (bulk) specimen is indeed possible.

Complementary to mapping the spatial part of electronic states, part II deals with the characterization of spin states using the energy-loss magnetic chiral dichroism (EMCD) technique. It includes significant improvements to the spatial resolution and the signal-to-noise ratio (SNR) of the technique, as well as the derivation of a formalism that facilitates the designing of experiments as well as investigating magnetic phase transitions.

Part III deals with designing, generating and using a new class of electron beam shapes, namely electron vortex beams (EVBs). The study of EVBs has its roots in EMCD, where EVBs occur naturally in the inelastic scattering process. Based on this observation, considerable research has been devoted over the last couple of years to deliberately creating and manipulating EVBs in an endeavor to enhance the capabilities and signal strength of EMCD as well as broaden the range of systems for which it can be used. The papers included in this part report on significant advances in producing EVBs and in understanding how they scatter inside amorphous samples.

Building in part on the beam shaping techniques first developed for the study of EMCD, part IV deals with fundamentally new prospects of quantum microscopy. The fact that beam shaping nowadays allows the experimenter to arbitrarily manipulate the quantum wave function of the probe beam both before and after it interacts with the sample opens many doors to entirely novel approaches for setting up a (scattering) experiment and for optimally measuring a quantity of interest. Going beyond the classical imaging and diffraction modes, this enables problem-specific custom approaches by suitably transforming the probe beam’s quantum state.

Two crucial aspects of quantum microscopy are highlighted in part IV, namely developing mechanisms to arbitrarily transform the beam and to understand the quantum-mechanical intricacies of the propagation of a general beam through “conventional” electron-optical lenses. The results, in particular those on arbitrary transformations, promise to solve one of the overarching problems of most advanced techniques (including those discussed in parts I and II): the low SNR.

All the papers in this thesis fall into one of two categories. They either significantly advance existing methods (in particular EMCD (part II) and electron vortices (part III)), or they pioneer novel techniques in new or emerging fields (in particular “orbital mapping” (part I) and “quantum microscopy” (part IV)). In all cases, I was particularly involved in the methodology: defining the research question, designing the experiments and/or simulations, performing the data analysis, as well as in the in-depth theoretical description of the underlying physical processes and numerical simulations. My focus lay on furthering the quantum mechanical understanding of the interaction between the three key actors in electron microscopy: the electron beam itself, the electron optical elements of the microscope, and the sample. This allowed me to simulate existing methods more accurately and in hitherto unexplored regimes (such as convergent-beam EMCD), while at the same time sparking new ideas (such as “how could the measurement basis be transformed to give more signal and less background?”).

Part I

Real-space Mapping of Electronic States

Electronic states shape the world around us. Almost all macroscopic properties of matter are influenced or governed by them, including chemical binding, crystal structure, as well as electric, optic and magnetic properties. While methods exist to map the total charge density (e.g., using elastically scattered electrons [10, 11]) and surface states (e.g., using scanning tunneling microscopy (STM) [12]), direct mapping of information concerning individual electronic states in the bulk has remained elusive.

One approach that can fill this gap in characterization techniques is core-loss EELS. Fundamentally, EELS provides access to the energy distribution of the probe beam after it traversed the sample. Core-loss EELS deals with probe electrons that have transferred a relatively large amount of energy ($\gtrsim 50\,\mathrm{eV}$) to the sample. This typically occurs when in exciting a tightly-bound (core) electron of a sample atom to a free state above the Fermi level.[3] Assuming different final states of interest lie at sufficiently different energies[4], specific transitions can be picked out, e.g., by a slit aperture in an energy-dispersive plane or in post-processing if an entire spectrum is recorded.

Thus, the real-space distribution of the probability to excite transitions to the chosen states can be mapped. While a single atom's scattering distribution is delocalized due to the long range Coulomb interaction [13], it is distinctly peaked around the scattering center [14]. This implies that real-space EELS data should allow Ångström and sub-Ångström features to be visible, albeit on some background. Strictly speaking, such high-resolution EELS maps only map the scattering probability of the incident probe beam. Practically speaking, under typical conditions they closely resemble the shape and orientation of the sample's final states as demonstrated below.

To understand the image formation, the quantum mechanical scattering process has to be modeled. In order to elegantly handle partial coherence effects, the density matrix formalism [14, 15] is used. A more exhaustive description of the theory can be found in the author's PhD thesis [16], but the general approach is as follows.

Before the inelastic interaction, the system (comprised of the probe beam and the target) is in the initial state given by

$$\sum\!\!\!\!\!\!\int_I p_I \left|I\right\rangle \left\langle I\right| \otimes \left|i\right\rangle \left\langle i\right| \tag{1}$$

where small letters denote the (sub)system of the probe beam and capital letters denote the (sub)system of the target, and p_I is the occupation probability of the state $|I\rangle$. For simplicity, an effective one-electron model of the target will be adopted in the following. The (incoherent) sum over I implies that a multitude of sample states could be realized, whereas the probe beam is assumed to be in a pure state ($|i\rangle \langle i|$) initially.

---

[3] In addition, multiple scattering can occur, caused, e.g., by an additional phonon or plasmon excitation. Such a situation will not be included here as the phonon/plasmon excitation intensity is expected to be very weak compared to the zero-loss peak at the sample thicknesses required for acquiring interpretable real-space maps of electronic states.

[4] I.e., they are not degenerate in energy and their splitting is large enough to be well-resolved experimentally, typically at least 1 eV to 2 eV.

After the interaction, mediated by the Coulomb operator $\hat{V}$, the system is in the state

$$\sum_I p_I \hat{V} \left|I\right\rangle \left|i\right\rangle \left\langle i\right| \left\langle I\right| \hat{V}^\dagger \tag{2}$$

Since the target's final state is not observed separately, it has to be traced out, leaving the probe beam's density operator after the inelastic interaction (for a specific energy transfer E) in the form

$$\hat{\rho}_f(E) = \sum_{I,F} p_I(1-p_F) \left\langle F|\hat{V}|I\right\rangle \left|i\right\rangle \left\langle i\right| \left\langle I|\hat{V}^\dagger|F\right\rangle \delta(E_F - E_I - E) \tag{3}$$

Calculating the density matrix in a reciprocal space basis yields

$$\rho_f(\boldsymbol{k},\boldsymbol{k}',E) = \iint \frac{S(\boldsymbol{q},\boldsymbol{q}',E)}{q^2 q'^2} \rho_i(\boldsymbol{k}+\boldsymbol{q},\boldsymbol{k}'+\boldsymbol{q}') \mathrm{d}\boldsymbol{q}\mathrm{d}\boldsymbol{q}' \tag{4}$$

with the incident density matrix of the probe beam

$$\rho_i(\boldsymbol{k},\boldsymbol{k}') = \left\langle \boldsymbol{k}|i\right\rangle \left\langle i|\boldsymbol{k}'\right\rangle, \tag{5}$$

the mixed dynamic form factor (MDFF) [14, 17, 18]

$$\begin{aligned} S(\boldsymbol{q},\boldsymbol{q}',E) = &\sum_{I,F} p_I(1-p_F) \left\langle \boldsymbol{k}\right| \left\langle F|\hat{V}|I\right\rangle \left|\boldsymbol{k}+\boldsymbol{q}\right\rangle \left\langle \boldsymbol{k}'+\boldsymbol{q}'\right| \left\langle I|\hat{V}^\dagger|F\right\rangle \left|\boldsymbol{k}'\right\rangle \\ &\delta(E_F - E_I - E) \\ = &\sum_{I,F} p_I(1-p_F) \left\langle F|\mathrm{e}^{-\mathrm{i}\boldsymbol{q}\cdot\hat{\boldsymbol{R}}}|I\right\rangle \left\langle I|\mathrm{e}^{\mathrm{i}\boldsymbol{q}'\cdot\hat{\boldsymbol{R}}}|F\right\rangle \delta(E_F - E_I - E) \end{aligned} \tag{6}$$

and the momentum transfer vectors $\boldsymbol{q}, \boldsymbol{q}'$.

The density operator of the probe contains the complete information fully characterizing the electron beam. Thus, it allows predicting any kind of measurement performed on the beam, be it a simple intensity measurement (determining the beam's probability distribution in real-space (imaging) or reciprocal space (diffraction)), an interferometric measurement (for determining phase differences) or a measurement of its energy spectrum (EELS).

There is one caveat, however: eq. 4 relates the pure state wavefunction of the beam *incident on the target atom* (eq. 5) to the beam's state *directly* after the inelastic scattering event. These are not the states typically available experimentally as the beam has to traverse part of the sample (as well as the microscope's gun and condenser systems) to get to the target atom, and the rest of the sample (as well as the remainder of the microscope) to get to the detector. For a complete and correct treatment of the entire process, elastic scattering both before and after the inelastic event has to be modeled.

An efficient way of calculating the MDFF for atoms in a crystal and for interfacing the results with elastic scattering calculations based on the multislice approach [19] can be found in chapter 1 and in my PhD thesis [16].

The formalism was first applied to study the hole distribution in a chain-ladder superconductor of $Sr_{14-x}Ca_xCu_{24}O_{41}$ (SCCO) type (see chap. 2). Without Ca doping, the material is electrically resistive, while superconducting behavior emerges for higher doping. Unlike other Cuprate-based (high-T_c) superconductors, this system does not feature 2D CuO planes, but rather quasi-1D CuO chains and ladders. The fact that superconductivity is still observed is remarkable and understanding the underlying physics may very well shed new light on the nature of superconductivity.

An accurate description of the physical properties of SCCO naturally hinges on the knowledge of the electron/hole distribution in the compound. Yet, no microscopic investigations were available, with electron/hole distributions proposed based on meso- and macroscopic measurements varying widely. In EELS, the holes give rise to a pre-peak to the O-K edge, which was mapped with atomic resolution across several unit cells. Indeed, more holes appeared to be on the "chain-atoms" than on the "ladder-atoms".

However, an accurate quantification at atomic resolution can easily be precluded by, e.g., elastic scattering as mentioned above. For example, when using a very small, highly convergent beam (as in scanning transmission electron microscopy (STEM)), beam spreading can occur. This means that even though the experimenter positions the beam on a particular atomic column, atoms in many neighboring columns could contribute to the overall EELS intensity. Furthermore, the beam's quantum state (including its propagation direction) when hitting an atom can influence the probability with which various transitions are excited, thus also influencing the spectral shape and the overall quantification.

Only detailed simulations including both elastic and inelastic scattering effects such as with the formalism outlined above allow predicting such "artifacts"[5]. Using combined elastic and inelastic scattering simulations, I was able to quantify the contribution of neighboring atoms in the experiment in chapter 2 to amount to around 16 %. This allowed an accurate and reliable determination of the hole distribution in $Sr_3Ca_{11}Cu_{24}O_{41}$, with $\approx$ 4 holes ($\approx$ 0.4 holes per Cu) in the chains and $\approx$ 2 holes ($\approx$ 0.14 holes per Cu) in the ladders.

In addition to predicting the complex interplay between elastic and inelastic scattering to simulate conventional high-resolution STEM-EELS experiments, eqs. 3–6 also enable the design and evaluation of new experiments with unprecedented spatial resolution. Eq. 3 indicates that the electron beam will predominantly scatter into final states $|f\rangle$ for which the matrix element $\langle f| \langle F|\hat{V}|I\rangle |i\rangle$ is large. For an incident plane wave (i.e., the case of ideal energy-filtered TEM (EFTEM); with

---

[5] I.e., the difference between the theoretical spectrum of a single, "ideal", free-floating atom hit by a perfect plane wave, which is closely related to the atom's DOS, and the real spectrum expected for a real sample with finite thickness through which the beam has to propagate.

$\rho_i(\boldsymbol{k}, \boldsymbol{k}') = \delta(\boldsymbol{k} - \boldsymbol{k}_0)\delta(\boldsymbol{k}' - \boldsymbol{k}_0))$, eq. 4 reduces to

$$\rho_f(\boldsymbol{k}, \boldsymbol{k}', E) = \frac{S(\boldsymbol{k}_0 - \boldsymbol{k}, \boldsymbol{k}_0 - \boldsymbol{k}', E)}{|\boldsymbol{k}_0 - \boldsymbol{k}|^2 |\boldsymbol{k}_0 - \boldsymbol{k}'|^2}. \tag{7}$$

Assuming $\boldsymbol{k}_0 \parallel \boldsymbol{z}$, $k_z = k'_z = k_{0z} - q_E$, and performing a Fourier transform $\{k_x, k_y\} \mapsto \{x, y\}$ yields

$$\rho_f(\boldsymbol{r}, \boldsymbol{r}', E) = \mathcal{F}[S(\boldsymbol{k}_0 - \boldsymbol{k}, \boldsymbol{k}_0 - \boldsymbol{k}', E)] * (K_0(rq_E)K_0(r'q_E)). \tag{8}$$

where $q_E = k_0 E/(\gamma m_0 c^2)$ is the characteristic momentum transfer due to the energy loss [8], K_0 is the modified Bessel of second kind and order zero, and $*$ denotes a convolution. As the Fourier transform of eq. 6 essentially results in δ-distributions in space, it is reasonable to assume that the outgoing density matrix is large in places where both $|I\rangle$ and $|F\rangle$ are strong. Indeed, initial calculations corroborated this conclusion (see chapter 1).

To design a suitable experiment, two key ingredients are crucial: spatial resolution of the instrument and energy separation of the investigated states. The importance of spatial resolution is obvious: the characteristic length scale of the features can be expected to be of the order of the size of the overlap region between $|I\rangle$ and $|F\rangle$, which is generally smaller than half the chemical bond length (i.e., half the inter-atomic distance), which is typically a few Å. Therefore, obtaining maps with well-resolved orbital information requires a spatial resolution of the maps of well below 1 Å.

The importance of the energy-separation of the states is less obvious at first glance. Naturally, when the states overlap in energy, they cannot be mapped separately using EELS. This, in turn, has severe implications for the possibility of distinguishing their effects on the map. Fig. 1 shows exemplary images calculated for graphene. In the 300 keV case[6], it is immediately apparent that no sp^2 directional information is visible when viewing the graphene perpendicular to the plane while such information is visible when viewing the sample parallel to the plane.

The visibility of the orientation dependence in graphene can also be derived analytically. The transitions are of the form $|s\rangle \to |sp^2\rangle$, with the real-space representations

$$\begin{aligned} \langle \boldsymbol{R}|I\rangle &= \langle \boldsymbol{R}|s\rangle = f_I(R) Y_0^0(\boldsymbol{R}/R) \\ \langle \boldsymbol{R}|F\rangle &= \langle \boldsymbol{R}|sp^2\rangle = \frac{f_F(R)}{\sqrt{3}} \left(Y_0^0(\boldsymbol{R}/R) + \mathrm{e}^{-\mathrm{i}\varphi_0} Y_1^1(\boldsymbol{R}/R) - \mathrm{e}^{\mathrm{i}\varphi_0} Y_1^{-1}(\boldsymbol{R}/R) \right) \end{aligned} \tag{9}$$

where Y_l^m are spherical harmonics and φ_0 determines the orientation of the sp^2 orbital. In the following, $p_I = 1$, $p_F = 0$ are assumed. In addition, the explicit energy-dependence of the MDFF is omitted for brevity. Thus, eq. 6 takes the form

$$S(\boldsymbol{q}, \boldsymbol{q}') = \sum_{\varphi_0 \in \{\alpha, \alpha + \frac{2\pi}{3}, \alpha + \frac{4\pi}{3}\}} \langle sp^2 | \mathrm{e}^{-\mathrm{i}\boldsymbol{q}\cdot\hat{\boldsymbol{R}}} | s \rangle \langle s | \mathrm{e}^{\mathrm{i}\boldsymbol{q}'\cdot\hat{\boldsymbol{R}}} | sp^2 \rangle \tag{10}$$

---

[6] This case is included for illustrative purpose only. Due to beam damage, graphene gradually becomes more and more unstable above around 80 keV [21–23]. Therefore, real experiments should be performed below that threshold. The case of 60 keV will be discussed below.

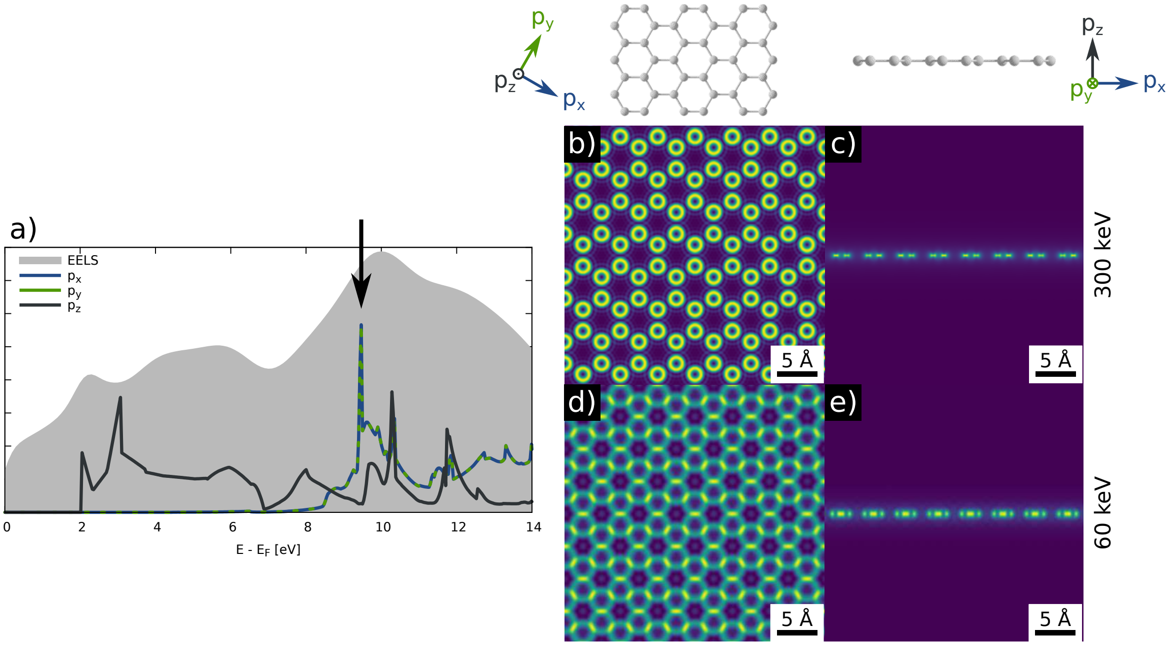

Figure 1.: Simulated real-space maps for the K-Edge of graphene. a) pDOS and total EELS spectrum as calculated with WIEN2k [20]. The arrow indicates the energy of the target's final states used in the maps. b–d) Calculated maps for a viewing direction perpendicular (b,d) and parallel (c,e) to the plane for an incident plane wave with an energy of 300 keV (b,c) and 60 keV (d,e), respectively. All calculations were performed without aberrations and with an acceptance angle of $\beta = 50\,\text{mrad}$.

with the global sample orientation given by α. Using the Rayleigh expansion [24],

$$\mathrm{e}^{\mathrm{i}\boldsymbol{q}\cdot\boldsymbol{R}} = 4\pi \sum_{\lambda=0}^{\infty} \sum_{\mu=-\lambda}^{\lambda} \mathrm{i}^{\lambda} Y_{\lambda}^{\mu}(\boldsymbol{q}/q)^{*} Y_{\lambda}^{\mu}(\boldsymbol{R}/R) j_{\lambda}(qR), \tag{11}$$

the angular integrals of the individual terms can be evaluated and written using Wigner-3j-symbols [24], resulting in

$$\begin{align}
&\sum_{\lambda,\mu} \int Y_0^0(\boldsymbol{R}/R)^{*} Y_{\lambda}^{\mu}(\boldsymbol{R}/R) Y_L^M(\boldsymbol{R}/R)\mathrm{d}\Omega \tag{12}\\
&= \sqrt{\frac{(2\lambda+1)(2L+1)}{4\pi}} \begin{pmatrix} 0 & \lambda & L \\ 0 & 0 & 0 \end{pmatrix} \begin{pmatrix} 0 & \lambda & L \\ 0 & \mu & M \end{pmatrix} \tag{13}\\
&= \frac{(2L+1)}{\sqrt{4\pi}} \begin{pmatrix} 0 & L & L \\ 0 & 0 & 0 \end{pmatrix} \begin{pmatrix} 0 & L & L \\ 0 & -M & M \end{pmatrix} \delta_{\lambda,L}\delta_{\mu,-M} \tag{14}\\
&= \frac{(-1)^M}{\sqrt{4\pi}} \delta_{\lambda,L}\delta_{\mu,-M}. \tag{15}
\end{align}$$

Direct evaluation then yields

$$\begin{align}
S(\boldsymbol{q},\boldsymbol{q}') &= g_0(q)g_0(q') + 3g_1(q)g_1(q')\cos(\varphi_q - \varphi_{q'})\sin(\theta_q)\sin(\theta_{q'}) \nonumber\\
&= g_0(q)g_0(q') + 3g_1(q)g_1(q')(q_x q'_x + q_y q'_y) \tag{16}
\end{align}$$

with

$$g_{\lambda}(q) = \int \frac{f_I(R) f_F(R)}{\sqrt{3}} j_{\lambda}(qR) R^2 \mathrm{d}R. \tag{17}$$

Note that the first term, which stems from the $s \to s$ monopole transitions, is spherically symmetric, while the second, stemming from $s \to p$ dipole transitions, is not.

When viewing graphene perpendicular to the lattice plane, i.e., the diffraction plane corresponding to the q_x, q_y plane with $q_z = q_E$, the diffraction intensity is proportional to

$$S(\boldsymbol{q},\boldsymbol{q}) = g_0(q)^2 + 3g_1^2(q)q_{\perp}^2, \tag{18}$$

i.e. it is rotationally symmetric[7]. Thus, no orientation dependence can be seen, corroborating the results in fig. 1.

When viewing graphene parallel to the lattice plane, e.g., the diffraction plane corresponding to the q_x, q_z plane with $q_y = q_E$, the diffraction intensity is proportional to

$$S(\boldsymbol{q},\boldsymbol{q}) = g_0(q)^2 + 3g_1^2(q)q_E^2 + 3g_1^2(q)q_x^2, \tag{19}$$

i.e. it features a distinct x-dependence, further corroborating the results in fig. 1.

It should be emphasized that the lack of orientation dependence when mapping graphene perpendicular to the plane is by no means obvious. In fact, fig. 1 shows that in the more realistic case of 60 keV, a pseudo-orientation-dependence seems to emerge

---

[7] The same holds for mapping in real-space as can be seen by Fourier-transforming the MDFF.

with an increased image intensity along the sp^2 bonding directions. This, however, comes solely from the (incoherent) superposition of ring-shaped features around each atom, just with a larger ring diameter due to a larger q_E.

This illustrates nicely that in-depth simulations are necessary both to accurately predict and correctly interpret real-space maps of electronic states, and that such maps can depend on many factors, including sample orientation and symmetry.

Symmetry implicitly enters into the pre-factors of the q_x and q_y terms. In the example of pristine graphene as shown above, the threefold rotational symmetry implies that the q_x and q_y terms have identical prefactors, thus giving rise to the ring-like $q_x^2 + q_y^2$ image dependence.

Chapter 3 explores the situation when the symmetry is deliberately broken, e.g., by dopant atoms or vacancies in graphene. As can be seen there, the symmetry breaking should indeed allow to distinguish electronic states close to the defect. As many interesting effects and applications usually happen at interfaces and defects rather than in perfect single crystals, this is a very valuable outcome.

The first experimental evidence of the novel method for mapping electronic states in real-space is described in chapter 4. In that work, rutile was used as it features a tetragonal unit cell, is more stable and easier to prepare and handle than graphene.

Chapter 5 highlights a very recent publication in which the in-plane graphene experiment described above was performed in a multi-layer graphene stack sandwiched between SiC and Bi_2Se_3. This work demonstrates the excellent quantitative agreement between the simulation and the experiment achievable with the approaches described above.

As shown in chapters 3–5, a crucial factor in the real-space mapping of electronic states is the inherently low SNR. This comes from the fact that even in low-symmetry cases, the energy-splitting between different states is a few eV at best. Therefore, very narrow energy ranges need to be used to selectively image individual states, resulting in a relatively low image intensity even for high incident doses. One possible approach to potentially overcoming the challenge of low SNR in the future will be discussed in part IV.

In summary, my work presented in this part substantially furthered the understanding of the interaction between the electron beam and the sample, in particular in the context of inelastic scattering. This not only allows to dramatically improve the accuracy of EELS quantifications on the atomic scale, it also allowed me to develop a new method for mapping the real-space distribution of individual electronic states inside the sample.

Chapter 1

A pure state decomposition approach of the mixed dynamic form factor for mapping atomic orbitals

S. Löffler, V. Motsch, and P. Schattschneider

Ultramicroscopy 131 (2013) 39–45
10.1016/j.ultramic.2013.03.021

Ultramicroscopy 131 (2013) 39–45

Contents lists available at SciVerse ScienceDirect

Ultramicroscopy

journal homepage: www.elsevier.com/locate/ultramic

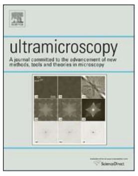

A pure state decomposition approach of the mixed dynamic form factor for mapping atomic orbitals

S. Löffler [a],*, V. Motsch [a], P. Schattschneider [a,b]

[a] Institute of Solid State Physics, Vienna University of Technology, Vienna, Austria
[b] University Service Centre for Electron Microscopy, Vienna University of Technology, Vienna, Austria

ARTICLE INFO

Article history:
Received 25 October 2012
Received in revised form
26 March 2013
Accepted 29 March 2013
Available online 6 April 2013

Keywords:
Inelastic scattering
Mixed dynamic form factor
Orbital mapping
EFTEM

ABSTRACT

We demonstrate how the mixed dynamic form factor (MDFF) can be interpreted as a quadratic form. This makes it possible to use matrix diagonalization methods to reduce the number of terms that need to be taken into account when calculating the inelastic scattering of electrons in a crystal. It also leads in a natural way to a new basis that helps elucidate the underlying physics. The new method is applied to several cases to show its versatility. In particular, predictions are made for directly imaging atomic orbitals in crystals.

1. Introduction

Nowadays, simulations are indispensable both for planning and for interpreting experiments in the transmission electron microscope (TEM), in particular when working with electron energy loss spectrometry (EELS). The key quantity for simulating inelastic electron scattering is the mixed dynamic form factor (MDFF) [1–4]. In many cases, this complex quantity is simplified by several approximations, like, for instance, the dipole approximation. Recently, it has been shown, however, that this can lead to quite severe errors [5]. Furthermore, with recent advances of aberration corrected microscopes, more accurate calculations of the MDFF will become essential for future experiments.

In this work, we will give a brief repetition of the mixed dynamic form factor. It has been well known for a long time that in dipole approximation, the MDFF can be written in the form $a\mathbf{q}\cdot\mathbf{q}'$ ($+\mathbf{q}\times\mathbf{q}'$ in the case of magnetism; see, e.g., [6,7]). Our work goes beyond this approximation by showing that all multipole orders can be written as a quadratic form. This is followed by an analysis of how a basis transformation can bring it into a simpler, diagonal form that is much easier to handle numerically. Furthermore, the physical significance of this procedure will be outlined. The general concept of factorizing and diagonalizing density matrices (i.e., writing the corresponding density operator as an incoherent sum of pure states) is well known [8,9] and is also applied in other fields (e.g., [10]). However, to the best of our knowledge, it was not yet applied in the way presented here to simplify the MDFF.

In the last part, the new formalism will be applied to both existing and new measurement setups to study its applicability and versatility.

2. The mixed dynamic form factor and its pure state decomposition

In the most general approach, the quantum mechanical system consisting of both the probe electron and the sample can best be described by a density operator $\hat{\rho}$ or its matrix elements, the so-called density matrix ρ [8]. Adopting the density matrix formalism instead of the simpler wave function approach is greatly beneficial as one cannot observe the target's final state directly. This ignorance of a part of the system after an inelastic interaction gives rise to a mixed state which can be described very effectively using the density matrix [3,4,8].

Before the interaction, the probe and the target systems can be considered independent. For the sake of simplicity, we will furthermore assume that both systems are initially in a pure state, i.e., each can be described by a single wave function. Then, the density operator of the whole system before the interaction is given by

$$\hat{\rho}_{\mathrm{tot},0} = |i\rangle\langle i|\otimes|I\rangle\langle I| = |I\rangle|i\rangle\langle i|\langle I|, \tag{1}$$

---

* Corresponding author. Tel.: +43 15880113815.
E-mail address: stefan.loeffler@tuwien.ac.at (S. Löffler).

0304-3991/$ - see front matter © 2013 Elsevier B.V. All rights reserved.
http://dx.doi.org/10.1016/j.ultramic.2013.03.021

where $\otimes$ denotes the direct product. Throughout this paper, we use small letters when referring to the probe beam and capital letters when referring to the target.

In first order Born approximation, the density operator after the inelastic interaction mediated by an interaction potential $\hat{V}$ is given by

$$\hat{\rho}_{\text{tot}} = \hat{V}|I\rangle|i\rangle\langle i|\langle I|\hat{V}^{\dagger}\delta(E+E_I-E_F), \tag{2}$$

where E is the "energy loss" of the probe beam (i.e., the energy transferred from the probe beam to the target electron), and E_I, E_F are the initial and final state energies of the target. Since the target system is not observed directly, one has to construct the reduced density operator for the probe beam by summing incoherently over all possible final states of the target. This reduced density operator is given by

$$\hat{\rho} = \sum_F \langle F|\hat{V}|I\rangle|i\rangle\langle i|\langle I|\hat{V}^{\dagger}|F\rangle\delta(E+E_I-E_F), \tag{3}$$

which can then be propagated elastically through the crystal and be used to predict the outcome of measurements in different geometries. It must be emphasized that the ordering of the terms is vital here, since $\hat{V}$ in general acts on both the probe and the target states, which results in an entanglement of the two.

In EELS experiments, the interaction operator $\hat{V}$ is the Coulomb interaction operator. Its two most common basis representations are in configuration space,

$$\begin{aligned}\hat{V}(\boldsymbol{r},\boldsymbol{r}') = \langle\boldsymbol{r}|\hat{V}|\boldsymbol{r}'\rangle &= \frac{e^2}{4\pi\epsilon_0}\frac{\delta(\hat{\boldsymbol{R}}-\hat{\boldsymbol{R}}')}{|\boldsymbol{r}-\hat{\boldsymbol{R}}|}\delta(\boldsymbol{r}-\boldsymbol{r}')\\ &=: \hat{V}(\boldsymbol{r})\delta(\boldsymbol{r}-\boldsymbol{r}'),\end{aligned} \tag{4}$$

and in reciprocal space,

$$\begin{aligned}\hat{V}(\boldsymbol{k},\boldsymbol{k}') = \langle\boldsymbol{k}|\hat{V}|\boldsymbol{k}'\rangle &= \frac{e^2}{4\pi\epsilon_0}\frac{\mathrm{e}^{\mathrm{i}(\boldsymbol{k}'-\boldsymbol{k})\cdot\hat{\boldsymbol{R}}}}{|\boldsymbol{k}'-\boldsymbol{k}|^2}\delta(\hat{\boldsymbol{R}}-\hat{\boldsymbol{R}}')\\ &=: \frac{e^2}{4\pi\epsilon_0}\frac{\mathrm{e}^{\mathrm{i}\boldsymbol{q}\cdot\hat{\boldsymbol{R}}}}{|\boldsymbol{q}|^2}\delta(\hat{\boldsymbol{R}}-\hat{\boldsymbol{R}}')\\ &=: \hat{V}(\boldsymbol{q}).\end{aligned} \tag{5}$$

Here, e is the elementary charge and ϵ_0 is the permittivity of vacuum.

In these two representations, the reduced density matrix reads

$$\begin{aligned}\rho(\boldsymbol{r},\boldsymbol{r}') &= -4\pi^2\sum_F\int \mathrm{d}\tilde{\boldsymbol{r}}\langle F|\langle\boldsymbol{r}|\hat{V}|\tilde{\boldsymbol{r}}\rangle|I\rangle\langle\tilde{\boldsymbol{r}}|i\rangle\\ &\quad\int \mathrm{d}\tilde{\boldsymbol{r}}'\langle i|\tilde{\boldsymbol{r}}'\rangle\langle I|\langle\tilde{\boldsymbol{r}}'|\hat{V}^{\dagger}|\boldsymbol{r}'\rangle|F\rangle\delta(E+E_I-E_F)\\ &= -4\pi^2\sum_F\langle F|\hat{V}(\boldsymbol{r})|I\rangle\langle I|\hat{V}^{\dagger}(\boldsymbol{r}')|F\rangle\\ &\quad\langle\boldsymbol{r}|i\rangle\langle i|\boldsymbol{r}'\rangle\delta(E+E_I-E_F)\\ &= S(\boldsymbol{r},\boldsymbol{r}')\langle\boldsymbol{r}|i\rangle\langle i|\boldsymbol{r}'\rangle\end{aligned}$$

$$\begin{aligned}\rho(\boldsymbol{k},\boldsymbol{k}') &= -4\pi^2\sum_F\int \mathrm{d}\tilde{\boldsymbol{k}}\langle F|\langle\boldsymbol{k}|\hat{V}|\tilde{\boldsymbol{k}}\rangle|I\rangle\langle\tilde{\boldsymbol{k}}|i\rangle\\ &\quad\int \mathrm{d}\tilde{\boldsymbol{k}}'\langle i|\tilde{\boldsymbol{k}}'\rangle\langle I|\langle\tilde{\boldsymbol{k}}'|\hat{V}^{\dagger}|\boldsymbol{k}'\rangle|F\rangle\delta(E+E_I-E_F)\\ &= -4\pi^2\sum_F\iint \mathrm{d}\boldsymbol{q}\,\mathrm{d}\boldsymbol{q}'\langle F|\hat{V}(\boldsymbol{q})|I\rangle\langle I|\hat{V}^{\dagger}(\boldsymbol{q}')|F\rangle\\ &\quad\langle\boldsymbol{k}+\boldsymbol{q}|i\rangle\langle i|\boldsymbol{k}'+\boldsymbol{q}'\rangle\delta(E+E_I-E_F)\\ &= \iint \mathrm{d}\boldsymbol{q}\,\mathrm{d}\boldsymbol{q}'S(\boldsymbol{q},\boldsymbol{q}')\langle\boldsymbol{k}+\boldsymbol{q}|i\rangle\langle i|\boldsymbol{k}'+\boldsymbol{q}'\rangle.\end{aligned} \tag{6}$$

Here, the MDFF $S(\boldsymbol{q},\boldsymbol{q}')$ and the real-space MDFF (rMDFF) $S(\boldsymbol{r},\boldsymbol{r}')$ were introduced which are related by a Fourier transformation.[1] It is noteworthy that — due to the particular properties of the Coulomb operator — the rMDFF can be multiplied on the initial probe wave functions, whereas the MDFF has to be convolved with them.

In order to perform calculations, one not only has to specify a basis for the probe states, but also for the target states. Usually, one chooses a spherical harmonics basis which is particularly useful for describing the tightly bound initial states that give rise to EELS core losses. Hence, the initial state is written as $|l\frac{1}{2}jj_z\rangle$,[2] while the final states are expanded in terms of $|LM\frac{1}{2}S\rangle$. In the following, we will also sum incoherently over j_z since that quantum number of the initial state is typically unknown. In the Kohn–Sham approximation, the MDFF is then given by [11–13]

$$\begin{aligned}S(\boldsymbol{q},\boldsymbol{q}') &= -4\pi^2\sum_{Fj_z}\sum_{LMSL'M'S'}\left\langle F|LM\frac{1}{2}S\right\rangle\left\langle LM\frac{1}{2}S|\hat{V}(\boldsymbol{q})|l\frac{1}{2}jj_z\right\rangle\\ &\quad\left\langle l\frac{1}{2}jj_z|\hat{V}^{\dagger}(\boldsymbol{q}')|L'M'\frac{1}{2}S'\right\rangle\left\langle L'M'\frac{1}{2}S'|F\right\rangle\delta(E+E_I-E_F)\\ &= -\frac{\pi e^4}{\epsilon_0^2q^2q'^2}(2l+1)(2j+1)\sum_{mm'}\sum_{LMSL'M'S'}\sum_{\lambda\mu}\sum_{\lambda'\mu'}\\ &\quad\mathrm{i}^{\lambda-\lambda'}\sqrt{(2\lambda+1)(2\lambda'+1)(2L+1)(2L'+1)}\\ &\quad Y_\lambda^\mu(\boldsymbol{q}/q)^*\langle j_\lambda(q)\rangle_{ELSj}Y_{\lambda'}^{\mu'}(\boldsymbol{q}'/q')\langle j_{\lambda'}(q')\rangle_{EL'S'j}\\ &\quad\begin{pmatrix} l & \lambda & L\\ 0 & 0 & 0\end{pmatrix}\begin{pmatrix} l & \lambda' & L'\\ 0 & 0 & 0\end{pmatrix}\\ &\quad\begin{pmatrix} l & \lambda & L\\ -m & \mu & M\end{pmatrix}\begin{pmatrix} l & \lambda' & L'\\ -m' & \mu' & M'\end{pmatrix}\\ &\quad\sum_{j_z}(-1)^{m+m'}\begin{pmatrix} l & \frac{1}{2} & j\\ m & S & -j_z\end{pmatrix}\begin{pmatrix} l & \frac{1}{2} & j\\ m' & S' & -j_z\end{pmatrix}\\ &\quad\sum_{\boldsymbol{k}n}D_{LMS}^{\boldsymbol{k}n}(D_{L'M'S'}^{\boldsymbol{k}n})^*\delta(E+E_{nlj}-E_{\boldsymbol{k}n}).\end{aligned} \tag{7}$$

Here,

$$\langle j_\lambda(q)\rangle_{ELSj} = \int u_{LS}(r)j_\lambda(qr)R_{lj}(r)r^2\,\mathrm{d}r \tag{8}$$

is the weighted radial wave function overlap [11,14] with the initial state's radial wave function $R_j(r)$, the final state's radial wave function $u_{LS}(r)$[3] and the spherical Bessel function j_λ. The $\sum_{\boldsymbol{k}n}D_{LMS}^{\boldsymbol{k}n}(D_{L'M'S'}^{\boldsymbol{k}n})^*$ (over a shell of constant energy) is the cross-density of states (XDOS) and the $\begin{pmatrix}\cdot & \cdot & \cdot\\ \cdot & \cdot & \cdot\end{pmatrix}$ are Wigner 3j symbols.

While this choice of basis is very convenient as a starting point (as it is used, e.g., in WIEN2k [15]), it is by no means the only or the optimal choice. This can be seen by collecting terms depending on $\boldsymbol{q}$ and terms depending on $\boldsymbol{q}'$. With the abbreviations

$$\alpha = (\lambda,\mu,L,S)$$

$$\alpha' = (\lambda',\mu',L',S')$$

$$g_\alpha(\boldsymbol{q}) = \frac{1}{q^2}Y_\lambda^\mu(\boldsymbol{q})\langle j_\lambda(q)\rangle_{ELSj}$$

$$\begin{aligned}\Xi_{\alpha\alpha'} &= -\frac{\pi e^4}{\epsilon_0^2}(2l+1)(2j+1)\sum_{mm'}\sum_{MM'}\\ &\quad\mathrm{i}^{\lambda-\lambda'}\sqrt{(2\lambda+1)(2\lambda'+1)(2L+1)(2L'+1)}\\ &\quad\begin{pmatrix} l & \lambda & L\\ 0 & 0 & 0\end{pmatrix}\begin{pmatrix} l & \lambda' & L'\\ 0 & 0 & 0\end{pmatrix}\\ &\quad\begin{pmatrix} l & \lambda & L\\ -m & \mu & M\end{pmatrix}\begin{pmatrix} l & \lambda' & L'\\ -m' & \mu' & M'\end{pmatrix}\end{aligned}$$

---

[1] Contrary to the convention adopted in previous works, we include the $1/q^2q'^2$ term in the definition of the MDFF as it makes the definition more concise and easy to use.

[2] This takes into account the spin-orbit coupling of the tightly bound core states [11].

[3] This is to be understood as the radial wave function of the projection of the (delocalized) final Bloch state onto an LS state at the scattering center, e.g., a muffin-tin state.

$$\sum_{j_z}(-1)^{m+m'}\begin{pmatrix} l & \frac{1}{2} & j \\ m & S & -j_z \end{pmatrix}\begin{pmatrix} l & \frac{1}{2} & j \\ m' & S' & -j_z \end{pmatrix}$$
$$\sum_{\boldsymbol{k}n} D^{\boldsymbol{k}n}_{LMS}(D^{\boldsymbol{k}n}_{L'M'S'})^{*}\delta(E+E_{nl\kappa}-E_{\boldsymbol{k}n}), \tag{9}$$

the MDFF can be rewritten as

$$\begin{aligned} S(\boldsymbol{q},\boldsymbol{q}') &= \sum_{\alpha\alpha'} g_\alpha(\boldsymbol{q})^{*}\Xi_{\alpha\alpha'}g_{\alpha'}(\boldsymbol{q}') \\ &= \boldsymbol{g}(\boldsymbol{q})^{\dagger}\cdot\boldsymbol{\Xi}\cdot\boldsymbol{g}(\boldsymbol{q}'), \end{aligned} \tag{10}$$

where the matrix $\boldsymbol{\Xi}$ collects all $\boldsymbol{q},\boldsymbol{q}'$ independent terms and can be computed in a straight-forward way once the XDOS is known (e.g., from DFT calculations; note that this is a property of the target alone, and therefore has to be calculated only once). The $\boldsymbol{g}$, in turn, can be interpreted as a vector of functions. Eq. (10) is a well-known quadratic form and an extension of the often-used simple dipole approximation $S(\boldsymbol{q},\boldsymbol{q}') = \boldsymbol{q}\cdot\boldsymbol{A}\cdot\boldsymbol{q}'$ [5–7,16] to arbitrary momentum transfers and multipole orders. In particular, it is noteworthy that $\boldsymbol{\Xi}$ is hermitian (as is shown in Appendix A).

With the default settings, the program WIEN2k produces data with $0\leq L, L'\leq 3$. When including transitions up to quadrupole order ($\lambda = 2$), $\boldsymbol{\Xi}$ is a 72×72 matrix, resulting in up to 5184 terms in the MDFF that in principle would all have to be handled separately. In practice, some of the entries vanish due to selection rules, while for some others the hermiticity of $\boldsymbol{\Xi}$ can be exploited. Still, many off-diagonal elements generally remain. These off-diagonal elements imply correlations between the basis vectors [4] and hence represent additional information (e.g., symmetries) about the underlying system that can be used to simplify the problem.

To exploit this additional information, one can insert a unitary matrix $\boldsymbol{U}$ in the following way:

$$S(\boldsymbol{q},\boldsymbol{q}') = \boldsymbol{g}(\boldsymbol{q})^{\dagger}\cdot\boldsymbol{U}^{\dagger}\boldsymbol{U}\cdot\boldsymbol{\Xi}\cdot\boldsymbol{U}^{\dagger}\boldsymbol{U}\cdot\boldsymbol{g}(\boldsymbol{q}'). \tag{11}$$

Since for any hermitian matrix, a unitary matrix exists such that $\boldsymbol{U}\boldsymbol{\Xi}\boldsymbol{U}^{\dagger}$ is a diagonal matrix $\boldsymbol{D}$, one only has to find such a $\boldsymbol{U}$. This is straight forward using, e.g., eigenvalue solvers, a singular value decomposition, or a Schur decomposition. With the abbreviation $\tilde{\boldsymbol{g}}(\boldsymbol{q}) = \boldsymbol{U}\cdot\boldsymbol{g}(\boldsymbol{q})$, the MDFF becomes

$$S(\boldsymbol{q},\boldsymbol{q}') = \tilde{\boldsymbol{g}}(\boldsymbol{q})^{\dagger}\cdot\boldsymbol{D}\cdot\tilde{\boldsymbol{g}}(\boldsymbol{q}'). \tag{12}$$

In terms of quadratic forms, the transformation $\boldsymbol{U}$ is a principal axis transformation. In quantum mechanical terms, it is a basis transformation into the eigensystem of the MDFF. In essence, it recovers the "physical" basis of independent — i.e., uncorrelated because of vanishing off-diagonal terms — transitions.[4] With the default settings of WIEN2k, this means that the problem was reduced from at most 5184 terms to at most 72 terms. This is related directly to the internal crystal symmetries that are taken into account in WIEN2k. The information theoretical aspect of the effect (general) symmetry groups have on inelastic electron scattering has recently been studied by Dwyer [17].

In practical applications, knowing the "physical" basis is important for understanding how the excitation process works. A priori, it is not clear how the independent transitions look like. One could have, e.g., a p_x-like transition as one would expect from $s\rightarrow p$ transitions, or a coherent superposition like a vortex-like transition similar to $(p_x - ip_y)/\sqrt{2}$, or something like an s–p hybrid transition, or something even more complicated. Of course, all this information is present in the $\boldsymbol{\Xi}$ matrix, but it is not readily accessible in general. However, knowing it is very important when planning experiments (e.g., for knowing the diffraction angles at which to place an objective aperture, or to interpret recorded images in terms of these transitions and possibly different involved final states of the target). For this, the diagonalization can help as it produces exactly these uncorrelated transitions.

In numerical simulations, it is usually beneficial to work with the rMDFF as it can be multiplied directly onto the incident density matrix. Since the rMDFF is related to the MDFF by a Fourier transformation and the $\boldsymbol{q}$ and $\boldsymbol{q}'$ dependencies have been decoupled, the rMDFF simply reads

$$S(\boldsymbol{r},\boldsymbol{r}') = \tilde{\boldsymbol{g}}(\boldsymbol{r})^{\dagger}\cdot\boldsymbol{D}\cdot\tilde{\boldsymbol{g}}(\boldsymbol{r}') \tag{13}$$

with the same matrix $\boldsymbol{D}$ as for the MDFF and $\tilde{\boldsymbol{g}}(\boldsymbol{r}) = FT_{\boldsymbol{q}}[\tilde{\boldsymbol{g}}(\boldsymbol{q})]$. By renormalizing the $\tilde{\boldsymbol{g}}$ such that $\overline{g}_\alpha(\boldsymbol{r}) := \sqrt{D_{\alpha\alpha}}\tilde{g}_\alpha(\boldsymbol{r})$, the MDFF can be further simplified to

$$S(\boldsymbol{r},\boldsymbol{r}') = \overline{\boldsymbol{g}}(\boldsymbol{r})^{\dagger}\cdot\overline{\boldsymbol{g}}(\boldsymbol{r}') = \sum_\alpha \overline{g}_\alpha(\boldsymbol{r})^{*}\overline{g}_\alpha(\boldsymbol{r}') \tag{14}$$

Hence, the reduced density matrix of the probe electron after the inelastic interaction in configuration space can be written as

$$\rho(\boldsymbol{r},\boldsymbol{r}') = \sum_\alpha(\overline{g}_\alpha(\boldsymbol{r})\phi(\boldsymbol{r}))^{*}\overline{g}_\alpha(\boldsymbol{r}')\phi(\boldsymbol{r}'), \tag{15}$$

where we wrote $\phi(\boldsymbol{r}) = \langle\boldsymbol{r}|i\rangle$ for the incident probe electron wave function. It is quite obvious that the diagonalization of the rMDFF has resulted in a pure state decomposition of the density operator $\hat{\rho} = \sum_\alpha|\alpha\rangle\langle\alpha|$. This is formally equivalent to the spectral decomposition of the cross-spectral density of quasi-monochromatic wave fields in optics [10]. However, contrary to the case in optics, we are dealing with the effects in electronic transitions. In particular, this results in the entanglement of the probe electron and the target, and thus in the necessity to construct the reduced density matrix of the probe beam.

Finally — when measuring a real space image —, the measurable intensity I is given by[5]

$$I(\boldsymbol{r}) = \rho(\boldsymbol{r},\boldsymbol{r}) = \sum_\alpha|\overline{g}_\alpha(\boldsymbol{r})\phi(\boldsymbol{r})|^2 \tag{16}$$

In the description above, elastic scattering of the probe beam after the inelastic scattering event has not been included for the sake of simplicity. Since each $|\alpha\rangle$ in itself is a pure state, it can be propagated elastically through the rest of the crystal with existing methods (e.g., the multislice approach [18]) in a straight-forward way.

For the simulations in Section 3.3, the multislice approach was used first to propagate the incident beam through the crystal. At each atomic position, an inelastic interaction was simulated by calculating the (diagonal) reduced density matrix in Eq. (15). The resulting independent pure states (or rather their corresponding wave functions) were then propagated through the rest of the crystal using the multislice approach again. Here, the diagonalization is of utmost importance as the number of multislice steps to perform is $\mathcal{O}(NL^2)$ where N is the number of non-negligible terms in the MDFF (which can be reduced significantly by the diagonalization procedure) and L is the number of layers (which is fixed by the geometry).

Obviously, the final image must be independent of the basis in which the inelastic scattering is described. However, using the diagonalization method presented here, the number of terms to calculate and hence the numerical complexity can be reduced considerably. In particular, it must be emphasized that this diagonalization has to be done only once, as a preprocessing step, but reduces the number of scattered wave function in each slice of

---

[4] Note that, depending on the EELS-edge and multipole orders considered, it may or may not be possible to determine the "physical" basis $|F\rangle$ of the *target* from these transitions. Considering, e.g., a dipole-allowed transition from an initial p state to a final d state, one has only three transition elements ($\mu\in\{-1,0,1\}$), but 5 final states. Under these circumstances, not all information about the final states can be probed, unless one takes into account other multipole orders or final states.

[5] Here, an ideal lens system is assumed. Real lenses will reduce the level of detail transferred to the image, but do not change the coherence properties of the partial waves.

the multislice calculation. Hence, it has a huge impact on the overall computation time.

3. Applications

In this section, we will apply the method outlined above to some model systems. The first two are included for didactic reasons as they demonstrate that the new method is consistent with previous findings. The third one is a more complicated real system.

3.1. Single atom

For single, individual atoms, all final states are independent of one another and hence uncorrelated. In addition, in the absence of a (strong) external magnetic field, states with the same L, but different M or S can be considered degenerate. For the XDOS, this means

$$\sum_{\mathbf{k}n} D^{\mathbf{k}n}_{LMS} (D^{\mathbf{k}n}_{L'M'S'})^* = D_L \delta_{LL'} \delta_{MM'} \delta_{SS'}. \tag{17}$$

In the case of no spin-polarization, the $\langle j_\lambda \rangle$ also do not depend on S, the sum over S, S' can be carried out, and the spin-dependence of α can be dropped. Using the orthogonality relations for the Wigner 3j symbols, a short calculation then yields

$$\Xi_{\alpha\alpha'} = 4\pi(2L+1)(2j+1) \begin{pmatrix} l & \lambda & L \\ 0 & 0 & 0 \end{pmatrix}^2 D_L \delta_{\lambda\lambda'} \delta_{\mu\mu'} \delta_{LL'}, \tag{18}$$

Hence, for single, isolated atoms, Ξ is diagonal in the (λ, μ, L, S) basis, i.e., no correlations occur, even in the untransformed basis. More precisely, for the case discussed later, it is $2(2\lambda+1)$ fold degenerate in μ and S (but not in L, in general). This is intimately connected to the fact that Ξ commutes with the rotation group of the single atom, and the λth irreducible representation of the full infinitesimal rotation group is $2(2\lambda+1)$ dimensional.

The angular dependence in the image is influenced only by the (azimuthal part of the) spherical harmonics.[6] Since all off-diagonal terms ($\mu \neq \mu'$) vanish and all μ have the same weighting, the incoherent summation over different $|\alpha\rangle$ in Eq. (16) gives terms of the form $\sum_\mu Y^\mu_\lambda(\mathbf{q}/q)^* Y^\mu_\lambda(\mathbf{q}/q)$. Since q_z is given by the energy-loss and is constant [5], this can be rewritten as $\sum_\mu Y^\mu_\lambda(\theta,\phi)^* Y^\mu_\lambda(\theta,\phi')$ with constant θ. Fourier transformation into real space transforms $\exp(i\mu\phi)$ into $\exp(i\mu\phi)$ up to a constant phase factor [19]. So, measuring in real space (this implies $\phi = \phi'$) gives $\sum_\mu |e^{i\mu\phi}|^2 = (2\lambda+1)/(4\pi)$ which is constant. This gives rise to circular intensity profiles regardless of the symmetries of the target's initial or final states.

3.2. Energy-loss magnetic chiral dichroism

Since its discovery in 2006 [11], interest in the energy loss magnetic chiral dichroism (EMCD) technique has been growing steadily. Using EMCD, one can determine the magnetic properties of the sample [20], similar to the X-ray magnetic circular dichroism which is a standard method in the synchrotron. The pure state decomposition approach outlined here can also be applied to EMCD.

For the sake of simplicity, we assume here a fully spin-polarized ($\delta_{S\frac{1}{2}} \delta_{S'\frac{1}{2}}$) dipole-allowed ($\lambda = \lambda' = 1$) transition from an initial p ($l = 1$) to a final d ($L = L' = 2$) state, as is the dominant contribution to the L-edge in most common magnetic materials. In addition, we assume that states with same L, but different M are (mostly) degenerate, as in the isolated atom case. Hence, the XDOS reads

$$\sum_{\mathbf{k}n} D^{\mathbf{k}n}_{LMS} (D^{\mathbf{k}n}_{L'M'S'})^* = D_2 \delta_{L2} \delta_{L'2} \delta_{MM'} \delta_{S\frac{1}{2}} \delta_{S'\frac{1}{2}}. \tag{19}$$

Under these assumptions, Ξ becomes a 3×3 matrix for both $j = 1/2$ (corresponding to the L_2 edge) and $j = 3/2$ (corresponding to the L_3 edge)

$$\Xi_{j=1/2} = \frac{4\pi D_2}{3} \begin{pmatrix} 1 & 0 & 0 \\ 0 & 2 & 0 \\ 0 & 0 & 3 \end{pmatrix}$$

$$\Xi_{j=3/2} = \frac{4\pi D_2}{3} \begin{pmatrix} 5 & 0 & 0 \\ 0 & 4 & 0 \\ 0 & 0 & 3 \end{pmatrix} \tag{20}$$

As in the single-atom case, Ξ is already diagonal in the spherical harmonics basis. Here, however, different μ have different weights. This means that transforming to any other basis will introduce off-diagonal elements (only (scalar multiples of) the identity matrix is invariant under rotations). Hence, the spherical harmonics basis is the only "physical" basis for EMCD.

Moreover, the Ξ matrices given above can be interpreted as a homogeneous average signal on which the μ-dependent EMCD signal is superimposed

$$\Xi_{j=1/2} = \frac{4\pi D_2}{3} \left[\begin{pmatrix} 2 & 0 & 0 \\ 0 & 2 & 0 \\ 0 & 0 & 2 \end{pmatrix} + \begin{pmatrix} -1 & 0 & 0 \\ 0 & 0 & 0 \\ 0 & 0 & 1 \end{pmatrix} \right]$$

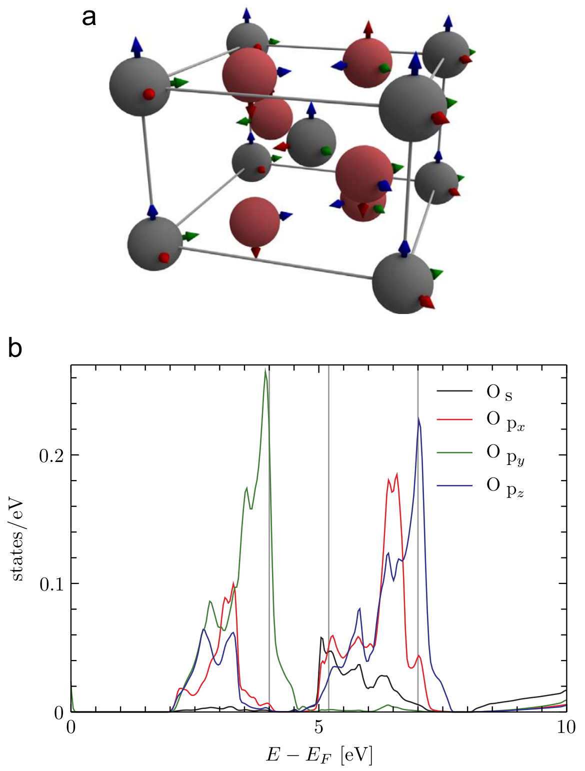

Fig. 1. (a) Schematic of the unit cell for Rutile (gray: Ti, red: O). The lattice constants are $a = 4.594$ Å and $c = 2.958$ Å. The arrows show the symmetry-adapted local coordinate systems (red: x, green: y, blue: z). (b) pDOS of the oxygen states as calculated by WIEN2k. The gray bars show energies used for simulations in this work. (For interpretation of the references to color in this figure caption, the reader is referred to the web version of this paper.)

---

[6] Assuming elastic scattering effects are negligible.

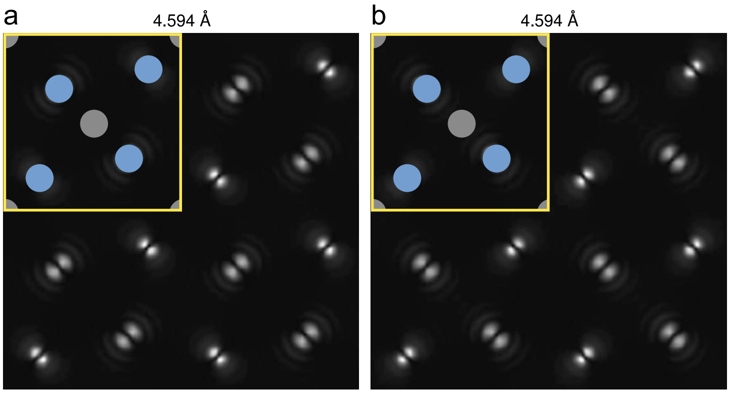

Fig. 2. Real-space intensity of the exit wave after propagation of an incident plane wave through a one unit-cell thick Rutile crystal oriented in [0 0 1] zone axis at 200 kV acceleration voltage. Only dipole-allowed transitions were taken into account. (a) shows the image at an energy loss of E_F+4 eV, whereas (b) shows the image at an energy loss of E_F+7 eV. The insets show the projected unit cell with Ti atoms in gray and O atoms in blue. (For interpretation of the references to color in this figure caption, the reader is referred to the web version of this paper.)

$$\Xi_{j=3/2} = \frac{4\pi D_2}{3}\left[\begin{pmatrix} 4 & 0 & 0 \\ 0 & 4 & 0 \\ 0 & 0 & 4 \end{pmatrix} + \begin{pmatrix} 1 & 0 & 0 \\ 0 & 0 & 0 \\ 0 & 0 & -1 \end{pmatrix}\right] \tag{21}$$

This immediately shows two features common to EELS and EMCD. On the one hand, the homogeneous average signal exhibits the typical, statistical 1:2 intensity ratio of the L_2:L_3 edges. On the other hand, the EMCD signal (the absolute magnitude of which is independent of j in this simple case) shows the typical sign reversal between L_2 and L_3 edges.

3.3. Crystals

In crystals, the situation is more complicated and simple toy-models are insufficient to grasp it completely. Hence, one needs sophisticated calculations to derive the XDOS that take into account the full crystal structure [13,21].[7]

Hence, we will use the oxygen K-edge of Rutile (TiO_2), a tetragonal system, as test case in this work. Fig. 1a shows a schematic of the unit cell, while Fig. 1b shows the partial density of states (pDOS) for oxygen as calculated by WIEN2k. From it, the lifting of the degeneracy of the different p orbitals is already evident.

For this system, WIEN2k produces 89 non-negligible[8] XDOS components at E_F+4 eV, whereas at E_F+7 eV, it produces 100 non-negligible elements in the spin-unpolarized case. In the simplest case of taking into account only dipole-allowed transitions ($\lambda=\lambda'=1$), the 3×3 matrix Ξ has 5 non-vanishing entries, which are reduced to 3 after diagonalization.

Fig. 2a shows the simulated exit wave function intensities (corresponding to an ideal lens system) for a single unit cell after an energy loss of E_F+4 eV. The p type character of the transitions is clearly visible to be pointing in the directions of the green axes in Fig. 1a. Because of the simple, spherically symmetric 1 s nature of the initial state of the oxygen, these p_y type transitions correspond directly to p_y type final states of the oxygen.

Likewise, Fig. 2b shows the simulated exit wave function intensities at an energy loss of E_F+7 eV. There, p type transitions pointing along the blue axes in Fig. 1a corresponding to oxygen p_z orbitals are clearly visible. Naturally, they are rotated by 90° with respect to the p_y orbitals.

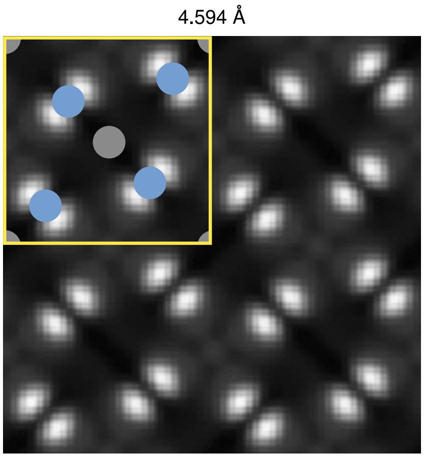

Fig. 3. Real-space intensity of the exit wave after propagation of an incident plane wave through a 10 nm thick Rutile crystal oriented in [0 0 1] zone axis at 200 kV acceleration voltage. A 24 mrad objective aperture was used. Only dipole-allowed transitions were taken into account. The image is taken at an energy loss of E_F+4 eV. The inset shows the projected unit cell with Ti atoms in gray and O atoms in blue. (For interpretation of the references to color in this figure caption, the reader is referred to the web version of this paper.)

Fig. 3 shows the situation for a 10 nm thick crystal and an objective aperture of 24 mrad. For these calculations, elastic scattering both before and after the inelastic interaction was taken into account using the multislice approach [18]. This demonstrates that these results are not only of theoretical interest, but should be measurable in real instruments. The contrast can be estimated to be 96% (after subtraction of the pre-edge background, e.g., using the three-window method).

More importantly, non-dipole transitions can easily be taken into account as well. For the oxygen K-edge, the most relevant non-dipole transition is the monopole transition from the 1 s state to final states with s symmetry.[9] Here, the number of non-negligible terms was reduced from 10 to 4 after diagonalization.

---

[7] The complete investigation of the effects of crystal symmetries on the XDOS and Ξ is beyond the scope of this work.

[8] Here, elements are considered non-negligible if they are larger than 1‰ of the largest element.

[9] The pDOS for d states as produced by WIEN2k that would be accessible by quadrupole-allowed transitions is negligibly small.

Fig. 4 compares the intensities and images of monopole-allowed transitions, dipole-allowed transitions, and the coupling term between the two. A similar effect was predicted recently for X-ray absorption spectrometry [22].

Interestingly, the coupling term gives intensity variations of about ±10% of the dipole-allowed transitions, which is comparable to the monopole transitions. Because the coupling term has a sign, this means that at some positions, it roughly cancels the monopole contributions, whereas at other positions, it can even double it. This acts in a way very similar to s–p hybridization, yielding an asymmetric image.

4. Conclusion and outlook

In this work, we demonstrated a method to diagonalize both the MDFF and the rMDFF leading to a pure state decomposition of the density operator. This was shown to yield obvious numerical

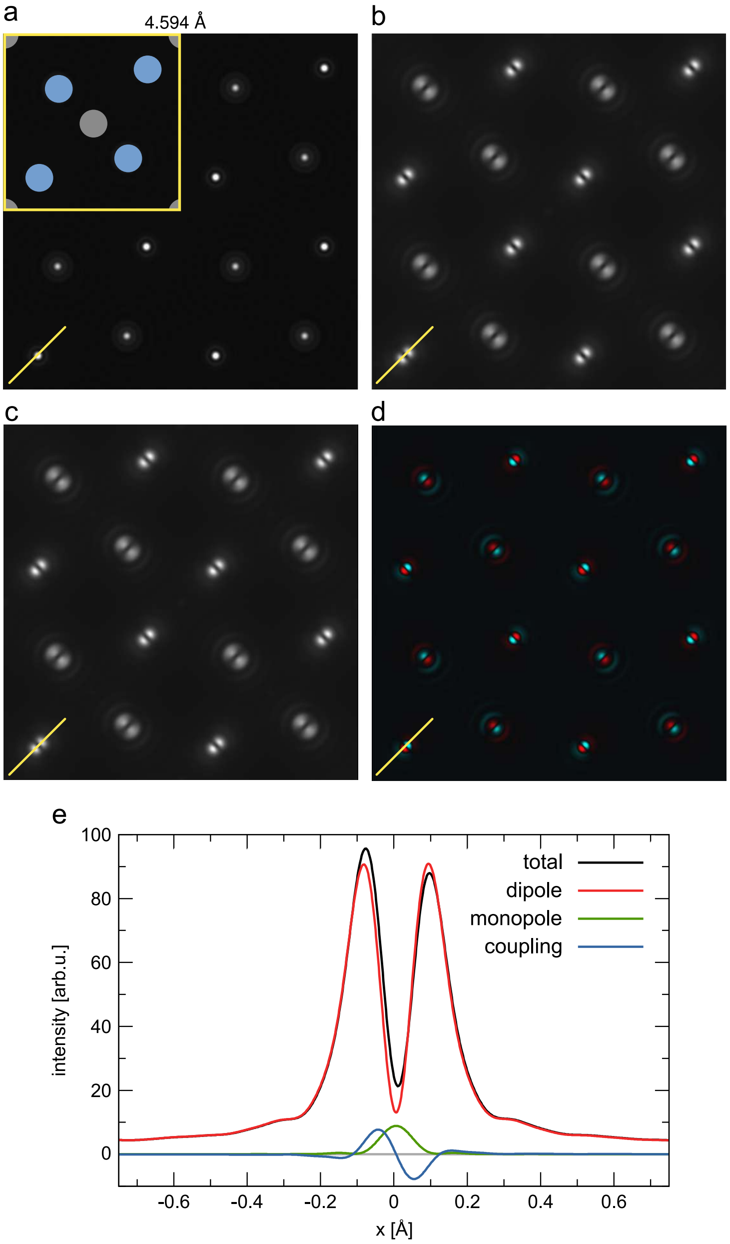

Fig. 4. (a)–(d) Real-space intensities of the exit wave after propagation of an incident plane wave through a one unit cell thick Rutile crystal oriented in [0 0 1] zone axis at 200 kV acceleration voltage. (a) shows only monopole contributions (contrast-enhanced by a factor of 15), (b) shows only dipole contributions, (c) shows the total intensity, and (d) shows the coupling contribution (contrast enhanced by a factor of 15; red indicates positive values while cyan represents negative ones). The images are taken at an energy loss of $E_F + 5.2$ eV. The inset shows the projected unit cell with Ti atoms in gray and O atoms in blue. (e) Traces over the different contributions. The places of the trace are marked by yellow lines in (a)–(d). (For interpretation of the references to color in this figure caption, the reader is referred to the web version of this paper.)

advantages by reducing the number of terms to include in image calculations. Moreover, the diagonalization leads to a new set of basis vectors that are helpful to elucidate the physics underlying the scattering process.

The new pure state decomposition method was applied to the isolated atom case, EMCD, and a Rutile crystal to show its versatility. In particular, the isolated atom and the EMCD cases could be treated analytically, giving results from which important properties such as the L_2:L_3 ratio or the sign reversal of the EMCD effect could be seen immediately.

For the Rutile crystal, it was shown that with latest-generation TEMs, it should be possible to directly map atomic orbitals, e.g., using energy filtered TEM (EFTEM) with high spatial resolution. However, contrary to the common assumption that non-dipole transitions are unimportant, it was shown that the monopole as well as the monopole–dipole coupling terms can change the signal measurably. The necessary condition to achieve this is to have a system with sufficiently low symmetry (otherwise off-diagonal terms vanish due to symmetry considerations [13,21]).

Based on this, the situation for other low-symmetry cases should be the same. Hence, this new technique gives rise to exciting new possibilities like directly studying the electronic structure of defects (see, e.g., [23]), interfaces, or other low-symmetry objects.

Acknowledgments

The authors acknowledge financial support by the Austrian Science Fund (FWF) under Grant number I543-N20. They also want to express their gratitude to Walid Hetaba for fruitful discussions about and help using WIEN2k.

Appendix A. Hermiticity of Ξ

For Ξ to be hermitian, the equation

$$\Xi_{\alpha'\alpha} = \Xi^*_{\alpha\alpha'} \tag{A.1}$$

must hold.

$$\begin{aligned}
\Xi_{\alpha'\alpha} &= 4\pi(2l+1)(2j+1)\sum_{m'm}\sum_{M'M}\delta(E+E_{nl\kappa}-E_{\boldsymbol{k}n})\\
&\times\sqrt{(2\lambda'+1)(2\lambda+1)(2L'+1)(2L+1)}\\
&\times\begin{pmatrix} l & \lambda' & L' \\ 0 & 0 & 0 \end{pmatrix}\begin{pmatrix} l & \lambda & L \\ 0 & 0 & 0 \end{pmatrix}\\
&\times\begin{pmatrix} l & \lambda' & L' \\ -m' & \mu' & M' \end{pmatrix}\begin{pmatrix} l & \lambda & L \\ -m & \mu & M \end{pmatrix}\\
&\times\sum_{j_z}(-1)^{m'+m}\begin{pmatrix} l & \frac{1}{2} & j \\ m' & S' & -j_z \end{pmatrix}\begin{pmatrix} l & \frac{1}{2} & j \\ m & S & -j_z \end{pmatrix}\\
&\mathrm{i}^{\lambda'-\lambda}\sum_{\boldsymbol{k}n} D^{\boldsymbol{k}n}_{L'M'S'}(D^{\boldsymbol{k}n}_{LMS})^*\\
&= 4\pi(2l+1)(2j+1)\sum_{mm'}\sum_{MM'}\delta(E+E_{nl\kappa}-E_{\boldsymbol{k}n})\\
&\times\sqrt{(2\lambda+1)(2\lambda'+1)(2L+1)(2L'+1)}\\
&\times\begin{pmatrix} l & \lambda & L \\ 0 & 0 & 0 \end{pmatrix}\begin{pmatrix} l & \lambda' & L' \\ 0 & 0 & 0 \end{pmatrix}\\
&\times\begin{pmatrix} l & \lambda & L \\ -m & \mu & M \end{pmatrix}\begin{pmatrix} l & \lambda' & L' \\ -m' & \mu' & M' \end{pmatrix}\\
&\times\sum_{j_z}(-1)^{m+m'}\begin{pmatrix} l & \frac{1}{2} & j \\ m & S & -j_z \end{pmatrix}\begin{pmatrix} l & \frac{1}{2} & j \\ m' & S' & -j_z \end{pmatrix}\\
&\times\left[\mathrm{i}^{\lambda-\lambda'}\sum_{\boldsymbol{k}n} D^{\boldsymbol{k}n}_{LMS}(D^{\boldsymbol{k}n}_{L'M'S'})^*\right]^* = \Xi^*_{\alpha\alpha'}
\end{aligned} \tag{A.2}$$

References

[1] H. Rose, Information transfer in transmission electron microscopy, Ultramicroscopy 15 (3) (1984) 173–191http://dx.doi.org/10.1016/0304-3991(84)90038-X, ISSN 0304-3991.

[2] H. Kohl, H. Rose, Theory of image formation by inelastically scattered electrons in the electron microscope, in: Peter W. Hawkes (Ed.), Advances in Electronics and Electron Physics, Advances in Electronics and Electron Physics, vol. 65, Academic Press, 1985, pp. 173–227, http://dx.doi.org/10.1016/S0065-2539(08)60878-1.

[3] P. Schattschneider, M. Nelhiebel, B. Jouffrey, Density matrix of inelastically scattered fast electrons, Physical Review B 59 (April (16)) (1999) 10959–10969, http://dx.doi.org/10.1103/PhysRevB.59.10959.

[4] P. Schattschneider, M. Nelhiebel, H. Souchay, B. Jouffrey, The physical significance of the mixed dynamic form factor, Micron 31 (4) (2000) 333–345, http://dx.doi.org/10.1016/S0968-4328(99)00112-2, ISSN 0968-4328.

[5] Stefan Löffler, Inga Ennen, Feng Tian, Peter Schattschneider, Nicolas Jaouen, Breakdown of the dipole approximation in core losses, Ultramicroscopy 111 (2011) 1163–1167, http://dx.doi.org/10.1016/j.ultramic.2011.03.006.

[6] P. Schattschneider, B. Jouffrey, M. Nelhiebel, Dynamical diffraction in electron-energy-loss spectrometry: the independent Bloch-wave model, Physical Review B 54 (August (6)) (1996) 3861–3868, http://dx.doi.org/10.1103/PhysRevB543861.

[7] Peter Schattschneider, Cécile Hébert, Stefano Rubino, Michael Stöger-Pollach, Jn Rusz, Pavel Novák, Magnetic circular dichroism in EELS: towards 10 nm resolution, Ultramicroscopy 108 (5) (2008) 433–438, http://dx.doi.org/10.1016/j.ultramic.2007.07.002, ISSN 0304-3991.

[8] Karl Blum, Density Matrix Theory and Applications, Physics of Atoms and Molecules, 2nd ed., Springer, ISBN 0-306-45341-X, 1996.

[9] E.R. Davidson, Natural Expansions of Exact Wave Functions. I. Method, The Journal of Chemical Physics 37 (3) (1962) 577–581, http://dx.doi.org/10.1063/1.1701377.

[10] H.M. Quiney, Coherent diffractive imaging using short wavelength light sources, Journal of Modern Optics 57 (13) (2010) 1109–1149, http://dx.doi.org/10.1080/09500340.2010.495459.

[11] P. Schattschneider, S. Rubino, C. Hebert, J. Rusz, J. Kunes, P. Novák, E. Carlino, M. Fabrizioli, G. Panaccione, G. Rossi, Detection of magnetic circular dichroism using a transmission electron microscope, Nature 441 (2006) 486–488, http://dx.doi.org/10.1038/nature04778.

[12] Ján Rusz, Stefano Rubino, Peter Schattschneider, First-principles theory of chiral dichroism in electron microscopy applied to 3d ferromagnets, Physical Review B 75 (21) (2007) 214425, http://dx.doi.org/10.1103/PhysRevB.75.214425.

[13] Michael Nelhiebel, Effects of Crystal Orientation and Interferometry in Electron Energy Loss Spectroscopy, Ph.D. Thesis, cole Centrale Paris, Châtenay-Malabry, May 1999.

[14] Stefan Löffler, Peter Schattschneider, Transition probability functions for applications of inelastic electron scattering, Micron 43 (9) (2012) 971–977, http://dx.doi.org/10.1016/j.micron.2012.03.020, ISSN 0968-4328.

[15] P. Blaha, K. Schwarz, G. Madsen, D. Kvasnicka, J. Luitz, WIEN2k, An Augmented Plane Wave + Local Orbitals Program for Calculating Crystal Properties, 2001. URL: ⟨http://www.wien2k.at⟩. (Karlheinz Schwarz, Techn. Universität Wien, Austria).

[16] Ján Rusz, Stefano Rubino, Olle Eriksson, Peter M. Oppeneer, Klaus Leifer, Local electronic structure information contained in energy-filtered diffraction patterns, Physical Review B 84 (August) (2011) 064444, http://dx.doi.org/10.1103/PhysRevB.84.064444.

[17] C. Dwyer, in preparation.

[18] Earl J. Kirkland, Advanced Computing in Electron Microscopy, Plenum Press, ISBN 0-306-45936-1, 1998.

[19] Qing Wang, Olaf Ronneberger, Hans Burkhardt, Rotational invariance based on fourier analysis in polar and spherical coordinates, IEEE Transactions on Pattern Analysis and Machine Intelligence 31 (2009) 1715–1722, http://dx.doi.org/10.1109/TPAMI.2009.29.

[20] Ján Rusz, Olle Eriksson, Pavel Novák, Peter M. Oppeneer, Sum rules for electron energy loss near edge spectra, Physical Review B 76 (6) (2007) 060408, http://dx.doi.org/10.1103/PhysRevB.76.060408.

[21] Kevin Jorissen, The Ab Initio Calculation of Relativistic Electron Energy Loss Spectra, Ph.D. Thesis, Universiteit Antwerpen, 2007.

[22] P. Hansmann, M.W. Haverkort, A. Toschi, G. Sangiovanni, F. Rodolakis, J. P. Rueff, M. Marsi, K. Held, Atomic and itinerant effects at the transition-metal x-ray absorption K pre-edge exemplified in the case of V_2O_3, Physical Review B 85 (March) (2012) 115136, http://dx.doi.org/10.1103/PhysRevB.85.115136.

[23] Jannik C. Meyer, Simon Kurasch, Hye Jin Park, Viera Skakalova, Daniela Künzel, Axel GroAndrey Chuvilin, Gerardo Algara-Siller, Siegmar Roth, Takayuki Iwasak, Ulrich Starke, Jurgen H. Smet, Ute Kaiser, Experimental analysis of charge redistribution due to chemical bonding by high-resolution transmission electron microscopy, Nature Materials 10 (3) (2011) 209–215, http://dx.doi.org/10.1038/nmat2941.

Chapter 2

Real-space localization and quantification of hole distribution in chain-ladder $Sr_3Ca_{11}Cu_{24}O_{41}$ superconductor

M. Bugnet, S. Löffler, D. Hawthorn, H. A. Dabkowska, G. Luke, P. Schattschneider, G. A. Sawatzky, G. Radtke, and G. A. Botton

Science Advances 2 (2016) e1501652
10.1126/sciadv.1501652

SUPERCONDUCTORS

10.1126/sciadv.1501652

Real-space localization and quantification of hole distribution in chain-ladder $Sr_3Ca_{11}Cu_{24}O_{41}$ superconductor

Matthieu Bugnet,[1]* Stefan Löffler,[1,2] David Hawthorn,[3] Hanna A. Dabkowska,[4] Graeme M. Luke,[5] Peter Schattschneider,[2] George A. Sawatzky,[6] Guillaume Radtke,[7] Gianluigi A. Botton[1]*

Understanding the physical properties of the chain-ladder $Sr_3Ca_{11}Cu_{24}O_{41}$ hole-doped superconductor has been precluded by the unknown hole distribution among chains and ladders. We use electron energy-loss spectrometry (EELS) in a scanning transmission electron microscope (STEM) at atomic resolution to directly separate the contributions of chains and ladders and to unravel the hole distribution from the atomic scale variations of the O-K near-edge structures. The experimental data unambiguously demonstrate that most of the holes lie within the chain layers. A quantitative interpretation supported by inelastic scattering calculations shows that about two holes are located in the ladders, and about four holes in the chains, shedding light on the electronic structure of $Sr_3Ca_{11}Cu_{24}O_{41}$. Combined atomic resolution STEM-EELS and inelastic scattering calculations is demonstrated as a powerful approach toward a quantitative understanding of the electronic structure of cuprate superconductors, offering new possibilities for elucidating their physical properties.

INTRODUCTION

The quasi–one-dimensional chain-ladder cuprate $Sr_{14-x}Ca_xCu_{24}O_{41}$ has attracted much attention over the past decades for its appealing physical properties. While it is electrically resistive for $x = 0$, it becomes conductive upon Ca doping. A superconducting behavior has been predicted (*1*–*3*) and then experimentally demonstrated (*4*) under high pressure (3 GPa) and at a high doping level ($x = 13.6$). Abbamonte *et al.* (*5*) suggested the existence of a hole Wigner crystal originating from electronic correlations within the hole-doped ladders of the parent compound $Sr_{14}Cu_{24}O_{41}$ (SCO), thereby demonstrating the competition between superconductivity and an insulating phase within the ladders. $Sr_{14-x}Ca_xCu_{24}O_{41}$ is also unique from a structural point of view. In all other cuprate superconductors, copper oxide units are solely arranged in CuO_2 planes. In contrast, $Sr_{14-x}Ca_xCu_{24}O_{41}$ is composed of two alternating stacked copper oxide planes: corner-shared CuO_2 chains and edge-shared Cu_2O_3 ladders interleaved with Sr(Ca) cation planes (Fig. 1). Following the conventional valency rules of Sr and Ca (2+), O (2−), and Cu (2+), there must be missing electrons (added holes) that are responsible for the conductive properties of $Sr_{14-x}Ca_xCu_{24}O_{41}$.

Understanding the physical properties of this chain-ladder compound requires the knowledge of the exact hole distribution within the chains and the ladders. SCO is naturally doped with six holes per formula unit (f.u.), and the total number of holes does not vary with isovalent Ca substitution for Sr. Several estimates of the hole distribution have been reported in literature, using different approaches such as x-ray absorption spectroscopy (XAS) (*6*–*9*), x-ray emission spectroscopy (XES) (*10*), nuclear magnetic resonance (NMR) (*11*, *12*), Hall effect measurements (*13*), infrared reflectivity (*14*), and bond valence sum analysis based on structural coordination data extracted from x-ray (*15*) or neutron (*16*, *17*) diffraction measurements. However, they present a wide disparity as a result of major differences in the interpretation of the results. Most studies indicate that more than 5 holes per f.u. are confined within the chains of SCO and that only a fraction of holes is transferred from the chains to the ladders upon Ca doping. In contrast, the analysis of optical measurements of Osafune *et al.* (*18*) indicates a transfer to ladders of ~2 holes per f.u. upon doping with $x = 11$, a result supported by the bond valence sum analysis of Deng *et al.* (*17*). Finally, O 1*s* XAS analysis indicates an equal distribution of holes among chains and ladders in SCO and the transfer to ladders of more than 1 hole per f.u. upon Ca doping (*7*). Nevertheless, all studies seem to agree on the linear dependence of the hole number in chains (or ladders) on Ca doping.

The vast majority of spectral information available on cuprate superconductors is gathered using probes with spatial resolutions of typically a few micrometers or several hundred nanometers, such as XAS, XES, angular-resolved photoemission spectroscopy, or x-ray photoemission spectroscopy, thus integrating over all Cu-O planes in the structure and making the distinction among the contributions of nonequivalent Cu planes challenging. It should be mentioned that electron energy-loss spectrometry (EELS) has also been used to study the character (*19*, *20*) and symmetry (*21*, *22*) of the hole states in cuprate superconductors with high critical temperature (T_c) but without atomic plane resolution. However, EELS combined with aberration-corrected scanning transmission electron microscopy (STEM) is highly spatially selective. The technique allows the probing of the chemical bonding and the electronic structure at the atomic scale (*23*, *24*) by

---

[1] Department of Materials Science and Engineering and the Canadian Centre for Electron Microscopy, McMaster University, 1280 Main Street West, Hamilton, Ontario L8S 4M1, Canada. [2] Institute of Solid State Physics and University Service Centre for Transmission Electron Microscopy, Vienna University of Technology, Wiedner Hauptstraße 8-10, A-1040 Vienna, Austria. [3] Department of Physics and Astronomy, University of Waterloo, 200 University Avenue West, Waterloo, Ontario N2L 3G1, Canada. [4] Brockhouse Institute for Materials Research, McMaster University, 1280 Main Street West, Hamilton, Ontario L8S 4M1, Canada. [5] Department of Physics and Astronomy, McMaster University, 1280 Main Street West, Hamilton, Ontario L8S 4M1, Canada. [6] Department of Physics and Astronomy, University of British Columbia, 6224 Agricultural Road, Vancouver, British Columbia V6T 1Z1, Canada. [7] Institut de Minéralogie, de Physique des Matériaux et de Cosmochimie (IMPMC), Sorbonne Universités, Université Pierre et Marie Curie (UPMC), Paris 6, CNRS UMR 7590, Muséum National d'Histoire Naturelle, IRD UMR 206, 4 Place Jussieu, F-75005 Paris, France.
*Corresponding author. E-mail: bugnetm@mcmaster.ca (M.B.); gbotton@mcmaster.ca (G.A.B.)

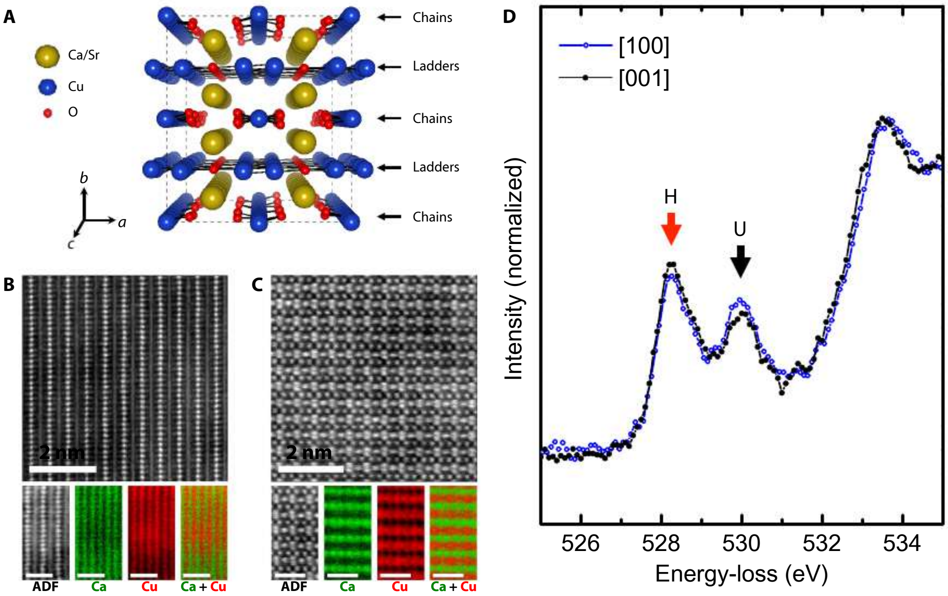

Fig. 1. Crystal structure of SCCO and O-K near-edge structures. (**A**) SCCO structure. (**B** and **C**) Annular dark-field (ADF)–STEM images viewed along the [100] (B) and [001] (C) zone axes. Ca and Cu elemental maps (bottom) were obtained using the Ca-$L_{2,3}$ and Cu-$L_{2,3}$ edges, respectively. Weighted principal component analysis (PCA) was applied to reduce the noise level. Unlabeled scale bars, 1 nm. (**D**) O-K edge onset recorded along the [100] and [001] zone axes. H and U indicate the O 2*p* hole and upper Hubbard band peaks, respectively. The energy resolution was obtained using a monochromator and was comparable to XAS measurements.

using inelastically scattered electrons from a sub-ångström probe and is therefore perfectly suited to separate signals from individual independent Cu planes (*25*–*27*). Furthermore, the energy-loss near-edge structures (ELNES) arising from transitions to unoccupied states of a particular energy allow the mapping of electronic orbitals (*28*) and the localization and identification of the relevant electronic structure information at the atomic scale. Recently, the qualitative real-space mapping of holes has been demonstrated in a series of $YBa_2Cu_3O_{6+\delta}$ compounds (*27*). Whereas a direct visualization of holes can be relevant in itself, the quantification of hole concentrations with atomic resolution is of paramount interest to further understanding the electronic structure and physical properties of hole-doped superconductors from the nano- to the macroscale. To date, this challenge has not been met.

RESULTS

Here, the hole distribution in the chain-ladder superconductor $Sr_3Ca_{11}Cu_{24}O_{41}$ (SCCO) is investigated with STEM-EELS at the atomic level, at room temperature and a pressure of about 10^{-8} mbar, using the O-K pre-edge ELNES (see Fig. 1D). The O-K pre-edge ELNES is composed of the hole band (peak H) associated with the O 2*p* orbitals (*19*, *20*) involved in the Zhang-Rice singlets (*29*) and the upper Hubbard band (peak U). The small anisotropy observed in the monochromated spectra is largely related to the averaging of orientation-dependent effects associated with the use of large convergence and collection angles in STEM-EELS. However, spectral features are in excellent agreement with previous data recorded in polarized XAS (*6*, *7*). Spectrum image (SI) data cubes were recorded with the incident electron beam along the [100] and [001] zone axes of SCCO, simultaneous with the annular dark-field images shown in Fig. 2. After correcting for spatial drift during acquisition (see the Supplementary Materials for details), the spectral information contained in each SI is projected along the direction parallel to the chains and ladders; the data recorded in the [001] zone axis are projected along [100] and vice versa. It is apparent that the O-K fine structures at the edge onset significantly vary from chains to ladders for both specimen orientations: peak H strongly fluctuates as a function of the spatial position, reaching its maximum intensity on the chains and its minimum on the ladders. This observation is further confirmed by a similar experiment at the Cu-L_3 edge (fig. S4), indicating that most holes lie within the CuO_2 chains of the structure.

To evaluate the relative hole concentration within the chains and the ladders, we quantified the spatial variation of the O 2*p* hole band by modeling the O-K pre-edge ELNES. The spatial separation of the chains and ladders achieved using STEM-EELS is highly important because it avoids having to resort to comparison with pure chain and pure ladder reference spectra (*9*), which can induce some material-dependent effects. Gaussian functions have been used to quantify the spectra following the methodology commonly used in XAS (*7*). Note that the present spatially resolved EELS data have been acquired with a lower energy resolution compared to typical XAS experiments, further justifying this choice as a reasonable approximation. Two Gaussian functions were used to fit the O 2*p* hole band and the upper Hubbard band, respectively. The

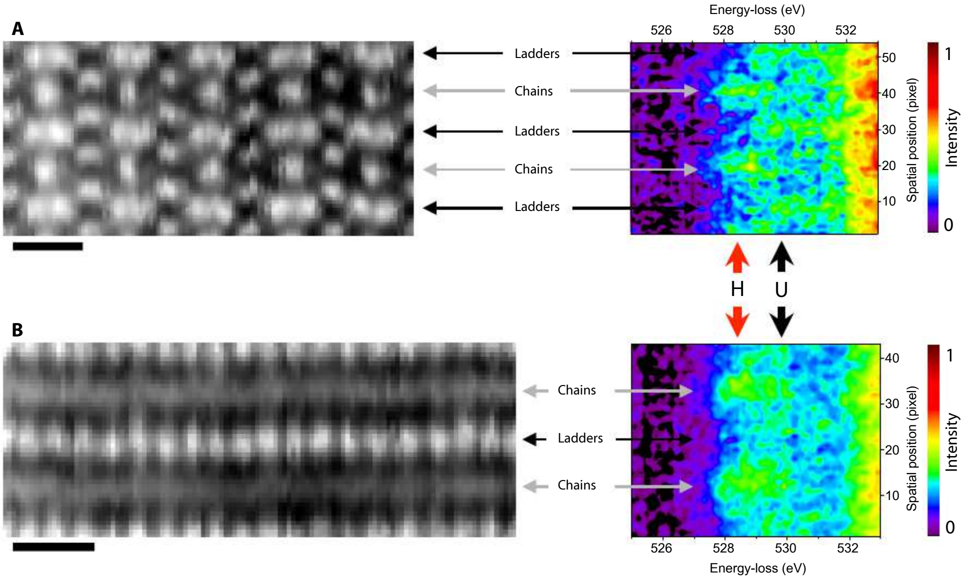

Fig. 2. Qualitative hole distribution. (**A** and **B**) ADF-STEM images and O-K edge onset in the [001] (A) and [100] (B) zone axes. The O-K edge onsets highlight intensity variations of the O 2*p* hole (H) and upper Hubbard (U) bands, whose positions are indicated by red and black arrows, respectively. The ADF-STEM images are represented after alignment (see the Supplementary Materials). Scale bars, 5 Å.

continuum of states at higher energy was modeled by a step function (*30*). The energy of the Gaussian functions was determined after modeling monochromated EELS data, as shown in Fig. 3, B and F, and their full widths at half maximum (FWHM) were evaluated by accounting for the energy resolution decrease between the monochromated and the non-monochromated electron source (see the Supplementary Materials). The spatially resolved data were fitted with the determined energy position and the extrapolated FWHM, leaving the peak intensities as the sole free parameters. It should be mentioned that the independent oxygen sites in chains and in ladders have different O 1*s* core electron binding energies, which would lead to different energies for the doped holes. However, the relative core-level shift estimated from electronic structure calculations in SCO is negligible (*8*), and the experimental chemical shift arising from hole doping in other cuprates such as $La_{2-x}Sr_xCuO_{4-\delta}$ is a few tenths of electron volts for doping levels of a few tenths of holes per Cu (*31*). In comparison with the spectral width of the present experimental peak H (~1.9 eV), the differences in O 1*s* core electron binding energy can be safely neglected.

Examples of the resulting fits of the STEM-EELS data are shown in Fig. 3. The intensity of the Gaussian function used to model the O 2*p* hole peak decreases from chains to ladders, as shown in Fig. 3, C and D, for [001] and Fig. 3, G and H, for [100]. The fitting process was applied to 10 SI data sets acquired in both zone axes. The hole concentrations obtained from this fit are reported in Table 1. Assuming a total of 6 holes per f.u., and that the hole number is directly related to the intensity of peak H with the same spectral weight for ladders and chains, the relative hole concentration within the chains and the ladders along [001] ([100]) is evaluated to be 4.08 ± 0.26 (4.01 ± 0.28) and 1.92 ± 0.26 (1.99 ± 0.28), respectively. As expected, the hole concentrations determined in the [100] and [001] zone axes are similar within the range of error, leading to average values of ~4 holes in the chains and ~2 holes in the ladders, corresponding to ~0.4 hole per Cu in chains and ~0.14 hole per Cu in ladders (considering a 10:14 ratio of Cu atoms in chains/ladders). Accordingly, the upper Hubbard band, which should decrease with higher doping, is weaker in the chains than in the ladders as shown in Fig. 3I. These measurements are consistent with a lower doping per Cu for the ladders, as suggested in $La_{2-x}Sr_xCuO_{4-\delta}$ (*32*).

A reliable quantitative interpretation of the O-K ELNES requires taking into account the channeling of the electron beam along the atomic columns and the relative sensitivity of the O 2*p* hole peak in chains and in ladders (that is, the spectral weight per hole in chains versus ladders). The nearly identical Cu-O interatomic spacing and similar chemistry in chains and ladders suggests that the hole sensitivity of the chains is similar to that of the ladders. To quantitatively evaluate the influences of electron-beam channeling and orientation dependence, we performed inelastic channeling scattering calculations (see the Supplementary Materials for details). The results are summarized in Table 2. On one hand, the inelastic intensity coming from the ladders when the electron beam is on the chains (and vice versa), which we will refer to as cross terms, represents less than ~17% of the total inelastic intensity, which is of the order of experimental uncertainty. In other words, a very good spatial separation of the chain and ladder signals is achieved under these experimental conditions. This result confirms the validity of the experimental STEM-EELS approach used here. On the other hand, these cross terms are of the same magnitude as the small differences in calculated inelastic intensities coming from the chains when the electron beam is in a chain

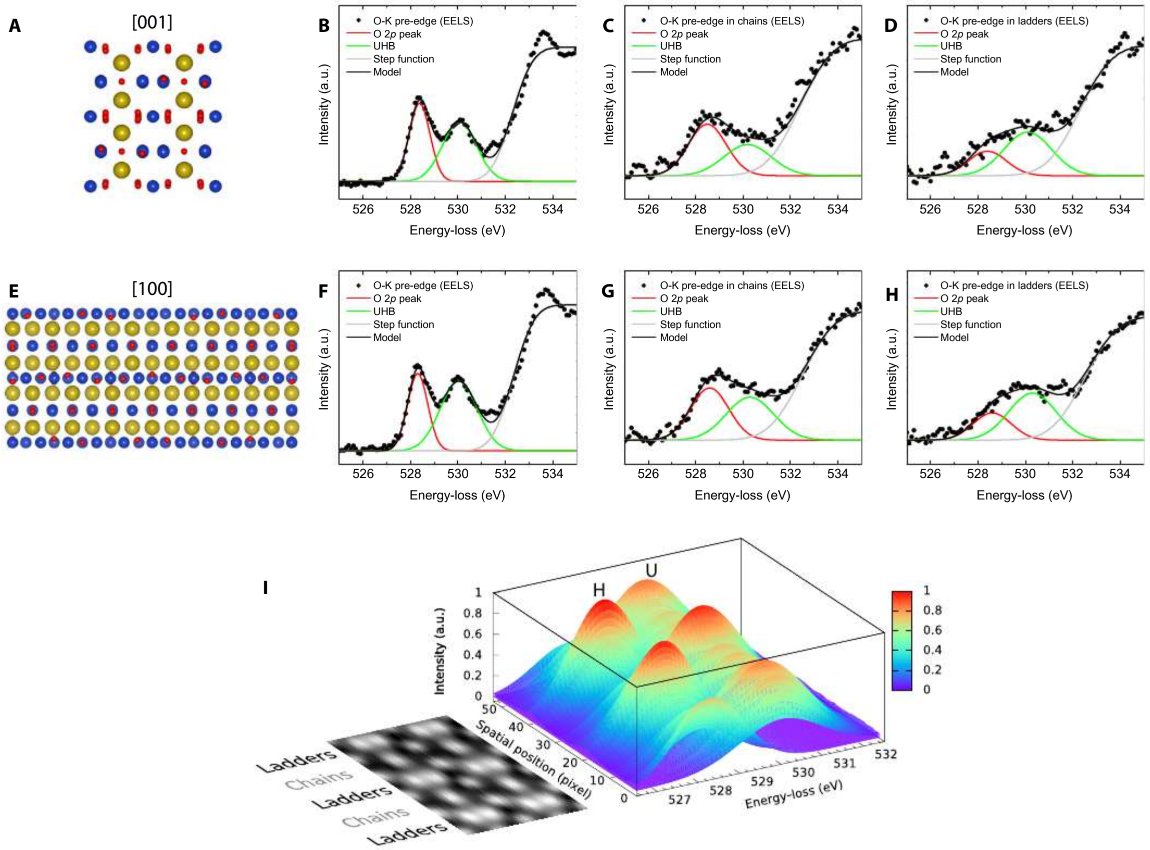

Fig. 3. Spectral fitting and quantitative hole distribution. (**A**) SCCO structure in the [001] zone axis. (**B**) Modeling of the monochromated O-K edge onset in SCCO in the [001] zone axis. (**C**) Modeling of the spatially resolved O-K edge onset in SCCO corresponding to chains in the [001] zone axis. (**D**) Same as in (C) for spectra corresponding to ladders. (**E** to **H**) Same as in (A) to (D) for the [100] zone axis. Two Gaussian functions were used to model the O 2*p* hole band (red solid lines) and the upper Hubbard band (UHB) (green solid lines). The edge onset at higher energy (gray solid lines) was modeled using a step function (*30*). The energy and FWHM of the Gaussian functions were determined from the monochromated spectra in (B) and (F), and only the intensity of the functions was left as free parameters during the fitting process. (**I**) O 2*p* hole band and upper Hubbard band fit over a full spectrum image acquired in the [001] zone axis.

Table 1. Hole concentrations (per f.u.) in chains and ladders. The error bars correspond to the SD over all data sets analyzed and adjustment of the absolute energy positions of the O 2*p* hole band and the upper Hubbard band.

	Ladders	Chains
[100]	1.99 ± 0.28	4.01 ± 0.28
[001]	1.92 ± 0.26	4.08 ± 0.26

position and from the ladders when the electron beam is in a ladder position. This suggests that the O-K ELNES has similar sensitivity to holes in chains and ladders under our experimental conditions and confirms that the expected inelastic intensities recorded in [100] and [001] are comparable.

DISCUSSION

The inelastic channeling calculations confirm the hole concentrations that were directly estimated from Gaussian fitting. First, it is important to highlight that this theoretical approach strongly suggests a spectral weight of 1:1 in chains/ladders, which validates the general assumption made to interpret the XAS data (*6*, *7*). Second, the extracted STEM-EELS data for $x = 11$ are compared with literature values in Fig. 4. Overall, the value of ~2 holes in the ladders follows the general tendency that most of the holes are in the chains upon heavy Ca doping. Specifically, this value is slightly higher than those reported in most of the existing studies (*6*, *9*, *11*, *13*). It is also lower than those extracted from optical measurements (*18*) and neutron diffraction using bond valence sum calculations (*17*). The present study qualitatively and quantitatively shows a higher hole concentration within the chains as compared to the XAS investigation of Rusydi *et al.* (*7*), where it was reported that the holes are

Table 2. Calculated contributions of chains and ladders to the total inelastic intensity.

Orientation	Beam position	Inelastic intensity from ladders (a.u.)	Inelastic intensity from chains (a.u.)
[100]	Ladders	155,956 (~84%)	28,902 (~16%)
	Chains	17,683 (~7%)	240,596 (~93%)
[001]	Ladders	139,527 (~84%)	26,567 (~16%)
	Chains	35,524 (~17%)	177,920 (~83%)

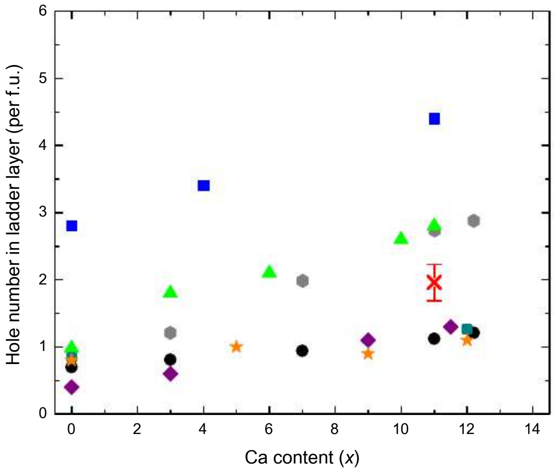

Fig. 4. Hole distribution within the ladders versus Ca content in $Sr_{14-x}Ca_xCu_{24}O_{41}$. The hole distribution from this work (red cross) is indicated in comparison with room-temperature data taken from published works [green triangle: optical measurements, Osafune *et al.* (*18*); orange star: O 1*s* XAS, Nücker *et al.* (*6*); purple diamond: Hall effect, Tafra *et al.* (*13*); black circle: Cu 2*p* XAS, Huang *et al.* (*9*); blue square: O 1*s* XAS, Rusydi *et al.* (*7*); dark cyan square: ^{63}Cu and ^{17}O NMR, Piskunov *et al.* (*11*); gray hexagon: neutron diffraction, Deng *et al.* (*17*)].

mainly localized in the ladders for $x = 11$, inducing a large hole transfer from chains to ladders upon Ca doping. It is important to stress that STEM-EELS coupled to inelastic channeling calculations is the only approach used so far that permits direct visualization and evaluation of hole concentrations in ladders and chains independently, highlighting the relevance and significance of the results reported here.

A major consequence of the STEM-EELS analysis is that the data reveal an apparent incompatibility between the hole distribution in superconducting SCCO and the presence of a hole Wigner crystal in SCO that was suggested by resonant x-ray scattering (*5*) and explained with a nearly equal distribution of holes (*7*) in chains and ladders for $x = 0$. However, note that the Wigner crystallization of holes has been reported on the parent compound ($x = 0$), in contrast to the present STEM-EELS experiments, and this calls for complementary experiments using both STEM-EELS for hole localization and resonant x-ray scattering on a wide range of Ca doping levels. Polarization-dependent work with sufficient spatial resolution to resolve chains and ladders is not possible with current instrumentation, but could be exploited in the future to further understand earlier experiments.

In summary, the hole distribution among chains and ladders in SCCO has been probed by STEM-EELS at atomic resolution. In contrast to XAS and other techniques that probe both chains and ladders simultaneously, STEM-EELS directly distinguishes the signals coming from chains and ladders independently. A qualitative analysis of the results indicates that the chains hold most of the holes. A quantitative analysis is proposed based on the Gaussian fitting of the O-K ELNES pre-edge structures and supported by inelastic channeling calculations, which account for both channeling effects and spectral weight differences in ladders and chains. The combination of the electronic structure fingerprint in the ELNES, atomic resolution in the aberration-corrected STEM, and inelastic scattering calculations opens the way to a better understanding of the electronic properties of cuprate superconductors.

MATERIALS AND METHODS

Crystal growth

Single crystals of SCCO were grown by the optical floating zone (OFZ) method (*33*). The starting materials were pre-annealed powders of $CaCO_3$ (99.9, CERAC), $SrCO_3$ (99.9, AlfaAesar), and CuO (99.9, CERAC). The appropriate stoichiometric mixture of powders was crushed and ground using mortar and pestle to ensure pulverization of the powders and homogeneous mixing, and then the mixture was transferred into a rubber tube. A vacuum pump was used to extract air from the rubber tube, and the material was placed in a hydrostatic press under 60 MPa for 20 min. This produced cylindrical rods of powder that were approximately 11 cm in length and 8 mm in diameter. These rods were sintered in a tube furnace in air for 48 hours at 1200°C and then cooled to room temperature before being removed from the furnace. High-quality single crystals were grown in the OFZ Canon furnace with 9 atm of O_2 overpressure, at a growth rate of 1 mm/hour. The feed and seed rods were counter-rotated at 20 rpm. As SCCO melted incongruently, a flux pellet made of 30 wt % SrO and 70 wt % CuO (0.5 g in total) was used to initiate growth.

Assessment of sample purity and stoichiometry

Energy dispersive x-ray experiments conducted in an FEI Titan 80-300 TEM, operated at 80 kV, confirmed the doping level, with a Sr/Ca content of ~3.1:10.9.

STEM-EELS

The SCCO crystal was oriented by Laue x-ray diffraction. Two specimens, with [100] and [001] orientations, were prepared by focused ion beam (FIB) cutting using a Zeiss NVision 40 dual beam apparatus. The specimens were subsequently thinned down by ion milling (Fischione Nanomill) at liquid nitrogen temperature with Ar beam energies in the range of 500 to 900 eV to remove the damaged areas from the FIB and to reach electron transparency. The thickness of the areas probed in high-resolution STEM-EELS were determined using EELS (*34*, *35*) as ~30 and ~45 nm in the [100] and [001] zone axes, respectively.

The STEM-EELS experiments were performed on an FEI Titan Cubed 80 300 TEM, equipped with C_s probe and image correctors, operated at 80 kV acceleration voltage, and fitted with a Gatan GIF Quantum Energy Filter. The SI data and the ADF signal were simultaneously acquired with a beam current of ~40 to 50 pA, a convergence semi-angle of 19 mrad, a GIF collection semi-angle of 55 mrad, and a pixel dwell time of 25 ms to maximize the signal while minimizing drift and beam damage artifacts.

Data processing

The elemental atomic resolution maps shown in Fig. 1 were processed by weighted PCA to minimize noise contributions. Data extraction for Figs. 2 and 3 was carried out on raw data. The spatial distortion and drift in the SIs were corrected using a homemade script in the Gatan Digital Micrograph software before projection along one crystallographic direction. See the Supplementary Materials for details. The crystal structure of SCCO is visualized using the computer program VESTA (*36*).

Simulations

Elastic scattering effects were taken into account before and after the inelastic scattering event using the multislice approach. Inelastic scattering was modeled by diagonalizing the mixed dynamic form factor (*37*) obtained from density functional theory calculations (FP-LAPW WIEN2k) (*38*) at the generalized gradient approximation level (*39*). A simplified 224-atom face-centered cubic unit cell, $Ca_{10}Cu_{17}O_{29}$, was used (*40*), assuming x =14 (that is, Sr was fully substituted by Ca), to maintain a reasonable computing time. See the Supplementary Materials for details.

SUPPLEMENTARY MATERIALS

Supplementary material for this article is available at http://advances.sciencemag.org/cgi/content/full/2/3/e1501652/DC1
Comparison with x-ray absorption spectroscopy
Quantitative evaluation of the hole distribution
Inelastic scattering calculations
Drift correction
Qualitative hole distribution from Cu 2*p* excitation
Table S1. Fitting parameters: SD and relative energy positions of Gaussian functions.
Fig. S1. Comparison of O-K XANES and ELNES.
Fig. S2. Inelastic channeling calculations.
Fig. S3. Spatial drift correction on the STEM-EELS data.
Fig. S4. Qualitative hole distribution from Cu 2*p* excitation.

REFERENCES AND NOTES

1. E. Dagotto, J. Riera, D. Scalapino, Superconductivity in ladders and coupled planes. *Phys. Rev. B* **45**, 5744–5767 (1992).
2. E. Dagotto, T. M. Rice, Surprises on the way from one- to two-dimensional quantum magnets: The ladder materials. *Science* **271**, 618–623 (1996).
3. M. Sigrist, T. M. Rice, F. C. Zhang, Superconductivity in a quasi-one-dimensional spin liquid. *Phys. Rev. B Condens. Matter.* **49**, 12058–12061 (1994).
4. M. Uehara, T. Nagata, J. Akimitsu, H. Takahashi, N. Môri, K. Kinoshita, Superconductivity in the ladder material $Sr_{0.4}Ca_{13.6}Cu_{24}O_{41.84.}$ *J. Phys. Soc. Jap.* **65**, 2764–2767 (1996).
5. P. Abbamonte, G. Blumberg, A. Rusydi, A. Gozar, P. G. Evans, T. Siegrist, L. Venema, H. Eisaki, E. D. Isaacs, G. A. Sawatzky, Crystallization of charge holes in the spin ladder of $Sr_{14}Cu_{24}O_{41}$. *Nature* **431**, 1078–1081 (2004).
6. N. Nücker, M. Merz, C. A. Kuntscher, S. Gerhold, S. Schuppler, R. Neudert, M. S. Golden, J. Fink, D. Schild, S. Stadler, V. Chakarian, J. Freeland, Y. U. Idzerda, K. Conder, M. Uehara, T. Nagata, J. Goto, J. Akimitsu, N. Motoyama, H. Eisaki, S. Uchida, U. Ammerahl, A. Revcolevschi, Hole distribution in $(Sr,Ca,Y,La)_{14}Cu_{24}O_{41}$ ladder compounds studied by x-ray absorption spectroscopy. *Phys. Rev. B* **62**, 14384–14392 (2000).
7. A. Rusydi, M. Berciu, P. Abbamonte, S. Smadici, H. Eisaki, Y. Fujimaki, S. Uchida, M. Rübhausen, G. A. Sawatzky, Relationship between hole density and charge-ordering wave vector in $Sr_{14-x}Ca_xCu_{24}O_{41}$. *Phys. Rev. B* **75**, 104510 (2007).
8. V. Ilakovac, C. Gougoussis, M. Calandra, N. B. Brookes, V. Bisogni, S. G. Chiuzbaian, J. Akimitsu, O. Milat, S. Tomić, C. F. Hague, Hole depletion of ladders in $Sr_{14}Cu_{24}O_{41}$ induced by correlation effects. *Phys. Rev. B* **85**, 075108 (2012).
9. M.-J. Huang, G. Deng, Y. Y. Chin, Z. Hu, J.-G. Cheng, F. C. Chou, K. Conder, J.-S. Zhou, T.-W. Pi, J. B. Goodenough, H.-J. Lin, C. T. Chen, Determination of hole distribution in $Sr_{14-x}Ca_xCu_{24}O_{41}$ using soft x-ray absorption spectroscopy at the Cu L_3 edge. *Phys. Rev. B* **88**, 014520 (2013).
10. E. Kabasawa, J. Nakamura, N. Yamada, K. Kuroki, H. Yamazaki, M. Watanabe, J. D. Denlinger, S. Shin, R. C. C. Perera, Hole distribution in $(Sr,Ca,Y,La)_{14}Cu_{24}O_{41}$ compounds studied by x-ray absorption and emission spectroscopy. *J. Phys. Soc. Jap.* **77**, 034704 (2008).
11. Y. Piskunov, D. Jérome, P. Auban-Senzier, P. Wzietek, A. Yakubovsky, Hole redistribution in $Sr_{14-x}Ca_xCu_{24}O_{41}$ (x=0,12) spin ladder compounds: ^{63}Cu and ^{17}O NMR studies under pressure. *Phys. Rev. B* **72**, 064512 (2005).
12. K. Magishi, S. Matsumoto, Y. Kitaoka, K. Ishida, K. Asayama, M. Uehara, T. Nagata, J. Akimitsu, Spin gap and dynamics in $Sr_{14-x}Ca_xCu_{24}O_{41}$ comprising hole-doped two-leg spin ladders: Cu NMR study on single crystals. *Phys. Rev. B* **57**, 11533–11544 (1998).
13. E. Tafra, B. Korin-Hamzić, M. Basletić, A. Hamzić, M. Dressel, J. Akimitsu, Influence of doping on the Hall coefficient in $Sr_{14-x}Ca_xCu_{24}O_{41}$. *Phys. Rev. B* **78**, 155122 (2008).
14. S. Frank, A. Huber, U. Ammerahl, M. Hücker, C. A. Kuntscher, Polarization-dependent infrared reflectivity study of $Sr_{2.5}Ca_{11.5}Cu_{24}O_{41}$ under pressure: Charge dynamics, charge distribution, and anisotropy. *Phys. Rev. B* **90**, 224516 (2014).
15. Y. Gotoh, I. Yamaguchi, Y. Takahashi, J. Akimoto, M. Goto, M. Onoda, H. Fujino, T. Nagata, J. Akimitsu, Structural modulation, hole distribution, and hole-ordered structure of the incommensurate composite crystal $(Sr_2Cu_2O_3)_{0.70}CuO_2$. *Phys. Rev. B* **68**, 224108 (2003).
16. M. Isobe, M. Onoda, T. Ohta, F. Izumi, K. Kimoto, E. Takayama-Muromachi, A. W. Hewat, K. Ohoyama, Low-temperature crystal and magnetic structures of the chain-ladder composite material $Sr_{0.4}Ca_{13.6}Cu_{24+y}O_{41+z}$: Hole redistribution and antiferromagnetic order. *Phys. Rev. B* **62**, 11667–11676 (2000).
17. G. Deng, V. Pomjakushin, V. Petříček, E. Pomjakushina, M. Kenzelmann, K. Conder, Structural evolution of one-dimensional spin-ladder compounds $Sr_{14-x}Ca_xCu_{24}O_{41}$ with Ca doping and related evidence of hole redistribution. *Phys. Rev. B* **84**, 144111 (2011).
18. T. Osafune, N. Motoyama, H. Eisaki, S. Uchida, Optical study of the $Sr_{14-x}Ca_xCu_{24}O_{41}$ system: Evidence for hole-doped Cu_2O_3 ladders. *Phys. Rev. Lett.* **78**, 1980–1983 (1997).
19. N. Nücker, J. Fink, J. C. Fuggle, P. J. Durham, W. M. Temmerman, Evidence for holes on oxygen sites in the high-T_c superconductors $La_{2-x}Sr_xCuO_4$ and $YBa_2Cu_3O_{7-y}$. *Phys. Rev. B* **37**, 5158–5163 (1988).
20. J. Fink, J. Fink, N. Nücker, H. Romberg, M. Alexander, S. Nakai, B. Scheerer, P. Adelmann, D. Ewert, Electron energy-loss studies on high-temperature superconductors. *Physica C* **162–164**, 1415–1418 (1989).
21. N. Nücker, H. Romberg, X. X. Xi, J. Fink, B. Gegenheimer, Z. X. Zhao, Symmetry of holes in high-T_c superconductors. *Phys. Rev. B* **39**, 6619–6629 (1989).
22. J. Fink, N. Nücker, E. Pellegrin, H. Romberg, M. Alexander, M. Knupfer, Electron energy-loss and x-ray absorption spectroscopy of cuprate superconductors and related compounds. *J. Electron Spectrosc. Relat. Phenom.* **66**, 395–452 (1994).
23. D. A. Muller, Structure and bonding at the atomic scale by scanning transmission electron microscopy. *Nat. Mater.* **8**, 263–270 (2009).
24. G.-z. Zhu, G. Radtke, G. A. Botton, Bonding and structure of a reconstructed (001) surface of $SrTiO_3$ from TEM. *Nature* **490**, 384–387 (2012).
25. T. Y. Chien, L. F. Kourkoutis, J. Chakhalian, B. Gray, M. Kareev, N. P. Guisinger, D. A. Muller, J. W. Freeland, Visualizing short-range charge transfer at the interfaces between ferromagnetic and superconducting oxides. *Nat. Commun.* **4**, 2336 (2013).
26. G. M. De Luca, G. Ghiringhelli, C. A. Perroni, V. Cataudella, F. Chiarella, C. Cantoni, A. R. Lupini, N. B. Brookes, M. Huijben, G. Koster, G. Rijnders, M. Salluzzo, Ubiquitous long-range antiferromagnetic coupling across the interface between superconducting and ferromagnetic oxides. *Nat. Commun.* **5**, 5626 (2014).
27. N. Gauquelin, D. G. Hawthorn, G. A. Sawatzky, R. X. Liang, D. A. Bonn, W. N. Hardy, G. A. Botton, Atomic scale real-space mapping of holes in $YBa_2Cu_3O_{6+\delta}$. *Nat. Commun.* **5**, 4275 (2014).

28. S. Löffler, Mapping electronic orbitals in real space. *Microsc. Microanal.* **21** (Suppl. S3), 2361–2362 (2015).
29. F. C. Zhang, T. M. Rice, Effective Hamiltonian for the superconducting Cu oxides. *Phys. Rev. B* **37**, 3759–3761 (1988).
30. J. Stöhr, *NEXAFS Spectroscopy* (Springer Science & Business Media, Berlin, 2013) vol. 25.
31. A. Ino, T. Mizokawa, A. Fujimori, K. Tamasaku, H. Eisaki, S. Uchida, T. Kimura, T. Sasagawa, K. Kishio, Chemical potential shift in overdoped and underdoped $La_{2-x}Sr_xCuO_4$. *Phys. Rev. Lett.* **79**, 2101–2104 (1997).
32. C. T. Chen, F. Sette, Y. Ma, M. S. Hybertsen, E. B. Stechel, W. M. C. Foulkes, M. Schulter, S.-W. Cheong, A. S. Cooper, L. W. Rupp Jr., B. Batlogg, Y. L. Soo, Z. H. Ming, A. Krol, Y. H. Kao, Electronic states in $La_{2-x}Sr_xCuO_{4+\delta}$ probed by soft-x-ray absorption. *Phys. Rev. Lett.* **66**, 104–107 (1991).
33. H. A. Dabkowska, A. B. Dabkowski, R. Hermann, J. Priede, G. Gerbet, in *Handbook of Crystal Growth*, T. Nishinaga, P. Rudolph, Eds. (Elsevier, Amsterdam, ed. 2, 2015), vol. 2, pp. 281–329.
34. R. F. Egerton, *Electron Energy-Loss Spectroscopy in the Electron Microscope* (Plenum Press, New York, ed. 2, 1996).
35. T. Malis, S. C. Cheng, R. F. Egerton, EELS log-ratio technique for specimen-thickness measurement in the TEM. *J. Electron Micr. Tech.* **8**, 193–200 (1988).
36. K. Momma, F. Izumi, VESTA: A three-dimensional visualization system for electronic and structural analysis. *J. Appl. Crystallogr.* **41**, 653–658 (2008).
37. S. Löffler, V. Motsch, P. Schattschneider, A pure state decomposition approach of the mixed dynamic form factor for mapping atomic orbitals. *Ultramicroscopy* **131**, 39–45 (2013).
38. P. Blaha, K. Schwarz, G. K. H. Madsen, D. Kvasnicka, J. Luitz, in *Wien2k, An Augmented Plane Wave + Local Orbitals Program for Calculating Crystal Properties*, K. Schwarz, Ed. (Technische Universität Wien, Austria, 2001).
39. J. P. Perdew, K. Burke, M. Ernzerhof, Generalized gradient approximation made simple. *Phys. Rev. Lett.* **77**, 3865–3868 (1996).
40. K. Kato, Strukturverfeinerung des Kompositkristalls im mehrdimensionalen Raum. *Acta Crystallogr. Sect. B: Struct. Sci. B* **46**, 39–44 (1990).

Acknowledgments: M.B. and G.A.B. are grateful to J. Huang and T. Casagrande for sample preparation using FIB and to A. Duft for TEM/STEM maintenance. H.A.D. and G.M.L. thank G. Wright for assistance with the crystal growth experiment. M.B. thanks J. Britten for fruitful discussions. **Funding:** The STEM-EELS work was performed at the Canadian Center for Electron Microscopy, a national facility supported by the Canada Foundation for Innovation under the MSI program, McMaster University, and the Natural Sciences and Engineering Research Council of Canada (NSERC). G.A.B. is grateful to NSERC for supporting this work. D.H., G.M.L., and G.A.S. acknowledge the Canadian Institute for Advanced Research (CIFAR) for research support. G.M.L. acknowledges NSERC for funding of the crystal growth experiment. M.B. acknowledges financial support from the University of British Columbia as a visiting researcher. S.L. acknowledges financial support by the Austrian Science Fund (FWF) under grant number J3732-N27. P.S. acknowledges financial support by the Austrian Science Fund (FWF) under grant number I543-N20. G.R. acknowledges the Institut de Physique (INP) of the French Centre National de la Recherche Scientifique (CNRS) for partial financial support through the International Program for Scientific Cooperation (PICS). **Author contributions:** M.B., G.R., and G.A.B conceived the study and the experiment. H.A.D. performed the crystal growth experiment. M.B. performed the STEM-EELS experiments. M.B., G.R., and S.L. analyzed the data. S.L. performed the channeling simulations. M.B., S.L., and G.R. wrote the manuscript. D.H., P.S., G.A.S., and G.A.B. contributed to data interpretation and the discussions in the manuscript. All authors discussed the results and contributed to the final text of the manuscript. **Competing interests:** The authors declare that they have no competing interests. **Data and materials availability:** All data needed to evaluate the conclusions in the paper are present in the paper and/or the Supplementary Materials. Additional data related to this paper may be requested from the authors.

Submitted 16 November 2015
Accepted 5 February 2016
Published 25 March 2016
10.1126/sciadv.1501652

Citation: M. Bugnet, S. Löffler, D. Hawthorn, H. A. Dabkowska, G. M. Luke, P. Schattschneider, G. A. Sawatzky, G. Radtke, G. A. Botton, Real-space localization and quantification of hole distribution in chain-ladder $Sr_3Ca_{11}Cu_{24}O_{41}$ superconductor. *Sci. Adv.* **2**, e1501652 (2016).

Chapter 3

Mapping atomic orbitals with the transmission electron microscope: Images of defective graphene predicted from first-principles theory

L. Pardini, S. Löffler, G. Biddau, R. Hambach, U. Kaiser, C. Draxl, and P. Schattschneider

Physical Review Letters 117 (2016) 036801
10.1103/PhysRevLett.117.036801

Mapping Atomic Orbitals with the Transmission Electron Microscope: Images of Defective Graphene Predicted from First-Principles Theory

Lorenzo Pardini,[1] Stefan Löffler,[2,3,4] Giulio Biddau,[1] Ralf Hambach,[5,6] Ute Kaiser,[5]
Claudia Draxl,[1,7] and Peter Schattschneider[2,3]
[1]*Physics Department and IRIS Adlershof, Humboldt-Universität zu Berlin, 12489 Berlin, Germany*
[2]*Institute of Solid State Physics, Vienna University of Technology, A-1040 Vienna, Austria*
[3]*University Service Centre for Transmission Electron Microscopy, Vienna University of Technology, A-1040 Vienna, Austria*
[4]*Department of Materials Science and Engineering, McMaster University, Hamilton, Ontario L8S 4L8, Canada*
[5]*Electron Microscopy Group of Materials Science, University of Ulm, 89081 Ulm, Germany*
[6]*Fraunhofer Institute for Applied Optics and precision engineering IOF, 07749 Jena, Germany*
[7]*European Theoretical Spectroscopy Facility (ETSF)*

(Received 26 May 2015; revised manuscript received 17 May 2016; published 14 July 2016)

Transmission electron microscopy has been a promising candidate for mapping atomic orbitals for a long time. Here, we explore its capabilities by a first-principles approach. For the example of defected graphene, exhibiting either an isolated vacancy or a substitutional nitrogen atom, we show that three different kinds of images are to be expected, depending on the orbital character. To judge the feasibility of visualizing orbitals in a real microscope, the effect of the optics' aberrations is simulated. We demonstrate that, by making use of energy filtering, it should indeed be possible to map atomic orbitals in a state-of-the-art transmission electron microscope.

DOI: 10.1103/PhysRevLett.117.036801

The possibility to *see* atomic orbitals has always attracted great scientific interest. At the same time, however, the real meaning of "measuring orbitals" has been a subject that scientists have long and much dwelt upon (see, e.g., [1] and references therein). In the past, significant efforts have been devoted to the development of experimental approaches and theoretical models that allow for orbital reconstruction from experimental data [1]. Based on the generation of higher harmonics by femtosecond laser pulses, a tomographic reconstruction of the highest occupied molecular orbital for simple diatomic molecules in the gas phase was proposed [2]. Direct imaging of the highest occupied molecular orbital and the lowest unoccupied molecular orbital of pentacene on a metallic substrate was theoretically predicted and experimentally verified with scanning tunneling microscopy (STM) [3]. More recently, real-space reconstruction of molecular orbitals from angle-resolved photoemission data has been demonstrated [4]. This method has been subsequently further developed to retrieve both the spatial distribution [5] and the phase of electron wave functions of pentacene and perylene-3,4,9,10-tetracarboxylic dianhydride adsorbed on silver [6].

The reconstruction of charge densities and chemical bonds using transmission electron microscopy (TEM) has been considered [7–11], but only recently the possibility of probing selected transitions to specific unoccupied orbitals by using energy-filtered TEM (EFTEM) was demonstrated theoretically. A first example for the capability of this approach was provided with the oxygen K edge of rutile TiO_2 [12]. However, the interpretation of experimental TEM images for systems like rutile would be complicated because of the multiple elastic scattering of electrons that occurs in thick samples.

In this Letter, we suggest defective graphene [13–17] as the prototypical two dimensional (2D) material to demonstrate the possibility of mapping atomic orbitals using EFTEM. We break the ideal sp^2 hybridization by introducing two different kinds of defects, namely a single isolated vacancy and a substitutional nitrogen atom. This lifts the degeneracy of the p states, inducing strong modifications to the electronic properties compared to the pristine lattice [15,18–24]. By selecting certain scattering angles, dipole-allowed transitions dominate the electron energy loss spectroscopy (EELS) signal [25]. A single-particle description can be safely adopted, since many-body effects do not play a major role in the excitation process. Overall, TEM images of these systems can be interpreted in terms of bare s-p transitions.

In an EFTEM experiment, an incoming beam of high-energy electrons (of the order of 100 keV) is directed to the target where it scatters at the atoms either elastically or inelastically. The outgoing electron beam is detected and analyzed. State of the art image simulations generally only include elastic scattering of the electrons using the multislice approach [26]. In the case of EFTEM for a thin sample, the influence of elastic scattering becomes negligible, and inelastic scattering gives the dominant contribution to the formation of the images.

The key quantity to describe the inelastic scattering of electrons, which is probed by EELS, is the mixed dynamic form factor (MDFF). It can be interpreted as a weighted sum of transition matrix elements between initial and final states ϕ_i and ϕ_j of the target electron [27–29]:

$$S(\mathbf{q},\mathbf{q}';E)=\sum_{i,j}\langle\phi_i|e^{i\mathbf{q}\cdot\mathbf{r}}|\phi_j\rangle\langle\phi_j|e^{-i\mathbf{q}'\cdot\mathbf{r}}|\phi_i\rangle\delta(E_j-E_i-E) \qquad (1)$$

with energies E_i and E_j. E is the energy loss of the fast electron of the incident beam, $\mathbf{q}$ and $\mathbf{q}'$ are the wave vectors of the perturbing and induced density fluctuations, respectively. If many-body effects can be neglected, this picture can be simplified for dipole-allowed transitions. In this case, using the spherical harmonics as basis for the target states and referring to transitions originating from a single state (as in s-p excitations), the MDFF is [12]

$$S(\mathbf{q},\mathbf{q}';E)\propto\sum_{\mu LM,\mu' L'M'}\langle j_{\lambda=1}(q)\rangle_{LE}\langle j_{\lambda=1}(q')\rangle_{L'E}Y^{\mu}_{\lambda=1}(\mathbf{q})^{*}Y^{\mu'}_{\lambda=1}(\mathbf{q}')\Xi_{\lambda=1\mu LM,\lambda=1\mu' L'M'}(E), \qquad (2)$$

where $Y^{\mu}_{\lambda=1}(\mathbf{q})$ are spherical harmonics, $\langle j_{\lambda=1}(q)\rangle_{LE}$ is an integral of the spherical Bessel function $j_{\lambda=1}(q)$ weighted over the initial and final radial wave functions. L and M indicate the azimuthal and magnetic quantum number of the final state of the target electron, and λ and μ are the angular momenta transferred during the transition. $\Xi_{\lambda\mu LM,\lambda'\mu' LM}(E)$ is a quantity that describes crystal-field effects and is proportional to the cross-density of states (XDOS)

$$\sum_{n\mathbf{k}}D^{n\mathbf{k}}_{LM}(D^{n\mathbf{k}}_{L'M'})^{*}\delta(E_n(\mathbf{k})-E), \qquad (3)$$

where $D^{n\mathbf{k}}_{LM}$ is the angular part of the final wave function, n is the band index, and $\mathbf{k}$ is a k point in the first Brillouin zone. Compared to the density of states (DOS), the XDOS includes also nondiagonal terms connecting states with different angular momenta. As $\Xi_{\lambda=1\mu LM,\lambda=1\mu' LM}(E)$ is a Hermitian matrix [12], the MDFF can be diagonalized. Therefore, assuming that the target's final states of the s-p excitation are not degenerate, the transition matrix elements reflect the azimuthal shape of the final single-particle states and can thus be separated by using energy filtering.

Ground-state calculations are performed using density-functional theory and the full-potential augmented plane wave plus the local-orbital method, as implemented in **exciting** [30]. Introducing a vacancy or a substitutional atom, a 5 × 5 supercell is set up, hosting 49 and 50 atoms, respectively (Figs. 1 and 2 in the Supplemental Material [31]). The space group and thus the number of inequivalent carbon atoms (13) is the same in both cases. We adopt a lattice parameter of $a=4.648$ bohr, corresponding to a bond length of 2.683 bohr, while the cell size perpendicular to the graphene plane is set to $c=37.794$ bohr in order to prevent interactions between the periodically repeated layers. Exchange-correlation effects are treated by the Perdew-Burke-Ernzerhof functional [32]. The Brillouin zone is sampled with an $8\times 8\times 1k$-point grid. The structures are relaxed down to a residual force lower than 0.0005 Ha/bohr acting on each atom. Interatomic distances between atoms of the relaxed structures, up to the seventh nearest neighbor, are given in Table I. Upon relaxation, the atoms surrounding the vacancy move slightly away from it, thus shortening the bond lengths with the next nearest neighbors, d_{1-2}, compared to the unperturbed system. The effect of the vacancy extends up to the fourth neighbors, whereas it is almost negligible for more distant atoms (more information about the relaxed structures can be found in the Supplemental Material [31]). In the case of nitrogen doping, the substitutional atom does not strongly influence the atomic configuration of the system. This happens because the nitrogen-carbon bond length is just slightly shortened with respect to the carbon-carbon bond length in pristine graphene. For all the systems, we have investigated dipole-allowed transitions at the K edge of

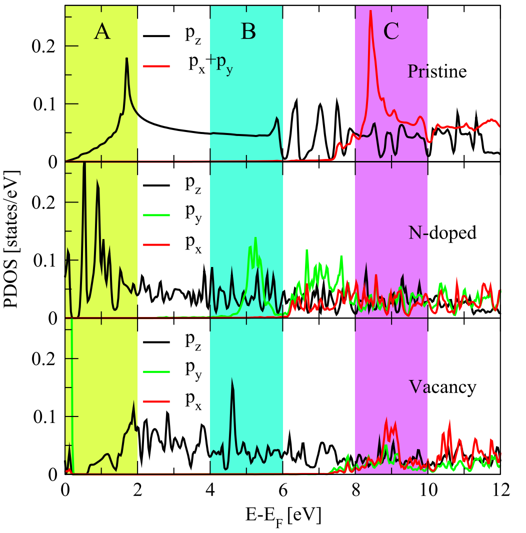

FIG. 1. Local projected density of states (PDOS) of carbon in pristine graphene (upper panel), and of the first nearest-neighbor atom for nitrogen-doped graphene (middle panel) and graphene with a single vacancy (bottom). p_x, p_y, and p_z states are indicated by the red, green, and black lines, respectively. Note that, in the lower panel, the peak close to the Fermi energy exceeds the boundary of the box, with a maximum at about 2 states/eV. In the case of pristine graphene, the red line indicates the sum of p_x and p_y. The three colored areas labeled as A, B, and C indicate the energy ranges for which the TEM images have been calculated.

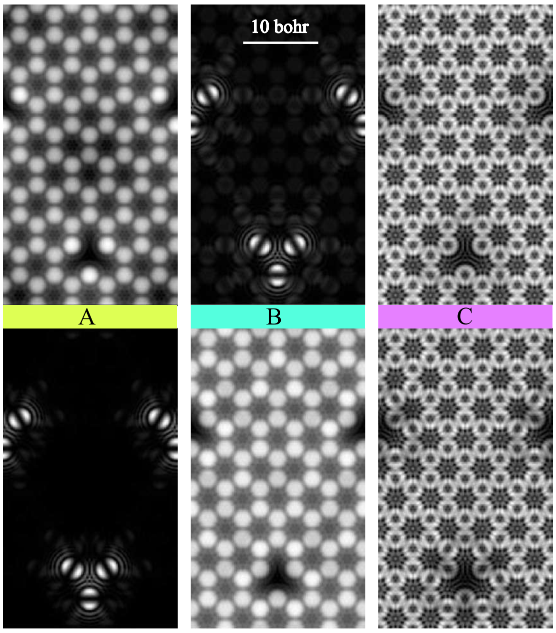

FIG. 2. Simulated real-space intensity of the electron's exit wave function after propagation of an incident plane wave through a graphene layer in presence of a nitrogen substitutional atom (upper panels) and a vacancy (bottom panels). The colored lines indicate the energy regions highlighted in Fig. 1.

carbon, assuming an incoming electron beam perpendicular to the graphene plane.

In Fig. 1, the projected density of states (PDOS) of pristine graphene (upper panel) and of the first nearest-neighbor atom for nitrogen-doped graphene (middle panel) and graphene with a single vacancy (bottom), respectively, is plotted for empty states up to 12 eV above the Fermi energy. Here, x, y, and z represent the local Cartesian coordinates at the individual atomic sites as determined by the point-group symmetry. In particular, z is the axis perpendicular to the graphene, i.e., (x, y) plane. All the other atoms of the defective systems exhibit a PDOS with very similar character as in pristine graphene, besides the second and third nearest neighbors which are slightly affected by the defect [31]. In pristine graphene, antibonding π^* and σ^* states are clearly recognizable at about 2 and 9 eV, respectively. As already reported in the literature [33–36], the introduction of a vacancy or a substitutional nitrogen has a significant influence on the electronic structure. A consequence of the doping atom is lifting the degeneracy of p_x and p_y that is significant for the first nearest neighbors (middle panel in Fig. 1). This effect is particularly evidenced by the appearance of bands at about 5 eV, which exhibit p_y character. Here, three different regions can be easily identified: (a) From 0 to 4 eV, the bands have only p_z character; energy ranges that present such DOS character will be referred to as T_{p_z}. (b) For energies higher than 6 eV, there are contributions from p_x, p_y, and p_z. The only difference to ideal graphene is the lifted degeneracy of p_x and p_y. This defines a new kind of region, named $T_{p_{x,y,z}}$. (c) Between 4 and 6 eV, the p_x character of the first nearest neighbor is much less pronounced than that of p_y, while all the other atoms have only p_z character; this region will be referred to as $T_{p_{y,z}}$. In the case of graphene with a vacancy, the same kinds of regions can be identified, but corresponding to different energy ranges. Here, the T_{p_z} type is found between 0.5 and 7 eV; $T_{p_{x,y,z}}$ encompasses energies above 7 eV; $T_{p_{y,z}}$ is a small energy window, just a few tenths of eV close to the Fermi energy. We find similar kinds of DOS characters also for damaged nitrogen-doped graphene, i.e., graphene with a substitutional nitrogen and a vacancy located near it; such defects have been reported recently in TEM measurements of nitrogen-doped graphene [37]. Details of this calculation and the corresponding simulated TEM images can be found in the Supplemental Material [31].

TABLE I. Bond lengths between atoms up to the seventh nearest neighbor, d_{0-1}, d_{1-2}, d_{2-3}, d_{2-4}, d_{4-6}, and d_{6-7}, for graphene doped with nitrogen (top row) and with a vacancy (bottom row). Δd are the relative deviations from those of pristine graphene. 0 indicates the defect site.

System	d_{0-1}	d_{1-2}	d_{2-3}	d_{2-4}	d_{4-6}	d_{4-7}
N-doped d [bohr]	2.675	2.675	2.683	2.689	2.683	2.692
Δd	−0.3%	−0.3%	···	+0.2%	···	+0.3%
Vacancy d [bohr]	2.689	2.665	2.678	2.712	2.676	2.687
Δd	+0.2%	−0.7%	−0.2%	+1.1%	−0.3%	+0.1%

To investigate the impact of the local electronic structure (PDOS) on the EFTEM images, we first consider the ideal case of a perfect microscope with an acceleration voltage of 300 keV. In this case, the recorded images correspond to the intensity of the exit wave function in the multislice simulation [38]. The finite resolution of the spectrometer is taken into account by simulating images every 0.05 eV in 2 eV-broad energy ranges (regions A, B, and C in Fig. 2) and then summing them up to get the final images. Each image is shown in contrast-optimized gray scale.

First, we analyze graphene with nitrogen doping (Fig. 2, upper panels). Here, in the region close to the Fermi level (A in Fig. 1) there are only contributions from p_z orbitals. The image is then formed by disklike features where their arrangement clearly visualizes the missing atoms (upper left panel in Fig. 2). At an energy loss between 4 and 6 eV above the carbon K edge (region B in Fig. 1), there is a $T_{p_{y,z}}$-like region. We expect to see contributions from p_y of the atom closest to the nitrogen, but no (or very little) signal coming from the other atoms. This happens because p_y lies on a plane perpendicular to the incoming electron beam and its magnitude is more intense than the one of p_z; thus, its contribution to the final signal overcomes the one from p_z states. Consequently, only the p_y orbitals of the three atoms surrounding the nitrogen are visible, which are pointing towards the defect, as imposed by the local D_{3h} symmetry (upper middle panel in Fig. 2). At an excitation energy between 8 and 10 eV above the K edge (region C in Fig. 1), instead, there are contributions from all the p states. Since, however, p_x and p_y lie in a plane perpendicular to the beam axis, their contribution to the final signal dominate over the one from p_z states. As a consequence, the image is composed of ringlike features, stemming solely from p_x and p_y states, arranged in hexagons (upper right panel in Fig. 2). Because of symmetry breaking, the intensity is not uniform, neither along a ring (since p_x and p_y states are nondegenerate) nor among different rings (due to nonequivalent atomic sites).

The corresponding images for the system with a vacancy (bottom panels in Fig. 2) appear nearly identical to the ones above, but at different energy ranges. This can be understood by comparing the PDOS of the two systems. Between 0 and 2 eV, for instance, we have a T_{p_z}-like region in the case of nitrogen-doped graphene, and both $T_{p_{y,z}}$ and T_{p_z} in the case of graphene with a vacancy. Because of the similarity of the two systems, we will, in the following, focus on doped graphene and show the corresponding analysis for graphene with a single vacancy in the Supplemental Material [31].

In order to predict the outcome of real experiments, we now visualize the effect of the optics' aberrations and of a more realistic acceleration voltage on these images. We have simulated an electron-beam acceleration voltage of 80 keV and the operating parameters of two different kinds of microscopes, the FEI Tecnai G^2 F20 and FEI Titan G^2 60–300. The former has a spherical aberration $C_S = 1.2$ mm, corresponding to a an extended Scherzer defocus of 849 Å, while the latter is a last-generation aberration-corrected microscope, i.e., exhibiting no spherical and chromatic aberrations. In view of that, chromatic aberrations are not included in the calculations. The images corresponding to the energy regions A, B, and C are shown in Fig. 3. Because of the lower resolution of the Tecnai microscope, all the features are blurred (lower panels) compared to the ideal images. Therefore, neither the atomic positions, nor the orbital shapes can be retrieved from them. On the other hand, images simulated by taking into account the aberration-corrected optics of the Titan microscope are very sharp and let us identify all the features already observed for the idealized situation previously described. This can be easily seen, comparing the upper panels of Figs. 3 and 2. In particular, at an energy loss of 5 eV (region B), the p_y orbitals are visible, as in the ideal images. This clearly demonstrates the potential ability of aberration-corrected microscopes to visualize atomic orbitals with EFTEM, especially in a system like graphene. This conclusion also holds when considering noise caused by the finite electron dose (see Supplemental Material [31] for corresponding images).

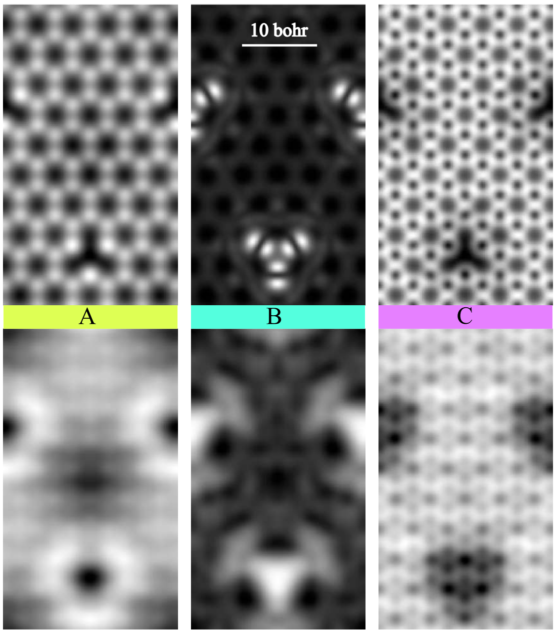

FIG. 3. Simulated TEM image of nitrogen-doped graphene. The colored lines indicate the energy regions highlighted in Fig. 1. 80 keV incident beam energy and lenses as in a Titan (upper panels) and a Tecnai microscope (bottom panels) were assumed.

In summary, we have predicted the possibility of performing orbital mapping in low-dimension systems using EFTEM and we have demonstrated it with the prototypical example of defective graphene. In particular, we have shown that, as far as the optics is concerned, reasonable image resolution may already nowadays be experimentally achievable with last-generation aberration-corrected microscopes like a FEI Titan G^2 60–300 and even more with improved instruments of the next generation. However, additional work is necessary to reduce artifacts such as noise, drift, instabilities, and damage. The inelastic cross section for the carbon K-edge ionization is about a factor of 10 smaller than the elastic scattering cross section on a carbon atom [39]. The intensity collected within an energy window of 2 eV as in Fig. 2 is $< 5\%$ of the total K-edge intensity. So, order-of-magnitude-wise, in order to obtain the same signal-to-noise ratio as in elastic imaging, we need at least 200 times more incident dose which means a dwell time of the order of several minutes for last-generation TEMs in the EFTEM mode. There is no fundamental law that would forbid such an experiment with today's equipment; however, it is hampered by drift (which must be well below the interatomic distance during the exposure time), instabilities, and radiation damage. A new route to circumvent radiation damage based on an EFTEM low-dose technique was proposed recently [40]. This may solve the problem in the future.

We have identified three different kinds of images that are expected to be acquired in an EFTEM experiment, depending on the character of the DOS: When only p_z states are present in the electronic structure, the corresponding images are composed of disklike features. When the DOS is characterized by contributions from all p states, ringlike features are seen that, however, only originate from a convolution of p_x and p_y states, while the p_z character is not visible. When the p_y character strongly exceeds the one of p_x, only a single orbital is recorded. We expect this work to trigger new experiments on defective graphene and similar systems.

Financial support by the Austrian Science Fund (Projects No. I543-N20 and No. J3732-N27) and the German Research Foundation within the DACH framework is acknowledged.

[1] W. H. E. Schwarz, Angew. Chem., Int. Ed. **45**, 1508 (2006).
[2] L. Itatani, J. Levesque, D. Zeidler, H. Niikura, H. Pepin, J. C. Kieffer, P. B. Corkum, and D. M. Villeneuve, Nature (London) **432**, 867 (2004).
[3] J. Repp, G. Meyer, S. M. Stojković, A. Gourdon, and C. Joachim, Phys. Rev. Lett. **94**, 026803 (2005).
[4] P. Puschnig, S. Berkebile, A. J. Fleming, G. Koller, K. Emtsev, T. Seyller, J. D. Riley, C. Ambrosch-Draxl, F. P. Netzer, and M. G. Ramsey, Science **326**, 702 (2009).
[5] P. Puschnig, E.-M. Reinisch, T. Ules, G. Koller, S. Soubatch, M. Ostler, L. Romaner, F. S. Tautz, C. Ambrosch-Draxl, and M. G. Ramsey, Phys. Rev. B **84**, 235427 (2011).
[6] D. Lüftner, T. Ules, E. M. Reinisch, G. Koller, S. Soubatch, F. S. Tautz, M. G. Ramsey, and P. Puschnig, Proc. Natl. Acad. Sci. U.S.A. **111**, 605 (2014).
[7] J. M. Zuo, M. Kim, M. O'Keeffe, and J. C. H. Spence, Nature (London) **401**, 49 (1999).
[8] J. C. Meyer, S. Kurasch, H. J. Park, V. Skakalova, D. Knzel, A. Gro, A. Chuvilin, G. Algara-Siller, S. Roth, T. Iwasaki, U. Starke, J. H. Smet, and U. Kaiser, Nat. Mater. **10**, 209 (2011).
[9] M. Haruta, T. Nagai, N. R. Lugg, M. J. Neish, M. Nagao, K. Kurashima, L. J. Allen, T. Mizoguchi, and K. Kimoto, J. Appl. Phys. **114**, 083712 (2013).
[10] M. J. Neish, N. R. Lugg, S. D. Findlay, M. Haruta, K. Kimoto, and L. J. Allen, Phys. Rev. B **88**, 115120 (2013).
[11] M. P. Oxley, M. D. Kapetanakis, M. P. Prange, M. Varela, S. J. Pennycook, and S. T. Pantelides, Microsc. Microanal. **20**, 784 (2014).
[12] S. Löffler, V. Motsch, and P. Schattschneider, Ultramicroscopy **131**, 39 (2013).
[13] A. K. Geim and K. S. Novoselov, Nat. Mater. **6**, 183 (2007).
[14] P. O. Lehtinen, A. S. Foster, Y. Ma, A. V. Krasheninnikov, and R. M. Nieminen, Phys. Rev. Lett. **93**, 187202 (2004).
[15] M. Sammalkorpi, A. Krasheninnikov, A. Kuronen, K. Nordlund, and K. Kaski, Phys. Rev. B **70**, 245416 (2004).
[16] J. M. Carlsson and M. Scheffler, Phys. Rev. Lett. **96**, 046806 (2006).
[17] O. V. Yazyev and L. Helm, Phys. Rev. B **75**, 125408 (2007).
[18] K. S. Novoselov, A. K. Geim, S. V. Morozov, D. Jiang, M. I. Katsnelson, I. V. Grigorieva, S. V. Dubonos, and A. A. Firsov, Nature (London) **438**, 197 (2005).
[19] Y.-W. Son, M. L. Cohen, and S. G. Louie, Nature (London) **444**, 347 (2006).
[20] H. B. Heersche, P. Jarillo-Herrero, J. B. Oostinga, L. M. K. Vandersypen, and A. F. Morpurgo, Nature (London) **446**, 56 (2007).
[21] G.-D. Lee, C. Z. Wang, E. Yoon, N.-M. Hwang, D.-Y. Kim, and K. M. Ho, Phys. Rev. Lett. **95**, 205501 (2005).
[22] Z. Hou, X. Wang, T. Ikeda, K. Terakura, M. Oshima, and M.-a. Kakimoto, Phys. Rev. B **87**, 165401 (2013).
[23] A. Hansson, M. Paulsson, and S. Stafström, Phys. Rev. B **62**, 7639 (2000).
[24] C. Ewels, M. Heggie, and P. Briddon, Chem. Phys. Lett. **351**, 178 (2002).
[25] K. Jorissen, The *ab initio* calculation of relativistic electron energy loss spectra, Ph.D. thesis, Universiteit Antwerpen, 2007.
[26] E. J. Kirkland, *Advanced Computing in Electron Microscopy* (Springer, New York, 2010).
[27] P. Schattschneider, M. Nelhiebel, H. Souchay, and B. Jouffrey, Micron **31**, 333 (2000).
[28] M. Nelhiebel, N. Luchier, P. Schorsch, P. Schattschneider, and B. Jouffrey, Philos. Mag. B **79**, 941 (1999).
[29] H. Kohl and H. Rose, *Theory of Image Formation by Inelastically Scattered Electrons in the Electron Microscopy*, Advances in Electronics and Electron Physics (Academic Press, New York, 1985).
[30] A. Gulans, S. Kontur, C. Meisenbichler, D. Nabok, P. Pavone, S. Rigamonti, S. Sagmeister, U. Werner, and C. Draxl, J. Phys. Condens. Matter **26**, 363202 (2014).
[31] See Supplemental Material at http://link.aps.org/supplemental/10.1103/PhysRevLett.117.036801 for more information about the DOS of the second nearest neighbors, the DOS of the atom most distant from the defect, the simulated EFTEM images of graphene with a single vacancy with lenses as in Tecnai and Titan microscopes, details of the calculation of damaged nitrogen-doped graphene and the corresponding images, and the simulated images with finite electron dose.
[32] J. P. Perdew, K. Burke, and M. Ernzerhof, Phys. Rev. Lett. **77**, 3865 (1996).
[33] H. Amara, S. Latil, V. Meunier, P. Lambin, and J.-C. Charlier, Phys. Rev. B **76**, 115423 (2007).
[34] Z. Hou, X. Wang, T. Ikeda, K. Terakura, M. Oshima, M.-a. Kakimoto, and S. Miyata, Phys. Rev. B **85**, 165439 (2012).
[35] A. A. El-Barbary, R. H. Telling, C. P. Ewels, M. I. Heggie, and P. R. Briddon, Phys. Rev. B **68**, 144107 (2003).
[36] P. Lambin, H. Amara, F. Ducastelle, and L. Henrard, Phys. Rev. B **86**, 045448 (2012).
[37] T. Susi, J. Kotakoski, R. Arenal, S. Kurasch, H. Jiang, V. Skakalova, O. Stephan, A. V. Krasheninnikov, E. I. Kauppinen, U. Kaiser, and J. C. Meyer, ACS Nano **6**, 8837 (2012).
[38] J. M. Cowley and A. F. Moodie, Acta Crystallogr. **10**, 609 (1957).
[39] L. Reimer, *Transmission Electron Microscopy* (Springer, New York, 1993).
[40] J. Meyer, J. Kotakoski, and C. Mangler, Ultramicroscopy **145**, 13 (2014).

Chapter 4

Real-space mapping of electronic orbitals

S. Löffler, M. Bugnet, N. Gauquelin, S. Lazar, E. Assmann, K. Held,
G. A. Botton, and P. Schattschneider

Ultramicroscopy 177 (2017) 26–29
10.1016/j.ultramic.2017.01.018

Ultramicroscopy 177 (2017) 26–29

Contents lists available at ScienceDirect

Ultramicroscopy

journal homepage: www.elsevier.com/locate/ultramic

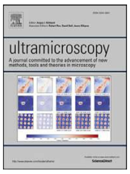

Real-space mapping of electronic orbitals

Stefan Löffler[a,b,c,*], Matthieu Bugnet[a], Nicolas Gauquelin[a], Sorin Lazar[d], Elias Assmann[c], Karsten Held[c], Gianluigi A. Botton[a], Peter Schattschneider[b,c]

[a] *Department for Materials Science and Engineering, McMaster University, 1280 Main Street West, L8S 4M1 Hamilton, Ontario, Canada*
[b] *University Service Centre for Transmission Electron Microscopy, TU Vienna, Wiedner Hauptstraße 8-10/E057B, 1040 Wien, Austria*
[c] *Institute for Solid State Physics, TU Vienna, Wiedner Hauptstraße 8-10/E138, 1040 Wien, Austria*
[d] *FEI Electron Optics, Achtseweg Noord 5, 5651 GG Eindhoven, The Netherlands*

ARTICLE INFO

Article history:
Received 27 July 2016
Revised 30 December 2016
Accepted 29 January 2017
Available online 31 January 2017

Keywords:
EELS
STEM
Orbitals
Electronic states
Mapping

ABSTRACT

Electronic states are responsible for most material properties, including chemical bonds, electrical and thermal conductivity, as well as optical and magnetic properties. Experimentally, however, they remain mostly elusive. Here, we report the real-space mapping of selected transitions between p and d states on the Ångström scale in bulk rutile (TiO_2) using electron energy-loss spectrometry (EELS), revealing information on individual bonds between atoms. On the one hand, this enables the experimental verification of theoretical predictions about electronic states. On the other hand, it paves the way for directly investigating electronic states under conditions that are at the limit of the current capabilities of numerical simulations such as, e.g., the electronic states at defects, interfaces, and quantum dots.

1. Introduction

Electronic states shape the world around us as their characteristics give rise to nearly all macroscopical properties of materials. Be it optical properties such as colour and refractive index, chemical properties such as bonding and valency, mechanical properties such as adhesion, strength and ductility, electromagnetic properties such as conductance and magnetisation, or the properties of trap states: ultimately, all these properties can be traced back to the electronic states in the material under investigation. Therefore, it is not surprising that electronic states are of paramount importance across many fields, including physics, materials science, chemistry and the life sciences. It does come as a surprise, however, that while some of their aspects can be inferred indirectly from macroscopical material properties or some diffraction techniques, the direct observation of individual electronic states in real space so far has succeeded only under very special circumstances (e.g. on an insulating surface using a scanning tunnelling microscope (STM) with a specially functionalised tip [1]) due to both experimental and theoretical challenges. In this work, we endeavour to remedy this situation by using a combination of transmission electron microscopy (TEM), electron energy-loss spectrometry (EELS), and state-of-the-art simulations.

TEM is a well-known technique for studying materials on the nanoscale while EELS adds element-specific information. Both are widely-used on a regular basis in many fields and are readily commercially available. Owing to these two techniques, tremendous progress has been made over the last decade in mapping atom positions with ≈ 10 pm accuracy [2–4], determining charge densities [5–7], and performing atom-by-atom chemical mapping [8–12]. Furthermore, the fine-structures of the spectra allow the determination of the local chemical and structural environment as well as the hybridisation state of the scattering atoms [11–18] in the bulk, which can be substantially different from the surface states probed by STM. This suggests to use the EELS signal to probe the local environment in real-space and map, e.g., crystal fields, conduction states, bonds, and orbitals. Recently, it has been shown on theoretical grounds [19,20] that such real-space mapping of transitions between orbitals on the Ångström scale should indeed be possible, even though the experimental realisation was expected to be extremely challenging.

The method of choice to demonstrate the possibility of this real-space mapping used throughout this work is high-resolution scanning TEM (STEM) together with EELS. In STEM, an electron beam is typically produced by a high-brightness field-emission gun, accelerated to a kinetic energy of the order of 100 keV, and subsequently focused to an Ångström-sized spot on the sample (see Fig. 1c and [21]). Inside the specimen, the probe electrons

---

[*] Corresponding author at: Department for Materials Science and Engineering, McMaster University, 1280 Main Street West, L8S 4M1 Hamilton, Ontario, Canada.
E-mail address: stefan.loeffler@tuwien.ac.at (S. Löffler).

http://dx.doi.org/10.1016/j.ultramic.2017.01.018

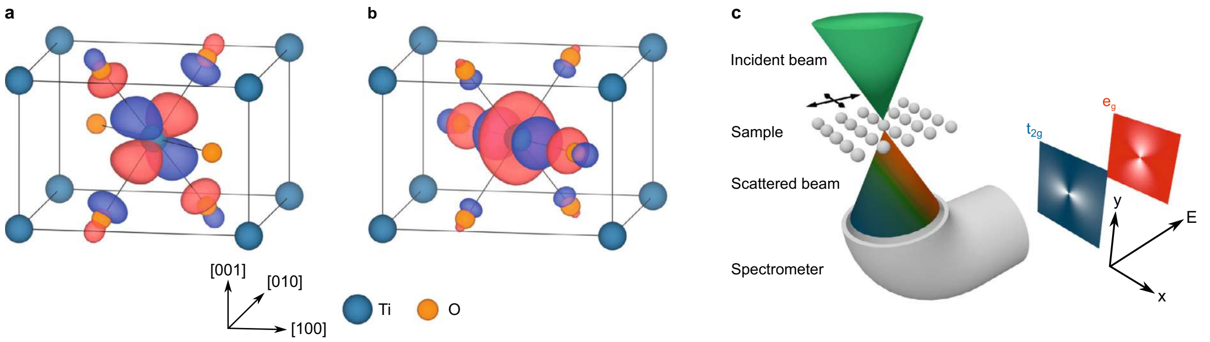

Fig. 1. Maximally-localized Wannier functions in rutile corresponding to unoccupied orbitals of Ti-e_g character (x^2-y^2-like Wannier function (a), z^2-like Wannier function (b)). (c) Sketch of the measurement setup. The incident beam is focused onto and scanned over the sample. It can exchange energy and momentum with the specimen, leading to a mixture of states in the scattered beam. Using a spectrometer comprised of a sector magnet and a subsequent imaging system, maps can be formed of all electrons that have transferred a certain amount of energy E corresponding to transitions to different unoccupied orbitals inside the sample. The blue and red planes symbolize the real-space distribution of the transition probabilities to different final states. (For interpretation of the references to colour in this figure legend, the reader is referred to the web version of this article.)

scatter off the nuclei and sample electrons via the Coulomb interaction.

Scattering by the nuclei is predominantly elastic, i.e., only momentum but no energy is transferred from the lattice (which is assumed to be infinitely heavy) to the probe electron. This gives rise to atomic column contrast in high-resolution TEM, as well as to channeling and dechanneling effects in samples that are thicker than a few tens of nanometres [22,23]. Dechanneling, which can be visualised as a hopping of the electron beam between adjacent columns, destroys the direct spatial correlation between the measured scattering intensity and its point of origin. Consequently, very thin specimens, as well as simulations taking elastic scattering into account, are needed to reduce artefacts and arrive at a reliable interpretation of the data.

Here, the interaction of primary interest is the scattering of the probe electrons on the sample electrons. Both energy and momentum can be transferred between the beam and the sample. Of particular importance for the real-space mapping of electronic transitions is the so-called core-loss regime of energy transfers of $\gtrsim 100$ eV. They trigger an excitation of a sample electron from an initial, occupied core state to a final, unoccupied conduction-band state. The initial states are typically localised in close proximity to the nucleus and are characterised by a large binding energy. Therefore, crystal-field effects are mostly negligible for core states, which typically exhibit atomic character. The final states, on the other hand, lie close to the Fermi energy, and are strongly influenced by the local environment (see Fig. 1a, b).

Due to the strong localisation of the probe beam, it is possible to map the position and energy-dependent transition matrix elements between the initial and the final states using STEM-EELS (see Fig. 1c). If the initial state is known — either from first principles or experiments [24] — it is furthermore possible to obtain both the angular and the radial dependence of the final states [19,25,26] and, thus, bonding information on individual atomic columns [15,27]. To that end, specific transitions can be selected by using a sufficiently narrow energy range.

2. Results

2.1. Experiments

As a model system, we have chosen rutile (TiO_2). It has a relatively simple, tetragonal unit cell and, together with the other titanium oxides, has great practical importance, e.g., in renewable energy and energy storage applications, photocatalysis, or as coating material (for a review, see [28] and other articles published in the same issue). Its tetragonal structure leads to a strong crystal-field splitting. In particular, the different Ti-O bond lengths give rise to a strong asymmetry and splitting [29] of the e_g and t_{2g} states. Most noticeably, the asymmetric shape of the orbitals is rotated by 90° for adjacent Ti atoms due to the crystal symmetry (see Fig. 2). We concentrate here solely on mapping the e_g states since the t_{2g} peak has a much lower intensity. Throughout its narrow energy range [30], there is always a sizeable e_g contribution (see the fitted Gaussian peaks in Fig. 2a), making it impossible to identify an unequivocal t_{2g} signal with todays instruments due to signal-to-noise ratio (SNR) limitations. Also note that in our simulations, the t_{2g} Wannier states are much more localized around the nucleus, which strongly reduces the asymmetry caused by crystal-field effects for t_{2g} states.

A rutile single crystalline sample (MTI corporation) was mechanically thinned down to electron transparency by using the wedge polishing technique with a Multiprep polishing apparatus (Allied High Tech Products Inc.). Further ion milling with a Gentle Mill (Technoorg Linda Ltd.) was performed for ion beam energies in the range of 500–900 eV to remove the damaged regions from the mechanical polishing and provide large, thin, and clean surfaces.

The experiments were performed at 80 kV acceleration voltage on a FEI Titan 80–300 TEM equipped with spherical aberration correctors and a Gatan GIF Quantum Energy Filter. During the experiments, the single-crystalline sample was oriented in [0 0 1] direction and the thickness was determined to be 20 nm using EELS [31,32]. A spectrum image (SI) data cube (see Fig. 2a) was recorded over several unit cells, together with the elastic dark-field (DF) signal (see Fig. 2c). The SI data and the DF signal were acquired simultaneously with a convergence semi-angle of 19 mrad, a GIF collection semi-angle of 20.7 mrad, and a pixel dwell time of 5 ms to maximize the signal while minimizing drift and beam damage artefacts. Optimising the acquisition conditions is essential for acquiring data with sufficient spatial and energy resolution, as well as sufficient SNR for the subsequent data analysis.

The residual lateral drift [33] was corrected using the DF data and the resulting data cube was averaged over 12 unit cells to improve the SNR. Finally, the map corresponding to L_2 transitions with energy transfers in the range 466.6 ± 1 eV was extracted. This corresponds to transitions from initial states with $2p_{1/2}$ character to final states with an energy in the range of 6 ± 1 eV above

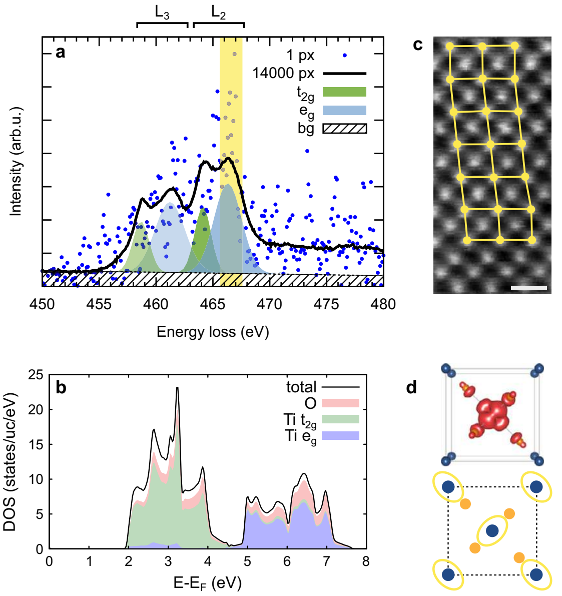

Fig. 2. (a) Ti $L_{2,3}$ edge extracted from a single pixel (dots), and averaged over all 14000 pixels (line) of the data set. The energy window used for the energy-filtered e_g maps is highlighted in yellow. Gaussian least squares fits representing the individual shapes of the e_g and t_{2g} contributions are depicted in blue and green. (b) Projected DOS above the Fermi energy E_F at the position of the Ti atoms as calculated by WIEN2k. (c) Dark field image acquired simultaneously with the spectrum image dataset. The spatial distortion, highlighted with yellow lines, is corrected and the unit cells are subsequently averaged. The scale bar indicates 5 Å. (d) Unit cell along the [0 0 1] direction used in the experiment with the summed three-dimensional charge density of the e_g Wannier functions in Fig. 1a, b. Also shown are the projected positions of Ti (blue) and O (orange) atoms as well as yellow ellipses indicating the nearest O neighbours of each Ti (due to the projection, only two of the four nearest neighbours are visible). (For interpretation of the references to colour in this figure legend, the reader is referred to the web version of this article.)

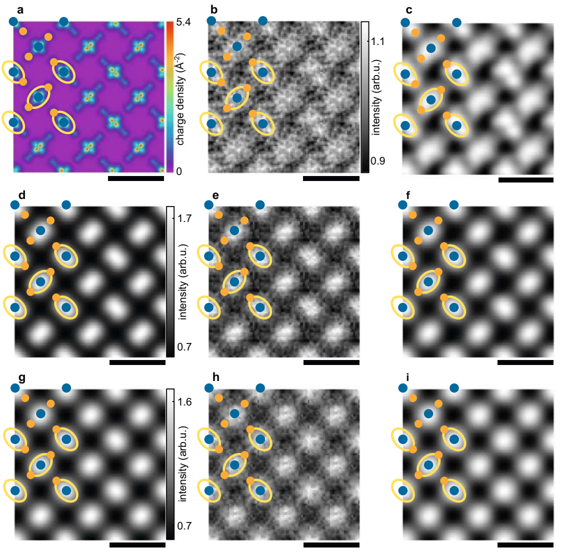

Fig. 3. (a) Charge density for the unoccupied e_g orbitals projected along the [0 0 1] crystallographic axis as calculated by WIEN2k. (b) Experimental energy-filtered map for the Ti L ionization edge for final states with e_g character after unit-cell averaging. (c) Same as (b), but after Gaussian smoothing. (d) Simulated energy-filtered map using the multislice algorithm and the MDFF approach after Gaussian blurring. (e) Same as (d) with added noise to better mimic the experimental conditions. (f) Same as (e) after Gaussian smoothing. (g)–(i) Same as (d)–(f) assuming independent atoms without bonding. All maps are replicated in a 3 × 3 raster for better visibility. Overlays show the projected positions of Ti (blue) and O (orange) atoms as well as yellow ellipses indicating the nearest O neighbours of each Ti (due to the projection, only two of the four nearest neighbours are visible). All scale bars indicate 5 Å. (For interpretation of the references to colour in this figure legend, the reader is referred to the web version of this article.)

the Fermi energy, which have mainly e_g character (see Fig. 2b and [30]). Fig. 3b shows the resulting energy-filtered map, while Fig. 3c shows the same map after Gaussian smoothing. The asymmetry around each Ti column is clearly visible, as is the expected 90° rotation between nearest neighbours, owing to the different electronic environment caused by the Ti-O bonds.

2.2. Simulations

As stated above, comparison to theory is indispensable for a reliable interpretation. To check the results, we simulated the energy-filtered image for the selected energy range and the experimental parameters. To that end, we used the mixed dynamic form factor (MDFF) approach [19,26,34] based on density functional theory data obtained from WIEN2k[1] [35] to model the inelastic interaction between the probe beam and the sample electrons, while the elastic scattering before and after the inelastic scattering event was taken care of using the multislice algorithm [39,40]. The resulting maps were blurred using a Gaussian filter to account for the finite source size in the experiment. Moreover, noise[2] equivalent to the experimental conditions was added to facilitate a visual comparison with the measured data. The resulting simulated map is shown in Fig. 3e. The map after Gaussian smoothing, with the same parameters as in Fig. 3c, is shown in Fig. 3f, where the intensity variations between nearest neighbours are a consequence of the added noise.

The resulting simulated images (see Fig. 3e and f) are found to be in very good agreement with the experimental data (see Fig. 3b and c). In particular, the intensity distribution around the Ti atoms is not circular but has a distinct asymmetry towards the nearest O atoms (those which lie in the plane of the $x^2 - y^2$ Wannier orbital in Fig. 1a). In a cubic crystal, there would be no such asymmetry between the [1 1 0] and [1 $\bar{1}$ 0] directions. Therefore, the experimental data shows the preferential bond direction towards the nearest O atoms. This is confirmed by the calculated charge density of the e_g conduction states as depicted in Fig. 3a which exhibits the same asymmetry as the experimental map.

To verify that the observed asymmetry is not an artefact, we also performed the same simulation assuming no bonds, i.e. independent, spherically symmetric individual atoms at the same lattice sites. The resulting data was processed as before to ensure comparability. The resulting maps are shown in Fig. 3g–i. In contrast to the e_g maps in Fig. 3d–f, the independent-atoms maps in Fig. 3g–i cannot reproduce the distinct asymmetry found in the measured data. Thus, it can be concluded that while elastic scattering does affect the signal in principle, under the conditions used in this work, elastic scattering alone is insufficient to describe the experimental e_g maps (Fig. 3b–c). As they can only be reproduced when taking into account inelastic scattering on realistic electronic

---

[1] The simulations were done based on WIEN2k [35] calculations with the PBE-GGA [36] exchange-correlation potential. Maximally-localised Wannier functions were computed from the e_g bands using the wien2wannier [37] and Wannier90 [38] packages and the disentanglement procedure to separate the target bands from the t_{2g} band which crosses them near Γ.

[2] Gaussian noise with $\sigma = 0.15\mu$, μ being the mean value of the map, was used.

states, the peculiar asymmetric shapes can clearly be attributed to the orbitals.

3. Conclusions and outlook

In this work, we have demonstrated that the real-space mapping of electronic transitions to specific orbitals is possible in a high-end TEM using EELS, thereby revealing information about both the electronic states themselves and the bonds between atoms. This method — together with soon realisable improvements in the SNR and accompanied by simulations — opens the road to studying electronic states in real-space, such as defect states at bulk grain boundaries, bonds at interfaces, or confined electron waves in quantum dots.

Acknowledgements

St.L. thanks Walid Hetaba for discussions about WIEN2k. St.L. and P.S. thank Ralf Hambach and Ute Kaiser for many valuable discussions. M.B. thanks Vienna University of Technology for travel support. St.L. and P.S. acknowledge financial support by the Austrian Science Fund (FWF) under grant number I543-N20, SFB F45 FOXSI; St.L. also acknowledges financial support by the Austrian Science Fund (FWF) under grant number J3732-N27. M.B., N.G., S.L. and G.A.B. performed the experimental work at the Canadian Center for Electron Microscopy, a national facility supported by McMaster University and the Natural Sciences and Engineering Research Council of Canada (NSERC). G.A.B. is grateful to NSERC for supporting this work.

References

[1] J. Repp, G. Meyer, S. Paavilainen, F.E. Olsson, M. Persson, Imaging bond formation between a gold atom and pentacene on an insulating surface, Science 312 (5777) (2006) 1196–1199, doi:10.1126/science.1126073.

[2] K. Urban, Studying atomic structures by aberration-corrected transmission electron microscopy, Science 321 (5888) (2008) 506–510, doi:10.1126/science.1152800.

[3] M.J. Hytch, J.-L. Putaux, J.-M. Penisson, Measurement of the displacement field of dislocations to 0.03 Å by electron microscopy, Nature 423 (6937) (2003) 270–273, doi:10.1038/nature01638.

[4] K.W. Urban, Is science prepared for atomic-resolution electron microscopy? Nat. Mater. 8 (4) (2009) 260–262, doi:10.1038/nmat2407.

[5] J.M. Zuo, M. Kim, M. O'Keeffe, J.C.H. Spence, Direct observation of d-orbital holes and Cu-Cu bonding in Cu_2O, Nature 401 (6748) (1999) 49–52, doi:10.1038/43403.

[6] J.C. Meyer, S. Kurasch, H.J. Park, V. Skakalova, D. Künzel, A. Groß, A. Chuvilin, G. Algara-Siller, S. Roth, T. Iwasaki, U. Starke, J.H. Smet, U. Kaiser, Experimental analysis of charge redistribution due to chemical bonding by high-resolution transmission electron microscopy, Nat. Mater. 10 (3) (2011) 209–215, doi:10.1038/nmat2941.

[7] P.N. Nakashima, A.E. Smith, J. Etheridge, B.C. Muddle, The bonding electron density in aluminum, Science 331 (6024) (2011) 1583–1586, doi:10.1126/science.1198543.

[8] K. Kimoto, T. Asaka, T. Nagai, M. Saito, Y. Matsui, K. Ishizuka, Element-selective imaging of atomic columns in a crystal using STEM and EELS, Nature 450 (7170) (2007) 702–704, doi:10.1038/nature06352.

[9] K. Suenaga, M. Koshino, Atom-by-atom spectroscopy at graphene edge, Nature 468 (7327) (2010) 1088–1090, doi:10.1038/nature09664.

[10] M. Bosman, V.J. Keast, J.L.G.-M. noz, A.J. D'Alfonso, S.D. Findlay, L.J. Allen, Two-dimensional mapping of chemical information at atomic resolution, Phys. Rev. Lett. 99 (8) (2007) 086102, doi:10.1103/PhysRevLett.99.086102.

[11] K. Suenaga, M. Tencé, C. Mory, C. Colliex, H. Kato, T. Okazaki, H. Shinohara, K. Hirahara, S. Bandow, S. Iijima, Element-selective single atom imaging, Science 290 (5500) (2000) 2280–2282, doi:10.1126/science.290.5500.2280.

[12] D.A. Muller, L.F. Kourkoutis, M. Murfitt, J.H. Song, H.Y. Hwang, J. Silcox, N. Dellby, O.L. Krivanek, Atomic-scale chemical imaging of composition and bonding by aberration-corrected microscopy, Science 319 (5866) (2008) 1073–1076, doi:10.1126/science.1148820.

[13] G.-Z. Zhu, G. Radtke, G.A. Botton, Bonding and structure of a reconstructed (001) surface of $SrTiO_3$ from TEM, Nature 490 (7420) (2012) 384–387, doi:10.1038/nature11563.

[14] H. Tan, S. Turner, E. Yücelen, J. Verbeeck, G. Van Tendeloo, 2d atomic mapping of oxidation states in transition metal oxides by scanning transmission electron microscopy and electron energy-loss spectroscopy, Phys. Rev. Lett. 107 (2011) 107602, doi:10.1103/PhysRevLett.107.107602.

[15] M.J. Neish, N.R. Lugg, S.D. Findlay, M. Haruta, K. Kimoto, L.J. Allen, Detecting the direction of oxygen bonding in $SrTiO_3$, Phys. Rev. B 88 (2013) 115120, doi:10.1103/PhysRevB.88.115120.

[16] W. Zhou, M. Kapetanakis, M. Prange, S. Pantelides, S. Pennycook, J.-C. Idrobo, Direct determination of the chemical bonding of individual impurities in graphene, Phys. Rev. Lett. 109(20). 10.1103/PhysRevLett.109.206803.

[17] M. Nelhiebel, P. Schattschneider, B. Jouffrey, Observation of ionization in a crystal interferometer, Phys. Rev. Lett. 85 (2000) 1847–1850, doi:10.1103/PhysRevLett.85.1847.

[18] N. Gauquelin, E. Benckiser, M.K. Kinyanjui, M. Wu, Y. Lu, G. Christiani, G. Logvenov, H.-U. Habermeier, U. Kaiser, B. Keimer, G.A. Botton, Atomically resolved EELS mapping of the interfacial structure of epitaxially strained $LaNiO_3/LaAlO_3$ superlattices, Phys. Rev. B 90 (2014) 195140, doi:10.1103/PhysRevB.90.195140.

[19] S. Löffler, V. Motsch, P. Schattschneider, A pure state decomposition approach of the mixed dynamic form factor for mapping atomic orbitals, Ultramicroscopy 131 (2013) 39–45, doi:10.1016/j.ultramic.2013.03.021.

[20] L. Pardini, S. Löffler, G. Biddau, R. Hambach, U. Kaiser, C. Draxl, P. Schattschneider, Mapping atomic orbitals with the transmission electron microscope: images of defective graphene predicted from first-principles theory, Phys. Rev. Lett. 117 (2016) 036801, doi:10.1103/PhysRevLett.117.036801.

[21] D.B. Williams, C.B. Carter, Transmission Electron Microscopy, Plenum Press, New York, 1996.

[22] P. Voyles, J. Grazul, D. Muller, Imaging individual atoms inside crystals with ADF-STEM, Ultramicroscopy 96 (3–4) (2003) 251–273, doi:10.1016/S0304-3991(03)00092-5.

[23] C. Dwyer, J. Etheridge, Scattering of Å-scale electron probes in silicon, Ultramicroscopy 96 (3–4) (2003) 343–360, doi:10.1016/S0304-3991(03)00100-1.

[24] J.S. Jeong, M.L. Odlyzko, P. Xu, B. Jalan, K.A. Mkhoyan, Probing core-electron orbitals by scanning transmission electron microscopy and measuring the delocalization of core-level excitations, Phys. Rev. B 93(16). 10.1103/physrevb.93.165140

[25] S. Löffler, I. Ennen, F. Tian, P. Schattschneider, N. Jaouen, Breakdown of the dipole approximation in core losses, Ultramicroscopy 111 (2011) 1163–1167, doi:10.1016/j.ultramic.2011.03.006.

[26] S. Löffler, Study of Real Space Wave Functions with Electron Energy Loss Spectrometry, Vienna University of Technology, 2013 Ph.d. thesis.

[27] W. Hetaba, S. Löffler, M.-G. Willinger, M.E. Schuster, R. Schlögl, P. Schattschneider, Site-specific ionisation edge fine-structure of rutile in the electron microscope, Micron 63 (2014) 15–19, doi:10.1016/j.micron.2014.02.008.

[28] D. Fattakhova-Rohlfing, A. Zaleska, T. Bein, Three-dimensional titanium dioxide nanomaterials, Chem. Rev. 114 (19) (2014) 9487–9558, doi:10.1021/cr500201c. PMID: 25137128

[29] B. Jiang, J.M. Zuo, N. Jiang, M. O'Keeffe, J.C.H. Spence, Charge density and chemical bonding in rutile, TiO_2, Acta Cryst. A 59 (4) (2003) 341–350, doi:10.1107/S010876730301122X.

[30] P. Guttmann, C. Bittencourt, S. Rehbein, P. Umek, X. Ke, G.V. Tendeloo, C.P. Ewels, G. Schneider, Nanoscale spectroscopy with polarized X-rays by NEXAFS-TXM, Nat. Photon 6 (1) (2012) 2529, doi:10.1038/nphoton.2011.268.

[31] T. Malis, S.C. Cheng, R.F. Egerton, EELS log-ratio technique for specimen-thickness measurement in the TEM, J. Electron Microsc. Tech. 8 (2) (1988) 193–200, doi:10.1002/jemt.1060080206.

[32] R.F. Egerton, Electron Energy-Loss Spectroscopy in the Electron Microscope, 2nd Edition, Plenum Press, New York, 1996.

[33] B. Schaffer, G. Kothleitner, W. Grogger, EFTEM spectrum imaging at high-energy resolution, Ultramicroscopy 106 (11–12) (2006) 1129–1138, doi:10.1016/j.ultramic.2006.04.028.

[34] P. Schattschneider, Fundamentals of Inelastic Electron Scattering, Springer, 1986.

[35] P. Blaha, K. Schwarz, G. Madsen, D. Kvasnicka, J. Luitz, 2001. Wien2k, an augmented plane wave + local orbitals program for calculating crystal properties. http://www.wien2k.at.

[36] J.P. Perdew, K. Burke, M. Ernzerhof, Generalized gradient approximation made simple, Phys. Rev. Lett. 77 (1996) 3865–3868, doi:10.1103/PhysRevLett.77.3865.

[37] J. Kuneŝ, R. Arita, P. Wissgott, A. Toschi, H. Ikeda, K. Held, Wien2wannier: from linearized augmented plane waves to maximally localized wannier functions, Comput. Phys. Commun. 181 (11) (2010) 1888–1895, doi:10.1016/j.cpc.2010.08.005.

[38] A.A. Mostofi, J.R. Yates, Y.-S. Lee, I. Souza, D. Vanderbilt, N. Marzari, wannier90: a tool for obtaining maximally-localised wannier functions, Comput. Phys. Commun. 178 (9) (2008) 685–699, doi:10.1016/j.cpc.2007.11.016.

[39] J.M. Cowley, A.F. Moodie, The scattering of electrons by atoms and crystals. I. A new theoretical approach, Acta Cryst. 10 (10) (1957) 609–619, doi:10.1107/S0365110X57002194.

[40] E.J. Kirkland, Advanced Computing in Electron Microscopy, Plenum Press, 1998.

Chapter 5

Imaging the spatial distribution of electronic states in graphene using electron energy-loss spectroscopy: the prospect of orbital mapping

M. Bugnet, M. Ederer, V. K. Lazarov, L. Li, Q. M. Ramasse, S. Löffler, and D. M. Kepaptsoglou

Phys. Rev. Lett. 128 (2022) 116401
10.1103/PhysRevLett.128.116401

PHYSICAL REVIEW LETTERS **128,** 116401 (2022)

Imaging the Spatial Distribution of Electronic States in Graphene Using Electron Energy-Loss Spectroscopy: Prospect of Orbital Mapping

M. Bugnet,[1,2,3,*] M. Ederer,[4] V. K. Lazarov,[5] L. Li,[6] Q. M. Ramasse,[1,2,7] S. Löffler,[4,†] and D. M. Kepaptsoglou[1,5,‡]
[1]*SuperSTEM Laboratory, SciTech Daresbury Campus, Daresbury WA4 4AD, United Kingdom*
[2]*School of Chemical and Process Engineering, University of Leeds, Leeds LS2 9JT, United Kingdom*
[3]*Univ Lyon, CNRS, INSA Lyon, UCBL, MATEIS, UMR 5510, 69621 Villeurbanne, France*
[4]*University Service Centre for Transmission Electron Microscopy, TU Wien, Wiedner Hauptstraße 8-10/E057-02, 1040 Wien, Austria*
[5]*Department of Physics, University of York, York YO10 5DD, United Kingdom*
[6]*Department of Physics and Astronomy, University of West Virginia, Morgantown, West Virginia 26506, USA*
[7]*School of Physics and Astronomy, University of Leeds, Leeds LS2 9JT, United Kingdom*

(Received 4 June 2021; revised 23 December 2021; accepted 25 January 2022; published 14 March 2022; corrected 6 May 2022)

The spatial distributions of antibonding π^* and σ^* states in epitaxial graphene multilayers are mapped using electron energy-loss spectroscopy in a scanning transmission electron microscope. Inelastic channeling simulations validate the interpretation of the spatially resolved signals in terms of electronic orbitals, and demonstrate the crucial effect of the material thickness on the experimental capability to resolve the distribution of unoccupied states. This work illustrates the current potential of core-level electron energy-loss spectroscopy towards the direct visualization of electronic orbitals in a wide range of materials, of huge interest to better understand chemical bonding among many other properties at interfaces and defects in solids.

DOI: 10.1103/PhysRevLett.128.116401

The vast majority of physical and chemical properties of crystalline materials originates from electronic states governing chemical bonding. In addition, defects, interfaces, and surfaces have a direct influence on macroscopic material properties. Imaging electronic states, such as chemical bonds at crystal imperfections and discontinuities in real space, is thus of fundamental and technological interest to enable the development of new materials with novel functionalities. While total electronic charge densities have been reconstructed using either electron diffraction [1,2] or high-resolution imaging [3] in the transmission electron microscope, and more recently imaged with atomic-scale resolution using four-dimensional scanning transmission electron microscopy (STEM) [4–6], the direct observation of individual electronic states has been achieved primarily using scanning tunneling microscopy [7–10], albeit with surface sensitivity only. Electron energy-loss spectroscopy (EELS) in an electron microscope is a spectroscopy technique probing site- and momentum-projected empty states in the conduction band [11]. Following the development of aberration correctors and high stability electron optics, atomic resolution EELS in the scanning transmission electron microscope has become routinely available, leading to elemental (chemical) mapping [12–14], and providing real-space atomic scale localization of electronic states [15–21] using the energy-loss near-edge structure (ELNES) of the spectroscopic signal.

The ELNES, or spectrum fine structure, arising from core-level excitation provides a wealth of information on chemical bonding between atoms, and can be interpreted by first-principles calculations in favorable cases. However, a quantitative interpretation of ELNES maps at atomic resolution requires to also take into account the channeling characteristics of the swift electron beam before and after the inelastic event [15,22–25], and resulting EELS signal mixing. The appropriate description and/or deconvolution of the electron beam propagation allows for the precise determination of the origin of spatially resolved variations in fine structures arising from orbital orientation [26] and localization [27]. It has been theoretically predicted that aberration-corrected STEM-EELS should allow for the mapping of electronic orbitals [24]. A first experimental proof of principle was reported through real-space mapping of electronic transitions to Ti d orbitals in bulk rutile TiO_2 [27], but thus far, mapping electronic orbitals in real space remains extremely challenging and elusive, be it in bulk crystals or at crystal imperfections and discontinuities.

Graphene, a flagship two-dimensional material with exceptional physical and mechanical properties, has received tremendous scientific interest for potential

---

electronic applications [28,29]. The atomic scale analysis of individual graphene flakes is almost exclusively achieved in the top surface view, thus enabling a path to probe single atom chemical bonding [30–32] and phononic response [33]. The chemical bonding in graphene can be described as in-C-plane (σ) and orthogonal out-of-C-plane (π) covalent bonds. The ELNES of the C-K edge therefore represents the excitation of core states probing in-C-plane σ^* ($1s \rightarrow 2p_{x,y}$) orbitals and out-of-C-plane π^* ($1s \rightarrow 2p_z$) orbitals, as illustrated schematically in Fig. S1 [49]. While π^* state distributions around nitrogen and boron dopants in monolayer graphene have been evidenced from the ELNES [34], the prospect of mapping orbitals at vacancies and nitrogen dopants in a single graphene sheet has been explored theoretically only a few years ago [35]. Nevertheless, even if this is intuitively the appropriate direction to observe individual in-C-plane σ bonds, inelastic channeling computations show that the STEM-EELS mapping of σ^* orbitals in top surface view in pristine graphene is not possible due to symmetry constraints [35,36]. The observation of graphene layers in side view, however, provides a pathway to directly visualizing the distribution of π^* states at the atomic scale using STEM-EELS. While the description of the atomic scale distribution of out-of-C-plane π^* and in-C-plane σ^* states may appear simple enough from a chemical bonding perspective, experimental evidence using STEM-EELS is lacking. Moreover, considering the aforementioned subtle effects associated with the localization of the EELS signal, due for instance to channeling of the incident electron beam, the interpretation of energy-filtered real-space maps can be very complex and must be validated through careful numerical work.

In this Letter, real-space maps of π^* and σ^* states in epitaxial graphene multilayers are recorded in side view, combining state-of-the-art high spatial and energy resolution STEM-EELS with inelastic channeling calculations. The interpretation of the spatial distribution of orbital signals, based on the excellent agreement between computed and experimental data, highlights the successful direct mapping of the π^* state distribution at atomic resolution in the transmission electron microscope. The theoretical approach provides a powerful platform to determine the origin of the energy-filtered signal.

The epitaxial graphene/SiC specimen was synthesized by thermal decomposition of SiC at 1300 °C in ultrahigh vacuum (UHV). For completeness, and as shown in Fig. 1(a), we note that a thin capping film of Bi_2Se_3 was additionally deposited on top of the graphene layers by molecular beam epitaxy at 275–325 °C [37]. This specimen was selected due to the convenient cross-section geometry of the graphene layers; the properties and electronic structure of interfaces with the 6H – SiC substrate and the Bi_2Se_3 capping film are the subject of separate studies and not discussed here. This results in a structure comprising of a so-called graphene “buffer layer” (BL) in contact with the underlying SiC substrate, capped with a number of layers of “epitaxial” graphene [here five such layers are seen in Fig. 1(a)], whose macroscopic properties are known to be nigh-on identical to those of free-standing graphene [38,39].

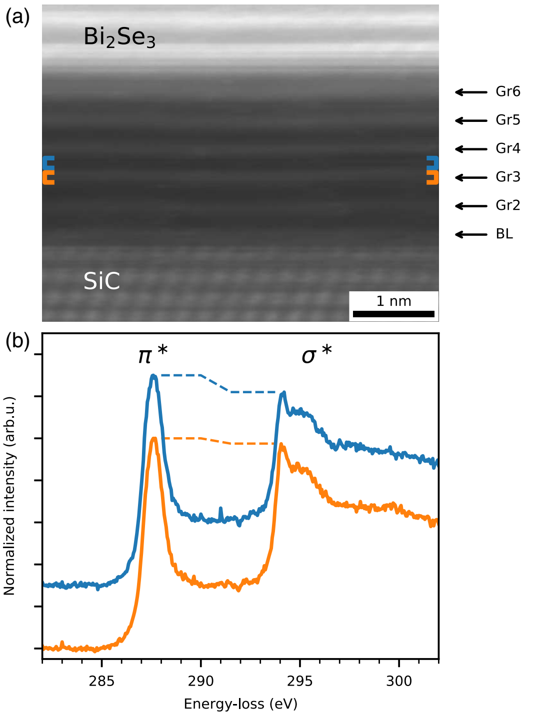

FIG. 1. (a) High resolution STEM-HAADF image of a six-layer epitaxial graphene assembly, grown on 6H – SiC and topped with Bi_2Se_3, simultaneously acquired with core-loss EELS data. (b) C-K edge spectra corresponding to the probe positionned in-C-plane (solid orange line) and between layers (solid blue line), as indicated in (a). Spectra are integrated over the width of the whole image, presented after background subtraction, and shifted vertically for visualization.

The cross-section STEM lamellae were prepared by focused ion beam milling. The thickness of the specimen in the regions of investigation was evaluated to $\sim$25 nm by Fourier-Log deconvolution of low-loss EELS spectra [11]. The STEM-EELS experiments were carried out using a Nion HERMES microscope, equipped with a high-energy-resolution monochromator, a C_s aberration corrector up to the fifth order, a Gatan Enfinium spectrometer, and operated at 60 kV. The convergence and collection semiangles were 30 and 66 mrad, respectively. The specimen was oriented in the $[1\,1\,\bar{2}\,0]$ zone axis of SiC, corresponding to the $[1\,0\,\bar{1}\,0]$ zone axis of graphene (see Fig. S1 [49]). The C-K edge was acquired with a 1.1 Å probe size and a step of $\sim$0.3 Å, providing high spatial sampling while preserving

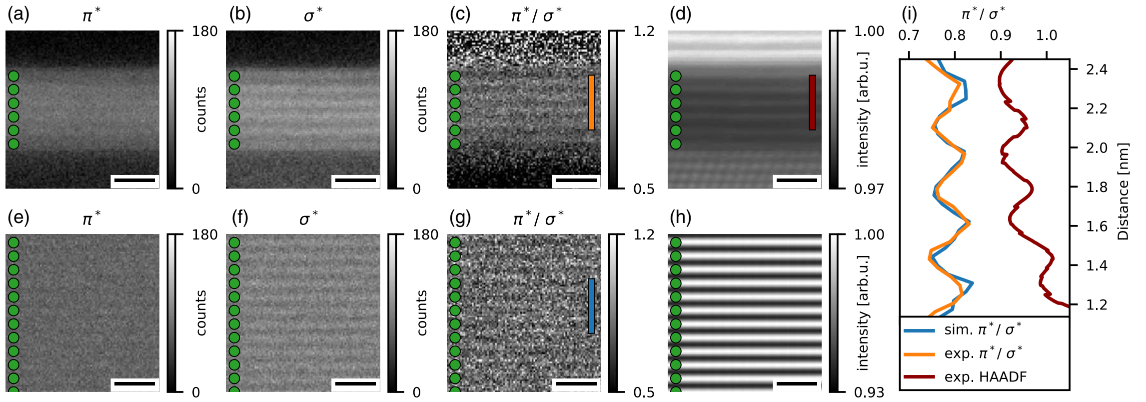

FIG. 2. (a),(b),(c),(d) Experimental π^*, σ^*, π^*/σ^* maps, and HAADF image, respectively. (e),(f),(g),(h) Theoretical π^*, σ^*, π^*/σ^* maps with shot noise, and ADF image, respectively. The position of atomic planes from the HAADF signal is indicated with green circles. (i) π^*/σ^* profiles from (c),(g), and HAADF intensity integrated in the range indicated by the vertical orange, blue, and red bars in (c),(g), and (d). All scale bars indicate 1 nm.

the specimen from electron beam damage. The monochromator slit width was adjusted to provide an effective energy resolution of ~100 meV, as measured at the zero-loss peak full width at half maximum. While not the highest achievable resolution on the instrument, these conditions provided a good compromise of beam current (given the chosen probe size) while still being narrower than expected spectral features. The presented STEM-EELS dataset was acquired from a region of 4.8×3.9 nm^2, with a sampling of 110×88 pixels^2. Subpixel scanning (16×16) was employed, hence leading to a 1760×1408 pixels^2 simultaneously acquired HAADF image in Fig. 1(a). The experimental EELS maps and HAADF image in Fig. 2 are directly cropped from a 88×88 pixels^2 region in the original dataset. The dwell time was 0.2 s, at a dispersion of 0.05 eV/pixel. The experimental maps were obtained after background extraction (modeled with a power-law function), and energy filtering with a 2 eV window for π^* and σ^* states.

The spatial variations of the C-K ELNES are highlighted in Fig. 1(b), where spectra corresponding to in-C-plane (solid orange line) and out-of-C-plane (solid blue line) probe positions are displayed. It is noteworthy that the instrumental broadening of the electron source is narrower than the intrinsic linewidth of the fine structures. This is expected to facilitate orbital mapping since the spectral features are not limited by the energy resolution of the electron source but by physical phenomena linked to, e.g., the excited state lifetime broadening, core-hole screening, or other multielectronic interactions. The π^* and σ^* fine structures are in good agreement with existing work on free-standing graphene layers [39,40], with a sharp excitonic feature visible around 294.5 eV. Although the edges overall look comparable for the in- and out-of-C plane probe positions, the π^* intensity increases noticeably between the epitaxial graphene layers at out-of-C-plane positions. This behavior was systematically observed and is characteristic of all C-K near-edge structures between the epitaxial graphene layers Gr2–Gr6 (see Fig. S2 [49]). The ELNES of the BL and between the graphene BL and Gr2 are influenced by significant covalent bonding between the graphene BL and SiC [39], and thus are not considered here. In a first approximation, the spectral variations observed for the Gr2–Gr6 graphene layers can be related to the simple picture of out-of-C-plane delocalization of π^* states, in contrast to the in-C-plane nature of σ^* states. Indeed, while the π^* bonding takes place between C neighboring atoms of a single graphene layer, the lobes of the antibonding π^* orbitals are delocalized around the C planes, as shown schematically in Fig. S1 of the Supplemental Material [49]. On the contrary, the σ^* orbitals are contained essentially within the graphene planes. Nevertheless, the magnitude of this out-of-C-plane delocalization measured by fine structure mapping, and the ability to spatially distinguish π^* from σ^* states using a convergent electron-probe in STEM-EELS are nontrivial.

In order to rationalize experimental findings, we carried out extensive numerical calculations of the fine structure maps. The effect of the graphene-SiC interface, partially influenced by covalent bonding, and of the graphene-Bi_2Se_3 interface on orbital mapping are beyond the scope of this Letter, therefore a structure made exclusively of graphene layers was considered for inelastic channeling calculations. For simulating the elastic electron propagation both before and after the inelastic scattering events, the multislice algorithm [41,42] was used. For the inelastic interaction between the probe beam and the sample electrons, we calculate the mixed dynamic form factor [24,43], based on density functional theory data obtained with WIEN2k [44]. All simulated STEM-EELS maps were

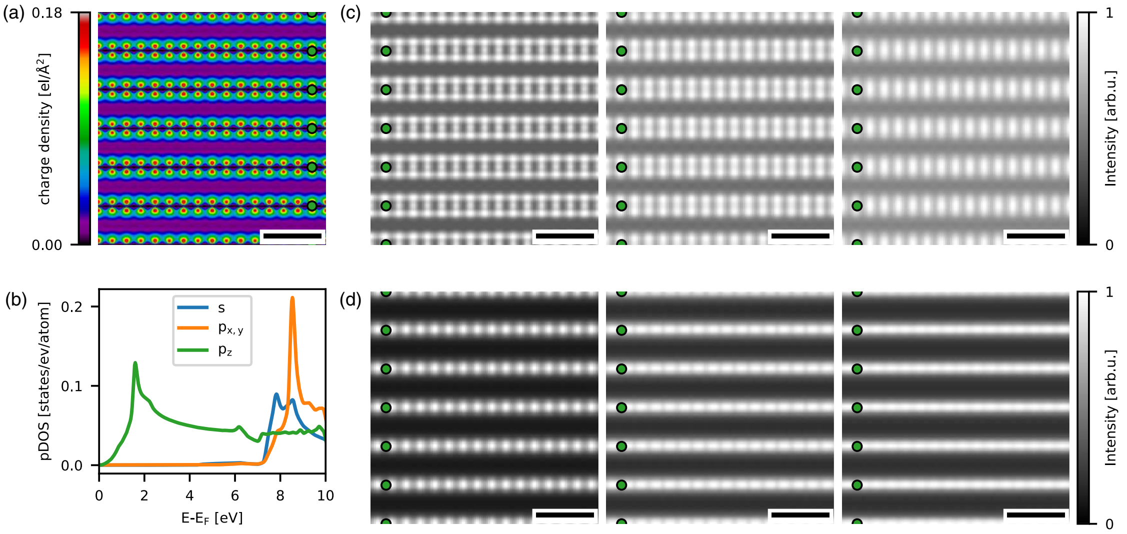

FIG. 3. (a) Charge density for the energy interval between 0.73 and 3.46 eV above the Fermi level. (b) Projected density of states in graphite. The z axis corresponds to the crystallographic c axis of graphite, perpendicular to the carbon layers. (c) π^* maps for projected thicknesses of 0.43 (left), 12.8 (middle), and 25.6 nm (right). The position of atomic planes is indicated with green circles. (d) σ^* maps for the same thicknesses. All maps are shown without noise and instrumental broadening. All scale bars indicate 5 Å.

calculated with the same parameters (acceleration voltage, convergence or collection angle, orientation, sampling, etc.) as used in the experiments. For Fig. 2, the simulated ideal maps were blurred using a Gaussian filter with a standard deviation of 1.1 Å to mimic instrumental broadening due to partial coherence of the electron source [45]. Subsequently, shot noise was added based on the experimental noise characteristics, which were evaluated from the electron intensity in the experimental maps; π^*: 31676.4, σ^*: 40026.5 $\mathrm{e}^-/\mathrm{nm}^2$.

The experimental π^* and σ^* maps, shown in Figs. 2(a) and 2(b), respectively, both display higher intensity where the C planes are located. The localization of the σ^* states on the C planes is expected. For the π^* states (which one might expect to be stronger around the C planes), the apparent, counterintuitive localization on the planes can be explained by channeling effects of the electron beam. These observations are confirmed in the computed maps obtained by inelastic channeling simulations in Figs. 2(e) and 2(f).

Rather than analyzing the absolute intensities, we investigate the ratio between the π^* and the σ^* intensities as shown in Figs. 2(c) and 2(g), as a way to normalize the π^* intensity variations. The ratio is maximized between the C planes in these maps, as exemplified by the vertical π^*/σ^* profiles plotted versus the HAADF intensity in Fig. 2(i). HAADF intensity minima coincide with π^*/σ^* intensity profile maxima, which are almost exactly equidistant from two graphene layers. The visual agreement between the calculated and experimental π^*, σ^*, and π^*/σ^* maps is supported by the remarkable overlap of the calculated and experimental π^*/σ^* line profiles. This successful reproduction of the experimental data underlines the robustness of the inelastic channeling calculations performed in this work to interpret the experimental spectral data. Most importantly, this result provides an undeniable proof that the contrast obtained from π^* and σ^* real-space fine-structure maps at high resolution does match the expected localization of corresponding unoccupied electronic orbitals. It also highlights that beyond the atomic site where core-level excitation takes place, the localization of the π^* and σ^* orbitals in two-dimensional maps is intimately linked to the channeling of the electron beam, and is thus strongly affected by the specimen projected thickness [46].

While the channeling of the swift electron beam primarily depends on the alignment of the electron beam path with the atomic columns, the projected thickness also strongly modifies the atomic-scale contrast in fine structure maps. To evaluate the influence of the projected thickness on the expected π^* and σ^* orbital contrast, we performed inelastic channeling calculations using the same simulation parameters as in Fig. 2 but considering specimens with different thicknesses: 0.43 (a single graphene unit cell), 12.8, and 25.6 nm. The latter corresponds to the estimated thickness of the TEM lamella considered experimentally. The π^* and σ^* maps corresponding to these projected thicknesses under ideal conditions (no noise, no instrumental broadening, etc.) are presented in Figs. 3(c) and 3(d), respectively. These maps differ from those displayed in Figs. 2(e), 2(f), which contain noise and instrumental broadening. The π^* map of the thinnest specimen displays lobes outside the C planes, in agreement with the π^* charge density in Fig. 3(a). Additional intensity is also visible on the C columns, and becomes more prominent for larger and more realistic projected thicknesses. At a thickness of 25.6 nm, the intensity of the π^* states on the C columns is stronger than outside the C planes, in agreement with the experimental π^* maps in Fig. 2. For all thicknesses, it is noteworthy that the intensity in the π^* maps is expected to fade out beyond ~1 Å away from the C planes. The intensity in the σ^* maps is, as expected, exclusively contained within the C planes, and peaked on the C columns. In addition, it is noteworthy that the atomic resolution contrast is smoothed out with increasing thickness. It should be noted that the σ^* maps also contain some intensity from p_z states, i.e., states with π^* symmetry, as shown in the PDOS in Fig. 3(b).

These simulated fine structure maps, in which the elastic channeling conditions of the electron beam were taken into account, highlight the fact that the specimen thickness must be considered carefully to interpret STEM-EELS orbital mapping experiments successfully. Halving the projected thickness down to 12.8 nm is expected to lead to a result similar to the current experimental thickness of 25.6 nm. The direct comparison of π^* orbital maps with the π^* charge density plot in Fig. 3(a) is not reasonable for the experimental thickness considered, nor even for 12.8 nm, but only for an unrealistically small thickness of the order of 0.43 nm. Therefore, it is suggested that smaller projected thickness will only be meaningful below few nm to provide better visualization of electronic orbitals using STEM-EELS in the present case. The noise level is also a major hurdle to overcome, and is clearly visible when comparing the π^* and σ^* maps in Figs. 2(e) (shot noise added) and 3(c) (no shot noise), and Figs. 2(f) (shot noise added) and 3(d) (no shot noise), respectively. It is expected that orbital mapping in STEM-EELS might benefit from a new generation of detectors with improved sensitivity and lower noise level [47,48].

In conclusion, the spatial distribution of antibonding π^* and σ^* orbitals in epitaxial graphene multilayers was mapped successfully by electron energy-loss spectroscopy in the aberration-corrected scanning transmission electron microscope. Inelastic channeling calculations unambiguously reproduce the experimental π^* and σ^* orbital maps with high level of accuracy, and demonstrate the decisive effect of the specimen thickness on the orbital mapping capabilities in graphene. The real-space visualization, at atomic resolution, of unoccupied electronic states with different symmetry defines a pathway to better understand chemical bonding at interfaces and defects in solids. This is particularly relevant to foster defect engineering and tune the properties of solids for a wide range of promising applications where physical and chemical phenomena occur at surfaces (e.g., photocatalysis) or interfaces (e.g., spintronics). This work further illustrates the potentiality of orbital mapping using STEM-EELS.

The electron microscopy work was supported by the EPSRC (UK). SuperSTEM Laboratory is the EPSRC National Research Facility for Advanced Electron Microscopy. The authors would like to thank Hitachi High-Tech Corporation (UK and Japan), Orsay Physics and Tescan for the preparation of FIB lamellae. M. B. is grateful to the SuperSTEM Laboratory for microscope access, and to the School of Chemical and Process Engineering at the University of Leeds for a visiting associate professorship and financial support. M. E. and S. L. acknowledge funding from the Austrian Science Fund (FWF) under Grant No. I4309-N36. L. L. acknowledges funding from U.S. National Science Foundation under Grant No. EFMA-1741673.

M. B. and M. E. contributed equally to this work.

---

[*] mbugnet@superstem.org
[†] stefan.loeffler@tuwien.ac.at
[‡] dmkepap@superstem.org

[1] J. M. Zuo, M. Kim, M. O'keeffe, and J. C. H. Spence, Nature (London) **401**, 49 (1999).

[2] P. N. H. Nakashima, A. E. Smith, J. Etheridge, and B. C. Muddle, Science **331**, 1583 (2011).

[3] J. C. Meyer, S. Kurasch, H. J. Park, V. Skakalova, D. Künzel, A. Groß, A. Chuvilin, G. Algara-Siller, S. Roth, T. Iwasaki, U. Starke, J. H. Smet, and U. Kaiser, Nat. Mater. **10**, 209 (2011).

[4] K. Müller, F. F. Krause, A. Béché, M. Schowalter, V. Galioit, S. Löffler, J. Verbeeck, J. Zweck, P. Schattschneider, and A. Rosenauer, Nat. Commun. **5**, 5653 (2014).

[5] W. Gao, C. Addiego, H. Wang, X. Yan, Y. Hou, D. Ji, C. Heikes, Y. Zhang, L. Li, H. Huyan, T. Blum, T. Aoki, Y. Nie, D. G. Schlom, R. Wu, and X. Pan, Nature (London) **575**, 480 (2019).

[6] G. Sánchez-Santolino, N. R. Lugg, T. Seki, R. Ishikawa, S. D. Findlay, Y. Kohno, Y. Kanitani, S. Tanaka, S. Tomiya, Y. Ikuhara, and N. Shibata, ACS Nano **12**, 8875 (2018).

[7] J. Repp, G. Meyer, S. M. Stojković, A. Gourdon, and C. Joachim, Phys. Rev. Lett. **94**, 026803 (2005).

[8] J. Repp, G. Meyer, S. Paavilainen, F. E. Olsson, and M. Persson, Science **312**, 1196 (2006).

[9] W. Wang, X. Shi, C. Lin, R. Q. Zhang, C. Minot, M. A. Van Hove, Y. Hong, B. Z. Tang, and N. Lin, Phys. Rev. Lett. **105**, 126801 (2010).

[10] L. Gross, N. Moll, F. Mohn, A. Curioni, G. Meyer, F. Hanke, and M. Persson, Phys. Rev. Lett. **107**, 086101 (2011).

[11] R. F. Egerton, *Electron Energy-Loss Spectroscopy in the Electron Microscope* (Springer Science & Business Media, New York, 2011).

[12] M. Bosman, V. J. Keast, J. L. Garcia-Munoz, A. J. D'Alfonso, S. D. Findlay, and L. J. Allen, Phys. Rev. Lett. **99**, 086102 (2007).

[13] K. Kimoto, T. Asaka, T. Nagai, M. Saito, Y. Matsui, and K. Ishizuka, Nature (London) **450**, 702 (2007).

[14] D. A. Muller, L. F. Kourkoutis, M. Murfitt, J. H. Song, H. Y. Hwang, J. Silcox, N. Dellby, and O. L. Krivanek, Science **319**, 1073 (2008).

[15] M. Bugnet, S. Löffler, D. Hawthorn, H. A. Dabkowska, G. M. Luke, P. Schattschneider, G. A. Sawatzky, G. Radtke, and G. A. Botton, Sci. Adv. **2**, e1501652 (2016).

[16] R. F. Klie, Q. Qiao, T. Paulauskas, A. Gulec, A. Rebola, S. Öğüt, M. P. Prange, J. C. Idrobo, S. T. Pantelides, S. Kolesnik, B. Dabrowski, M. Ozdemir, C. Boyraz, D. Mazumdar, and A. Gupta, Phys. Rev. Lett. **108**, 196601 (2012).

[17] N. Gauquelin, E. Benckiser, M. K. Kinyanjui, M. Wu, Y. Lu, G. Christiani, G. Logvenov, H.-U. Habermeier, U. Kaiser, B. Keimer, and G. A. Botton, Phys. Rev. B **90**, 195140 (2014).

[18] M. Haruta, Y. Fujiyoshi, T. Nemoto, A. Ishizuka, K. Ishizuka, and H. Kurata, Phys. Rev. B **97**, 205139 (2018).

[19] Y. Wang, M. R. S. Huang, U. Salzberger, K. Hahn, W. Sigle, and P. A. van Aken, Ultramicroscopy **184**, 98 (2018).

[20] A. Teurtrie, E. Popova, I. Koita, E. Chikoidze, N. Keller, A. Gloter, and L. Bocher, Adv. Funct. Mater. **29**, 1904958 (2019).

[21] A. Gloter, V. Badjeck, L. Bocher, N. Brun, K. March, M. Marinova, M. Tencé, M. Walls, A. Zobelli, O. Stéphan, and C. Colliex, Mater. Sci. Semicond. Process. **65**, 2 (2017).

[22] H. Tan, S. Turner, E. Yücelen, J. Verbeeck, and G. Van Tendeloo, Phys. Rev. Lett. **107**, 107602 (2011).

[23] N. R. Lugg, M. Haruta, M. J. Neish, S. D. Findlay, T. Mizoguchi, K. Kimoto, and L. J. Allen, Appl. Phys. Lett. **101**, 183112 (2012).

[24] S. Löffler, V. Motsch, and P. Schattschneider, Ultramicroscopy **131**, 39 (2013).

[25] M. J. Neish, M. P. Oxley, J. Guo, B. C. Sales, L. J. Allen, and M. F. Chisholm, Phys. Rev. Lett. **114**, 106101 (2015).

[26] M. J. Neish, N. R. Lugg, S. D. Findlay, M. Haruta, K. Kimoto, and L. J. Allen, Phys. Rev. B **88**, 115120 (2013).

[27] S. Löffler, M. Bugnet, N. Gauquelin, S. Lazar, E. Assmann, K. Held, G. A. Botton, and P. Schattschneider, Ultramicroscopy **177**, 26 (2017).

[28] K. S. Novoselov, A. K. Geim, S. V. Morozov, D. Jiang, Y. Zhang, S. V. Dubonos, I. V. Grigorieva, and A. A. Firsov, Science **306**, 666 (2004).

[29] A. K. Geim and K. S. Novoselov, Nat. Mater. **6**, 183 (2007).

[30] K. Suenaga and M. Koshino, Nature (London) **468**, 1088 (2010).

[31] W. Zhou, M. D. Kapetanakis, M. P. Prange, S. T. Pantelides, S. J. Pennycook, and J.-C. Idrobo, Phys. Rev. Lett. **109**, 206803 (2012).

[32] Q. M. Ramasse, C. R. Seabourne, D.-M. Kepaptsoglou, R. Zan, U. Bangert, and A. J. Scott, Nano Lett. **13**, 4989 (2013).

[33] F. S. Hage, G. Radtke, D. M. Kepaptsoglou, M. Lazzeri, and Q. M. Ramasse, Science **367**, 1124 (2020).

[34] D. M. Kepaptsoglou, T. P. Hardcastle, C. R. Seabourne, U. Bangert, R. Zan, J. A. Amani, H. Hofsäss, R. J. Nicholls, R. M. D. Brydson, A. J. Scott, and Q. M. Ramasse, ACS Nano **9**, 11398 (2015).

[35] L. Pardini, S. Löffler, G. Biddau, R. Hambach, U. Kaiser, C. Draxl, and P. Schattschneider, Phys. Rev. Lett. **117**, 036801 (2016).

[36] A. H. Tavabi, P. Rosi, E. Rotunno, A. Roncaglia, L. Belsito, S. Frabboni, G. Pozzi, G. C. Gazzadi, P.-H. Lu, R. Nijland, M. Ghosh, P. Tiemeijer, E. Karimi, R. E. Dunin-Borkowski, and V. Grillo, Phys. Rev. Lett. **126**, 094802 (2021).

[37] Y. Liu, Y. Y. Li, S. Rajput, D. Gilks, L. Lari, P. L. Galindo, M. Weinert, V. K. Lazarov, and L. Li, Nat. Phys. **10**, 294 (2014).

[38] C. Berger, Z. Song, X. Li, X. Wu, N. Brown, C. Naud, D. Mayou, T. Li, J. Hass, A. N. Marchenkov, E. H. Conrad, P. N. First, and W. A. de Heer, Science **312**, 1191 (2006).

[39] G. Nicotra, Q. M. Ramasse, I. Deretzis, A. La Magna, C. Spinella, and F. Giannazzo, ACS Nano **7**, 3045 (2013).

[40] I. Palacio, A. Celis, M. N. Nair, A. Gloter, A. Zobelli, M. Sicot, D. Malterre, M. S. Nevius, W. A. de Heer, C. Berger, E. H. Conrad, A. Taleb-Ibrahimi, and A. Tejeda, Nano Lett. **15**, 182 (2015).

[41] E. J. Kirkland, *Advanced Computing in Electron Microscopy* (Plenum Press, New York, 1998).

[42] J. M. Cowley and A. F. Moodie, Acta Crystallogr. **10**, 609 (1957).

[43] S. Löffler, Study of real space wave functions with electron energy loss spectrometry, Ph.D. thesis, Vienna University of Technology, 2013.

[44] P. Blaha, K. Schwarz, F. Tran, R. Laskowski, G. K. H. Madsen, and L. D. Marks, J. Chem. Phys. **152**, 074101 (2020).

[45] P. Schattschneider, M. Stöger-Pollach, S. Löffler, A. Steiger-Thirsfeld, J. Hell, and J. Verbeeck, Ultramicroscopy **115**, 21 (2012).

[46] R. Hovden, H. L. Xin, and D. A. Muller, Phys. Rev. B **86**, 195415 (2012).

[47] B. Plotkin-Swing, G. J. Corbin, S. De Carlo, N. Dellby, C. Hoermann, M. V. Hoffman, T. C. Lovejoy, C. E. Meyer, A. Mittelberger, R. Pantelic, L. Piazza, and O. L. Krivanek, Ultramicroscopy **217**, 113067 (2020).

[48] S. Cheng, A. Pofelski, P. Longo, R. D. Twesten, Y. Zhu, and G. A. Botton, Ultramicroscopy **212**, 112942 (2020).

[49] See Supplemental Material at http://link.aps.org/supplemental/10.1103/PhysRevLett.128.116401 for a structural model of the samples used for inelastic channeling simulations, and further spectral and mapping data used to produce the figures in the main manuscript.

Correction: The zone axes listed in the sixth paragraph of the paper were given incorrectly and have been fixed. A corresponding change to the Supplemental Material has also been made.

Part II

Energy-Loss Magnetic Chiral Dichroism

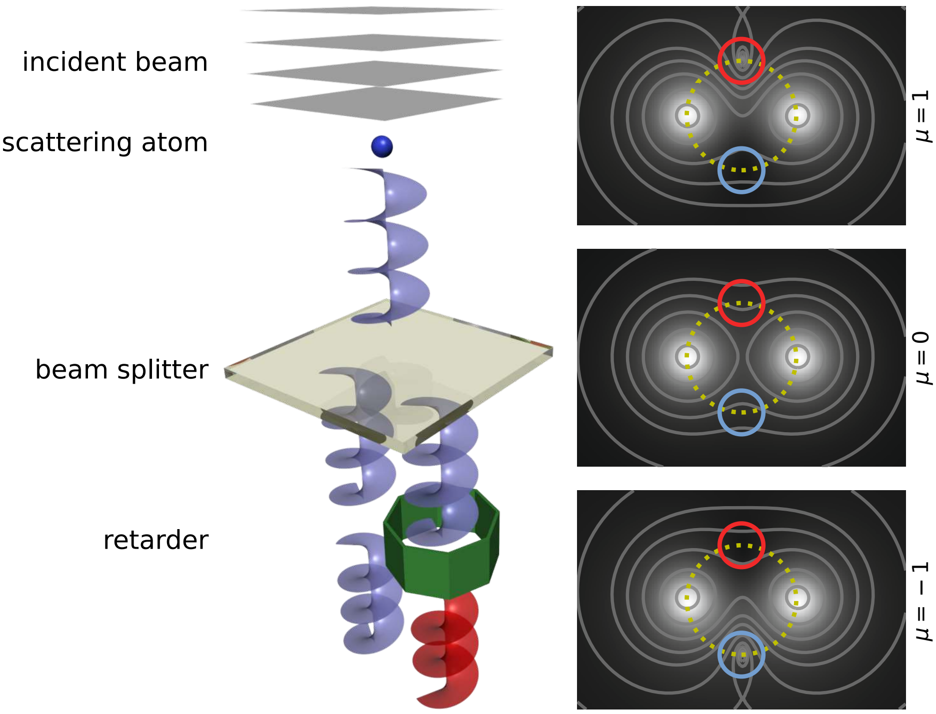

Figure 2.: Left: schematic principle of EMCD. Right: idealized intensity distribution in the diffraction plane for different μ-components in an incident two-beam case with overlaid contours (gray, logarithmic spacing), Thales circle (dotted yellow) and two detector positions (red/blue circles).

The characterization of the spin state can be just as important as the mapping of the real-space probability distribution of electronic states discussed in part I. One method for achieving this goal is EMCD [25, 26]. EMCD exploits the fact that in spin-polarized samples, the MDFF becomes spin-dependent. This, in turn, results in different weights for different μ components in the Rayleigh expansion eq. 11 (see chapter 1 as well as, e.g., [16, 27]). Owing to

$$\hat{L}_z Y_\lambda^\mu(\Omega) = \hbar\mu Y_\lambda^\mu(\Omega),$$

each μ-component corresponds to an orbital angular momentum (OAM) transfer of an integer multiple of $\hbar$ and results in a scattering component with an $\mathrm{e}^{\mathrm{i}\mu\varphi}$ phase factor where φ is the polar angle in the plane perpendicular to the direction of propagation. Such components are EVBs.

The key to EMCD thus is to determine the relative weights of the different $\mathrm{e}^{\mathrm{i}\mu\varphi}$ scattering components. The classical way to achieve this is by interferometry, as shown schematically in fig. 2. After inelastic interaction with the scattering atom, an incident plane wave can obtain OAM, turning it into an EVB. This EVB is subsequently sent through a beam splitter and a retarder which (globally) modifies the beam's phase. In practice, this happens automatically in any crystalline sample, as the crystal lattice acts as beam splitter by diffraction, and each diffracted beam accumulates a different phase shift [8]. Finally, the two beams are superimposed again and measured. This typically occurs in the diffraction plane. Owing to the quasi-Lorentzian scattering distribution [28, 29], there is a small, but non-negligible overlap between the momentum distributions of the two beams in the area between the diffraction spots. There, interference effects occur.

It was shown [16, 30, 31] that under some idealizing assumptions (considering only dipole-allowed transitions in an isotropic material), the MDFF in the spin-polarized case can be written as

$$S(\boldsymbol{q},\boldsymbol{q}',E) = A(q,q',E)\frac{\boldsymbol{q}\cdot\boldsymbol{q}'}{qq'} + \mathrm{i}B(q,q',E)\frac{\boldsymbol{q}\times\boldsymbol{q}'}{qq'}\cdot\frac{\boldsymbol{m}}{m_{\text{sat}}}, \tag{20}$$

where $\boldsymbol{m}$ is the magnetization vector, m_{sat} is the saturation magnetization when all spins are oriented parallel to one another, and $A(E,q,q'), B(E,q,q')$ are material-dependent real pre-factors. From eq. 20, it is clear that the magnetic information is contained in the imaginary part of the MDFF. Additionally, it is evident that the largest contributions of the magnetic part of the MDFF occur for $\boldsymbol{q}\perp\boldsymbol{q}'$, where $\boldsymbol{q}\times\boldsymbol{q}' = qq'$ and $\boldsymbol{q}\cdot\boldsymbol{q}' = 0$. This occurs slightly inside the Thales circle through the adjacent/strong diffraction spots (depicted in fig. 2) due to the fact that $q_z = q_z' = q_E$ is fixed.

Using eq. 20 together with beam propagation algorithms, it is in principle straightforward, albeit time-consuming, to numerically predict the diffraction pattern and, hence, the expected EMCD signal strength for a given material and orientation. However, there are two major caveats: the low SNR and the geometry dependence.

For the classical plane wave method outlined above, the SNR is inherently very low. As indicated in fig. 2, measurements are typically performed far away from the diffraction spots where the intensity is extremely low. Paired with the fact that one is looking for small variations due to interference effects on top of a sizable background signal makes matters even worse. Therefore, classical EMCD often features long exposure times that can easily reach minutes for a single exposure, thus putting extreme demands on the stability of both the TEM and the sample.

The second major caveat of EMCD is its complicated geometry dependence. As EMCD is inherently an interferometric method, its outcome crucially depends on the relative phase shift between superposed beams. This relative phase shift depends on many factors, including which plane wave components are contributing and how far the waves travel through the sample before and after reaching the scattering atom. Therefore, the EMCD signal strength depends on the chosen sample orientation as well as the sample thickness in a complex manner. Thus, finding an optimal or even suitable geometry typically requires an exhaustive numerical search in a vast parameter space.

To overcome the SNR problem in EMCD, two possible methods are presented in this part (an additional, more general future approach is discussed in part IV). In chapter 6, the possibilities and current limitations of an alternative to classical interferometry are investigated. Instead of superposing several diffracted beams, the central beam is sent directly through a holographic mask (a “vortex filter”) designed to modify the wavefunction based on its OAM distribution, i.e., based on the $e^{i\mu\varphi}$ components. The result is a series of ring-like intensity distributions where the EMCD effect can be derived from the central intensities of the $m = \pm 1$ rings. The paper shows that measuring EMCD with a vortex filter setup works in principle, but requires a relatively unusual alignment of the lenses. This result contributed to resolving a long-standing discussion in the community regarding the reproducibility of the first vortex-EMCD experiments [32]. In addition, the vortex-filter method also allows to study EMCD in amorphous samples (which cannot be used as beam splitter and retarder) without the need for, e.g., a biprism.

In chapter 7, another method to reduce the SNR issue is shown, namely convergent-beam EMCD. Convergent beams have been used experimentally to qualitatively improve the signal and/or the spatial resolution (see, e.g., [30, 33–38]). However, how the use of convergent beams changes the achievable EMCD signal strength as well as the SNR had not been explored before. My results show that while using a convergent beam slightly decreases the expected maximal EMCD signal, it allows to dramatically increase the SNR, with the additional benefit of an improved spatial resolution. Additionally, the paper gives a recipe for the optimal range of convergence angles.

The challenge of the complex geometry dependence is overcome in the paper in chapter 8. There, a complete analytical derivation of the EMCD signal strength including elastic scattering both before and after the inelastic scattering event is given for the classical “plane wave” method. This not only allows to predict the orientation and thickness dependence of EMCD without extensive numerical simulations, it also accurately describes the pertinent features of the EMCD thickness dependence, i.e., its oscillatory nature and dampening. Furthermore, the paper investigates the acceleration voltage dependence of EMCD, which can be used, e.g., to study magnetic phase transitions [39].

In summary, my work presented in this part substantially improved the understanding of EMCD, describes concrete recipes for using vortex filtering and convergent beams for the measurement, and gives simple, quantitative predictions for optimizing the achievable signal and SNR.

Chapter 6

EMCD with an electron vortex filter: Limitations and possibilities

T. Schachinger, S. Löffler, A. Steiger-Thirsfeld, M. Stöger-Pollach, S. Schneider, D. Pohl, B. Rellinghaus, and P. Schattschneider

Ultramicroscopy 179 (2017) 15–23
10.1016/j.ultramic.2017.03.019

Ultramicroscopy 179 (2017) 15–23

Contents lists available at ScienceDirect

Ultramicroscopy

journal homepage: www.elsevier.com/locate/ultramic

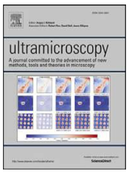

EMCD with an electron vortex filter: Limitations and possibilities

T. Schachinger[a,b,*], S. Löffler[b], A. Steiger-Thirsfeld[b], M. Stöger-Pollach[a,b], S. Schneider[c], D. Pohl[c], B. Rellinghaus[c], P. Schattschneider[a,b]

[a] *Institute of Solid State Physics, TU Wien, Wiedner Hauptstraße 8-10, 1040 Wien, Austria*
[b] *University Service Centre for Transmission Electron Microscopy, TU Wien, Wiedner Hauptstraße 8-10, 1040 Wien, Austria*
[c] *Institute for Metallic Materials, IFW Dresden, P.O. Box 270116, 01171 Dresden, Germany*

ARTICLE INFO

Article history:
Received 6 April 2016
Revised 2 March 2017
Accepted 15 March 2017
Available online 16 March 2017

ABSTRACT

We discuss the feasibility of detecting spin polarized electronic transitions with a vortex filter. This approach does not rely on the principal condition of the standard electron energy-loss magnetic chiral dichroism (EMCD) technique, the precise alignment of the crystal in order to use it as a beam splitter, and thus would pave the way for the application of EMCD to new classes of materials and problems, like amorphous magnetic alloys and interface magnetism. The dichroic signal strength at the $L_{2,3}$-edge of ferromagnetic Cobalt (Co) is estimated on theoretical grounds using a single atom scattering approach. To justify this approach, multi-slice simulations were carried out in order to confirm that orbital angular momentum (OAM) is conserved in amorphous materials over an extended range of sample thickness and also in very thin crystalline specimen, which is necessary for the detection of EMCD. Also artefact sources like spot size, mask tilt and astigmatism are discussed. In addition, the achievable SNR under typical experimental conditions is assessed.

1. Introduction

The discovery in 2006 that electron energy-loss magnetic chiral dichroism (EMCD) can be observed in the transmission electron microscope (TEM) [1] provided an unexpected alternative to X-ray magnetic circular dichroism (XMCD) in the synchrotron. Both EMCD and XMCD are based on the fact that in spin-polarized (magnetic) samples, the interaction of the probe beam with the target electrons depends on the transfer of orbital angular momentum (OAM) between the two. This has its origin in the spin-orbit-interaction of the target electrons' initial states. By means of sum rules [2], it is even possible to determine the spin and orbital magnetic moments. EMCD has seen tremendous progress [3–7], achieving nanometre resolution [8], and even sub-lattice resolution [5,9,10].

The discovery of electron vortex beams (EVBs) [11,12] has spurred efforts to use them for EMCD because of their intrinsic chirality. In spite of much progress in the production and application of vortex beams [13–18], it soon became clear that atom-sized vortices incident on the specimen are needed for EMCD experiments [19–21]. Attempts to produce such beams and to use them for EMCD measurements did not show an effect so far [22]. Nevertheless, faint atomic resolution EMCD signals have been shown without the need for atom-sized EVBs using intelligent shaping of the incident wavefront with a C_s corrector instead [23,24].

The fact that OAM can be transferred to the probing electron when it excites electronic transitions to spin polarized final states in the sample manifests itself in a vortical structure of the inelastically scattered probe electron. The latter could be detected by a holographic vortex mask (HVM) after the specimen and various other techniques like triangular shaped apertures, knife edges, astigmatic phase shifts [25] and pinhole arrangements [26]. We are focusing on using a HVM because the other techniques mentioned show drawbacks, like that the analysis is fundamentally more complicated or that they are not practical for beams which are not OAM eigenstates or incoherent superpositions of different OAM states as is the case in EMCD. Additionally, using a HVM as chiral filter is already well-established in optics [27–29]. If successful, this ansatz would open up the possibility to measure magnetic properties of amorphous materials, since the specimen no longer needs to act as a beam splitter itself. Also, technologically interesting questions like interface magnetism could be an application of this technique. Additionally, it could provide an alternative method to determine the magnetic properties of nano-crystalline samples [30].

---

* Corresponding author.
E-mail address: thomas.schachinger@tuwien.ac.at (T. Schachinger).

http://dx.doi.org/10.1016/j.ultramic.2017.03.019
0304-3991/© 2017 Elsevier B.V. All rights reserved.

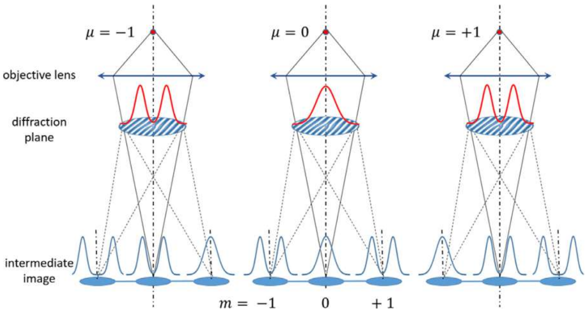

Fig. 1. Principle of the vortex filter: The red dot represents the scattering centre, i.e. the atom in the object plane, with its three scattering channels, $\mu = \pm 1, 0$. The resulting vortices are then incident on a HVM in the far-field, adding topological charges $m \in \mathbb{Z}$, thereby creating a line of vortices of topological charges $\mu + m$ in the image plane. Subsequently, the EMCD signal can be derived from the difference in the vortex orders $m = \pm 1$, according to Eq. (6). (For interpretation of the references to colour in this figure legend, the reader is referred to the web version of this article.)

2. Possibilities

In order to get an idea of the achievable EMCD signal strength of a vortex filter setup, first, an experimental scheme using a HVM in the diffraction plane (DP) as a vorticity filter will be described by means of an idealised single atom scattering model. Subsequently, an alternative experimental setup, similar to the one used in [12], where the HVM is placed in the selected area aperture (SAA) holder will be described and its ability to filter the vorticity of an incident electron beam will be shown. At the end of this section, multi-slice simulation results on the conservation of OAM, which is an important prerequisite for detecting an EMCD signal using a vortex filter, in an extended specimen (an amorphous magnetic alloy) will be shown in order to justify the single atom scattering model.

2.1. Principle and experimental setup of a HVM in the DP

As stated above, the key aspect of EMCD is the transfer of OAM between the probe beam and the target electron. Assuming the incident beam has no OAM, the inelastic scattering event will transform it into a vortex or, more generally, a superposition of several vortex orders. Thus, it is natural to use a vorticity filter such as a HVM to separate the different OAM components and measure their respective weights (see Fig. 1). Ideally, one would place the HVM in the sample's far-field (i.e. the DP) so that it operates on all outgoing vortices irrespective of their point of origin and measure in the image plane.

Dealing with transition metals, dichroism measurements typically involve 2p-core to d-valence excitations at the $L_{2,3}$ ionization edges. The $L_{2,3}$-edges are used due to their strong spin-orbit interaction in the initial state. Besides, their dichroic signal is an order of magnitude higher compared to using K-edges, which were originally used in X-ray magnetic circular dichroism measurements to show the dichroic effect [31,32]. The most dominant contribution to the ionisation edges are electric dipole-allowed transitions. Higher multi-pole transitions show low transition amplitudes contributing less than 10% at scattering angles of < 20 mrad relevant in electron energy-loss spectrometry (EELS) [33–35].

In case of an L-edge dipole-allowed transition which transfers an OAM of $\hbar\mu$ and, thereby, changes the magnetic quantum number of an atom by μ, an incident plane wave electron transforms into an outgoing wave [36]

$$\psi_\mu(\mathbf{r}) = e^{-i\mu\varphi_r} f_\mu(r) \tag{1}$$

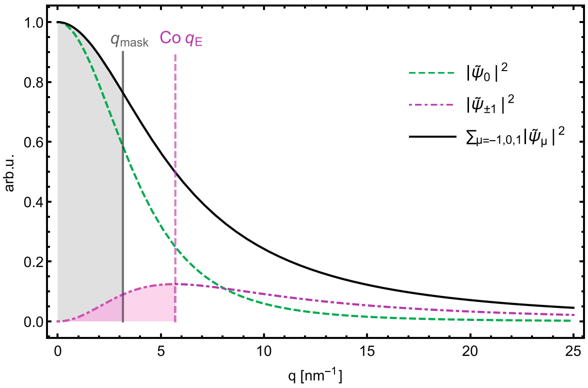

Fig. 2. Scattering profiles of $|\tilde{\psi}_0|^2$ and $|\tilde{\psi}_{\pm 1}|^2$ and their sum $\sum_{\mu=-1,0,1} |\tilde{\psi}_\mu|^2$, giving the Lorentz profile for non-magnetic isotropic transitions in momentum space for the Co L_3-edge. The radius of the HVM $q_{mask} = 3.16$ nm^{-1}, which was used to estimate the SNR in Section 3.3, is indicated by the grey shaded area terminated by the full vertical line, q_E is indicated by the dashed vertical line and the magenta shaded area. (For interpretation of the references to colour in this figure legend, the reader is referred to the web version of this article.)

where φ_r is the azimuthal angle, and

$$f_\mu(r) = \frac{i^\mu}{2\pi} q_E^{1-|\mu|} \int_0^\infty \frac{q^{1+|\mu|} J_{|\mu|}(qr) \langle j_1(Q) \rangle_{ELSj}}{Q^3} dq, \tag{2}$$

with $\langle j_1(Q) \rangle_{ELSj}$ the matrix element of the spherical Bessel function between the initial and final radial atomic wave functions, and $Q = \sqrt{q^2 + q_E^2}$. Here, q is the transverse scattering vector that relates to the experimental scattering angle θ as $q = k_0\theta$, and $\hbar q_E = \hbar k_0 \theta_E$ is the scalar difference of linear momenta of the probe electron before and after the inelastic interaction, also known as the characteristic momentum transfer in EELS [37]. The characteristic scattering angle θ_E is given by $\theta_E \sim \Delta E / 2E_0$, with ΔE being the threshold energy of the dipole-allowed L-edge and E_0 the primary beam energy. For the Co-L_3 threshold energy of 779 eV, the characteristic scattering angle θ_E amounts to ~ 2 mrad at an acceleration voltage of 200 kV.

The dichroic signal in the diffraction plane can readily be calculated via Fourier transforming Eq. (1). According to a theorem for the Fourier–Bessel transform of a function of azimuthal variation $e^{-i\mu\varphi}$ [38], one has

$$\tilde{\psi}_\mu(\mathbf{q}) = \frac{i^\mu}{2\pi} e^{-i\mu\varphi_q} \int_0^\infty f_\mu(r) J_{|\mu|}(qr)\, r dr. \tag{3}$$

The outgoing electron in the DP still carries topological charge μ, showing that the wave function is topologically protected. The radial intensity profiles $|\tilde{\psi}_\mu(q)|^2$ for the possible transitions with $\mu \in \{-1, 0, 1\}$ and their sum $\sum_{\mu=-1,0,1} |\tilde{\psi}_\mu|^2$, which represents the Lorentz profile for non-magnetic isotropic transitions, for the Co L_3-edge are shown in Fig. 2.

A HVM adds topological charges $m \in \mathbb{Z}$ to the incident beam of topological charge μ. Due to the grating nature of the HVM, the m-dependent deflections are separated by $2\theta_{Bragg} = \lambda / g$, where λ is the electrons' wavelength and g is the HVM periodicity. Thus, such a mask creates a line of vortices of topological charge $m + \mu$ in the image plane, see Fig. 1. The radial profiles in the image plane are given by the back-transform of Eq. (3) with the respective vortex order m added by the mask:

$$\psi_{m\mu}(\mathbf{r}) = \frac{i^{m+\mu}}{2\pi} e^{-i(m+\mu)\varphi_r} \int_0^{q_{mask}} \tilde{\psi}_\mu(q) J_{|m+\mu|}(qr)\, q\, dq \tag{4}$$

where $q_{mask} = k_0 \theta_{mask}$ is given by the mask aperture limiting the maximum momentum transfer. The observed vortices are finally

Table 1
Coefficents C^μ for the L$_3$-edge taken from [9]. The weighting factors for the transitions when the final states are completely up-spin polarized show an asymmetry for $m+\mu=0$, i.e. in the centre of the $m=\pm1$ vortices.

m	-1			0			$+1$		
μ	-1	0	$+1$	-1	0	$+1$	-1	0	$+1$
$m+\mu$	-2	-1	0	-1	0	$+1$	0	$+1$	$+2$
C^μ	0.278	0.222	0.167	0.278	0.222	0.167	0.278	0.222	0.167

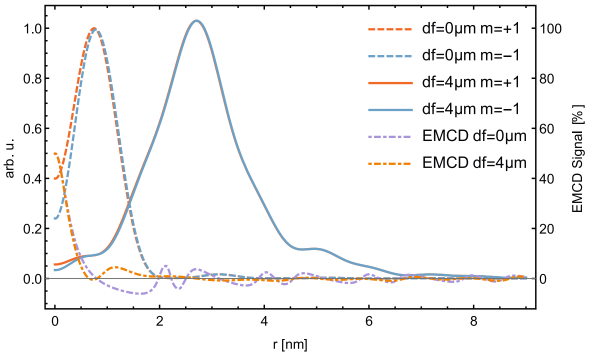

Fig. 3. Radial intensity profiles of a $m=\pm1$ filtered image of a single atomic ionisation, for the fully spin polarized case according to Eq. (6), with a defocus of 0 μm and 4 μm, respectively. The resulting r-dependent EMCD signal is given by the dot-dashed curves, according to Eq. (7), and amounts to 50% at r=0 nm for both defocus values. The signals are normalised to their respective total intensities.

calculated with Eq. (4), but now including the defocus df and the spherical aberration C_s:

$$\psi_{m\mu}(\mathbf{r}) = \frac{i^{m+\mu}}{2\pi}\, e^{-i(m+\mu)\varphi_r} \times \int_0^{q_{mask}} \tilde{\psi}_\mu(q) J_{|m+\mu|}(qr) \times e^{i(dfq^2/2k_0 + C_s q^4/4k_0^3)}\, q\, dq. \tag{5}$$

The respective intensities are azimuthally symmetric with distinct radial profiles. Fig. 1 shows schematically the central three vortices for the three dipole-allowed transition channels. Note that the central vortex ($m=0$) does not show any asymmetry for $\mu=+1$ and $\mu=-1$. This is the reason why such transitions cannot be distinguished with standard EELS.

Each panel of Fig. 1 describes the situation where only one transition channel (μ) is present. For several transition channels at the same energy, as is usually the case, the outgoing probe electron is in a mixed state, described by the reduced density matrix [39,40] and the paths of the rays cannot be visualized in such an easy way. Note that the total intensity is the trace of the matrix, i.e. the sum over all intensities in the respective channels. For fully spin-polarized systems (i.e. ideal EMCD)

$$I_m = \sum_{\mu=-1}^{1} C^\mu \, |\psi_{m\mu}|^2 \tag{6}$$

where the C^μ are derived from the Clebsch–Gordan coefficients [9,41] and given in Table 1.

In Fig. 3, the resulting radial intensity profiles are drawn with no additional broadening added (which will be discussed in more detail in Section 3.1). The radial extension of the intensity profiles in Fig. 3 is considerably broader than it is directly at the scattering atom, due to the limited extent q_{mask} of the vortex filtering mask shown in Fig. 1.

In this geometry, we define the EMCD signal as the relative difference of the intensities with $m=\pm1$

$$\text{EMCD} = 2\cdot\frac{I_{+1}-I_{-1}}{I_{+1}+I_{-1}}. \tag{7}$$

The EMCD signal is a function of the radius which has been omitted for clarity here.

Fig. 3 shows an ideal case for a single atom excitation and a HVM radius of $q_{mask} = 3.16\ \text{nm}^{-1}$ for the focused case and for a defocus value of 4 μm. The EMCD signal is strong in the centre of the vortices but rapidly decreases above $r \approx 1$ nm. For this idealised approach, it reaches 50% for both defocus values in the central region of the vortices. Note that, especially for the df=0 μm case, not only the central regions of the radial profiles show distinct differences but there is also an apparent difference of the positions of the maxima. This is due to the asymmetry in the OAM content of the respective vortex order.

2.2. Experimental setup of a HVM in the SAA plane

Even though there are proposals to use spiral-phase-plates in the DP, e.g. to determine chiral crystal symmetries and the local OAM content of an electron wave [42,43], to date no successful implementation of a vortex mask in the DP of a TEM has been shown. This can be attributed to the fact that placing the vortex filtering HVM in the DP is not straightforward because strip apertures are used due to the limited space in the pole piece gap. These strips cannot be loaded with conventional ⌀3 mm frame apertures. Instead, the whole strip needs to be replaced each time, including all commonly used contrast apertures.

Instead, here we describe a setup that is functionally equivalent to the one described in the previous section, but with a HVM positioned inside the SAA holder. Obviously, changing the HVM position also requires changing the experimental settings. The HVM in the SAA holder creates a demagnified virtual image in the eucentric plane with small lattice constant (see Fig. 4a). In order that the virtual image of the mask remains in the sample's far field, the specimen has to be lifted in height by dz.

Due to the limitations discussed in Section 3.1, it is essential for obtaining a large EMCD effect to minimize the illuminated area. Typically, this can be achieved by focussing the beam. In that case, the C$_2$ condenser lens needs to be adjusted to account for the different sample position (see Fig. 5). Note that focusing the beam onto the specimen guarantees that the probability density current is essentially aligned parallel to the optical axis all over the illuminated area such that the scattering "light cones" all point in the same direction towards the vortex filter mask. This is due to the fact that the Rayleigh range of the incident beam[1] is of the order of 600 nm (for a convergence semi-angle of 3.8 mrad) which is much larger than the sample thickness, e.g. ∼ 70 nm, and thus the incident wavefronts are almost flat everywhere inside the specimen, see Fig. 4b and c. It can be seen that the tilt angle at a radial position of 0.7 nm in the entrance plane amounts to ∼ 70 μrad

---

[1] Note that the Rayleigh range was determined using the diffraction limited spot size of the C$_2$ aperture [44,45].

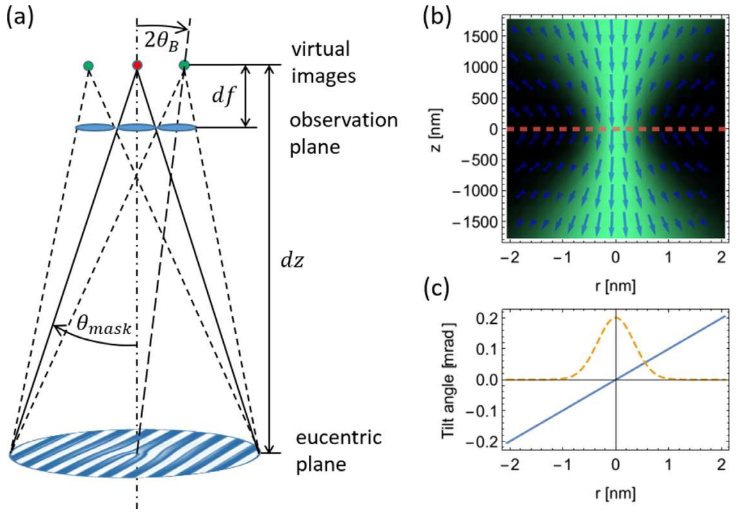

Fig. 4. Scattering geometry, intensity, phase gradient and tilt angles of the wavefront of the incident focused probe: (a) Inserting a HVM in the SAA creates a virtual image of the HVM in the eucentric plane. The specimen is lifted by dz such that the HVM is in the far field, subtending an angle θ_{mask}. It creates a linear series of atom sized vortices. Their virtual images in the object plane, separated by $2\theta_B$, are sketched in green here. The observation plane is df below the object plane, in order to obtain sufficient radial resolution. (b) Intensity of the focused probe with a convergence semi-angle of 3.8 mrad incident on the specimen (the red atom in (a)), given in green, and its phase gradient represented by the blue arrows. The red rectangles represent atomic columns, with a spacing of 250 pm and a thickness of 70 nm. Qualitatively, it can be seen that the atomic columns practically see a plane wave front (arrows aligned parallel to the atomic columns) because of the relatively high Rayleigh range ~ 600 nm of the beam. (c) quantifies the residual tilt of the incident wavefront. The solid blue line represents the tilt angle of the electron wavefront at 35 nm above the focus, whereas the dashed orange line indicates the lateral beam profile at that position. At the beam's waist, the tilt angles are as low as 70 µrad, justifying the assumption of an incident plane wave. (For interpretation of the references to colour in this figure legend, the reader is referred to the web version of this article.)

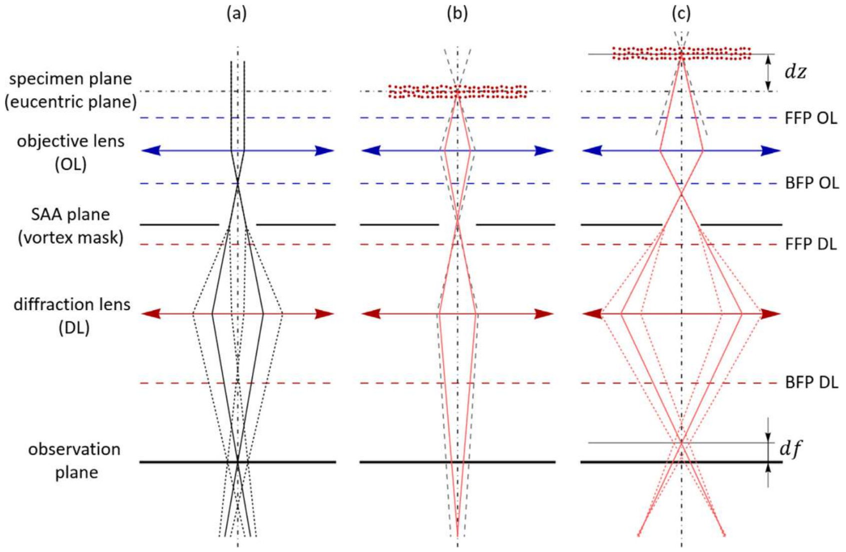

Fig. 5. Ray diagrams (not to scale) of (a) a standard TEM diffraction setup, (b) a standard STEM setup and (c) the EMCD vortex filter setup. Full and dashed black lines represent rays of elastically scattered electrons whereas red lines depict inelastically scattered ones. FFP and BFP stand for front-focal plane and back-focal plane, respectively. (For interpretation of the references to colour in this figure legend, the reader is referred to the web version of this article.)

which can be considered negligible compared to the characteristic scattering angle $\theta_E \sim 2$ mrad of e.g. Co.

Lifting the specimen ensures that the (virtual) HVM is now in the far field of the excited atom and creates a series of images of the ionization process as depicted in Fig. 4a. Practically, this setup is comparable to a standard STEM geometry but with the specimen lifted far off the eucentric plane. For better understanding the scattering setup, Fig. 5 compares the standard TEM setup in diffraction, Fig. 5a, and the standard STEM setup, Fig. 5b, to the setup described here, Fig. 5c. Note that there are slight changes in the focal position of elastic- to inelastically scattered electrons in Fig. 5b. It can be seen that when the vortex filter mask is placed in the SAA holder, diffracted beams emerge from the vortex mask in Fig. 5a and c but not in Fig. 5b because there the image of the inelastically scattered electrons in the SAA plane (≈ 8 nm) is much smaller than the grating periodicity (≈ 500 nm) such that the vor-

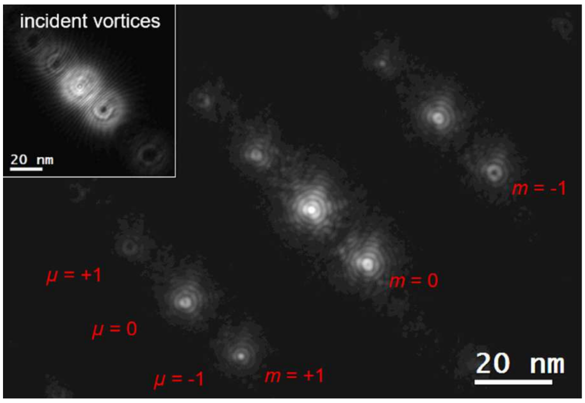

Fig. 6. Proof of vortex filter functionality in vacuum: In order to verify the working principle of the vortex filter in the EMCD vortex filter geometry, EVBs produced by a HVM in the condenser aperture holder ($\mu = \pm 1, 0$) were incident on a the vortex filter HVM placed in the SAA holder ($m = \pm 1, 0$). Due to the orthogonal orientation of the two HVMs, one can beautifully see the addition and subtraction of OAM.

tex mask is not illuminated. Lifting the specimen by dz (of the order of 100 µm) as depicted in Fig. 5c ensures that the vortex filter mask is properly illuminated. Moreover, due to electron optical reasons, this lifting is essentially reducing the size of the first image of the focused probe on the (lifted) specimen, comparable to the reduction of the effective source size in the condenser system of a TEM by adjusting the C_1 lens excitation.

In order to verify that the setup in Figs. 4a and 5c is capable of filtering the OAM content of an incoming electron wave, it was tested using EVBs incident on the SAA HVM, comparable to the work done in [25]. These incident EVBs were produced by a second HVM placed in the C_2 condenser aperture holder and, as the beam has to be focused on the lifted specimen in the actual experiment, the incident EVBs were massively over-focused by ~ 100 µm. Due to the roughly orthogonal orientation of the two HVMs, one can beautifully see the addition and subtraction of OAM in Fig. 6, where $\mu = \pm 1, 0$ denote the incident EVB and $m = \pm 1, 0$ represent the vortex orders stemming from the SAD HVM. This clearly shows the applicability of the proposed setup to filter the vorticity of the incoming electron beam, and, thus measure EMCD.

2.3. OAM conservation

As shown in [15,20], the expectation value of the angular momentum $\langle \hat{L}_z \rangle = \langle \psi | \hat{L}_z | \psi \rangle / \langle \psi | \psi \rangle$ of an (atom sized) EVB propagating through a crystal lattice can be subject to strong changes, indicating OAM exchange with the specimen via elastic scattering processes. The single atom scattering approach is neglecting elastic scattering of the EVBs produced in the ionisation process in the specimen, thus, one could question its applicability here. However, it has been reported that atomic sized EVBs (when aligned exactly at the atomic columns) do channel along atomic columns over tens of nanometres [15,46]. As the vortices produced in the inelastic scattering event are intrinsically centred on the atom, sufficiently thin crystalline samples in zone axis (ZA) should give an EMCD signal in reasonably good agreement with the simple single atom scattering ansatz used above.

In amorphous materials with their non-existent long range order, one can expect the exchange of OAM to be minimal. To further clarify if the OAM of the inelastically scattered probe electron is indeed conserved when propagating through an amorphous material, multi-slice simulations [47] were carried out. Fig. 7 shows the propagation of an atomic scale EVB (waist radius: 1.14 Å and $m = 1$) incident on a 70 nm $Fe_{80}Si_6B_{13}C_1$. It can be seen that the colour coded phase structure of the EVB does not change significantly upon propagation through the material. Also, the expectation value of the angular momentum $\langle \hat{L}_z \rangle$ deviates only moderately over the course of the propagation. Especially for material thicknesses below 30 nm, the OAM of the EVB evolving from the inelastic scattering process is hardly affected by the sample.

Thus, the multi-slice simulation results shown in Fig. 7 strongly support the assumption that neither the expectation value of the angular momentum operator $\langle \hat{L}_z \rangle$, nor the single OAM components, see Fig. 7c, show strong OAM transfer to the amorphous sample for thicknesses below 30 nm, justifying the single atom scattering approach. Nevertheless, effects like incoherent broadening must be taken into account by additional means and will be discussed in the following section.

3. Limitations

The situation described in Section 2 is, of course, an idealisation. In order to estimate if and under which conditions EMCD signals can be detected in practice, we analyse the most important limitations in this section.

3.1. Illuminated specimen area

If more than one atom is illuminated by the focused electron probe, there will be an incoherent superposition of signals from all excited atoms. The fine details of the radial profiles will be smoothed by the convolution with the spot shape,[2] thus reducing the expected EMCD effect [19,20]. This incoherent broadening effect caused by the finite illuminated area of the specimen is taken into account by a convolution with a Gaussian as described in [48]. Thus, the final simulated radial intensity distribution is given by

$$I_m^{\sigma}(r) = e^{-(1/2)(r/\sigma)^2} \int_0^{\infty} I_m(r')\, e^{-(1/2)(r'/\sigma)^2} I_0\left(\frac{rr'}{\sigma^2}\right) r'\, dr', \tag{8}$$

where I_0 represents the modified Bessel function of first kind of order zero and σ the amount of incoherent broadening. The resulting illuminated area (FWHM) at the specimen is ~ 2.4σ. This incoherent broadening effect strongly reduces the expected EMCD signal as shown in Fig. 8 for the focused case and Fig. 9 for the defocused case.

Fig. 8 is a simulation of this effect for an atomic monolayer. The central dip in the focused case disappears completely and the EMCD signal drops from 50% to 3%. In the defocussed case, Fig. 9, the dip remains, but the EMCD signal also decreases to 3%. This emphasises the need for a small spot in order to be able to obtain a sufficiently large EMCD effect in the centre.

Going to smaller spot sizes seems to be a rewarding route but one has to be aware that smaller spot sizes inherently decrease the Rayleigh range of the incident beam, therefore putting stronger limitations on the sample thickness. For example, a typical probe corrected beam with a semi-convergence angle of 20 mrad has a Rayleigh range of ~ 35 nm demanding a much thinner specimen than that for a straight forward interpretation. In addition, the derivation in Section 2.1 assumed that the incident wave was constant over the scattering atom. If that is not fulfilled, the scattering cross-section becomes position-dependent. Also, for ultra-thin specimens, not only the inelastic signal drops drastically but also

---

[2] This is comparable to the incoherent source size broadening effect. Note that the signal from atoms at different depths will also exhibit a slight defocus. However, this defocus (< 40 nm) is small compared to the Rayleigh range (~ 600 nm) and gives only negligibly small changes in the centre of the vortices as confirmed by simulations (not shown). The main changes caused by this defocus naturally occur in the tails of the vortices where no EMCD effect is expected.

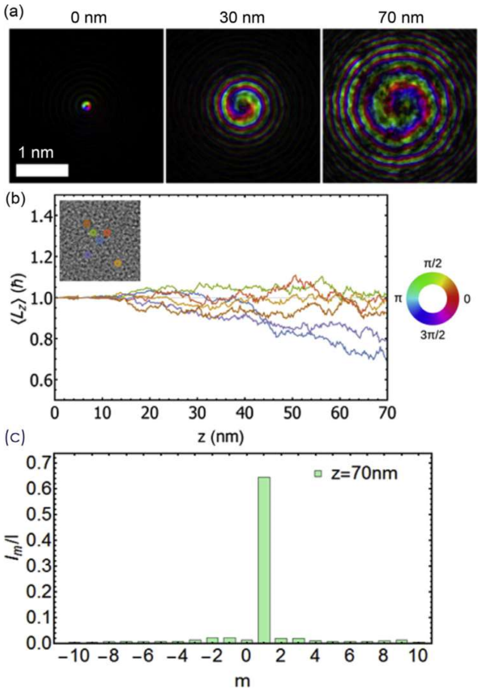

Fig. 7. OAM conservation: (a) Elastic multi-slice simulations showing the propagation of a 1.14 Å $m = 1$ EVB incident on an amorphous Fe-based alloy ($Fe_{80}Si_6B_{13}C_1$ $\times\ 10^{22}$, atoms/cm^3) of 70 nm thickness. Even though the propagation distance is 70 nm, no significant changes are visible in the vortical phase structure of the EVB which is represented by the relatively good conservation. Only a phase noise is added by the amorphous material. (b) Expectation value $\langle \hat{L}_z \rangle$ for the $m = 1$ EVB for different probe positions (indicated in the 5 × 5 nm^2 inset) as a function of penetration depth. Up to a thickness of ≈ 30 nm there are reasonably low changes visible. (c) Shows the relative intensities of different OAM components after propagation through 70 nm. Note that the relative intensity of all $m \neq 1$ vortex orders stays well below 3%.

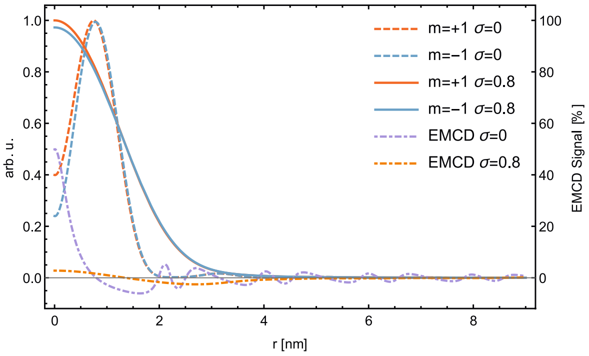

Fig. 8. Effect of incoherent broadening by a Gaussian with $\sigma = 0.8$ nm and a defocus value of 0 µm. The EMCD is strongly affected by the spot size effect and the signal drops to 3%.

the likelihood of beam damage increases. However, the requirement for ultra-thin specimens may be relaxed by the application of non-diffracting Bessel beams [49–51].

So far, the question of lateral extended illumination was elucidated. We also tested the case when the single atom scattering centres sit at various z-positions, by incoherently summing up multiple defocused wave functions. The results (not shown here) indicated that no significant contribution to the EMCD signal below $r < 1$ nm from this longitudinal arrangement of scattering centres can be observed.

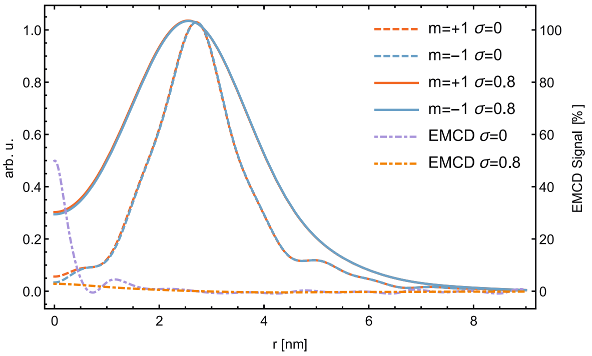

Fig. 9. Effect of incoherent broadening by a Gaussian with $\sigma = 0.8$ nm and a defocus value of 4 µm. The EMCD signal is strongly reduced by the spot size effect and the signal drops also to 3%.

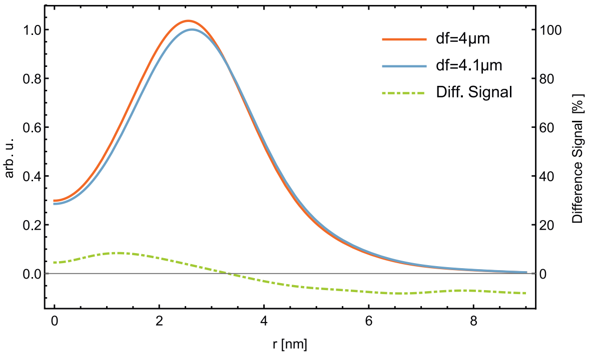

Fig. 10. Effect of 100 nm defocus difference between left and right vortex order of a hypothetical non-dichroic signal at 4 µm defocus. The radial profiles were normalized to the respective total intensity. The difference signal in the centre is 5% and its maximum is as high as 8%.

3.2. Vortex size differences, mask tilt and astigmatism

Besides the broadening effects mentioned above, there are several ways of unintentionally introducing an artificial intensity difference that could easily be misinterpreted as an EMCD effect. They all have in common that the position of the maxima (i.e., the vortex size) is different for the $m = -1$ and the $m = +1$ vortices. Upon normalization, this can lead to differences in the centre of the beam. In the simplest case, this can effectively be modelled as a defocus difference between the different vortices. Fig. 10 shows the case of a non-magnetic simulation (i.e., $m = -1$ and $m = +1$ *should* have the same radial profiles) but with a defocus difference of 100 nm between the two vortices. This gives rise to a relative difference signal which reaches a maximum of 8% at $r = 1.2$ nm and still amounts to 5% in the centre. With that, it grows nearly twice as strong as the EMCD signal predicted for the fully spin-polarized case for the same simulation parameters without defocus (see above). Perhaps the most obvious candidates for a vortex order dependent defocus are a geometric tilt of the optical axis and OAM-dependent differences in the lenses' focal lengths. A trivial geometric estimation of the amount of the defocus differences expected from image tilts of the order of mrad shows that this effect is of the order of ∼ 0.5 nm, and thus negligible. Defocus changes

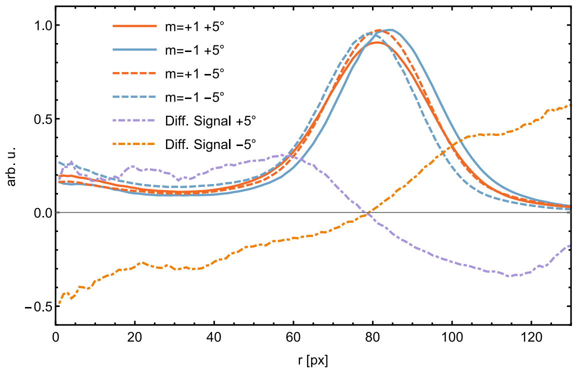

Fig. 11. An experimental test showing the influence of tilting a HVM in the sample holder ± 5° relative to the electron beam. A significant defocus difference between left and right diffraction order can be observed for both tilt angles. Profiles normalized to respective maxima.

due to Zeeman splitting in the magnetic field of TEM lenses are between 1 pm and 0.5 nm, and thus also negligible [52].

In contrast to that, we found that a tilt of the HVM with respect to the optical axis (of the order of a few degrees) due to mounting misalignments and/or bending of the thin membranes can induce significant maxima shifts equivalent to effective defocus differences of the order of a few hundred nanometres, see Fig. 11. In this experiment, a HVM was inserted into the specimen holder such that its primary grating was aligned parallel to the α-tilt axis of the specimen holder. Fig. 11 shows that for mask tilts as small as ± 5°, there are significant changes in the radial profiles of the $m = -1$ and $m = +1$ vortices, amounting to intensity differences in the centre of 25% for 5° and −50% for −5°. Note that this experiment was conducted in vacuum (there was no specimen present), but produces a signal that appears to be roughly 8 to 16 times larger than the EMCD effect predicted above. This can possibly be attributed to electron-wall interactions, e.g. electrostatically induced image charge formation in the grating bar walls, see [53,54]. Alternatively, the tilted grating geometry could resemble a kind of blazed grating, which also redistributes the diffraction orders intensity, see for example [55].

This effect can be compensated by preparing the HVM on strong support membranes and carefully mounting it in the aperture holder. Also, the absence of this artefact can be verified before conducting an EMCD experiment by using the elastically scattered electrons which should not exhibit any intensity asymmetry of the different vortex orders.

An additional source of artificial EMCD signals has been found to be the astigmatism of the objective lens. Fig. 12 exemplifies that behaviour for two opposing settings of the objective astigmatism corrector coils (the value of a_1 denotes the corrector excitation value as shown in the Tecnai user interface).[3] Again, these radial profiles are attained from EVBs in vacuum, no sample was used in this experiment. Still, the artificial EMCD effects amount to 90% for the positive a_1 setting and −20% for the negative one – that is more than 7 to 30 times larger than the predicted EMCD effect. Two dimensional image simulations (not shown here) also exhibit the same behaviour of introducing an EMCD-like artefact by changing the astigmatism of the objective lens.

This artefact can be corrected by a thorough pre-alignment of the EVBs at zero energy loss (but with the high tension increased by the energy loss of the respective element of interest to ensure equal imaging conditions) prior to the actual EMCD experiment where special care must be taken that the central regions of the vortices show a highly symmetric radial intensity profile for $m = \pm 1$.

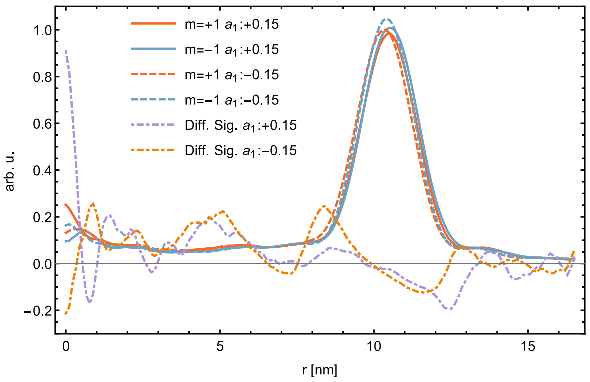

Fig. 12. An experimental test, without a sample, shows the influence of the (twofold) objective astigmatism (denoted by a_1) on the radial profiles (especially their centres) of $m = \pm 1$ vortex orders. Strong differences between left and right diffraction order can be observed. The profiles are normalized to their respective total intensity.

3.3. Noise level

The detection of faint EMCD signals in the vortex filtering setup proposed in Section 2 strongly depends on the achievable SNR. Therefore, we carried out a trial experiment using a ∼ 70 nm thin layer of Co placed in a FEI TECNAI FEG TEM equipped with a GATAN GIF Tridiem spectrometer (GIF) and a high-brightness XFEG to assess the typically achievable SNR. The sample was lifted by $dz = 75$ µm. The acceleration voltage was set to 200 kV, whereas the condenser system was set up in a way to achieve a high beam current at a sufficiently small spot size on the sample, i.e. providing a beam current of ∼ 500 pA incident on the sample in a ∼ 1.9 nm probe (FWHM, $\sigma = 0.8$) with a convergence semi-angle of 3.8 mrad.

The vortex filtering SAA HVM was prepared by FIB milling, it was a $m = 1$ HVM with a diameter of 10 µm, a primary grating periodicity of 500 nm (back-projected: 9.4 nm) and an orthogonal secondary stabilisation grating with a periodicity of 4 µm. The primary grating Bragg angle θ_B=5 µrad separated the central spot from the first vortex orders in the eucentric plane by ∼ 20 nm.[4] As a result, the vortex orders $m = \pm 1$ are still well separated from the central peak for defocus values of $df = 4$ µm and higher, see Fig. 13. The HVMs collection angle was $q_{mask} = 3.16$ nm^{-1} ($\theta_{mask} =$ 1.2 mrad).

Fig. 13 shows the experimental energy filtered image using the SAA HVM at an energy threshold of 780 eV and an energy selecting slit of 15 eV. This image was acquired taking four frames with an acquisition time of 100 s per frame using four fold binning. Subsequently, the frames were stacked and aligned using Image J [56]. Then, *Digital Micrograph* scripts were used to determine the exact vortex orders' centres, to crop them and to extract the rotational (azimuthal) average from each image of the aligned stack. The rotational averaged radial profile of each vortex order was then normalized using the total intensity of the respective vortex order $\int_0^\infty I_m(r) r dr$. With that, we obtained an error estimate by calculating the root-mean-square (RMS) value for each radial pixel. Using

---

[3] Note that at these settings, the vortices still *look* sufficiently round.

[4] The separation distance was calculated using $2\theta_{Bragg}\, dz$, with a camera-length of dz=75 µm and the back-projected grating periodicity $g = 9.4$ nm.

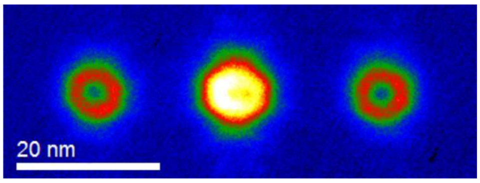

Fig. 13. Experimental energy filtered image showing the well separated vortex orders $m = +1$ (left) and $m = -1$ (right) next to the intense central $m = 0$ beam (middle), produced by the SAA vortex filter at the Co L_3-edge defocused by 4 µm.

the stacked images to get the RMS value pixel by pixel has the advantage that systematic errors, e.g. stemming from the azimuthal intensity variations of the vortices, are minimized. We have done two dimensional image simulations to clarify that the azimuthal intensity variations are systematic effects due to the presence of the stabilisation bars used in the HVM design.[5] The resulting intensity values of each vortex orders' rotational average ($I_{\pm1}$) and absolute RMS values ($\sigma_{I_{\pm1}}$) of that analysis have been used to estimate the relative RMS value of an EMCD signal σ_{EMCD} by error propagation [57]. The relation

$$\sigma_{EMCD} \approx \sqrt{2}\left|\frac{I_{+1}-I_{-1}}{I_{+1}+I_{-1}}\right|\sqrt{\frac{(I_{+1}^2+I_{-1}^2)(\sigma_{I_{+1}}^2+\sigma_{I_{-1}}^2)}{(I_{+1}^2-I_{-1}^2)^2}} \approx \sqrt{2}\frac{\sigma_{I_{+1}}}{I_{+1}} = \frac{\sqrt{2}}{SNR} \qquad (9)$$

uses the approximation that the differences between I_{+1} and I_{-1} are small, thus $I_{+1} \approx I_{-1}$ and that their RMS values are approximately the same $\sigma_{I_{+1}} \approx \sigma_{I_{-1}}$. The radial dependency was omitted for clarity.

The averaged counts of both vortex orders and their RMS value for the central region ($r < 0.7$ nm) amount to 108 ± 9 ($SNR = 12$).[6] Using Eq. (9) leads to a relative error of the difference signal $\sigma_{EMCD} = 12\%$. Hence, using this experimental parameters (HVM size, spot size, dz), the SNR must be improved by an order of magnitude in order to be able to discern the theoretically predicted EMCD signal of 3%.

In view of these results, it is clear that further measures to enhance the SNR have to be taken. One possibility to achieve this goal would be to increase the diameter of the HVM to at least 30 µm while maintaining the high quality and stability. Additionally, reducing the spot size is the second route towards SNR enhancement, see Figs. 8 and 9.

4. Conclusions

In this work, we investigated the feasibility of detecting an EMCD signal when incorporating a HVM as a vortex filter, either in the DP or in the SAA holder of a standard field emission TEM. By lifting the sample far above the eucentric position, a vortex filter mask in the SAA plane can be properly illuminated and produces well separated vortex orders which carry the EMCD information in the asymmetry of their respective central intensities.

Vortex filtering is a promising method for studying magnetic properties of amorphous materials, without the need for the crystal to act as a beam splitter as in the classical EMCD setup. Using a single atom scattering approach, which was justified showing the OAM conservation in amorphous materials via multi-slice simulations, theory predicts an EMCD effect of 50% for (non-broadened) single atom illumination, which drops to 3% for relatively broad beams of 2 nm. This is a tempting aspect in terms of high resolution EMCD measurements, but the very short Rayleigh range of atomic sized beams would call for extremely thin samples with all their drawbacks considering core loss EELS measurements.

Experimentally, it was shown that the SAA HVM setup described is capable of filtering the OAM content of incident vortices. Also, artefact sources like HVM tilt and astigmatism have been identified and routes towards their elimination have been suggested. A trial experiment demonstrates that the SNR is currently ten times too low and that for a successful experimental realisation, substantial progress in the experimental conditions is compulsory. For example, to improve the SNR, future experiments should incorporate larger SAA HVMs. On the one hand, such HVMs would increase the acceptance angle. On the other hand, the sample could be lifted further without strong reduction of the collection angle, which would strongly increase the predicted EMCD effect due to the resulting reduced effective source size.

Hence, despite its current limitations, post-specimen vorticity filtering offers considerable possibilities for new, technologically important EMCD applications, thus encouraging future work in this exciting field.

Acknowledgements

The authors acknowledge the valuable work of Stefan Sack on implementing amorphous materials in the multi-slice code as well as financial support by the Austrian Science Fund (FWF), projects I543-N20 and J3732-N27, and by the European research council, projects ERC-StG-306447 and ERC-2011-ADG.

References

[1] P. Schattschneider, S. Rubino, C. Hébert, J. Rusz, J. Kuneš, P. Novák, E. Carlino, M. Fabrizioli, G. Panaccione, G. Rossi, Detection of magnetic circular dichroism using a transmission electron microscope, Nature 441 (2006) 486–488, doi:10.1038/nature04778.
[2] J. Rusz, O. Eriksson, P. Novák, P. Oppeneer, Spin and orbital moment sum-rules for the electron energy loss chiral magnetic dichroism, Phys. B 403 (5–9) (2008) 1614–1615, doi:10.1016/j.physb.2007.10.322.
[3] J. Verbeeck, C. Hébert, S. Rubino, P. Novák, J. Rusz, F. Houdellier, C. Gatel, P. Schattschneider, Optimal aperture sizes and positions for emcd experiments, Ultramicroscopy 108 (9) (2008) 865–872, doi:10.1016/j.ultramic.2008.02.007.
[4] B. Warot-Fonrose, C. Gatel, L. Calmels, V. Serin, E. Snoeck, S. Cherifi, Magnetic properties of FeCo alloys measured by energy-loss magnetic chiral dichroism, J. Appl. Phys. 107 (9) (2010) 09D301, doi:10.1063/1.3358217.
[5] Z. Wang, X. Zhong, R. Yu, Z. Cheng, Z. J., Quantitative experimental determination of site-specific magnetic structures by transmitted electrons, Nat. Commun. 4 (2013), doi:10.1038/ncomms2323.
[6] T. Thersleff, J. Rusz, S. Rubino, B. Hjörvarsson, Y. Ito, N.J. Zaluzec, K. Leifer, Quantitative analysis of magnetic spin and orbital moments from an oxidized iron (1 1 0) surface using electron magnetic circular dichroism, Sci. Rep. 5 (2015), doi:10.1038/srep13012.
[7] S. Schneider, D. Pohl, S. Löffler, J. Rusz, D. Kasinathan, P. Schattschneider, L. Schultz, B. Rellinghaus, Magnetic properties of single nanomagnets: electron energy-loss magnetic chiral dichroism on FePt nanoparticles, Ultramicroscopy 171 (2016) 186–194, doi:10.1016/j.ultramic.2016.09.009.
[8] P. Schattschneider, M. Stöger-Pollach, S. Rubino, M. Sperl, C. Hurm, J. Zweck, J. Rusz, Detection of magnetic circular dichroism on the two-nanometer scale, Phys. Rev. B - Condensed Matter Mater. Phys. 78 (10) (2008) 104413, doi:10.1103/PhysRevB.78.104413.
[9] P. Schattschneider, B. Schaffer, I. Ennen, J. Verbeeck, Mapping spin-polarized transitions with atomic resolution, Phys. Rev. B 85 (2012) 134422, doi:10.1103/PhysRevB.85.134422.
[10] I. Ennen, S. Löffler, C. Kübel, D. Wang, A. Auge, A. Hütten, P. Schattschneider, Site-specific chirality in magnetic transitions, J. Magn. Magn. Mater 324 (18) (2012) 2723–2726, doi:10.1016/j.jmmm.2012.03.050.
[11] M. Uchida, A. Tonomura, Generation of electron beams carrying orbital angular momentum, Nature 464 (2010) 737–739, doi:10.1038/nature08904.
[12] J. Verbeeck, H. Tian, P. Schattschneider, Production and application of electron vortex beams, Nature 467 (7313) (2010) 301–304, doi:10.1038/nature09366.
[13] B. McMorran, A. Agrawal, I. Anderson, A. Herzing, H. Lezec, J. McClelland, J. Unguris, Electron vortex beams with high quanta of orbital angular momentum, Science 331 (6014) (2011) 192–195, doi:10.1126/science.1198804.

---

[5] Also the sixfold symmetry visbile can be attributed to that.

[6] The SNR is defined as the quotient of the intensity and the RMS value.

[14] K.Y. Bliokh, P. Schattschneider, J. Verbeeck, F. Nori, Electron vortex beams in a magnetic field: a new twist on landau levels and aharonov-bohm states, Phys. Rev. X 2 (4) (2012), doi:10.1103/PhysRevX.2.041011.

[15] S. Löffler, P. Schattschneider, Elastic propagation of fast electron vortices through crystals, Acta Crystallograph. Sec. A A68 (2012) 443447, doi:10.1107/S0108767312013189.

[16] J. Verbeeck, H. Tian, G. Van Tendeloo, How to manipulate nanoparticles with an electron beam? Adv. Mater. 25 (8) (2013) 1114–1117, doi:10.1002/adma.201204206.

[17] G. Guzzinati, P. Schattschneider, K. Bliokh, F. Nori, J. Verbeeck, Observation of the larmor and gouy rotations with electron vortex beams, Phys. Rev. Lett. 110 (9) (2013), doi:10.1103/PhysRevLett.110.093601.

[18] A. Lubk, L. Clark, G. Guzzinati, J. Verbeeck, Topological analysis of paraxially scattered electron vortex beams, Phys. Rev. A 87 (2013) 033834, doi:10.1103/PhysRevA.87.033834.

[19] P. Schattschneider, S. Löffler, M. Stöger-Pollach, Verbeeck, Is magnetic chiral dichroism feasible with electron vortices? Ultramicroscopy 136 (2014) 81–85. http://dx.doi.org/10.1016/j.ultramic.2013.07.012.

[20] J. Rusz, S. Bhowmick, Boundaries for efficient use of electron vortex beams to measure magnetic properties, Phys. Rev. Lett. 111 (2013) 105504, doi:10.1103/PhysRevLett.111.105504.

[21] J. Rusz, S. Bhowmick, M. Eriksson, N. Karlsson, Scattering of electron vortex beams on a magnetic crystal: towards atomic-resolution magnetic measurements, Phys. Rev. B 89 (2014) 134428, doi:10.1103/PhysRevB.89.134428.

[22] D. Pohl, S. Schneider, J. Rusz, B. Rellinghaus, Electron vortex beams prepared by a spiral aperture with the goal to measure EMCD on ferromagnetic films via STEM, Ultramicroscopy 150 (2015) 16–22, doi:10.1016/j.ultramic.2014.11.025.

[23] J. Rusz, J.C. Idrobo, S. Bhowmick, Achieving atomic resolution magnetic dichroism by controlling the phase symmetry of an electron probe, Phys. Rev. Lett. 113 (14) (2014), doi:10.1103/PhysRevLett.113.145501.

[24] J.C. Idrobo, J. Rusz, J. Spiegelberg, M.A. McGuire, C.T. Symons, R.R. Vatsavai, C. Cantoni, A.R. Lupini, Detecting magnetic ordering with atomic size electron probes, Adv. Struct. Chem. Imag. 2 (1) (2016) 5, doi:10.1186/s40679-016-0019-9.

[25] G. Guzzinati, L. Clark, A. Béché, J. Verbeeck, Measuring the orbital angular momentum of electron beams, Phys. Rev. A 89 (2014) 025803, doi:10.1103/PhysRevA.89.025803.

[26] L. Clark, A. Béché, G. Guzzinati, J. Verbeeck, Quantitative measurement of orbital angular momentum in electron microscopy, Phys. Rev. A 89 (2014) 053818, doi:10.1103/PhysRevA.89.053818.

[27] R. Fickler, R. Lapkiewicz, W.N. Plick, M. Krenn, C. Schaeff, S. Ramelow, A. Zeilinger, Quantum entanglement of high angular momenta, Science 338 (6107) (2012) 640–643, doi:10.1126/science.1227193.

[28] V. Bazhenov, M. Vasnetsov, M. Soskin, Laser beams with screw dislocations in their wavefronts, JETP Lett. 52 (8) (1990) 429–431.

[29] R. Steiger, S. Bernet, M. Ritsch-Marte, Mapping of phase singularities with spiral phase contrast microscopy, Opt. Express 21 (14) (2013) 16282–16289, doi:10.1364/OE.21.016282.

[30] S. Muto, J. Rusz, K. Tatsumi, R. Adam, S. Arai, V. Kocevski, P.M. Oppeneer, D.E. Bürgler, C.M. Schneider, Quantitative characterization of nanoscale polycrystalline magnets with electron magnetic circular dichroism, Nat. Commun. 5 (2014), doi:10.1038/ncomms4138.

[31] Y. Wu, J. Stöhr, B.D. Hermsmejer, M.G. Samant, D. Keller, Enhanced orbital magnetic moment on Co atoms in Co/Pd multilayers: A magnetic circular X-ray dichroism study, Phys. Rev. Lett. 69 (15) (1992) 2307–2310, doi:10.1103/PhysRevLett.69.2307.

[32] G. Schütz, W. Wagner, W. Wilhelm, P. Kienle, R. Zeller, R. Frahm, G. Materlik, Absorption of circularly polarized X-rays in iron, Phys. Rev. Lett. 58 (7) (1987) 737–740, doi:10.1103/PhysRevLett.58.737.

[33] S.T. Manson, Inelastic collisions of fast charged particles with atoms: ionization of the aluminum L-shell, Phys. Rev. A 6 (1972) 1013–1024, doi:10.1103/PhysRevA.6.1013.

[34] S. Löffler, I. Ennen, F. Tian, P. Schattschneider, N. Jaouen, Breakdown of the dipole approximation in core losses, Ultramicroscopy 111 (8) (2011) 1163–1167, doi:10.1016/j.ultramic.2011.03.006.

[35] J.M. Auerhammer, P. Rez, Dipole-forbidden excitations in electron-energy-loss spectroscopy, Phys. Rev. B 40 (1989) 2024–2030, doi:10.1103/PhysRevB.40.2024.

[36] P. Schattschneider, J. Verbeeck, V. Mauchamp, M. Jaouen, A. Hamon, Real-space simulations of spin-polarized electronic transitions in iron, Phys. Rev. B - Condensed Matter Mater. Phys. 82 (14) (2010), doi:10.1103/Physrevb.82.144418.

[37] R.F. Egerton, Electron energy-loss spectroscopy in the TEM, Rep. Prog. Phys. 72 (1) (2009), doi:10.1088/0034-4885/72/1/016502. 016502 (25pp).

[38] M. Abramowitz, I. Stegun, Handbook of Mathematical Functions, Dover Publications, 1965.

[39] P. Schattschneider, M. Nelhiebel, B. Jouffrey, Density matrix of inelastically scattered fast electrons, Phys. Rev. B 59 (1999) 10959–10969, doi:10.1103/PhysRevB.59.10959.

[40] S. Löffler, P. Schattschneider, Transition Probability Functions for Applications of Inelastic Electron Scattering, Micron (Oxford, England : 1993) 43 (9) (2012) 971977, doi:10.1016/j.micron.2012.03.020.

[41] P. Schattschneider, I. Ennen, S. Löffler, M. Stöger-Pollach, J. Verbeeck, Circular dichroism in the electron microscope: progress and applications (invited), J. Appl. Phys. 107 (9) (2010) 09D311, doi:10.1063/1.3365517.

[42] R. Juchtmans, J. Verbeeck, Orbital angular momentum in electron diffraction and its use to determine chiral crystal symmetries, Phys. Rev. B 92 (2015) 134108, doi:10.1103/PhysRevB.92.134108.

[43] R. Juchtmans, J. Verbeeck, Local orbital angular momentum revealed by spiral-phase-plate imaging in transmission-electron microscopy, Phys. Rev. A 93 (2016) 023811, doi:10.1103/PhysRevA.93.023811.

[44] G. Guzzinati, P. Schattschneider, K.Y. Bliokh, F. Nori, J. Verbeeck, Observation of the Larmor and Gouy rotations with electron vortex beams, Phys. Rev. Lett. 110 (2013) 093601, doi:10.1103/PhysRevLett.110.093601.

[45] T. Schachinger, S. Löffler, M. Stöger-Pollach, P. Schattschneider, Peculiar rotation of electron vortex beams, Ultramicroscopy 158 (2015) 17–25, doi:10.1016/j.ultramic.2015.06.004.

[46] H.L. Xin, H. Zheng, On-column 2p bound state with topological charge 1 excited by an atomic-size vortex beam in an aberration-corrected scanning transmission electron microscope, Microsci. Microanal. 18 (2012) 711, doi:10.1017/S1431927612000499.

[47] E.J. Kirkland, Advanced Computing in Electron Microscopy, Springer US, 2010, doi:10.1007/978-1-4419-6533-2.

[48] P. Schattschneider, M. Stöger-Pollach, S. Löffler, A. Steiger-Thirsfeld, J. Hell, J. Verbeeck, Sub-nanometer free electrons with topological charge, Ultramicroscopy 115 (2012) 21–25, doi:10.1016/j.ultramic.2012.01.010.

[49] V. Grillo, E. Karimi, G.C. Gazzadi, S. Frabboni, M.R. Dennis, R.W. Boyd, Generation of nondiffracting electron bessel beams, Phys. Rev. X 4 (2014) 011013, doi:10.1103/PhysRevX.4.011013.

[50] K. Saitoh, K. Hirakawa, H. Nambu, N. Tanaka, M. Uchida, Generation of electron bessel beams with nondiffractive spreading by a nanofabricated annular slit, J. Phys. Soc. Jpn. 85 (4) (2016) 043501, doi:10.7566/JPSJ.85.043501.

[51] C. Zheng, T.C. Petersen, H. Kirmse, W. Neumann, J. Etheridge, Efficient generation of electron bessel beams using generic magnetic vortex structures, The 16th European Microscopy Congress, Lyon, France, 2016, doi:10.1002/9783527808465.EMC2016.6055.

[52] T.R. Harvey, V. Grillo, B.J. McMorran, Stern-Gerlach-like approach to electron orbital angular momentum measurement, Phys. Rev. A 95 (2) (2017) 021801, doi:10.1103/PhysRevA.95.021801.

[53] B. Barwick, G. Gronniger, L. Yuan, S.-H. Liou, H. Batelaan, A measurement of electron-wall interactions using transmission diffraction from nanofabricated gratings, J. Appl. Phys. (2006), doi:10.1063/1.2357000.

[54] B. McMorran, J.D. Perreault, T. Savas, A. Cronin, Diffraction of 0.5 keV electrons from free-standing transmission gratings, Ultramicroscopy 106 (4–5) (2006) 356–364. http://dx.doi.org/10.1016/j.ultramic.2005.11.003.

[55] V. Grillo, G.C. Gazzadi, E. Karimi, E. Mafakheri, R.W. Boyd, S. Frabboni, Highly efficient electron vortex beams generated by nanofabricated phase holograms, Appl. Phys. Lett. 104 (2014) 043109, doi:10.1063/1.4863564.

[56] C. Schneider, W. Rasband, K. Eliceiri, NIH Image to ImageJ: 25 years of image analysis, Nat. Methods 9 (2012) 671–675, doi:10.1038/nmeth.2089.

[57] J.R. Taylor, An Introduction to Error Analysis: The Study of Uncertainties in Physical Measurements, 2nd ed., University Science Books, 1997.

Chapter 7

Convergent-beam EMCD: benefits, pitfalls and applications

S. Löffler and W. Hetaba

Microscopy 67 (2018) i60–i71
10.1093/jmicro/dfx129

MICROSCOPY

Microscopy, 2018, i60–i71
doi: 10.1093/jmicro/dfx129
Advance Access Publication Date: 23 January 2018

Article

Convergent-beam EMCD: benefits, pitfalls and applications

S. Löffler[1,2,*] **and W. Hetaba**[1,3]

[1]University Service Centre for Transmission Electron Microscopy, TU Wien, Vienna, Austria and [2]Department for Materials Science and Engineering, McMaster University, Hamilton, Ontario, Canada

[3]Present address: Fritz-Haber-Institut der Max-Planck-Gesellschaft, Berlin, Germany
[*]To whom correspondence should be addressed. E-mail: stefan.loeffler@tuwien.ac.at

Received 26 May 2017; Editorial Decision 8 December 2017; Accepted 16 December 2017

Abstract

Energy-loss magnetic chiral dichroism (EMCD) is a versatile method for studying magnetic properties on the nanoscale. However, the classical EMCD technique is notorious for its low signal-to-noise ratio (SNR), which is why many experimentalists have adopted a convergent-beam approach. Here, we study the theoretical possibilities of using a convergent beam for EMCD. In particular, we study the influence of detector positioning as well as convergence and collection angles on the detectable EMCD signal. In addition, we analyse the expected SNR and give some guidelines for achieving optimal EMCD results.

Key words: EMCD, convergence angle, collection angle, aperture position, signal-to-noise ratio, STEM

Introduction

Electron magnetic chiral dichroism (EMCD), the electron microscopic equivalent to X-ray magnetic circular dichroism (XMCD), is a very versatile tool for investigating magnetic materials on the nanometer scale. Ever since its theoretical prediction [1] and subsequent realization [2], EMCD has been gaining popularity in many fields, including magnetic nano-engineering and spintronics.

There are, however, two severe limitations with the classical EMCD approach: spatial resolution and signal-to-noise (SNR) ratio. In the classical EMCD approach, one sends a plane wave into a crystal that was tilted into systematic row condition and subsequently measures the inelastically scattered electrons at particular points of the diffraction plane far away from the diffraction spots (see also Fig. 1). While plane waves are well suited for an elegant theoretical treatment, they are not so useful in practice. First of all, from a fundamental point of view, it is impossible to actually create or measure true plane waves, due to the limited extent of the microscope and the apertures, as well as the beam rotation induced by the magnetic lenses [3]. Secondly, from an experimental point of view, a (quasi) plane wave has a very low current density at the sample. Together with the fact that the signal has to be measured off-axis — where it can be orders of magnitude smaller than on-axis — with (ideally infinitely) small detectors, this results in a notoriously low SNR. Another issue is resolution. When acquiring spectra in diffraction mode, the spatial resolution is usually defined by using a selected area aperture (typically of the order of 100 nm), thereby reducing the signal even further. Alternatively, one can measure in image mode using energy-filtered TEM (EFTEM) [4,5]. Due to the required energy-slit, this again leads to low intensity, in addition to poor energy resolution.

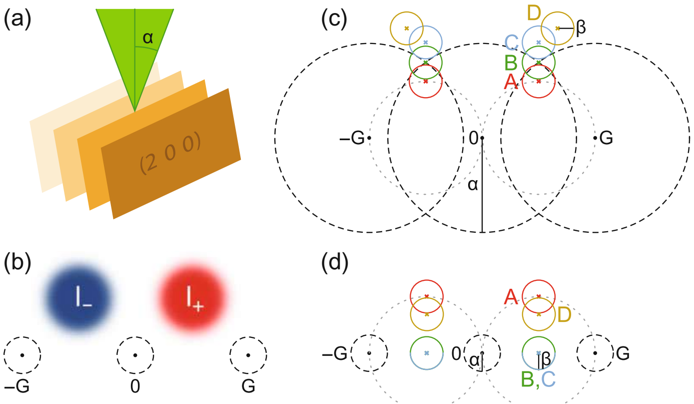

Fig. 1. Sketch of the convergent beam setup. (a) The incident beam with convergence semi-angle α is centered on a crystal plane. (b) Sketch of the general positions of the areas with 'positive' (i.e. higher than non-magnetic) signal I_+ and 'negative' (i.e. lower than non-magnetic) signal I_-. (c) Schematic elastic diffraction pattern for large α. (d) Schematic elastic diffraction pattern for small α. The diffraction spots are labeled 0, G and −G. Diffraction disks are depicted as black dashed lines, the Thales circles are depicted as gray dotted lines. α is the convergence semi-angle, β is the collection semi-angle. The four detector positions A–D are described in the text.

To overcome these limitations, several new approaches have been proposed and tested, ranging from alternative measurement geometries in scanning transmission electron microscopy (STEM) [6–10], over vortex beams [11–13], to the use of aberration correctors to manipulate the phase of the electron beam [14,15]. However, all these methods exhibit very low signal are typically limited to atomic resolution [16,17], and may require changing components of the microscope or operating it under non-standard conditions. Thus, these new methods are not yet usable for many practical applications.

However, there is a third alternative that has gained increasing popularity in experimental EMCD in recent years: convergent-beam EMCD. It improves both the spatial resolution and the SNR at the same time while still making use of the original, straight-forward measurement setup by using a convergent beam and finite collection apertures instead of plane waves. This method has been used experimentally to boost the spatial resolution of classical EMCD (see, e.g. [18–24], and it has long been known that large collection apertures can improve the SNR [25]. Therefore, it is surprising that, to our knowledge, the influence of the convergence angle and the effect the interplay between convergence and collection angle has on both the signal and the SNR has not been studied extensively from a theoretical point of view so far (although it has been studied, e.g. for aberrated probes [26]).

In this work, we present simulations that show that convergent beam EMCD is in many ways superior to classical EMCD. In particular, we present simple rules of thumb for how to obtain close-to-optimal SNR while at the same time improving the spatial resolution to close to atomic resolution. This is expected to open new avenues for optimizing EMCD measurements in general, but particularly for the characterization of fine grained materials, thin films, as well as the magnetic structure in the vicinity of interfaces and defects. Thus, it is expected to lead to great advances in material science.

Methods

In this work, we present extensive simulations for the model system of a 10 nm thick bcc Fe crystal, tilted 10° from the [0 0 1] zone axis (ZA) to produce a systematic row case including the (2 0 0) diffraction spot. All simulations were performed using an acceleration voltage of 300 kV without spherical aberration. (The spherical aberration is not expected to play a major role here, though, as we are working mostly in the diffraction plane.) The beam was focused (with varying convergence semi-angle α) onto the entry surface of the sample and positioned on an atomic plane. The complete measurement setup is depicted in Fig. 1.

The inelastic scattering was performed using the mixed dynamic form factor (MDFF) approach [2,27,28]. The MDFF was modeled with an idealized fully spin-polarized cross-density of states [28] and Slater-type orbital wavefunctions [29], taking into account the dipole allowed transitions $2p \rightarrow d$. The elastic scattering both before and after the inelastic scattering was taken into account using the multislice algorithm [30]. A 2048×2048 grid with ca. 0.09 Å/px was used together with a slice thickness of 1 Å and the electrostatic potentials given by Kirkland [30].

For extracting the EMCD effect, one needs to measure and compare the signal strengths at two different positions I_+, I_-. In the context of this work, two different (albeit closely related) definitions of the EMCD effect are used. On the one hand, we use the 'difference signal', sometimes also referred to as 'absolute EMCD effect', defined as

$$\Delta I_0 = I_+ + I_-. \tag{1}$$

On the other hand, we use the 'quotient signal', sometimes also referred to as 'relative signal', defined as

$$S = 2 \cdot \frac{I_+ - I_-}{I_+ + I_-} = \frac{\Delta I}{I_0} \text{ with } I_0 = \frac{I_+ + I_-}{2}. \tag{2}$$

The quotient signal is the one originally proposed (up to the prefactor of 2) and used in several later works [1,5,7,31–33]. By dividing by the average intensity I_0, it is automatically normalized to the incident dose — although it still depends on the sample thickness. For quantitative work, the difference signal is the method of choice as it allows for the application of sum rules for determining the m_l/m_s ratio [34–36].

To find the optimal conditions for extracting an EMCD signal, two different schemes were used. On the one hand, a point-wise comparison of corresponding points on the upper/lower or left/right halves of the diffraction plane was performed to obtain a visual indication of the distribution of the EMCD effect. On the other hand, circular collection apertures (of varying collection semi-angle β) were centered at four different sets of points of the diffraction plane: (A) on the Thales circle, (B) at the intersection of adjacent elastic diffraction disks (in case the elastic diffraction disks did not overlap, the apertures were centered on the systematic row), (C) just outside the elastic diffraction disks such that the collection aperture touched adjacent diffraction disks (in case such a touching configuration was not possible, the apertures were positioned on the systematic row), (D) in an 'optimal position', i.e. at a convergence and collection angle dependent point where the maximal EMCD effect can be obtained as determined by a downhill simplex optimization algorithm [37]. All four positions are also depicted schematically in Fig. 1.

Results

Position of the EMCD effect

In order to check the applicability of convergent beam EMCD, it is first necessary to determine where an EMCD effect can be expected in the diffraction plane (if at all). To that end, Fig. 2a–d shows simulated energy-filtered diffraction patterns for the Fe L_3 edge for different convergence angles. For classical EMCD (i.e. the first column in Fig. 2), it is well known that there are four areas exhibiting magnetic information, one in each quadrant of the diffraction plane. Therefore, in Fig. 2e–h, we plotted the difference EMCD effect ΔI calculated pixel by pixel from the difference of the upper and the lower half-plane. Likewise, Fig. 2i–l shows the difference EMCD effect ΔI calculated pixel by pixel from the difference of the right and the left half-plane. Figure 2m–p shows the quotient EMCD effect S calculated from the difference of the upper and lower half-plane, while Fig. 2q–t shows the quotient EMCD effect S calculated from the difference of the right and left half-plane.

The first main result from those maps is that with increasing convergence angle, the areas where the quotient EMCD is strong is 'pushed out' such that it can generally be found close to the rim of the elastic diffraction disks. The same is mostly true also for the left/right half-plane subtracted difference signal (Fig. 2i–l). Only the top/bottom subtracted difference signal (Fig. 2e–h) exhibits strong signal inside the diffraction disks which can be attributed to artifacts caused by the Ewald sphere curvature as discussed below.

The fact that the areas with strong EMCD signal are 'pushed out' can be explained qualitatively by considering the relative contributions of the different scattering vectors. Assuming ideal conditions, a point-like detector, and using the dipole approximation [7,38,39], the EMCD difference signal is proportional to

$$\int \frac{\vec{q} \times \vec{q}\,'}{q^2 q'^2} d^2q d^2q', \tag{3}$$

where one has to integrate over *all* combinations of scattering vectors connecting points inside the convergence disks (with radii α, see Fig. 1) with the point-like detector. Due to the $1/(q^2q'^2)$ dependence, contributions from short scattering vectors are dominant and due to the $\vec{q} \times \vec{q}\,'$ dependence, contributions are strongest for perpendicular scattering vectors.

In the limit of small convergence angles, only one pair of scattering vectors is possible and the situation reduces to the case of classical EMCD: the perpendicularity requirement suggests that the signal is strongest close to the Thales circle. (The exact position depends on the characteristic momentum transfer, as well as the details of the elastic scattering.) For large convergence angles, this explanation no longer holds as then, many combinations of scattering vectors can contribute.

First, we consider detector positions inside the diffraction disks. Without loss of generality, we will assume a detector position inside the 0 diffraction disk. As stated above, the dominant contributions stem from short scattering vectors. For the sake of simplicity, we assume that the complex

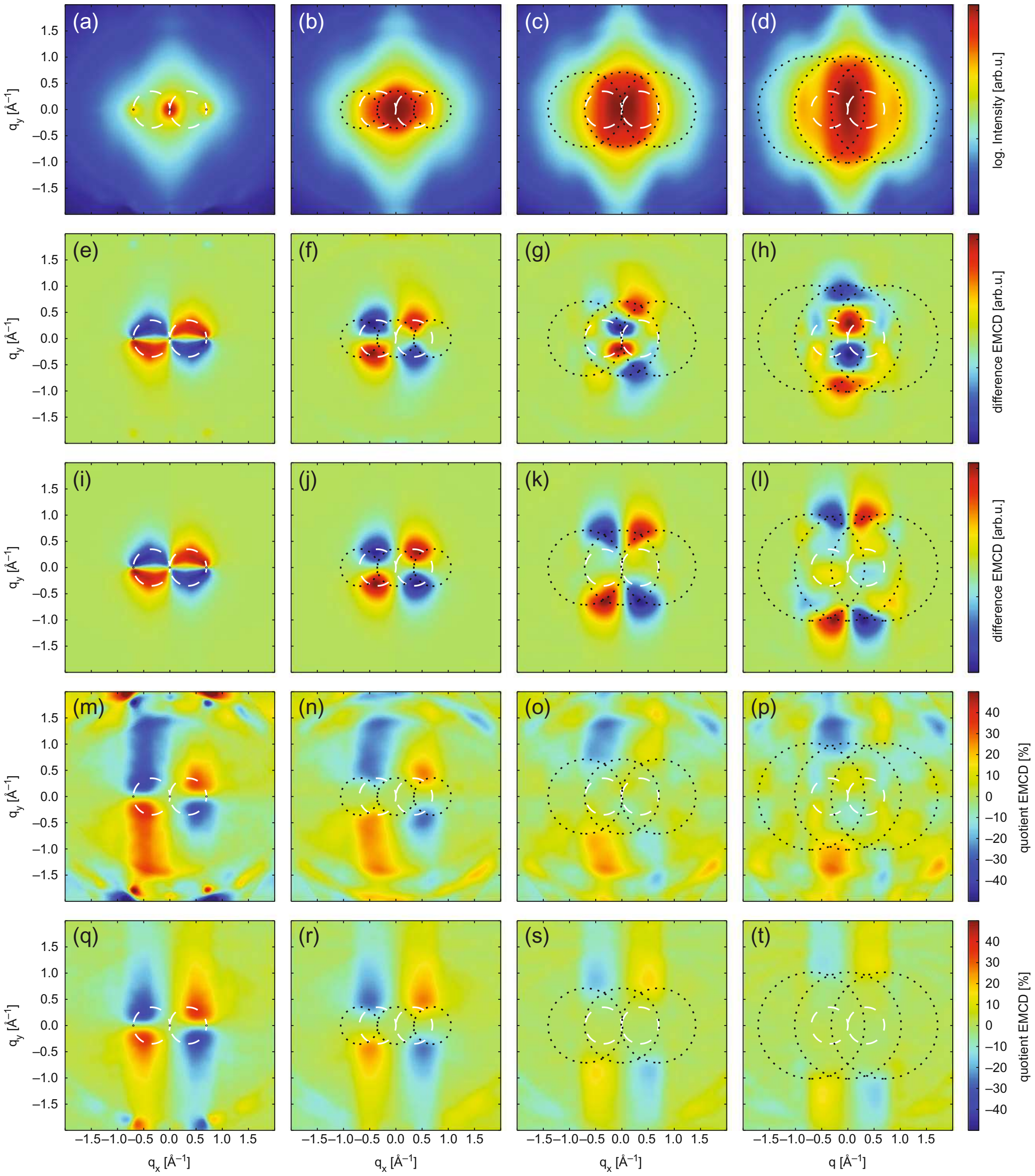

Fig. 2. Energy-filtered diffraction patterns (a–d), point-wise difference EMCD maps based on upper/lower half-plane subtraction (e–h), point-wise difference EMCD maps based on left/right half-plane subtraction (i–l), point-wise quotient EMCD maps based on upper/lower half-plane subtraction (m–p) and point-wise quotient EMCD maps based on left/right half-plane subtraction (q–t) for convergence semi-angles of 0 mrad (a, e, i, m, q), 7 mrad (b, f, j, n, r), 14 mrad (c, g, k, o, s) and 20 mrad (d, h, l, p, t). The black dotted circles indicate the three most intense elastic diffraction disks, whereas the white dashed circles indicate the classical Thales circles. The energy-filtered diffraction patterns are shown in contrast-optimized logarithmic scale.

prefactor coming from elastic scattering is approximately constant in the immediate surrounding of the detector where $|\vec{q}|$ is small. For any sufficiently short scattering vector $\vec{q}$ from a point inside the diffraction disk to the detector, the scattering vector $-\vec{q}$ also connects a point inside the diffraction disk to the detector. As the contributions of $(\vec{q}, \vec{q}\,')$ and

$(-\vec{q}, \vec{q}\,')$ are equal in magnitude but opposite in sign for any scattering vector $\vec{q}\,'$, all these contributions will average out. This implies that inside the elastic diffraction disks, the difference EMCD effect will be small. In addition, the very strong total intensity inside the diffraction disks will cause the quotient EMCD effect to be suppressed even stronger than the difference EMCD effect.

Secondly, if the detector is positioned far away from large diffraction disks, neither the perpendicularity constraint nor the shortness requirement can be fulfilled, thus leading to an asymptotically vanishing EMCD effect.

Thirdly, if the detector is positioned close to the intersection of the diffraction disks, there are always pairs of scattering vectors that are short and fulfill the orthogonality requirement, thus yielding an appreciable EMCD effect.

From Fig. 2, it is also obvious that the upper/lower difference shows severe left/right differences, particularly for larger scattering angles. The origin of these different symmetry properties can be found in the tilting of the Ewald sphere with respect to the crystal and the influence of higher order Laue zones (HOLZs), causing an inherent upper/lower asymmetry of the signal [40–42]. Some artifacts introduced by the HOLZ can be seen particularly well close to the edges of Fig. 2m. (Note that the figures show only a subset of the total simulated area, so the 'artifacts' close to the edge are not calculation artifacts but actually coincide with HOLZ reflections consistent with the chosen scattering geometry.) Due to the asymmetric Ewald sphere and the HOLZ contributions, the intensity in the upper half-plane is slightly lower than the corresponding intensity in the lower half-plane. While this intensity difference is not caused by the spin-polarization of the sample, it can easily be misinterpreted as a 'fake' EMCD effect. While this is of some concern already for classical EMCD, where one typically measures at the Thales circle, it does become a vital issue for larger convergence angles, where one is forced to measure at larger scattering angles. Especially when dealing with the difference EMCD signal, the upper/lower asymmetry can give rise to very large artifacts (see Fig. 2g and h). One way to overcome this could be to use the double-difference technique [35].

However, as the setup is symmetric with respect to a right/left mirror operation (provided the sample is oriented in a perfect systematic row condition [4,42]), the right/left difference maps do not suffer from this effect. Therefore, in the remainder of this work, we use the right/left difference method to extract EMCD signals.

EMCD signal strength and SNR

In this section, we will analyse both the achievable signal strengths ΔI and S as well as the SNRs $\Delta I/\delta\Delta I$ and $S/\delta S$ associated with them as a function of convergence and collection angles for the four detector positions A–D defined above. This is conceptionally similar to previous studies that included estimations for the SNR for plane wave illumination [25] and for aberrated probes [26]. To calculate the SNR, we will include the pre-edge background intensity B, which does not contribute to the signal but does increase the noise. We will also use the jump ratio defined by

$$r = \frac{I_0 + B}{B} \tag{4}$$

to simplify the equations.

Note that while we will give general formulas that should be applicable to all cases at the beginning of each section, further derivations will be based on the assumption of pure Poissonian shot noise to derive simplified formulas and actual numbers. This neglects other noise sources such as readout noise and electronic noise (which will be low compared to the shot noise for the intensity requirements derived below), or uncertainties introduced by the background subtraction process [43]. Nevertheless, the numbers calculated below will give a good rule of thumb for the intensity necessary to obtain a statistically significant EMCD signal.

In addition, the EMCD signal strength itself will depend on a number of parameters, including the sample material, sample thickness, and scattering geometry. Therefore, angles will be discussed in relation to the Bragg angle (here: $\theta_B \approx 6.9$ mrad) and may differ in different systems.

Difference EMCD effect

First, we will treat the difference EMCD effect ΔI which is most useful for quantifying EMCD signals using sum rules [34]. Figure 3a–d shows the difference EMCD signal dependence on the convergence and collection semi-angles for the four sets of detector positions A–D defined above. The first thing that catches the eye is the fact that if the convergence or the collection angle (or both) are small, both the difference EMCD signal and the SNR vanish. This is to be expected as in those cases the overall intensity decreases rapidly, which is why experimentalists started using convergent beam EMCD in the first place. However, using extremely large collection angles is usually not recommended either, as then positive and negative contributions to the difference EMCD signal could average out.

From Fig. 3, it is apparent that positioning the detectors on the Thales circle (position A) gives a large signal (albeit not the best SNR) when both the convergence and collection angle are slightly larger than the Bragg angle. This is due to the 'pushing out' of the area of strong difference EMCD signal with increasing convergence angle (see also Fig. 2), combined with the increasing intensity for larger

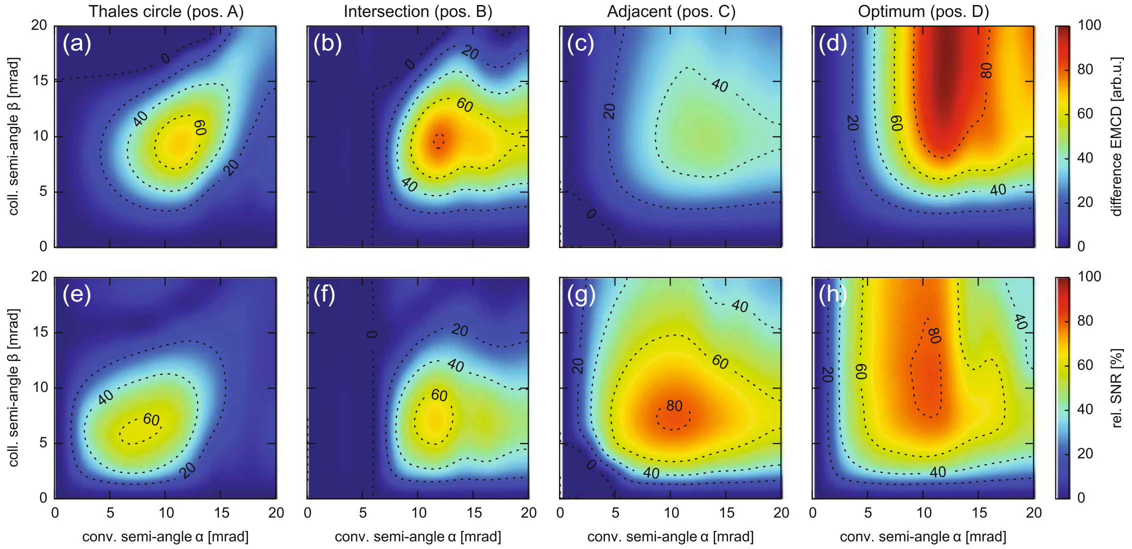

Fig. 3. Difference signal ΔI (a–d) and SNR $\Delta I/\delta\Delta I$ (e–h) for the four sets of detector positions A–D as a function of convergence and collection semi-angles. The SNR is given for a jump ratio of $r = 2$ in fractions of the maximum SNR.

convergence angles. Compared to the Thales circle position, the intersection position (position B) gives both better overall signal and better SNR. In fact, one can reach 80% of the optimal signal at about 70% of the optimal SNR in the present case. The adjacent position (position C) yields a lower signal overall, but a nearly optimal SNR. In addition, it allows to use a relatively large range of convergence and collection angles with little to no impact on signal strength and SNR. Finally, the optimum position (position D) data are shown for reference.

To calculate the SNR, the following approach was used. If shot noise dominates over other noise sources (such as readout noise), $I_\pm$ follows a Poisson distribution. By the central limit theorem, this can be approximated well by a Gaussian distribution with a standard deviation of $\delta I_\pm = \sqrt{I_\pm + B}$ for sufficiently large signal, where B is the background intensity. Then, the variance $(\delta\Delta I)^2$ of the signal ΔI is given by

$$(\delta\Delta I)^2 = (\delta I_+)^2 + (\delta I_-)^2 = I_+ + I_- + 2B = 2(I_0 + B). \quad (5)$$

Therefore, the SNR reads

$$\frac{\Delta I}{\delta\Delta I} = \frac{I_+ - I_-}{\sqrt{(\delta I_+)^2 + (\delta I_-)^2}} = \frac{SI_0}{\sqrt{2(I_0 + B)}} \quad (6)$$

Not surprisingly, the SNR increases with average intensity I_0 and dichroic fraction (quotient signal) S while it decreases with pre-edge background B. A similar expression was also reported for maps with an aberrated probe [26], although for larger convergence angles.

To answer the question of how many counts need to be recorded to achieve a certain statistical significance, one naturally needs to consider the ratio between the elemental edge and the pre-edge background (which increases the noise level but not the signal). Assuming a jump ratio r of

$$r = \frac{I_0 + B}{B} \Leftrightarrow B = \frac{I_0}{r - 1} \Leftrightarrow I_0 + B = I_0 \cdot \frac{r}{r - 1}, \quad (7)$$

the SNR can be rewritten as

$$\frac{\Delta I}{\delta\Delta I} = \frac{S\sqrt{I_0(r - 1)}}{\sqrt{2r}}. \quad (8)$$

If $B = I_0$, i.e. for a jump ratio of $r = 2$, the SNR takes the form

$$\frac{\Delta I}{\delta\Delta I} = \frac{\Delta I}{2\sqrt{I_0}} = \frac{S\sqrt{I_0}}{2}. \quad (9)$$

To reach a SNR of k, one needs to achieve a total intensity of

$$I_0 + B \geq \frac{2r^2k^2}{S^2(r - 1)^2} \quad (10)$$

counts. This prediction is in good agreement with the order of magnitude of the intensity threshold found experimentally [24]. For the special case of $k = 3$ and $r = 2$, this gives

$$I_0 + B \geq \frac{72}{S^2} \tag{11}$$

i.e. for an expected dichroic fraction of $S = 10\%$, an intensity of at least 7200 counts needs to be achieved in this case.

Quotient EMCD effect

Figure 4a–d shows the dependence of the quotient EMCD effect on the convergence and collection angles for the four different sets of detector positions A–D defined above. As was already noted in the Section "Position of the EMCD effect", placing the detectors on the Thales circle (position A) only gives a large EMCD signal for small convergence and collection angles. For angles larger than roughly θ_B, the signal decreases rapidly as one is then measuring 'inside' the elastic diffraction disk, which will increase I_0 and therefore decrease S. Putting the detectors on the intersection of the elastic diffraction disks (position B) gives an extremely low quotient signal, unlike the difference signal. Again, this is due to the fact that there is a strong contribution to I_0 inside the diffraction disks which will strongly decrease the quotient signal. Putting the detectors adjacent to the elastic diffraction disks (position C) gives a medium quotient EMCD effect, but over a large range of convergence and collection angles, similar to the difference EMCD signal. Also like the difference signal, the SNR is close to optimal in this case. In addition, it is interesting to note that the adjacent position is mostly complementary to the Thales circle position in terms of the quotient signal. Finally, the optimum position (position D) is shown for reference.

For calculating the SNR, the same assumption as for the difference signal case is used. Here, the variance $(\delta S)^2$ of the signal S can be calculated by error propagation to read

$$(\delta S)^2 = 16 \cdot \frac{(\delta I_+)^2 I_-^2 + I_+^2 (\delta I_-)^2}{(I_+ + I_-)^4}. \tag{12}$$

with a SNR of

$$\frac{S}{\delta S} = \frac{I_+^2 - I_-^2}{2\sqrt{(\delta I_+)^2 I_-^2 + I_+^2 (\delta I_-)^2}}. \tag{13}$$

Assuming only shot-noise as above, the former can be simplified to

$$(\delta S)^2 = \frac{16 I_+ I_-}{(I_+ + I_-)^3} + 16B \cdot \frac{I_+^2 + I_-^2}{(I_+ + I_-)^4}. \tag{14}$$

By virtue of

$$\begin{aligned} I_+ - I_- &= S I_0 \\ I_+ + I_- &= 2 I_0 \\ 4 I_+ I_- &= I_0^2 (4 - S^2) \\ 2(I_+^2 + I_-^2) &= I_0^2 (4 + S^2) \end{aligned} \tag{15}$$

this can also be written as

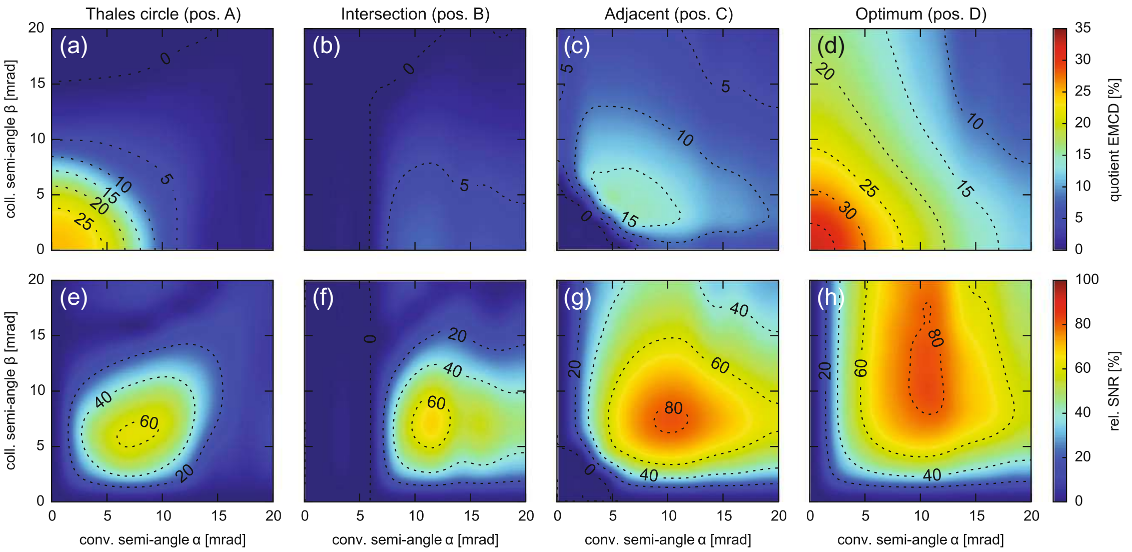

Fig. 4. EMCD effect S (a–d) and SNR $S/\delta S$ (e–h) for the four sets of detector positions A–D as a function of convergence and collection semi-angles. The SNR is given for a jump ratio of r = 2 in fractions of the maximum SNR.

$$(\delta S)^2 = \frac{I_0(4 - S^2) + B\cdot(4 + S^2)}{2I_0^2}. \tag{16}$$

Thus, the SNR becomes

$$\frac{S}{\delta S} = \frac{\sqrt{2}\,SI_0}{\sqrt{I_0(4 - S^2) + B\cdot(4 + S^2)}}. \tag{17}$$

This can also be written in terms of the jump ratio as

$$\frac{S}{\delta S} = \frac{\sqrt{2I_0}\,S}{\sqrt{4 - S^2 + \frac{4+S^2}{r-1}}} = \frac{S\sqrt{2(r-1)I_0}}{\sqrt{r(4 - S^2) + 2S^2}}. \tag{18}$$

If $B = I_0$, i.e. for a jump ratio of $r = 2$, the SNR takes the same form as for the difference EMCD signal, i.e.

$$\frac{S}{\delta S} = \frac{S\sqrt{I_0}}{2}. \tag{19}$$

To reach a SNR of at least k, I_0 must be chosen such that

$$I_0 \geq \frac{k^2}{2S^2}\left(4 - S^2 + \frac{4 + S^2}{r - 1}\right) \tag{20}$$

or, equivalently, that the total intensity fulfills

$$I_0 + B \geq \frac{k^2 r}{2S^2(r-1)}\left(4 - S^2 + \frac{4 + S^2}{r - 1}\right). \tag{21}$$

For the special case of $k = 3$ and $r = 2$, this again gives

$$I_0 + B \geq \frac{72}{S^2}. \tag{22}$$

Discussion

Difference EMCD effect vs. quotient EMCD effect

As mentioned above, the difference EMCD signal is the one typically used for quantification due to the applicability of sum rules. However, in some cases, determining the m_l/m_s ratio may not be required. Instead, it might be sufficient to check if there is any dichroic signal at all or how it changes, e.g. with the position across defects. In such cases, using the quotient signal instead of the difference signal may even be beneficial in terms of SNR, as a comparison of Eqs. 17 and 6 shows:

$$\frac{\sqrt{2}\,SI_0}{\sqrt{I_0(4 - S^2) + B\cdot(4 + S^2)}} < \frac{SI_0}{\sqrt{2(I_0 + B)}} \tag{23}$$

$$4(I_0 + B) < I_0(4 - S^2) + B\cdot(4 + S^2) \tag{24}$$

$$0 < S^2\cdot(B - I_0). \tag{25}$$

This means that only for $B > I_0 \Leftrightarrow r < 2$, i.e. for thick specimens, using the difference signal is actually better than using the quotient signal in terms of SNR. However, thick specimens typically yield a low overall EMCD effect owing to oscillations and sign reversal caused by the elastic scattering and pendellösung [32,39]. Therefore, the quotient signal should be preferred unless the application of sum rules is required.

Beam position dependence

In this section, we investigate the dependence of the convergent beam EMCD signal on the beam position. For small convergence and collection angles, one can expect that the EMCD signal is largely independent of the beam position due to the large illuminated area and, consequently, the low spatial resolution. For convergence and collection semi-angles significantly larger than the Bragg angle, however, one can expect a position dependence [10]. To study the effect this has on the signal strengths at the various detector positions as well as on the SNR, we also performed calculations with the beam displaced by half a lattice plane distance so that it was positioned directly in-between adjacent lattice planes.

Figure 5 compares the energy-filtered diffraction patterns and point-wise EMCD effects for on-plane and off-plane beam positions for a large convergence angle. While there are obvious differences, it is remarkable that both difference and quotient EMCD effects with the same sign can be found at similar positions adjacent to the diffraction disks. While these contributions from adjacent positions are weaker for the difference signal (with stronger contributions with reversed sign showing up close to the Thales circle), the quotient EMCD effect is even stronger for the off-plane condition than for the on-plane condition. Qualitatively, this can be understood from the fact that the inelastic scattering kernels contributing to EMCD have the same shape as electron vortex beams: an azimuthal phase ramp combined with a donut-shaped intensity distribution [28,44,45]. Thus, the highest probability for exciting a transition that contributes to the EMCD signal with a very small probe is actually not on the atomic nuclei, but in the area surrounding them. (This can also be understood from the fact that the initial p-states contributing to the L-edge have vanishing probability density at the position of the nucleus.) Of course, the

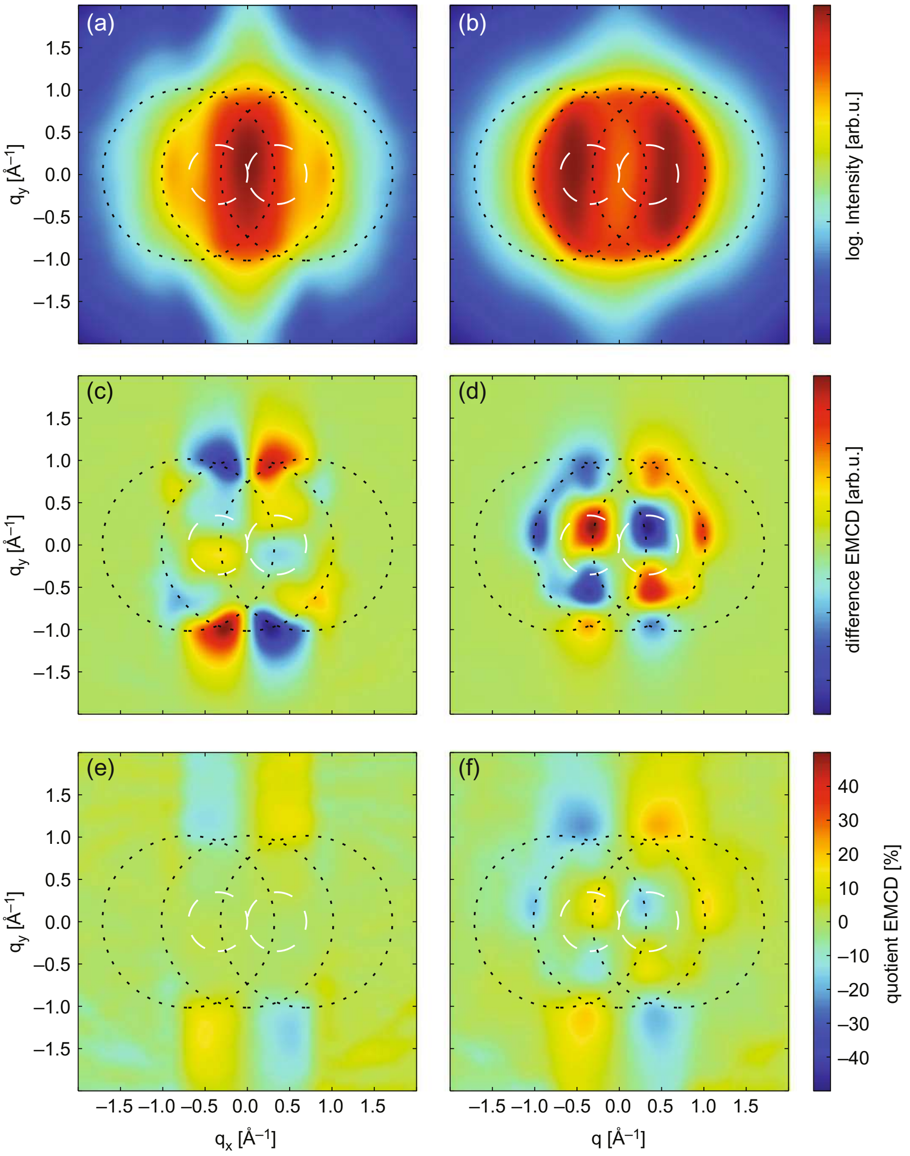

Fig. 5. Energy-filtered diffraction patterns (a, b), point-wise difference EMCD maps based on left/right half-plane subtraction (c, d) and point-wise quotient EMCD maps (e, f) for on-plane (a, c, e) and off-plane (b, d, f) beam positions. The convergence semi-angle is 20 mrad. The black dotted circles indicate the three most intense diffraction disks, whereas the white dashed circles indicate the classical Thales circles. The energy-filtered diffraction patterns are shown in contrast-optimized logarithmic scale.

question of how much which atom contributes to the EMCD effect depends crucially on how the incident and outgoing electron beams channel through the crystal [46,47]. However, a full quantitative description of the resulting thickness dependence is beyond the scope of this work.

Figure 6 shows the convergence and collection semi-angle dependence of the EMCD signals for a probe beam positioned between atomic planes, together with the corresponding SNR (which, for the chosen jump ratio of $r = 2$, is the same for the difference and for the quotient signal). Qualitatively, it looks similar to the on-plane case depicted in Fig. 4. In particular for small convergence and collection semi-angles, the maps are identical, as is to be expected. However, at larger angles, several changes are visible. Note that this is actually wanted in order to be able to perform lattice-resolved EMCD experiments [10].

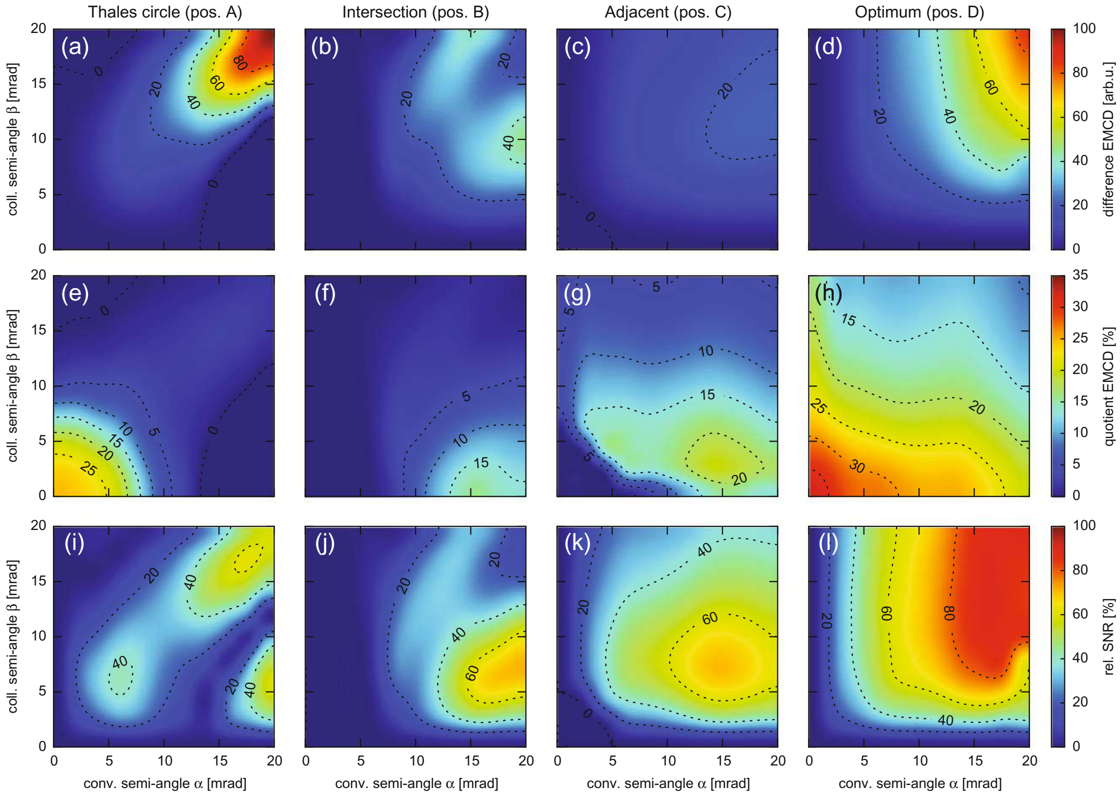

Fig. 6. Difference EMCD effect (a–d), quotient EMCD effect (e–h) and SNR (i–l) for the four sets of detector positions A–D as a function of convergence and collection semi-angles for a beam position in-between atomic planes. The SNR is given for a jump ratio of $r = 2$ in fractions of the maximum SNR.

Perhaps the most striking difference is the large difference signal enhancement at the Thales circle for large convergence and collection angles. This is in agreement with Fig. 5, which shows the well-known strong position dependence of the intensity in the regions of overlapping diffraction disks, leading to the appearance of a strong EMCD difference signal close to the Thales circle. In addition, for the intersection and adjacent positions, the difference signal is somewhat decreased. Interestingly, the quotient signal shows an increase at the same positions. Regarding the SNR, the same general trend is seen at the off-plane beam position as at the on-plane beam position: the highest values can usually be achieved at medium angles, in this case particularly with convergence angles of approximately $2\theta_B$ (i.e. slightly larger than on-plane) and collection angles of ca. θ_B (i.e. slightly smaller than on-plane).

Concluding remarks

In this work, we have explored the possibilities of convergent-beam EMCD using numerical simulations. We found that this method gives similar EMCD signals as the classical, parallel beam EMCD method while having superior SNR characteristics, in accordance with previous works. As a rule of thumb, choosing a convergence semi-angle slightly larger than the Bragg angle, a collection angle close to the Bragg angle, and positioning the collection aperture just outside the elastic diffraction disks should give close to optimal results. In addition, we estimated that more than approximately 7200 counts at the edge under investigation are required (the exact value will depend on the peak-to-background ratio and the expected dichroic fraction, which, in turn, will depend on the sample material, thickness, and orientation as well as the scattering geometry).

Especially the improvements in SNR, as well as in spatial resolution, open exciting new possibilities for EMCD that may soon lead to an even broader applicability of this exciting technique for material science.

Acknowledgements

The authors gratefully acknowledge access to the USTEM computational facilities, as well as fruitful discussions with Peter Schattschneider.

Funding

The Austrian Science Fund (FWF) (J3732-N27).

References

1. Hébert C, and Schattschneider P (2003) A proposal for dichroic experiments in the electron microscope. *Ultramicroscopy* 96 (3–4): 463–468. doi:10.1016/S0304-3991(03)00108-6.
2. Schattschneider P, Rubino S, Hebert C, Rusz J, Kunes J, Novák P, Carlino E, Fabrizioli M, Panaccione G, and Rossi G (2006) Detection of magnetic circular dichroism using a transmission electron microscope. *Nature* 441: 486–488. doi:10.1038/nature04778.
3. Eyidi D, Hébert C, and Schattschneider P (2006) Short note on parallel illumination in the TEM. *Ultramicroscopy* 106 (11–12): 1144–1149. doi:10.1016/j.ultramic.2006.04.029.
4. Lidbaum H, Rusz J, Rubino S, Liebig A, Hjörvarsson B, Oppeneer P M, Eriksson O, and Leifer K (2010) Reciprocal and real space maps for EMCD experiments. *Ultramicroscopy* 110 (11): 1380–1389. doi:10.1016/j.ultramic.2010.07.004.
5. Stöger-Pollach M, Treiber C, Resch G, Keays D, and Ennen I (2011) EMCD real space maps of magnetospirillum magnetotacticum. *Micron* 42 (5): 456–460. doi:10.1016/j.micron.2011.01.003.
6. Schattschneider P, Ennen I, Stöger-Pollach M, Verbeeck J, Mauchamp V, and Jaouen M (2010) Real space maps of magnetic moments on the atomic scale: theory and feasibility. *Ultramicroscopy* 110 (8): 1038–1041. doi:10.1016/j.ultramic.2009.11.020.
7. Schattschneider P, Ennen I, Löffler S, Stöger-Pollach M, and Verbeeck J (2010) Circular dichroism in the electron microscope: progress and applications (invited). *J. Appl. Phys.* 107 (9): 09D311. doi:10.1063/1.3365517.
8. Schattschneider P, Verbeeck J, Mauchamp V, Jaouen M, and Hamon A-L (2010) Real-space simulations of spin-polarized electronic transitions in iron. *Phys. Rev. B* 82: 144418. doi:10.1103/PhysRevB.82.144418.
9. Schattschneider P, Schaffer B, Ennen I, and Verbeeck J (2012) Mapping spin-polarized transitions with atomic resolution. *Phys. Rev. B* 85: 134422. doi:10.1103/PhysRevB.85.134422.
10. Rusz J, Muto S, Spiegelberg J, Adam R, Tatsumi K, Bürgler D E, Oppeneer P M, and Schneider C M (2016) Magnetic measurements with atomic-plane resolution. *Nat. Commun.* 7: 12672. doi:10.1038/ncomms12672.
11. Verbeeck J, Tian H, and Schattschneider P (2010) Production and application of electron vortex beams. *Nature* 467 (7313): 301–304. doi:10.1038/nature09366.
12. Pohl D, Schneider S, Rusz J, and Rellinghaus B (2015) Electron vortex beams prepared by a spiral aperture with the goal to measure EMCD on ferromagnetic films via STEM. *Ultramicroscopy* 150: 16–22. doi:10.1016/j.ultramic.2014.11.025.
13. Rusz J, Bhowmick S, Eriksson M, and Karlsson N (2014) Scattering of electron vortex beams on a magnetic crystal: Towards atomic-resolution magnetic measurements. *Phys. Rev. B* 89: 134428. doi:10.1103/PhysRevB.89.134428.
14. Rusz J, Idrobo J-C, and Bhowmick S (2014) Achieving atomic resolution magnetic dichroism by controlling the phase symmetry of an electron probe. *Phys. Rev. Lett.* 113: 145501. doi:10.1103/PhysRevLett.113.145501.
15. Idrobo J C, Rusz J, Spiegelberg J, McGuire M A, Symons C T, Vatsavai R R, Cantoni C, and Lupini A R (2016) Detecting magnetic ordering with atomic size electron probes. *Adv. Struct. Chem. Imaging* 2 (1): 5. doi:10.1186/s40679-016-0019-9.
16. Rusz J, and Bhowmick S (2013) Boundaries for efficient use of electron vortex beams to measure magnetic properties. *Phys. Rev. Lett.* 111: 105504. doi:10.1103/PhysRevLett.111.105504.
17. Schattschneider P, Löffler S, Stöger-Pollach M, and Verbeeck J (2014) Is magnetic chiral dichroism feasible with electron vortices? *Ultramicroscopy* 136: 81–85. doi:10.1016/j.ultramic.2013.07.012.
18. Warot-Fonrose B, Houdellier F, Hÿtch M, Calmels L, Serin V, and Snoeck E (2008) Mapping inelastic intensities in diffraction patterns of magnetic samples using the energy spectrum imaging technique. *Ultramicroscopy* 108 (5): 393–398. doi:10.1016/j.ultramic.2007.05.013.
19. Schattschneider P, Hébert C, Rubino S, Stöger-Pollach M, Rusz J, and Novák P (2008) Magnetic circular dichroism in EELS: towards 10 nm resolution. *Ultramicroscopy* 108 (5): 433–438. doi:10.1016/j.ultramic.2007.07.002.
20. Schattschneider P, Stöger-Pollach M, Rubino S, Sperl M, Hurm C, Zweck J, and Rusz J (2008) Detection of magnetic circular dichroism on the two-nanometer scale. *Phys. Rev. B* 78 (10): 104413. doi:10.1103/PhysRevB.78.104413.
21. Salafranca J, Gazquez J, Pérez N, Labarta A, Pantelides S T, Pennycook S J, Batlle X, and Varela M (2012) Surfactant organic molecules restore magnetism in metal-oxide nanoparticle surfaces. *Nano. Lett.* 12 (5): 2499–2503. doi:10.1021/nl300665z.
22. Thersleff T, Rusz J, Rubino S, Hjörvarsson B, Ito Y, Zaluzec N J, and Leifer K (2015) Quantitative analysis of magnetic spin and orbital moments from an oxidized iron (1 1 0) surface using electron magnetic circular dichroism. *Sci. Rep.* 5: 13012. doi:10.1038/srep13012.
23. Song D, Ma L, Zhou S, and Zhu J (2015) Oxygen deficiency induced deterioration in microstructure and magnetic properties at $Y_3Fe_5O_{12}$/Pt interface. *Appl. Phys. Lett.* 107 (4): 042401. doi:10.1063/1.4927551.
24. Thersleff T, Rusz J, Hjörvarsson B, and Leifer K (2016) Detection of magnetic circular dichroism with subnanometer convergent electron beams. *Phys. Rev. B* 94 (13): 134430. doi:10.1103/PhysRevB.94.134430.
25. Verbeeck J, Hébert C, Rubino S, Novák P, Rusz J, Houdellier F, Gatel C, and Schattschneider P (2008) Optimal aperture sizes and positions for EMCD experiments. *Ultramicroscopy* 108 (9): 865–872. doi:10.1016/j.ultramic.2008.02.007.
26. Rusz J, and Idrobo J C (2016) Aberrated electron probes for magnetic spectroscopy with atomic resolution: theory and practical aspects. *Phys. Rev. B* 93: 104420. doi:10.1103/PhysRevB.93.104420.
27. Schattschneider P, Nelhiebel M, Souchay H, and Jouffrey B (2000) The physical significance of the mixed dynamic form factor. *Micron* 31 (4): 333–345. doi:10.1016/S0968-4328(99)00112-2.
28. Löffler S, Motsch V, and Schattschneider P (2013) A pure state decomposition approach of the mixed dynamic form factor for mapping atomic orbitals. *Ultramicroscopy* 131: 39–45. doi:10.1016/j.ultramic.2013.03.021.
29. Löffler S, and Schattschneider P (2012) Transition probability functions for applications of inelastic electron scattering. *Micron* 43 (9): 971–977. doi:10.1016/j.micron.2012.03.020.

30. Kirkland E J (1998) *Advanced computing in electron microscopy*, (Plenum Press, New York).
31. Hébert C, Schattschneider P, Rubino S, Novak P, Rusz J, and Stöger-Pollach M (2008) Magnetic circular dichroism in electron energy loss spectrometry. *Ultramicroscopy* 108 (3): 277–284. doi:10.1016/j.ultramic.2007.07.011.
32. Rusz J, Rubino S, and Schattschneider P (2007) First-principles theory of chiral dichroism in electron microscopy applied to 3d ferromagnets. *Phys. Rev. B* 75 (21): 214425. doi:10.1103/PhysRevB.75.214425.
33. Ennen I, Löffler S, Kübel C, Wang D, Auge A, Hütten A, and Schattschneider P (2012) Site-specific chirality in magnetic transitions. *J. Magn. Magn. Mater.* 324 (18): 2723–2726. doi:10.1016/j.jmmm.2012.03.050.
34. Rusz J, Eriksson O, Novák P, and Oppeneer P M (2007) Sum rules for electron energy loss near edge spectra. *Phys. Rev. B* 76 (6): 060408. doi:10.1103/PhysRevB.76.060408.
35. Lidbaum H, Rusz J, Liebig A, Hjörvarsson B, Oppeneer P M, Coronel E, Eriksson O, and Leifer K (2009) Quantitative magnetic information from reciprocal space maps in transmission electron microscopy. *Phys. Rev. Lett.* 102: 037201. doi:10.1103/PhysRevLett.102.037201.
36. Wang Z, Zhong X, Yu R, Cheng Z, and Zhu J (2013) Quantitative experimental determination of site-specific magnetic structures by transmitted electrons. *Nat. Commun.* 4 (1): 1395. doi:10.1038/ncomms2323.
37. Nelder J A, and Mead R (1965) A simplex method for function minimization. *Comput. J.* 7 (4): 308–313. doi:10.1093/comjnl/7.4.308.
38. Schattschneider P, Rubino S, Stöger-Pollach M, Hébert C, Rusz J, Calmels L, and Snoeck E (2008) Energy loss magnetic chiral dichroism: A new technique for the study of magnetic properties in the electron microscope (invited). *J. Appl. Phys.* 103 (7): 07D931. doi:10.1063/1.2836680.
39. Löffler S, and Schattschneider P (2010) A software package for the simulation of energy-loss magnetic chiral dichroism. *Ultramicroscopy* 110 (7): 831–835. doi:10.1016/j.ultramic.2010.02.044.
40. Rusz J, Oppeneer P, Lidbaum H, Rubino S, and Leifer K (2010) Asymmetry of the two-beam geometry in EMCD experiments. *J. Microsc.* 237 (3): 465–468. doi:10.1111/j.1365-2818.2009.03295.x.
41. Song D, Wang Z, and Zhu J (2015) Effect of the asymmetry of dynamical electron diffraction on intensity of acquired EMCD signals. *Ultramicroscopy* 148: 42–51. doi:10.1016/j.ultramic.2014.08.012.
42. Muto S, Tatsumi K, and Rusz J (2013) Parameter-free extraction of EMCD from an energy-filtered diffraction datacube using multivariate curve resolution. *Ultramicroscopy* 125 (0): 89–96. doi:10.1016/j.ultramic.2012.09.008.
43. Egerton R F (1996) *Electron Energy-Loss Spectroscopy in the Electron Microscope*, 2nd edn, (Plenum Press, New York).
44. Schattschneider P, Verbeeck J, and Hamon A (2009) Real space maps of atomic transitions. *Ultramicroscopy* 109 (7): 781–787. doi:10.1016/j.ultramic.2009.01.016.
45. Verbeeck J, Schattschneider P, Lazar S, Stöger-Pollach M, Löffler S, Steiger-Thirsfeld A, and Van Tendeloo G (2011) Atomic scale electron vortices for nanoresearch. *Appl. Phys. Lett.* 99 (20): 203109. doi:10.1063/1.3662012.
46. Xin H L, and Zheng H (2012) On-column 2p bound state with topological charge ±1 excited by an atomic-size vortex beam in an aberration-corrected scanning transmission electron microscope. *Microsc. Microanal.* 18: 711–719. doi:10.1017/S1431927612000499.
47. Löffler S, Schattschneider P (2012) Elastic propagation of fast electron vortices through crystals. *Acta Crystallogr. A* 68(4): 443–447. doi:10.1107/S0108767312013189.

Chapter 8

Exploiting the Acceleration Voltage Dependence of EMCD

S. Löffler, M. Stöger-Pollach, A. Steiger-Thirsfeld, W. Hetaba, and P. Schattschneider

Materials 14 (2021) 1314
10.3390/ma14051314

materials MDPI

Article

Exploiting the Acceleration Voltage Dependence of EMCD

Stefan Löffler [1,*], Michael Stöger-Pollach [1], Andreas Steiger-Thirsfeld [1], Walid Hetaba [2] and Peter Schattschneider [1,3]

[1] University Service Centre for Transmission Electron Microscopy, TU Wien, Wiedner Hauptstraße 8-10/E057-02, 1040 Wien, Austria; michael.stoeger-pollach@tuwien.ac.at (M.S.-P.); andreas.steiger-thirsfeld@tuwien.ac.at (A.S.-T.); peter.schattschneider@tuwien.ac.at (P.S.)
[2] Max Planck Institute for Chemical Energy Conversion, Stiftstraße 34-36, 45470 Mülheim an der Ruhr, Germany; hetaba@fhi-berlin.mpg.de
[3] Institute of Solid State Physics, TU Wien, Wiedner Hauptstraße 8-10/E138-03, 1040 Wien, Austria
* Correspondence: stefan.loeffler@tuwien.ac.at

Abstract: Energy-loss magnetic chiral dichroism (EMCD) is a versatile method for measuring magnetism down to the atomic scale in transmission electron microscopy (TEM). As the magnetic signal is encoded in the phase of the electron wave, any process distorting this characteristic phase is detrimental for EMCD. For example, elastic scattering gives rise to a complex thickness dependence of the signal. Since the details of elastic scattering depend on the electron's energy, EMCD strongly depends on the acceleration voltage. Here, we quantitatively investigate this dependence in detail, using a combination of theory, numerical simulations, and experimental data. Our formulas enable scientists to optimize the acceleration voltage when performing EMCD experiments.

Keywords: EMCD; TEM; EELS; magnetism; acceleration voltage

check for updates

Citation: Löffler, S.; Stöger-Pollach, M.; Steiger-Thirsfeld, A.; Hetaba, W.; Schattschneider, P. Exploiting the Acceleration Voltage Dependence of EMCD. *Materials* **2021**, *14*, 1314. https://doi.org/10.3390/ma14051314

Academic Editors: Lucia Nasi and Matteo Ferroni

Received: 18 December 2020
Accepted: 26 February 2021
Published: 9 March 2021

1. Introduction

Circular dichroism in X-ray Absorption Spectroscopy (XAS) probes the chirality of the scatterer, related either to a helical arrangement of atoms or to spin polarized transitions as studied in X-ray Magnetic Circular Dichroism (XMCD). Before the new millenium, it was considered impossible to see such chirality in electron energy-loss spectrometry (EELS). On the other hand, the formal equivalence between the polarization vector in XAS and the scattering vector in EELS tells us that any effect observable in XAS should have its counterpart in EELS. For instance, anisotropy in XAS corresponds to anisotropy of the double differential scattering cross section (DDSCS) in EELS. A well known example is the directional prevalence of either $s \to \pi^*$ and $s \to \sigma^*$ transitions in the carbon K-edge of graphite, depending on the direction of the scattering vector [1,2].

In XMCD, the polarization vector is helical—a superposition of two linear polarization vectors $\mathbf{e}_x \pm i\mathbf{e}_y$ orthogonal to each other—resembling a left- and right-handed helical photon, respectively. However, what is the counterpart of photon helicity in EELS?

In 2002, one of the authors and their postdoc speculated about what the counterpart of photon helicity could be in EELS—an arcane issue at the time. This led to a keen proposal to study spin polarized transitions in the electron microscope [3]. Closer inspection revealed that in EELS, a superposition of two scattering vectors orthogonal to each other with a relative phase shift of $\pm\pi/2$ is needed, exactly as the formal similarity with XMCD dictated. This, in turn, called for a scattering geometry that exploits the coherence terms in the DDSCS [4,5]. These insights led to the CHIRALTEM project [6].

The multidisciplinary team elaborated the appropriate geometry for the analysis of ionization edges in the spirit of XMCD. The first EELS spectrum was published in 2006 [7]. In that paper, the new method was baptized EMCD—Electron (Energy Loss) Magnetic Chiral Dichroism—in analogy to XMCD. The term "chiral" was deliberately chosen instead of "circular" because the chirality of electronic transitions was to be detected, and because there is no circular polarization in EELS. The experiment confirmed that the physics behind EMCD is very similar to the physics of XMCD. Rapid progress followed: consolidation of the theory [8,9], optimization of experimental parameters [10], dedicated simulation software [11,12], and spatial resolution approaching the nm [13,14] and the atomic scale [15–23].

A genuine feature of EMCD is the ability to probe selected crystallographic sites [18,24], e.g., in Heusler alloys [25], ferrimagnetic spinels [26], or perovskites [27,28]. The high spatial resolution of the method allows the study of nanoparticles [14], 3d–4f coupling in superlattices [29], specimens with stochastically oriented crystallites and even of amorphous materials [30]. EMCD has also been used to investigate spin polarization of non-magnetic atoms in dilute magnetic semiconductors [31], magnetic order breakdown in MnAs [32], GMR of mixed phases [33] and magnetotactic bacteria [34]. A key experiment on magnetite, exploiting the combination of atomic resolution in STEM with the site specificity showed the antiferromagnetic coupling of adjacent Fe atoms directly in real space [16]. An overview of EMCD treating many aspects of anisotropy and chirality in EELS can be found in [35].

To date, EMCD measurements have predominantly been performed at the highest available acceleration voltages—typically 200 keV to 300 keV—which has several advantages such as better resolution, a larger inelastic mean free path, and optimal detector performance resulting in a reasonable signal-to-noise ratio. However, by limiting oneself to a specific acceleration voltage and hence electron energy, EMCD cannot be used to its full potential.

One example where choosing a lower acceleration voltage can be tremendously helpful is the reduction or avoidance of beam damage [36–39]. Another is the investigation of the magnetization dependence: in a TEM, the sample is placed inside the objective lens with a typical field strength of the order of 2 T for 200 keV electrons. By changing the acceleration voltage, the objective lens field applied at the sample position is changed as well [40], thereby enabling magnetization-dependent investigations. This can even be used to drive magnetic field induced phase transitions [27]. Moreover, EMCD is strongly affected by elastic scattering, and, hence, thickness and sample orientation [8,11,25,41]. Therefore, changing the electron energy and therefore the details of the elastic scattering processes enables EMCD measurements even at a thickness and orientation where no significant EMCD effect is observable at a high acceleration voltage. This proposition is corroborated by early numerical simulations [42], which to our knowledge have not been followed up on or widely adopted by the community.

2. Results

2.1. Theory

The general formula governing EMCD has already been outlined in the original publications theoretically predicting the effect and demonstrating it experimentally [3,7]. Detailed ab initio studies soon followed [8]. However, those formulations all aimed at very high accuracy; none of them gave a simple, closed form to quickly calculate the EMCD effect and easily see the influence parameters such as, e.g., the acceleration voltage have on the outcome. Recently, Schneider et al. [41] published such a formula; however, they neglected any elastic scattering the beam can undergo after an inelastic scattering event by approximating the outgoing wave by a simple plane wave.

Here, we present a derivation of a simple formula taking into account elastic scattering both before and after the inelastic scattering event. In the process, we will make four major assumptions:

1. We limit the derivation to an incident three-beam and outgoing two-beam case in the zero-order Laue zone of a sample that is single-crystalline in the probed region with a centro-symmetric crystal structure;
2. We assume that the sample is a slab of thickness t with an entrance and an exit plane essentially perpendicular to the beam propagation axis;
3. We assume that the inelastic scattering process is at least four-fold rotationally symmetric around the optical axis and that the characteristic momentum transfer q_e is

much smaller than the chosen reciprocal lattice distance $|\boldsymbol{G}|$. This implies that the inelastic scattering in the chosen geometry is only dependent on the scattering atom's spin-state, but not influenced significantly by any anisotropic crystal field;

4. We assume that the atoms of the investigated species are homogeneously distributed along the beam propagation axis and that $\boldsymbol{G} \cdot \boldsymbol{x} = 2m\pi, m \in \mathbb{Z}$ for all atom positions $\boldsymbol{x}$ and the chosen lattice vector $\boldsymbol{G}$.

Assumption 1 comes from the conventional EMCD setup: the (crystalline) sample is tilted into systematic row condition and the detector is placed on (or close to) the Thales circle between neighboring diffraction spots. In a symmetric systematic row condition, the strongest diffraction spots are the central one (**0**) and the two diffraction spots at $-\boldsymbol{G}, \boldsymbol{G}$, which have the same intensity. Any higher-order diffraction spots are comparatively weak and will therefore be neglected.

To understand the reason behind the outgoing two-beam case, we follow the reciprocity theorem [43,44]. A (point-like) detector in reciprocal space detects exact plane-wave components. If we trace those back to the exit plane of the sample, we can expand them into Bloch waves. For the typical EMCD detector positions, they correspond exactly to the Bloch waves we get in a two-beam case (where the Laue circle center is positioned somewhere along the bisector of the line from **0** to $\boldsymbol{G}$.

The probability of measuring a particular state $|\psi_{\text{out}}\rangle$ (a "click" in the detector corresponding to a plane wave at the exit plane of the sample) given a certain incident state $|\psi_{\text{in}}\rangle$ (a plane wave incident on the entry plane of the sample) is given by Fermi's Golden rule [45–49]:

$$p = \sum_{I,F} p_I(1-p_F) \langle\psi_{\text{out}}| \langle F|\hat{V}|I\rangle |\psi_{\text{in}}\rangle \langle\psi_{\text{in}}| \langle I|\hat{V}^\dagger|F\rangle |\psi_{\text{out}}\rangle \, \delta(E_F - E_I - E), \tag{1}$$

where I, F run over all initial and final states of the sample, p_I, p_F are their respective occupation probabilities, E_I, E_F are their respective energies, E is the EELS energy loss, and $\hat{V}$ is the transition operator. In momentum representation, $\hat{V}$ for a single atom is given by

$$\langle\tilde{\boldsymbol{k}}|\hat{V}|\boldsymbol{k}\rangle = \frac{\mathrm{e}^{\mathrm{i}\boldsymbol{q}\cdot\hat{\boldsymbol{R}}}}{q^2} \quad \text{with} \quad \boldsymbol{q} = \boldsymbol{k} - \tilde{\boldsymbol{k}}. \tag{2}$$

With the mixed dynamic form factor (MDFF) [45,49–51],

$$S(\boldsymbol{q}, \boldsymbol{q}', E) = \sum_{I,F} p_I(1-p_F) \langle\tilde{\boldsymbol{k}}| \langle F|\mathrm{e}^{\mathrm{i}\boldsymbol{q}\cdot\hat{\boldsymbol{R}}}|I\rangle |\boldsymbol{k}\rangle \langle\boldsymbol{k}'| \langle I|\mathrm{e}^{-\mathrm{i}\boldsymbol{q}'\cdot\hat{\boldsymbol{R}}}|F\rangle |\tilde{\boldsymbol{k}}'\rangle \, \delta(E_F - E_I - E), \tag{3}$$

the probability for a "click" in the detector can be written as [8,45,48–50]

$$p = \iiiint \sum_{\boldsymbol{x}} \mathrm{e}^{\mathrm{i}(\boldsymbol{q}-\boldsymbol{q}')\cdot\boldsymbol{x}} \psi_{\text{out}}(\tilde{\boldsymbol{k}})^* \psi_{\text{out}}(\tilde{\boldsymbol{k}}') \frac{S(\boldsymbol{q}, \boldsymbol{q}', E)}{q^2 q'^2} \psi_{\text{in}}(\boldsymbol{k}) \psi_{\text{in}}(\boldsymbol{k}')^* \mathrm{d}\boldsymbol{k} \mathrm{d}\boldsymbol{k}' \mathrm{d}\tilde{\boldsymbol{k}} \mathrm{d}\tilde{\boldsymbol{k}}', \tag{4}$$

where the $\sum_{\boldsymbol{x}} e^{\mathrm{i}(\boldsymbol{q}-\boldsymbol{q}')\cdot\boldsymbol{x}}$ stems from the summation over all atoms (of the investigated species) in the sample and the MDFF is taken to be the MDFF of a single such atom located at the origin.

Specific expressions for the MDFF for various models under different conditions and approximations are well known (see, e.g., [7,49,52]), but their details will be irrelevant for the majority of our derivation for which we will keep the general expression $S(\boldsymbol{q}, \boldsymbol{q}', E)$.

Using the Bloch wave formalism [8,36,53–55], the three-beam incident wavefunction and the two-beam outgoing wave function can be written as

$$|\psi_{\text{in}}\rangle = \sum_{j\in\{1,2,3\}} \sum_{\boldsymbol{g}\in\{-\boldsymbol{G},\boldsymbol{0},\boldsymbol{G}\}} C^*_{j,\boldsymbol{0}} C_{j,\boldsymbol{g}} |\boldsymbol{\chi} + \gamma_j \boldsymbol{n} + \boldsymbol{g}\rangle \tag{5}$$

$$|\psi_{\text{out}}\rangle = \sum_{l\in\{1,2\}} \sum_{\boldsymbol{h}\in\{\boldsymbol{0},\boldsymbol{G}\}} \tilde{C}^*_{l,\boldsymbol{0}} \mathrm{e}^{-\mathrm{i}\tilde{\gamma}_l t} \tilde{C}_{l,\boldsymbol{h}} |\tilde{\boldsymbol{\chi}} + \tilde{\gamma}_l \tilde{\boldsymbol{n}} + \boldsymbol{h}\rangle, \tag{6}$$

where j, l are the Bloch wave indices, $\boldsymbol{g}, \boldsymbol{h}$ run over the diffraction spots, the $C_{j,g}$ are the Bloch wave coefficients, the γ_j are the so-called anpassung, $\boldsymbol{n}$ is the surface normal vector, t is the sample thickness, and $\chi, \tilde{\chi}$ are the wave vectors of the incident and outgoing plane waves, respectively.

The derivation of the EMCD effect can be found in Appendix A. The final expression is

$$\eta = \frac{A \sin^2(\kappa t) - B \sin^2(\kappa' t)}{t + C \sin(2\kappa t)} \cdot \frac{\Im[S(\boldsymbol{q}_1, \boldsymbol{q}_2, E)]}{S(\boldsymbol{q}_1, \boldsymbol{q}_1, E)}, \tag{7}$$

where t is the sample thickness and the coefficients A, B, C, κ, κ' are defined in Equation (A18) (with Equations (A1) and (A3)).

Figure 1 shows a comparison of the thickness dependence predicted by Equation (7) and a full simulation based on Equation (4) for some typical, simple magnetic samples. Owing to the approximations made in the derivation, there naturally are some small differences (which are more pronounced at small thicknesses), but they are well within typical experimental uncertainties.

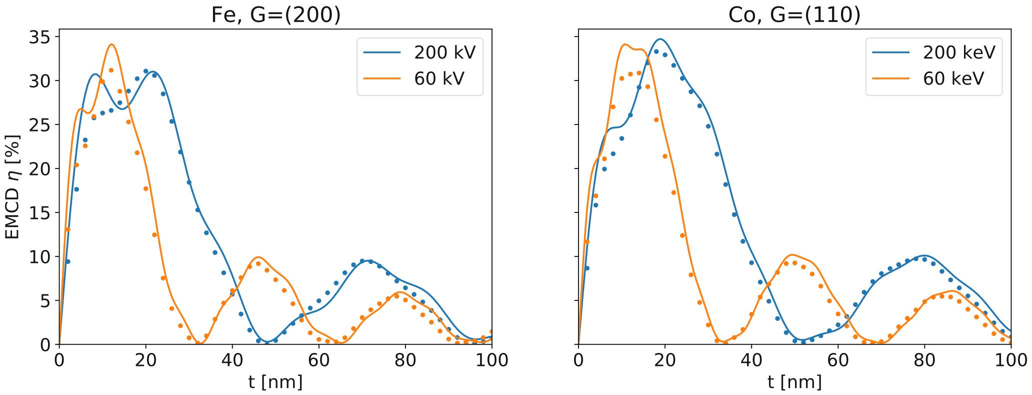

Figure 1. Comparison of the thickness dependence of the EMCD effect η predicted by Equation (7) (solid lines) and by the "bw" software using Equation (4) (dotted lines) for different acceleration voltages for bcc Fe and hcp Co.

Two main conclusions about the thickness-variation of the EMCD effect can be drawn from Equation (7). On the one hand, the numerator nicely shows the oscillatory nature of the effect. On the other hand, the denominantor clearly implies that the strength of the EMCD effect decreases approximately as $1/t$.

The numerator is composed of two oscillations with different amplitudes (A, B) and the frequencies

$$\kappa = \frac{\gamma_1 - \gamma_2}{2} = \frac{\sqrt{(|\boldsymbol{G}|^2 - U_{2G})^2 + 8U_G^2}}{4\chi \cdot \boldsymbol{n}} \quad \text{and} \quad \kappa' = \frac{\tilde{\gamma}_1 - \tilde{\gamma}_2}{2} = \frac{U_G}{2\tilde{\chi} \cdot \tilde{\boldsymbol{n}}} \tag{8}$$

which are closely related to the extinction distances for the incident and outgoing beams. As the wavevectors $\chi, \tilde{\chi}$ scale with the square root of the acceleration voltage $\sqrt{V}$, the frequencies of the oscillations of the EMCD effect scale with $1/\sqrt{V}$. This is corroborated by Figure 2.

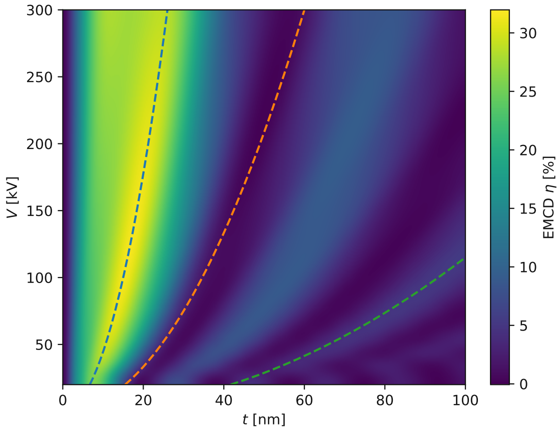

Figure 2. EMCD effect η for various acceleration voltages V and thicknesses t for bcc Fe as simulated with "bw". The dashed lines show (arbitrary) curves with $t \propto \sqrt{V}$ as guides for the eye.

Both the oscillations and the $1/t$ decay can be understood from the fact that EMCD is essentially an interferometry experiment. As such, it crucially depends on the relative phases of the different density matrix components after traversing the sample from the scattering center to the exit plane. Some scattering centers are positioned in a way that the resulting components contribute positively to the EMCD effect, other scattering centers are positioned such that their contribution to the EMCD effect is negative. As a result, there are alternating "bands" of atoms contributing positively and negatively [11], where the size of the bands is related to the extinction length. With increasing thickness, more and more alternating bands appear—the non-magnetic signal increases linearly with t, but the magnetic EMCD signal of all but one band averages out, ultimately resulting in a $1/t$ behavior of the relative EMCD effect.

Our theoretical results have several important implications. First, the EMCD effect can indeed be recorded at a wide variety of acceleration voltages as already proposed on numerical grounds in [42], thereby enabling magnetization-dependent measurements. Second, the thickness dependence scales with $1/t$, thus necessitating thin samples. Third, for a given sample thickness in the region of interest, a candidate for the optimal high tension yielding the maximal EMCD effect can easily be identified based on any existing simulation and the $\sqrt{V}$ scaling behavior (note, however, that other effects such as multiple plasmon scattering can put further constraints on the useful range of sample thicknesses, particularly at very low voltages).

2.2. Experiments

To corroborate our theoretical finding, we performed experiments at various high tensions to compare to the simulations. The experiments were performed on a ferrimagnetic magnetite (Fe_3O_4) sample [56], which has the advantage over pure Fe that it is unaffected by oxidation (it may, however, be partially reduced to Wüstite by prolonged ion or electron irradiation). The individual recorded spectra are shown in Figure 3. It is clearly visible that the EMCD effect changes with the high tension as predicted in Section 2.1. A quantitative comparison between the calculations and the experiments is shown in Figure 4 and shows excellent agreement.

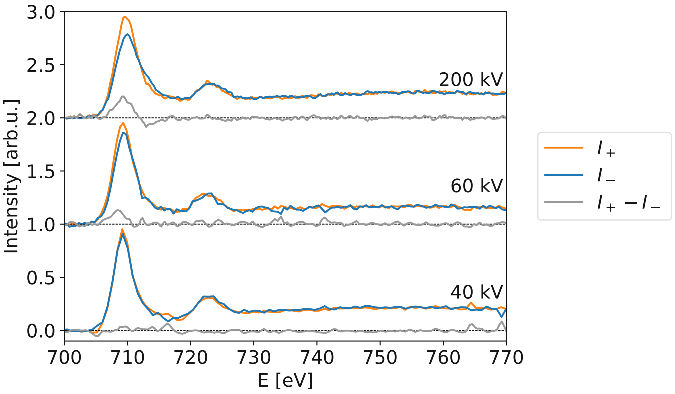

Figure 3. EMCD spectra for different acceleration voltages (as indicated) after background subtraction and post-edge normalization using the Fe L-edge in Magnetite tilted to a $(4\,0\,0)$ systematic row condition. The sample-thickness was determined to be $t \approx 35\,\mathrm{nm}$ for the 40 kV and 60 kV measurement positions and $t \approx 45\,\mathrm{nm}$ for the 200 kV measurement position.

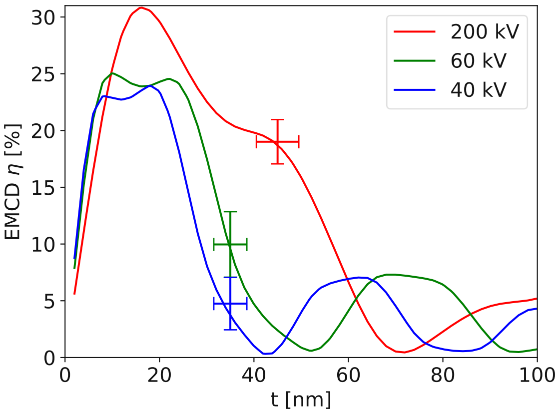

Figure 4. Comparison between numerical EMCD simulations ("bw", solid curves) and experiments (points) for Magnetite for three different acceleration voltages. For the experimental points, η was calculated from the data in Figure 3 according to Equation (9), the measured thickness values are given in the caption of Figure 3, and the error bars were determined as described in [57,58].

3. Discussion

Although Equation (7) is—to our knowledge—the first complete, analytical, closed form predicting the EMCD effect, several assumptions and approximations were made in its derivation. As such it is no replacement for full simulations with sophisticated software packages if ultimate accuracy is vital. Nevertheless, it can be a good starting point for EMCD investigations, and it helps elucidating the underlying physical principles and understanding the effects the experimental parameters have on EMCD. In this section, we will discuss the limits of the theoretical derivation based on the approximations made.

Assumption one deals with the scattering geometry and the crystal structure. The incident three-beam and outgoing two-beam case is the simplest approximation taking into account elastic scattering both before and after an inelastic scattering event. Adding more beams to the calculation can, of course, improve the results somewhat. However, the effect was found to be very small and well within typical experimental uncertainties [11], owing primarily to the $1/q^2 q'^2$ term in Equation (4) (any additional beams would give rise to much longer $\boldsymbol{q}$ vectors). The crystal structure was assumed to be centro-symmetric, resulting in $U_{\boldsymbol{G}} = U_{-\boldsymbol{G}}$. While this limits the applicability of the formula to relatively simple crystals, very complex, non-symmetric crystals will likely violate some of the other assumptions as well. In addition, the constraints implied by centro-symmetry are necessary in the first place to arrive at a reasonably simple final formula.

Assumption two requires the sample's surface to be essentially perpendicular to the beam direction. This requirement is necessary to avoid complex phase factors down the line. A small tilt of up to a few degrees is not expected to cause any major issues, and larger tilts of $\gtrsim$45 °C are not recommended (and often not even possible) in practice anyway.

Assumption three requires the inelastic scattering process to be invariant under rotations around the optical axis by integer multiples of 90°. Strong anisotropy would lead to a distinct directional dependence of the MDFF [48,59,60], thereby making it impossible to reason about the intensities at the various detector positions. In such cases, however, the classical EMCD setup would fail to properly measure the magnetic properties anyway. In addition, assumption three states $q_e \ll |\boldsymbol{G}|$, which implies $\Im[S(\boldsymbol{q}_1, \boldsymbol{q}_2, E)] \ll \Re[S(\boldsymbol{q}_1, \boldsymbol{q}_2, E)]$ in dipole approximation [11,61]. This is fulfilled reasonably well for typical EMCD experiments (for example, for Fe $(2\,0\,0)$, $|\boldsymbol{G}| \approx 7\,\mathrm{nm}^{-1}$; for the Fe L-edge, $q_e \approx 0.8\,\mathrm{nm}^{-1}$ at 200 keV and $q_e \approx 1.5\,\mathrm{nm}^{-1}$ at 40 keV).

Assumption four requires the investigated atoms to be distributed homogeneously and fulfill the condition $\boldsymbol{G} \cdot \boldsymbol{x} = 2m\pi$. The homogeneity requirement excludes involved situations such as multi-layer systems and ultimately allows to replace the sum over all atoms by an integral over the sample thickness. In practice, homogeneity is facilitated by tilting into a systematic row condition and probing a large area of the sample, as a large probed volume and a (small) tilt mean that some atoms can be found in each of the investigated lattice planes at any depth z.

The condition $\boldsymbol{G} \cdot \boldsymbol{x} = 2m\pi\ \forall \boldsymbol{x}$ is perhaps the most severe limitation as it implies that all atoms fall exactly onto one of the probed set of lattice planes. This excludes, e.g., $\boldsymbol{G} = (1\,0\,0)$ for Fe (which is forbidden anyway), or $\boldsymbol{G} = (1\,0\,0)$ for Co, as for these, only some (for Fe) or none (for Co) of the atoms fulfill the condition. The reason for requiring $\boldsymbol{G} \cdot \boldsymbol{x} = 2m\pi$ is that it implies that phase factors of the form $\exp(\mathrm{i}\boldsymbol{G} \cdot \boldsymbol{x})$ are all 1. If that is not the case, different phases have to be applied to different components, thereby reducing the EMCD effect [41]. Hence, choosing a $\boldsymbol{G}$ vector not fulfilling the condition is unfavorable anyway.

As can be seen from Figure 1, Equation (7) reproduces sophisticated numerical simulations quite well for reasonably simple samples despite all approximations. The strongest deviations can be found for small t, as can be expected. For larger sample thicknesses and, consequently, many atoms, small differences that might arise for individual atoms tend to average out.

4. Materials and Methods

The numerical simulations were performed using the "bw" code [11], a software package for calculating EELS data based on Bloch waves and the MDFF. The crystal structure data for magnetite was taken from [62], all other crystallographic data was taken from the EMS program (version 4.5430U2017) [63].

The wedge-shaped magnetite sample was prepared by a FEI Quanta 200 3D DBFIB (FEI Company, Hillsboro, OR, USA) from a high-quality, natural single crystal purchased from SurfaceNet GmbH (Rheine, Germany) [64] and subsequently thinned and cleaned using a Technoorg Linda Gentlemill.

The EMCD measurements were performed on a FEI Tecnai T20 (FEI Company, Hillsboro, OR, USA) equipped with a $\mathrm{LaB_6}$ gun and a Gatan GIF 2001 spectrometer (Gatan Inc., Pleasanton, CA, USA). The system has an energy resolution (full width at half maximum) of 1.1 eV at 200 kV which improves down to 0.3 eV at 20 kV [65]. First, a suitable sample position with a sample thickness around 40 nm and an easily recognizable, distinctly-shaped feature nearby was found and the sample was oriented in systematic row condition including the $(4\,0\,0)$ diffraction spot (see Figure 5). At each high tension, the instrument was carefully aligned, the sample position was readjusted, the EMCD experiment was performed, and a thickness measurement was taken. Both the convergence and the collection semi-angle were approximately 3 mrad [58].

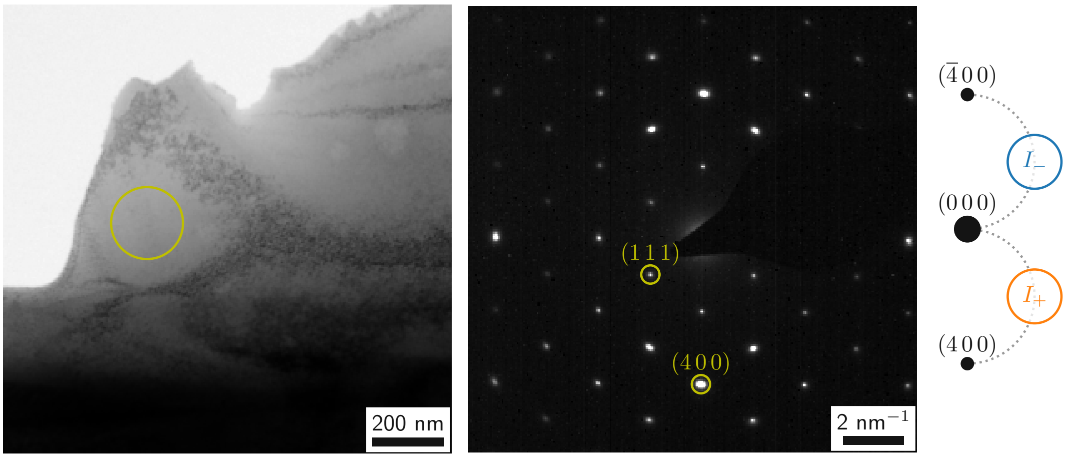

Figure 5. TEM bright-field overview image (**left**), corresponding diffraction pattern in $(0\,1\,\bar{1})$ zone axis (**middle**) and schematic of the EMCD measurement positions in systematic row condition (**right**). The sample position used for the EMCD experiments is marked by a yellow circle in the bright-field image, the positions for I_+ and I_- are marked by the orange and blue circles. Both the image and the diffraction pattern were recorded at 200 kV. Note that the weak, kinematically forbidden $(2\,0\,0)$ reflections can be attributed to double diffraction [36] in the thicker part of the sample visible at the bottom of the bright-field image; they are negligible in the thin part of the sample used for the EMCD measurements.

For data analysis, all spectra were background-subtracted using a pre-edge power-law fit and normalized in the post-edge region. The EMCD effect was calculated based on the L_3-edge maxima according to the formula [9,58]

$$\eta = \frac{I_+ - I_-}{\frac{I_+ + I_-}{2}}. \tag{9}$$

The errors were estimated as described in [57,58].

5. Conclusions

In this work, we have derived an analytical formula for predicting the EMCD effect, taking into account elastic scattering both before and after inelastic scattering events. This formula not only helps elucidate the physics underlying EMCD, it also allows to directly predict the influence of various parameters on the EMCD effect. In particular, we have focused on the acceleration voltage V and on the thickness t. We showed that the periodicity of the EMCD effect scales with $\sqrt{V}$, while its total intensity decreases as $1/t$. In addition, we have performed experiments at different acceleration voltages to corroborate these predictions. Our results will not only help to optimize the EMCD effect for a given sample thickness by tuning the high tension accordingly, it will also pave the way for magnetization-dependent measurements by employing different magnetic fields in the objective lens at different acceleration voltages.

Author Contributions: Conceptualization, S.L., P.S.; methodology, S.L., M.S.-P., W.H., P.S.; software, S.L.; formal analysis, S.L.; investigation, S.L., M.S.-P.; resources, A.S.-T., W.H.; data curation, S.L.; writing—original draft preparation, S.L., P.S.; writing—review and editing, M.S.-P., A.S.-T., W.H.;

visualization, S.L.; supervision, P.S.; project administration, S.L., P.S.; funding acquisition, S.L., P.S. All authors have read and agreed to the published version of the manuscript.

Funding: This research was funded by the Austrian Science Fund (FWF) under grant numbers I4309-N36 and P29687-N36.

Institutional Review Board Statement: Not applicable.

Informed Consent Statement: Not applicable.

Data Availability Statement: Data is contained within the article.

Conflicts of Interest: The authors declare no conflict of interest. The funders had no role in the design of the study; in the collection, analyses, or interpretation of data; in the writing of the manuscript, or in the decision to publish the results.

Abbreviations

The following abbreviations are used in this manuscript:

DDSCS	Double-differential scattering cross-Section
EMCD	Energy-loss magnetic chiral dichroism
EELS	Electron energy-loss spectrometry
MDFF	Mixed dynamic form factor
TEM	Transmission electron microscopy
XAS	X-ray absorption spectroscopy
XMCD	X-ray magnetic circular dichroism

Appendix A. Derivation of the EMCD Effect

In the following, we will extensively use the abbreviations

$$\alpha = \frac{U_G}{2\chi \cdot \boldsymbol{n}} \qquad \tilde{\alpha} = \frac{U_G}{2\tilde{\chi} \cdot \tilde{\boldsymbol{n}}} \tag{A1}$$

$$V = \frac{U_{2G} - |\boldsymbol{G}|^2}{2U_G} \tag{A2}$$

$$W = \frac{\sqrt{(|\boldsymbol{G}|^2 - U_{2G})^2 + 8U_G^2}}{2U_G} = \sqrt{V^2 + 2}, \tag{A3}$$

where the U_g are the Fourier coefficients of the crystal potential $V(\boldsymbol{r}) = \frac{h^2}{2me} \sum_g U_g e^{2\pi i \boldsymbol{g} \cdot \boldsymbol{r}}$ with Planck's constant h, electron mass m and elementary charge e. We note in passing that in the present case, $U_G = U_G^* = U_{-G}$.

With these abbreviations and the assumptions mentioned above, the Bloch wave parameters can be calculated analytically and take the form

$$\begin{array}{lll}
\gamma_1 = \alpha(V+W) & \gamma_2 = \alpha(V-W) & \gamma_3 = -\alpha \cdot \dfrac{|\boldsymbol{G}|^2 + U_{2G}}{U_G} \\
C_{1,-G} = \dfrac{1}{\sqrt{|V-W|^2+2}} & C_{2,-G} = \dfrac{1}{\sqrt{|V+W|^2+2}} & C_{3,-G} = -\dfrac{1}{\sqrt{2}} \\
C_{1,0} = -\dfrac{V-W}{\sqrt{|V-W|^2+2}} & C_{2,0} = -\dfrac{V+W}{\sqrt{|V+W|^2+2}} & C_{3,0} = 0 \\
C_{1,G} = \dfrac{1}{\sqrt{|V-W|^2+2}} & C_{2,G} = \dfrac{1}{\sqrt{|V+W|^2+2}} & C_{3,G} = \dfrac{1}{\sqrt{2}}
\end{array} \tag{A4}$$

for $|\psi_{\text{in}}\rangle$ and

$$\begin{array}{ll}
\tilde{\gamma}_1 = \tilde{\alpha} & \tilde{\gamma}_2 = -\tilde{\alpha} \\
\tilde{C}_{1,0} = \dfrac{1}{\sqrt{2}} & \tilde{C}_{2,0} = \dfrac{1}{\sqrt{2}} \\
\tilde{C}_{1,G} = \dfrac{1}{\sqrt{2}} & \tilde{C}_{2,G} = -\dfrac{1}{\sqrt{2}}
\end{array} \tag{A5}$$

for $|\psi_{\mathrm{out}}\rangle$.

Inserting Equations (5) and (6) into Equation (4), evaluating the integrals, collecting all terms with the same Bloch wave index, and neglecting the weak dependence of $S(\boldsymbol{q},\boldsymbol{q}',E)/(q^2q'^2)$ on j,j',l,l' [8,41,55] yields

$$p = \sum_{\boldsymbol{x}} \sum_{\boldsymbol{g},\boldsymbol{g}',\boldsymbol{h},\boldsymbol{h}'} D_{\boldsymbol{g}} D^*_{\boldsymbol{g}'} \tilde{D}^*_{\boldsymbol{h}} \tilde{D}_{\boldsymbol{h}'} \mathrm{e}^{\mathrm{i}(\boldsymbol{g}-\boldsymbol{g}'-\boldsymbol{h}+\boldsymbol{h}')\cdot\boldsymbol{x}} \frac{S(\boldsymbol{q},\boldsymbol{q}',E)}{q^2q'^2} \tag{A6}$$

with

$$D_{\boldsymbol{g}} = \sum_j C^*_{j,\boldsymbol{0}} C_{j,\boldsymbol{g}} \mathrm{e}^{\mathrm{i}\gamma_j \boldsymbol{n}\cdot\boldsymbol{x}} \qquad \tilde{D}_{\boldsymbol{g}} = \sum_l \tilde{C}^*_{l,\boldsymbol{0}} \mathrm{e}^{-\mathrm{i}\tilde{\gamma}_l t} \tilde{C}_{l,\boldsymbol{h}} \mathrm{e}^{\mathrm{i}\tilde{\gamma}_j \tilde{\boldsymbol{n}}\cdot\boldsymbol{x}} \tag{A7}$$

and

$$\boldsymbol{q} = \Delta\boldsymbol{\chi} + \boldsymbol{g} - \boldsymbol{h} \qquad \boldsymbol{q}' = \Delta\boldsymbol{\chi} + \boldsymbol{g}' - \boldsymbol{h}' \qquad \Delta\boldsymbol{\chi} = \boldsymbol{\chi} - \tilde{\boldsymbol{\chi}}. \tag{A8}$$

Direct summation results in

$$\begin{aligned} D_{-\boldsymbol{G}} = D_{\boldsymbol{G}} &= \frac{\mathrm{i}}{W} \mathrm{e}^{\mathrm{i}\alpha V \boldsymbol{n}\cdot\boldsymbol{x}} \sin(\alpha W \boldsymbol{n}\cdot\boldsymbol{x}) \\ D_{\boldsymbol{0}} &= \mathrm{e}^{\mathrm{i}\alpha V \boldsymbol{n}\cdot\boldsymbol{x}} \left[\cos(\alpha W \boldsymbol{n}\cdot\boldsymbol{x}) - \frac{\mathrm{i}V}{W}\sin(\alpha W \boldsymbol{n}\cdot\boldsymbol{x})\right] \\ \tilde{D}_{\boldsymbol{0}} &= \cos(\tilde{\alpha}(\tilde{\boldsymbol{n}}\cdot\boldsymbol{x} - t)) \\ \tilde{D}_{\boldsymbol{G}} &= \mathrm{i}\sin(\tilde{\alpha}(\tilde{\boldsymbol{n}}\cdot\boldsymbol{x} - t)). \end{aligned} \tag{A9}$$

Performing the complete sums over $\boldsymbol{g},\boldsymbol{g}',\boldsymbol{h},\boldsymbol{h}'$ in Equation (A6) produces very many terms, some of which are very small. This can be understood from the fact that $\Delta\boldsymbol{\chi}\cdot\boldsymbol{G} = \pm G/2$ in the chosen setup. Therefore, $\Delta\boldsymbol{\chi}$ and $\Delta\boldsymbol{\chi} - \boldsymbol{G}$ have the same magnitude, whereas $\Delta\boldsymbol{\chi} + \boldsymbol{G}$ and $\Delta\boldsymbol{\chi} - 2\boldsymbol{G}$ are significantly larger. Owing to the $1/q^2q'^2$ term, large $\boldsymbol{q}$ are strongly suppressed. Hence, only the combinations $\boldsymbol{g} - \boldsymbol{h} = \boldsymbol{0}$ and $\boldsymbol{g} - \boldsymbol{h} = -\boldsymbol{G}$ are retained (the same applies to the primed versions as well). Hence, we end up with two distinct $\boldsymbol{q}$ vectors, namely

$$\boldsymbol{q}_1 = \Delta\boldsymbol{\chi} \quad \text{and} \quad \boldsymbol{q}_2 = \Delta\boldsymbol{\chi} - \boldsymbol{G}. \tag{A10}$$

Note that, due to the symmetry of the setup $q_1 = |\boldsymbol{q}_1| = |\boldsymbol{q}_2| = q_2$.

Using $S(\boldsymbol{q},\boldsymbol{q}',E) = S(\boldsymbol{q}',\boldsymbol{q},E)^*$ [45], Equation (A6) now takes the form

$$\begin{aligned} p = \frac{1}{q_1^4} \sum_{\boldsymbol{x}} \Big[& \left|D_{\boldsymbol{0}}\tilde{D}^*_{\boldsymbol{0}} + D_{\boldsymbol{G}}\tilde{D}^*_{\boldsymbol{G}}\right|^2 S(\boldsymbol{q}_1,\boldsymbol{q}_1,E) + \\ & \left|D_{-\boldsymbol{G}}\tilde{D}^*_{\boldsymbol{0}} + D_{\boldsymbol{0}}\tilde{D}^*_{\boldsymbol{G}}\right|^2 S(\boldsymbol{q}_2,\boldsymbol{q}_2,E) + \\ & 2\Re\left[\left(D_{\boldsymbol{0}}\tilde{D}^*_{\boldsymbol{0}} + D_{\boldsymbol{G}}\tilde{D}^*_{\boldsymbol{G}}\right)\left(D^*_{-\boldsymbol{G}}\tilde{D}_{\boldsymbol{0}} + D^*_{\boldsymbol{0}}\tilde{D}_{\boldsymbol{G}}\right)\mathrm{e}^{\mathrm{i}\boldsymbol{G}\cdot\boldsymbol{x}} S(\boldsymbol{q}_1,\boldsymbol{q}_2,E)\right]\Big] \\ = \frac{1}{q_1^4} \big[& A_{11} S(\boldsymbol{q}_1,\boldsymbol{q}_1,E) + A_{22} S(\boldsymbol{q}_2,\boldsymbol{q}_2,E) + 2\Re[A_{12} S(\boldsymbol{q}_1,\boldsymbol{q}_2,E)]\big] \\ = \frac{1}{q_1^4} \big[& (A_{11} + A_{22}) S(\boldsymbol{q}_1,\boldsymbol{q}_1,E) + 2\Re[A_{12} S(\boldsymbol{q}_1,\boldsymbol{q}_2,E)]\big]. \end{aligned} \tag{A11}$$

In the last line, the four-fold rotational symmetry was used, i.e., $S(\boldsymbol{q}_1,\boldsymbol{q}_1,E) = S(\boldsymbol{q}_2,\boldsymbol{q}_2,E)$ since $\boldsymbol{q}_2 = \hat{C}_4[\boldsymbol{q}_1]$ with $\hat{C}_4$ as the operator performing a 90° rotation around the optical axis.

To calculate the probability for a "click" in the detector at the second EMCD position, we have to replace $\boldsymbol{q}_1 \mapsto \hat{C}_4^3[\boldsymbol{q}_1] = \hat{C}_4^2[\boldsymbol{q}_2]$ and $\boldsymbol{q}_2 \mapsto \hat{C}_4[\boldsymbol{q}_2] = \hat{C}_4^2[\boldsymbol{q}_1]$. Owing to the assumed rotational symmetry of the MDFF, this replacement results in $S(\hat{C}_4^2[\boldsymbol{q}_2],\hat{C}_4^2[\boldsymbol{q}_1],E) = S(\boldsymbol{q}_2,\boldsymbol{q}_1,E) = S(\boldsymbol{q}_1,\boldsymbol{q}_2,E)^*$ and hence

$$p' = \frac{1}{q_1^4}[(A_{11} + A_{22}) S(\boldsymbol{q}_1,\boldsymbol{q}_1,E) + 2\Re[A_{12} S(\boldsymbol{q}_1,\boldsymbol{q}_2,E)^*]]. \tag{A12}$$

Thus, the quotient EMCD effect is

$$\eta = 2\cdot\frac{p-p'}{p+p'} = 2\cdot\frac{-2\Im[A_{12}]\Im[S(\boldsymbol{q}_1,\boldsymbol{q}_2,E)]}{(A_{11}+A_{22})S(\boldsymbol{q}_1,\boldsymbol{q}_1,E)+2\Re[A_{12}]\Re[S(\boldsymbol{q}_1,\boldsymbol{q}_2,E)]} \tag{A13}$$

Assuming that the scattering vectors were chosen such that $S(\boldsymbol{q}_1,\boldsymbol{q}_2,E)$ is purely imaginary (technically, (in dipole approximation) this occurs slightly inside the Thales circle where $q_y^2 = G^2/4 - q_e^2$; as $q_e \ll G$ in typical EMCD experiments, the real part of $S(\boldsymbol{q}_1,\boldsymbol{q}_2,E)$, which is of the order q_e^2, can be neglected compared to $S(\boldsymbol{q}_1,\boldsymbol{q}_1,E)$, which is of the order of $G^2/2$), this can be simplified further to

$$= -4\cdot\frac{\Im[A_{12}]}{A_{11}+A_{22}}\cdot\frac{\Im[S(\boldsymbol{q}_1,\boldsymbol{q}_2,E)]}{S(\boldsymbol{q}_1,\boldsymbol{q}_1,E)}. \tag{A14}$$

The coefficients can be calculated directly as

$$\begin{aligned}
A_{11}+A_{22} &= \sum_{\boldsymbol{x}}\left[1-\frac{1}{W^2}\sin^2(\alpha W\boldsymbol{n}\cdot\boldsymbol{x})\right]\\
\Im[A_{12}] &= \sum_{\boldsymbol{x}}\frac{1}{2}\left[\left(1-\frac{3}{W^2}\sin^2(\alpha W\boldsymbol{n}\cdot\boldsymbol{x})\right)\sin(2\tilde{\alpha}(\tilde{\boldsymbol{n}}\cdot\boldsymbol{x}-t))\right.\\
&\qquad\left.-\frac{1}{W}\sin(2\alpha W\boldsymbol{n}\cdot\boldsymbol{x})\cos(2\tilde{\alpha}(\tilde{\boldsymbol{n}}\cdot\boldsymbol{x}-t))\right].
\end{aligned} \tag{A15}$$

with the assumptions 2 and 4, the dot products can be evaluated and the sums can be replaced by integrals over z, yielding

$$\begin{aligned}
A_{11}+A_{22} &= t\left(1-\frac{1}{2W^2}\right)+\frac{\sin(2tW\alpha)}{4W^3\alpha}\\
\Im[A_{12}] &= \frac{1}{4(W^2\alpha^2-\tilde{\alpha}^2)}\left[-\left(2\alpha+\frac{3\tilde{\alpha}}{W^2}\right)\sin^2(\alpha Wt)\right.\\
&\qquad\left.+\left(\frac{(3-2W^2)\alpha^2}{\tilde{\alpha}}+2(\alpha+\tilde{\alpha})\right)\sin^2(\tilde{\alpha}t)\right]
\end{aligned} \tag{A16}$$

Hence the full formula for the EMCD effect reads

$$\begin{aligned}
\eta &= \frac{4W^3\alpha}{(W^2\alpha^2-\tilde{\alpha}^2)}\frac{\left[\left(2\alpha+\frac{3\tilde{\alpha}}{W^2}\right)\sin^2(\alpha Wt)-\left(\frac{(3-2W^2)\alpha^2}{\tilde{\alpha}}+2(\alpha+\tilde{\alpha})\right)\sin^2(\tilde{\alpha}t)\right]}{2W(2W^2-1)\alpha t+\sin(2tW\alpha)}\cdot\frac{\Im[S(\boldsymbol{q}_1,\boldsymbol{q}_2,E)]}{S(\boldsymbol{q}_1,\boldsymbol{q}_1,E)}\\
&= \frac{A\sin^2(\kappa t)-B\sin^2(\kappa' t)}{t+C\sin(2\kappa t)}\cdot\frac{\Im[S(\boldsymbol{q}_1,\boldsymbol{q}_2,E)]}{S(\boldsymbol{q}_1,\boldsymbol{q}_1,E)}
\end{aligned} \tag{A17}$$

with

$$\begin{aligned}
A &= C\cdot\frac{4\kappa\kappa'}{\kappa^2-\kappa'^2}\left(2W\frac{\kappa}{\kappa'}+3\right)\\
B &= C\cdot\frac{4\kappa\kappa'}{\kappa^2-\kappa'^2}\left(2W\frac{\kappa}{\kappa'}+\frac{3\kappa^2}{\kappa'^2}+2W^2\left(1-\frac{\kappa^2}{\kappa'^2}\right)\right)\\
C &= \frac{1}{2\kappa(2W^2-1)}\\
\kappa &= \alpha W = \frac{\gamma_1-\gamma_2}{2}\\
\kappa' &= \tilde{\alpha} = \frac{\tilde{\gamma}_1-\tilde{\gamma}_2}{2}.
\end{aligned} \tag{A18}$$

References

1. Botton, G. A new approach to study bonding anisotropy with EELS. *J. Electron Spectrosc. Relat. Phenom.* **2005**, *143*, 129–137. [CrossRef]
2. Schattschneider, P.; Hébert, C.; Franco, H.; Jouffrey, B. Anisotropic relativistic cross sections for inelastic electron scattering, and the magic angle. *Phys. Rev. B* **2005**, *72*, 045142. [CrossRef]
3. Hébert, C.; Schattschneider, P. A proposal for dichroic experiments in the electron microscope. *Ultramicroscopy* **2003**, *96*, 463–468. [CrossRef]
4. Schattschneider, P.; Jouffrey, B. Channeling, localization and the density matrix in inelastic electron scattering. *Ultramicroscopy* **2003**, *96*, 453–462. [CrossRef]
5. Schattschneider, P.; Werner, W. Coherence in electron energy loss spectrometry. *J. Electron Spectrosc. Relat. Phenom.* **2005**, *143*, 81–95. [CrossRef]
6. CHIRALTEM. Available online: https://cordis.europa.eu/project/id/508971 (accessed on 9 of February, 2021).
7. Schattschneider, P.; Rubino, S.; Hebert, C.; Rusz, J.; Kunes, J.; Novák, P.; Carlino, E.; Fabrizioli, M.; Panaccione, G.; Rossi, G. Detection of magnetic circular dichroism using a transmission electron microscope. *Nature* **2006**, *441*, 486–488. [CrossRef]
8. Rusz, J.; Rubino, S.; Schattschneider, P. First-principles theory of chiral dichroism in electron microscopy applied to 3d ferromagnets. *Phys. Rev. B* **2007**, *75*, 214425. [CrossRef]
9. Hébert, C.; Schattschneider, P.; Rubino, S.; Novak, P.; Rusz, J.; Stöger-Pollach, M. Magnetic circular dichroism in electron energy loss spectrometry. *Ultramicroscopy* **2008**, *108*, 277–284. [CrossRef]
10. Verbeeck, J.; Hébert, C.; Rubino, S.; Novák, P.; Rusz, J.; Houdellier, F.; Gatel, C.; Schattschneider, P. Optimal aperture sizes and positions for EMCD experiments. *Ultramicroscopy* **2008**, *108*, 865–872. [CrossRef] [PubMed]
11. Löffler, S.; Schattschneider, P. A software package for the simulation of energy-loss magnetic chiral dichroism. *Ultramicroscopy* **2010**, *110*, 831–835. [CrossRef] [PubMed]
12. Rusz, J. Modified automatic term selection v2: A faster algorithm to calculate inelastic scattering cross-sections. *Ultramicroscopy* **2017**, *177*, 20–25. [CrossRef]
13. Schattschneider, P.; Stöger-Pollach, M.; Rubino, S.; Sperl, M.; Hurm, C.; Zweck, J.; Rusz, J. Detection of magnetic circular dichroism on the two-nanometer scale. *Phys. Rev. B* **2008**, *78*, 104413. [CrossRef]
14. Schneider, S.; Pohl, D.; Löffler, S.; Rusz, J.; Kasinathan, D.; Schattschneider, P.; Schultz, L.; Rellinghaus, B. Magnetic properties of single nanomagnets: Electron energy-loss magnetic chiral dichroism on FePt nanoparticles. *Ultramicroscopy* **2016**, *171*, 186–194. [CrossRef]
15. Verbeeck, J.; Schattschneider, P.; Lazar, S.; Stöger-Pollach, M.; Löffler, S.; Steiger-Thirsfeld, A.; Van Tendeloo, G. Atomic scale electron vortices for nanoresearch. *Appl. Phys. Lett.* **2011**, *99*, 203109. [CrossRef]
16. Schattschneider, P.; Schaffer, B.; Ennen, I.; Verbeeck, J. Mapping spin-polarized transitions with atomic resolution. *Phys. Rev. B* **2012**, *85*, 134422. [CrossRef]
17. Schachinger, T.; Löffler, S.; Steiger-Thirsfeld, A.; Stöger-Pollach, M.; Schneider, S.; Pohl, D.; Rellinghaus, B.; Schattschneider, P. EMCD with an electron vortex filter: Limitations and possibilities. *Ultramicroscopy* **2017**, *179*, 15–23. [CrossRef]
18. Rusz, J.; Muto, S.; Spiegelberg, J.; Adam, R.; Tatsumi, K.; Bürgler, D.E.; Oppeneer, P.M.; Schneider, C.M. Magnetic measurements with atomic-plane resolution. *Nat. Commun.* **2016**, *7*, 12672. [CrossRef]
19. Warot-Fonrose, B.; Houdellier, F.; Hÿtch, M.; Calmels, L.; Serin, V.; Snoeck, E. Mapping inelastic intensities in diffraction patterns of magnetic samples using the energy spectrum imaging technique. *Ultramicroscopy* **2008**, *108*, 393–398. [CrossRef]
20. Salafranca, J.; Gazquez, J.; Pérez, N.; Labarta, A.; Pantelides, S.T.; Pennycook, S.J.; Batlle, X.; Varela, M. Surfactant Organic Molecules Restore Magnetism in Metal-Oxide Nanoparticle Surfaces. *Nano Lett.* **2012**, *12*, 2499–2503. [CrossRef]
21. Thersleff, T.; Rusz, J.; Rubino, S.; Hjörvarsson, B.; Ito, Y.; Zaluzec, N.J.; Leifer, K. Quantitative analysis of magnetic spin and orbital moments from an oxidized iron (1 1 0) surface using electron magnetic circular dichroism. *Sci. Rep.* **2015**, *5*, 13012. [CrossRef]
22. Song, D.; Ma, L.; Zhou, S.; Zhu, J. Oxygen deficiency induced deterioration in microstructure and magnetic properties at $Y_3Fe_5O_{12}$/Pt interface. *Appl. Phys. Lett.* **2015**, *107*, 042401. [CrossRef]
23. Wang, Z.; Tavabi, A.H.; Jin, L.; Rusz, J.; Tyutyunnikov, D.; Jiang, H.; Moritomo, Y.; Mayer, J.; Dunin-Borkowski, R.E.; Yu, R.; et al. Atomic scale imaging of magnetic circular dichroism by achromatic electron microscopy. *Nature Materials* **2018**, *17*, 221–225. [CrossRef]
24. Wang, Z.; Zhong, X.; Yu, R.; Cheng, Z.; Zhu, J. Quantitative experimental determination of site-specific magnetic structures by transmitted electrons. *Nat. Commun.* **2013**, *4*, 1395. [CrossRef]
25. Ennen, I.; Löffler, S.; Kübel, C.; Wang, D.; Auge, A.; Hütten, A.; Schattschneider, P. Site-specific chirality in magnetic transitions. *J. Magn. Magn. Mater.* **2012**, *324*, 2723–2726. [CrossRef]
26. Loukya, B.; Negi, D.S.; Dileep, K.; Pachauri, N.; Gupta, A.; Datta, R. Effect of Bloch wave electron propagation and momentum-resolved signal detection on the quantitative and site-specific electron magnetic chiral dichroism of magnetic spinel oxide thin films. *Phys. Rev. B Condens. Matter Mater. Phys.* **2015**, *91*, 134412. [CrossRef]
27. Wallisch, W.; Stöger-Pollach, M.; Navickas, E. Consequences of the CMR effect on EELS in TEM. *Ultramicroscopy* **2017**, *179*, 84–89. [CrossRef]

28. Wang, Z.C.; Zhong, X.Y.; Jin, L.; Chen, X.F.; Moritomo, Y.; Mayer, J. Effects of dynamic diffraction conditions on magnetic parameter determination in a double perovskite Sr_2FeMoO_6 using electron energy-loss magnetic chiral dichroism. *Ultramicroscopy* **2017**, *176*, 212–217. [CrossRef]
29. Fu, X.; Warot-Fonrose, B.; Arras, R.; Dumesnil, K.; Serin, V. Quantitative moment study and coupling of 4f rare earth and 3d metal by transmitted electrons. *Phys. Rev. B* **2016**, *94*, 140416. [CrossRef]
30. Lin, J.; Zhong, X.Y.; Song, C.; Rusz, J.; Kocevski, V.; Xin, H.L.; Cui, B.; Han, L.L.; Lin, R.Q.; Chen, X.F.; Zhu, J. Detection of magnetic circular dichroism in amorphous materials utilizing a single-crystalline overlayer. *Phys. Rev. Mater.* **2017**, *1*, 071404. [CrossRef]
31. He, M.; He, X.; Lin, L.; Song, B.; Zhang, Z.H. Study on spin polarization of non-magnetic atom in diluted magnetic semiconductor: The case of Al-doped 4H-SiC. *Solid State Commun.* **2014**, *197*, 44–48. [CrossRef]
32. Fu, X.; Warot-Fonrose, B.; Arras, R.; Seine, G.; Demaille, D.; Eddrief, M.; Etgens, V.; Serin, V. In situ observation of ferromagnetic order breaking in MnAs/GaAs(001) and magnetocrystalline anisotropy of α-MnAs by electron magnetic chiral dichroism. *Phys. Rev. B* **2016**, *93*, 104410. [CrossRef]
33. Chen, X.; Higashikozono, S.; Ito, K.; Jin, L.; Ho, P..; Yu, C..; Tai, N..; Mayer, J.; Dunin-Borkowski, R.E.; Suemasu, T.; Zhong, X. Nanoscale measurement of giant saturation magnetization in α''-$Fe_{16}N_2$ by electron energy-loss magnetic chiral dichroism. *Ultramicroscopy* **2019**, *203*, 37–43. [CrossRef] [PubMed]
34. Stöger-Pollach, M.; Treiber, C.D.; Resch, G.P.; Keays, D.A.; Ennen, I. EMCD real space maps of Magnetospirillum magnetotacticum. *Micron* **2011**, *42*, 456–460. [CrossRef] [PubMed]
35. Schattschneider, P., Ed. *Linear and Chiral Dichroism in the Electron Microscope*; Pan Stanford Publishing Pte Ltd.: Singapore, 2011.
36. Williams, D.B.; Carter, C.B. *Transmission Electron Microscopy*; Plenum Press: New York, NY, USA, 1996.
37. Egerton, R.; Li, P.; Malac, M. Radiation damage in the TEM and SEM. *Micron* **2004**, *35*, 399–409. [CrossRef] [PubMed]
38. Egerton, R. Control of radiation damage in the TEM. *Ultramicroscopy* **2013**, *127*, 100–108. [CrossRef] [PubMed]
39. Jiang, N. Electron beam damage in oxides: A review. *Rep. Prog. Phys.* **2015**, *79*, 016501. [CrossRef] [PubMed]
40. Hurm, C. Towards an Unambiguous Electron Magnetic Chiral Dichroism (EMCD) Measurement in a Transmission Electron Microscope (TEM). Ph.D. Thesis, Universität Regensburg, Regensburg, Germany, 2008.
41. Schneider, S.; Negi, D.; Stolt, M.J.; Jin, S.; Spiegelberg, J.; Pohl, D.; Rellinghaus, B.; Goennenwein, S.T.B.; Nielsch, K.; Rusz, J. Simple method for optimization of classical electron magnetic circular dichroism measurements: The role of structure factor and extinction distances. *Phys. Rev. Mater.* **2018**, *2*, 113801. [CrossRef]
42. Rusz, J.; Novák, P.; Rubino, S.; Hébert, C.; Schattschneider, P. Magnetic Circular Dichroism in Electron Microscopy. *Acta Phys. Pol. A* **2008**, *113*, 599–644. [CrossRef]
43. Pogany, A.P.; Turner, P.S. Reciprocity in electron diffraction and microscopy. *Acta Cryst. A* **1968**, *24*, 103–109. [CrossRef]
44. Findlay, S.; Schattschneider, P.; Allen, L. Imaging using inelastically scattered electrons in CTEM and STEM geometry. *Ultramicroscopy* **2007**, *108*, 58–67. [CrossRef]
45. Kohl, H.; Rose, H. Theory of Image Formation by Inelastically Scattered Electrons in the Electron Microscope. *Adv. Electron. Electron Phys.* **1985**, *65*, 173–227. [CrossRef]
46. Schattschneider, P. *Fundamentals of Inelastic Electron Scattering*; Springer Wien: New York, NY, USA, 1986.
47. Nelhiebel, M. Effects of Crystal Orientation and Interferometry in Electron Energy Loss Spectroscopy. Ph.D. Thesis, École Centrale Paris, Châtenay-Malabry, France, 1999.
48. Löffler, S.; Motsch, V.; Schattschneider, P. A pure state decomposition approach of the mixed dynamic form factor for mapping atomic orbitals. *Ultramicroscopy* **2013**, *131*, 39–45. . [CrossRef]
49. Löffler, S. Study of Real Space Wave Functions with Electron Energy Loss Spectrometry. Ph.D. Thesis, TU Wien, Vienna, Austria, 2013.
50. Schattschneider, P.; Nelhiebel, M.; Jouffrey, B. Density matrix of inelastically scattered fast electrons. *Phys. Rev. B* **1999**, *59*, 10959–10969. [CrossRef]
51. Schattschneider, P.; Nelhiebel, M.; Souchay, H.; Jouffrey, B. The physical significance of the mixed dynamic form factor. *Micron* **2000**, *31*, 333–345. [CrossRef]
52. Schattschneider, P.; Ennen, I.; Löffler, S.; Stöger-Pollach, M.; Verbeeck, J. Circular dichroism in the electron microscope: Progress and applications (invited). *J. Appl. Phys.* **2010**, *107*, 09D311. [CrossRef]
53. Stadelmann, P. *Dynamical Theory of Elastic Electron Diffraction at Small Angles*; Technical Report; École Polytechnique Fédérale de Lausanne: Lausanne, Switzerland, 2003.
54. Metherell, A. J., F. Diffraction of Electrons by Perfect Crystals. In *Electron Microscopy in Materials Science*; Valdrè, U.; Ruedl, E., Eds.; Commission of the European Communities: Brussels, Belgium, 1975; Volume 2, pp. 397–552.
55. Schattschneider, P.; Jouffrey, B.; Nelhiebel, M. Dynamical diffraction in electron-energy-loss spectrometry: The independent Bloch-wave model. *Phys. Rev. B* **1996**, *54*, 3861–3868. [CrossRef] [PubMed]
56. Hetaba, W. The Theory and Application of Inelastic Coherence in the Electron Microscope. Ph.D. Thesis, TU Wien, Vienna, Austria 2015.
57. Egerton, R.F. Electron energy-loss spectroscopy in the TEM. *Rep. Prog. Phys.* **2009**, *72*, 016502. [CrossRef]
58. Löffler, S.; Hetaba, W. Convergent-beam EMCD: Benefits, pitfalls and applications. *Microscopy* **2018**, *67*, i60–i71. [CrossRef]

59. Löffler, S.; Bugnet, M.; Gauquelin, N.; Lazar, S.; Assmann, E.; Held, K.; Botton, G.A.; Schattschneider, P. Real-space mapping of electronic orbitals. *Ultramicroscopy* **2017**, *177*, 26–29. [CrossRef]
60. Löffler, S.; Hambach, R.; Kaiser, U.; Schattschneider, P. Symmetry-constraints for mapping electronic states with EELS. **2021**, in preparation.
61. Schattschneider, P.; Hébert, C.; Rubino, S.; Stöger-Pollach, M.; Rusz, J.; Novák, P. Magnetic circular dichroism in EELS: Towards 10 nm resolution. *Ultramicroscopy* **2008**, *108*, 433–438. [CrossRef] [PubMed]
62. Fleet, M.E. The structure of magnetite. *Acta Crystallogr. Sect. B Struct. Crystallogr. Cryst. Chem.* **1981**, *37*, 917–920. [CrossRef]
63. Stadelmann, P. EMS—A software package for electron diffraction analysis and HREM image simulation in materials science. *Ultramicroscopy* **1987**, *21*, 131–145. [CrossRef]
64. SurfaceNet GmbH. Oskar-Schindler-Ring 7, 48432 Rheine, Germany. Available online: https://www.surfacenet.de/ (accessed on 9 of February, 2021).
65. Stöger-Pollach, M. Low voltage TEM: Influences on electron energy loss spectrometry experiments. *Micron* **2010**, *41*, 577–584. [CrossRef]

Part III

Electron Vortices and Beam Shaping

As discussed in part II, EVBs play a crucial role in EMCD. They are characterized by their peculiar phase structure in the plane perpendicular to the direction of propagation. A pure vortex with an OAM of $m\hbar$ is described by the real-space wavefunction

$$\langle \boldsymbol{r}|\psi\rangle = f(r_\perp, z)\mathrm{e}^{\mathrm{i}m\varphi}\mathrm{e}^{\mathrm{i}k_z z}, \tag{21}$$

where $(r_\perp, \varphi, z)$ are the cylindrical coordinates, $f(r_\perp, z)$ describes the evolution of the radial dependence, $\mathrm{e}^{\mathrm{i}m\varphi}$ is the characteristic EVB phase factor, and $\mathrm{e}^{\mathrm{i}k_z z}$ describes the fast-oscillating plane wave part in propagation direction (taken to be the z axis). It can readily be verified that this wavefunction is an eigenstate of the $\hat{L}_z$ operator, namely

$$\hat{L}_z\,|\psi\rangle = m\hbar\,|\psi\rangle\,. \tag{22}$$

In addition to their natural occurrence in EMCD and being eigenfunctions of the OAM operator $\hat{L}_z$, EVBs form an eigenbasis of the free-space Hamiltonian in cylindrical coordinates, and are, thus, of fundamental interest (on par with plane waves (an eigenbasis in Cartesian coordinates) and spherical waves (an eigenbasis in spherical coordinates)). These facts ultimately gave rise to a new field of research focusing directly on the creation, manipulation and analysis of EVBs independently of EMCD [32, 40–50]. Proposed (and partly realized) applications include — apart from EMCD [51–55] — the study of free-electron Landau states [56–59], nanoparticle manipulation [60], crystal chirality measurements [61], the probing of plasmon symmetry [62] as well as detecting dark plasmon modes [63], and even spin-polarization [64, 65].

While the majority of research focuses on EVBs, many other beam shapes have been proposed and demonstrated [66], including Hermite Gauss beams [67], π beams [62, 68], self-accelerating/Airy beams [69, 70], aberration-corrected beams [71, 72], caustics [73], and 3D beam shapes [54, 74], each with its own unique physical properties. Recent work even features first designs for programmable phase manipulators [75–78] which in principle allow to change the beam shape "on-the-fly" during an experiment. However, as EVBs form an eigenbasis of the Hamiltonian, all of these other shapes can, in principle, be described by a coherent superposition of EVBs.

The first step in studying and using EVBs is producing them. Several methods exist for this purpose, from holographic fork masks [32] to phase masks [40, 79, 80] to employing electro-magnetic fields [42, 64]. All of these methods face the same challenges: producing a reproducible, single, intense, pure vortex that ideally is easy to use for the experimenter, "switchable" (between different OAM modes, e.g., between $m = +1$ and $m = -1$), and does not require extensive changes to the microscope. While each method excels at some of the requirements, generally none excels at all of them.

Another, hitherto mostly overlooked possibility for creating EVBs is mode conversion (see fig. 3) as described in detail in chapter 9. EVB creation by mode conversion uses the close relation between Hermite-Gauss (HG) and Laguerre-Gauss (LG) beams, i.e., a relative phase shift of the horizontal component with respect to the vertical one, similar to the relation between linearly and circularly polarized light. In fact, mode conversion was originally proposed and demonstrated for producing optical vortices by

Figure 3.: Schematic principle of the mode converter. A HG beam rotated by 45° (left) enters a lens system comprised of a pair of cylindrical lenses (which can be realized in the TEM as a combination of a round lens and a quadrupole). One component goes through the focus, resulting in a phase shift that can be tuned to produce an LG EVB (right).

means of cylindrical lenses [81, 82]. In a TEM, HG-like beams can be generated, e.g., with very simple phase masks without the need for high-precision mask patterning or adding custom electro-magnetic devices to the TEM [83, 84]. Subsequent mode conversion allows for the creation of a single, pure EVB with high brightness (due to the absence of beam-blocking devices) [83]. The OAM of the EVB produced this way can be switched easily and fast by adjusting the settings of the mode converter. As only the existing TEM lenses are used, the operation of the mode converter should be straight-forward for an experienced TEM operator. The general formalism developed in chapter 9 details how the lenses have to be set up and how they can be tuned to accommodate varying input or output beam sizes requirements.

Apart from EVB production, another crucial, but so far relatively little studied aspect of EVBs is their propagation through and interaction with matter. For crystalline samples, it was shown that the wavefunction of EVBs will generally change as the beam scatters elastically inside the sample [85, 86]. Naturally, this complicates any application of EVBs. Apart from crystalline structures, amorphous areas are frequently observed in TEM as well, be it as samples in their own right, as protective layers at the surface of the sample, or in the form of an (unwanted) damage layer caused, e.g., during sample preparation. For amorphous magnetic samples, EVB-based EMCD is a promising candidate for magnetic characterization on the nanoscale [50]. But also for crystalline regions of interest with (intentional or unintentional) amorphous surface layers, the question how EVBs incident on the sample or produced in the crystal are modified when traversing through the amorphous areas is very important. After all, the incident beam will scatter when propagating through an amorphous layer analogously to the propagation through a crystal. This potentially changes the EVB characteristic of the beam, meaning that the beam reaching an inelastic scattering center may be different from the intended ideal EVB sent into the sample.

In chapter 10, the propagation of EVBs through amorphous samples is studied in detail. For this purpose, I developed a cylindrical multislice algorithm to elucidate OAM transfer during propagation. My numerical simulations for various materials show how the average OAM as well as the OAM spread depend on sample composition, sample thickness, and beam convergence angle. This allows making quantitative predictions of the EVB quality after propagation through a given amorphous layer.

In summary, my work presented in this part made substantial contributions to the field of studying EVBs and, thus, to using them efficiently and routinely in advanced characterization techniques. On the one hand, it contains a detailed description of and recipe for using the mode-conversion for producing single, intense, pure, and switchable EVBs. On the other hand, it improves our understanding of the propagation of EVBs through matter by developing a new formalism for modeling the elastic scattering of EVB in amorphous materials.

Chapter 9

$\pi/2$ mode converters and vortex generators for electrons

C. Kramberger, S. Löffler, T. Schachinger, P. Hartel, J. Zach, and P. Schattschneider

Ultramicroscopy 204 (2019) 27–33
10.1016/j.ultramic.2019.05.003

Ultramicroscopy 204 (2019) 27–33

Contents lists available at ScienceDirect

Ultramicroscopy

journal homepage: www.elsevier.com/locate/ultramic

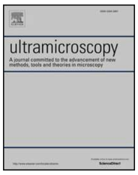

π/2 mode converters and vortex generators for electrons

C. Kramberger[a], S. Löffler[a,b], T. Schachinger[b], P. Hartel[c], J. Zach[c], P. Schattschneider[*,a,b]

[a] Institute of Solid State Physics, TU Wien, Wiedner Hauptstraße 8-10/E138, Wien 1040, Austria
[b] University Service Center for Transmission Electron Microscopy, TU Wien, Wiedner Hauptstraße 8-10/E057-02, Wien 1040, Austria
[c] CEOS Corrected Electron Optical Systems GmbH, Englerstraße 28, Heidelberg 69126, Germany

ARTICLE INFO

Keywords:
Electron microscopy
Vortex beams
Mode conversion
Orbital angular momentum

ABSTRACT

In optics, mode conversion is an elegant way to switch between Hermite Gaussian and Laguerre Gaussian beam profiles and thereby impart orbital angular momentum onto the beam and to create vortices. In optics such vortex beams can be produced in a setup consisting of two identical cylinder lenses. In electron optics, quadrupole lenses can be used for the same purpose. Here we investigate generalized asymmetric designs of a quadrupole mode converter that may be realized within the constraints of existing electron microscopes and can steer the development of dedicated vortex generators for high brilliance electron vortex probes of atomic scale.

1. Introduction

A vortex beam can be characterized by a discontinuity in the phase that dictates a central void in the intensity profile. Further it features a quantized orbital angular momentum (OAM) in units of $\hbar$. The associated magnetic moment and chirality make electron vortex probes sensitive to magnetic excitations and even give them the ability to discriminate chiral crystals [1–3]. The development in the field was propelled by the close analogy to the established methods for optical vortex generation [4–6] as well as their application in helical spectroscopy [7–9]. While light optics has stimulated several methods of electron vortex generation [10–12], electron vortices can also be formed by multipoles [13] or magnetic fields [14,15]. Each of these methods has its own merits and challenges, but none of them offers a pure singular OAM state without the need to block out unwanted portions of the intensity.

Yet one particular optical setup holds the promise to work on the entire beam in high purity, so that there would not be any need to filter out other diffraction orders or spurious unwanted angular states: the π/2 mode converter (MC) [16] converts Hermite Gaussian (HG) beams to corresponding Laguerre Gaussians (LG) ones and *vice versa*. The first order cases are:

$$HG(x, y) \propto 2x \cdot e^{-\frac{x^2+y^2}{w^2}}, \tag{1}$$

$$LG(r, \phi) \propto 2r \cdot e^{-\frac{r^2}{w^2}} \cdot e^{i\phi}. \tag{2}$$

(x, y) and (r, ϕ) are the Cartesian and polar coordinates, respectively. w is the width defining parameter. While two-way LG to HG beam conversion was demonstrated in a proof of principle experiment for electron beams [17], mode matching could not be achieved. Therefore the donut profile was only transient and could not be projected to another plane.

To picture how mode conversion occurs we can replace an incident beam with a straight central phase jump of π (a Hilbert beam) by two sub-waves that possess the same mirror symmetry as vertical and horizontal HG modes. Fig. 1 demonstrates quite generally the essence of mode conversion: The two subwaves propagate independently from the entrance to the exit, where they will have accumulated a relative phase (i.e. Gouy shift) of π/2. Thus their coherent superposition creates an azimuthal 'stair case' phase ramp and a corresponding ring current. The beam has now non-zero OAM.

We propose that the quadrupole lenses in existing aberration correctors can be re-purposed to realize a fully functional π/2 MC. When an incoming beam is prepared with a suitable wavefront pattern, it would be completely transformed into a vortex beam without sacrificing intensity. Switching between left and right handed helical operation would be as stable and reproducible as setting electron lenses. The ability to perform mode conversion on electron beams will doubtlessly also open new avenues in mode sorting [18], especially in conjunction with programmable phase masks [19].

We present an analytical treatment of general asymmetric setups and also run simulations for entire electron optical setups of different π/2 MCs.

---

[*] Corresponding author at: TU Wien, 1040 Wien, Austria.
E-mail addresses: c.kramberger@gmail.com (C. Kramberger), peter.schattschneider@tuwien.ac.at (P. Schattschneider).

https://doi.org/10.1016/j.ultramic.2019.05.003
Received 22 November 2018; Received in revised form 7 May 2019; Accepted 12 May 2019

2. Gaussian mode converters

2.1. The optical π/2 mode converter

We reproduce shortly the principle of the symmetric π/2 MC given in Ref. [16]. The schematic of the setup is illustrated in Fig. 2. There is an astigmatic beam waist located at $z = 0$ and two cylinder lenses at positions $z = -a$ and $z = a$ with a separation of $d = 2a$. The symmetric cylinder lenses have a focal length of f. In light optics with static lenses this separation is the only adjustable degree of freedom in the setup. Apart from the incident Gaussian beam, there are 3 conditions to be fulfilled. The conditions are:

- The widths of Gaussian profile evolve as

$$w(z) = \sqrt{1+\left(\frac{z}{z_r}\right)^2}\cdot\sqrt{\frac{2z_r}{k}}. \tag{3}$$

Here z_r is the Rayleigh range. The wavenumber k and wavelength λ follow $k\lambda = 2\pi$. The widths in the xz and yz cuts must be equal at the exit plane $z = +a$:

$$w_x(a) = w_y(a). \tag{4}$$

- The Gouy phase difference of the xz and yz components accumulated at the second cylinder lens must be π/2. Due to center symmetry this is equivalent to:

$$\tan^{-1}\left(\frac{a}{z_{rx}}\right) - \tan^{-1}\left(\frac{a}{z_{ry}}\right) = \frac{\pi}{4}. \tag{5}$$

- The radii of curvature

$$R(z) = z\left(1+\left(\frac{z_r}{z}\right)^2\right) \tag{6}$$

in the xz and in the yz cuts after the second cylinder lens must fulfill

$$R_{x,z}(a) = R_{y,z}(a) = -R(-a). \tag{7}$$

Eqs. (4) and (5) give immediately

$$z_{rx} = a(\sqrt{2}-1), \quad z_{ry} = a(\sqrt{2}+1). \tag{8}$$

With this result, the widths at the entrance and exit planes follow as:

$$w(-a) = w(a) = \sqrt{\frac{\sqrt{2}\cdot d}{k}}. \tag{9}$$

With Newton's equations,

$$\frac{1}{R_i} = \frac{1}{R_x(-a)} + \frac{1}{f} = \frac{1}{R_y(-a)}, \tag{10}$$

and the previous results for the width Eq. (9) and the Rayleigh ranges Eq. (8), this gives

$$d = \sqrt{2}\cdot f \tag{11}$$

for a symmetric optical π/2 MC.

2.2. The quadrupole π/2 mode converter

The key differences between electron and light optics are that the distances and positions are fixed but the focal lengths can be controlled via lens excitations. Also, quadrupoles (QPs) are widely available. For electrons we thus propose to replace the cylinder lenses with QPs. This has no effect on Eqs. (4) and (5) and hence on the Rayleigh ranges z_R. If the QPs are always focusing the xz component and defocusing the yz component, then Newton's equations read as:

$$\frac{1}{R_i} = \frac{1}{R_x(-a)} + \frac{1}{f} = \frac{1}{R_y(-a)} - \frac{1}{f}. \tag{12}$$

This modifies the relation from Eq. (11) to

$$f = \sqrt{2}\cdot d \tag{13}$$

and the widths at the entrance and exit plane scale accordingly:

$$w(-a) = w(a) = \sqrt{\frac{2\cdot\sqrt{2}\cdot d}{k}}. \tag{14}$$

Notably, the curvatures of the incident and outgoing beam simplifies to

$$R_i = -R_o = -d. \tag{15}$$

Replacing cylinder lenses with QPs simplifies the solutions of the mode matching conditions considerably. The incoming and outgoing curvatures and the quadrupole focusing (or defocusing) are functions of the distance d only, and not of the wavenumber k. Only the beam widths scale with $\sqrt{d/k}$. The actions of round lenses and QPs correspond to two orthogonal Zernike polynomials (Z_2^0 and Z_2^2, respectively), while a cylinder lens is a superposition of the two. QPs are therefore better suited for aligning a π/2 MC.

2.3. The asymmetric π/2 mode converter

If the constraint of equal focal lengths of the two QPs is relaxed, then the beam waists will be at different positions for the xz and yz component. In addition, the incoming and outgoing widths will differ, but the radii of curvature in Eq. (15) are not affected.

If Eqs. (4) and (7) are met, (i.e. the astigmatism is canceled) then the relative Gouy shift Ψ is given by the distance d as well as the QPs focal lengths f_i and f_o.

$$\tan\Psi = \frac{2u}{1-u^2}, \quad u^2 = \frac{f_i f_o}{d^2} - 1. \tag{16}$$

In a properly aligned π/2 MC, Ψ is π/2 and the dimensionless parameter u becomes 1. The conditions read (see supplementary information):

$$f_i\cdot f_o = 2\cdot d^2, \tag{17}$$

$$w_i = \sqrt{\frac{2\cdot f_i}{k}}, \qquad w_o = \sqrt{\frac{2\cdot f_o}{k}}. \tag{18}$$

The proper choice of quadrupole focal lengths Eq. (17) for an incoming beam width w_i according to Eq. (18) allows to achieve $u = 1$ with a magnification of w_o/w_i. A schematic example is sketched in Fig. 3.

2.4. Practical considerations

When it comes to electron optical alignment, the very appealing benefit of the asymmetric π/2 MC design is, that there is only one prior requirement on the non-astigmatic incoming beam. Its curvature has to

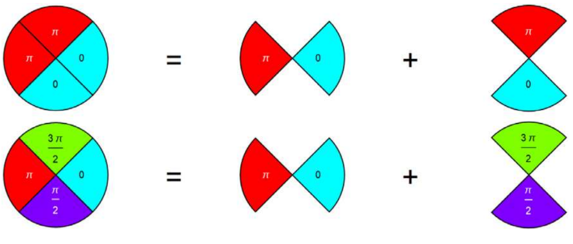

Fig. 1. principle of π/2 mode conversion. The output beam of a Hilbert device can be split into a sum of two HG-like components. Acquiring a Gouy shift of π/2 in one of the components produces a stepwise azimuthal phase ramp.

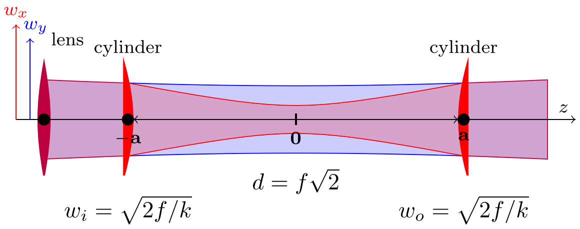

Fig. 2. Symmetric optical π/2 mode converter. The blue shaded *yz* component is a quasi-collimated beam. The identical cylinder lenses only act on the red shaded *xz* component. (For interpretation of the references to colour in this figure legend, the reader is referred to the web version of this article.)

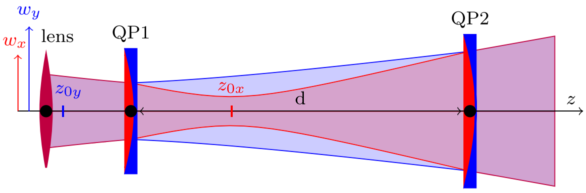

Fig. 3. Schematics of an asymmetric π/2 MC for electrons with $w_o/w_i = 2.12$ as in the simulations in Figs. 6 and 9. The preceding round lens provides the correct curvature. The quadrupoles (QP1 & QP2) focus the *xz* component (red shading) and defocus the *yz* component (blue shading). (For interpretation of the references to colour in this figure legend, the reader is referred to the web version of this article.)

be centered onto the principal plane of QP2. This can be readily achieved by focusing a wide enough beam onto QP2. If the incoming width w_i is several times larger than the width w that would be required in a symmetric π/2 MC (Eq. (14)), $z_r < \, < d$ will also hold, and the required lens excitations can be found by minimizing the effects of wobbling QP2. Then a smaller condenser aperture can be used with the same lens settings, to provide a smaller w_i with the correct curvature. If the reduced w_i is comparable to the w of the symmetric π/2 MC, the required f_i and f_o will also be comparable. Since the outgoing radius of curvature does not depend on the Gouyshift, pairs of f_i and f_o can be realized by choosing any one and adjusting the other one, until u from Eqn. 16 becomes 1. There is no need to match the width of the symmetric π/2 MC exactly.

3. Spherical mode converters

3.1. Gouy phase

Sculpting a Gaussian intensity profile is impractical if not impossible in electron microscopy. Instead we consider standard spherical waves as an input. The Gouy phase of an astigmatic higher order HG_{nm} beam follows a $\tan^{-1}$ function.

$$\Psi = \left(n + \frac{1}{2}\right)\tan^{-1}\left(\frac{z - z_x}{z_{rx}}\right) + \left(m + \frac{1}{2}\right)\tan^{-1}\left(\frac{z - z_y}{z_{ry}}\right) \tag{19}$$

where z_x and z_y are the positions of the line foci and z_{rx} and z_{ry} are the respective Rayleigh lengths. A spherical wave has a different Gouy phase. A typical example of an incoming electron beam in the geometric optic regime is shown in Fig. 4.

It is linear around zero defocus [20], and for small defocus values up to one Rayleigh range it approximates well that of a HG_{00} beam with the same focus under the condition that the aperture radius is $\sqrt{2}$ times as large as the width w of the incoming Gaussian. The traces for the Gouy phase at roughly 1/3 and 2/3 of the radius of the Airy disk are also very linear up to $z = z_R$. This comparison illustrates that a Gaussian input for the π/2 MC can be replaced by a spherical wave with a scaled diameter.

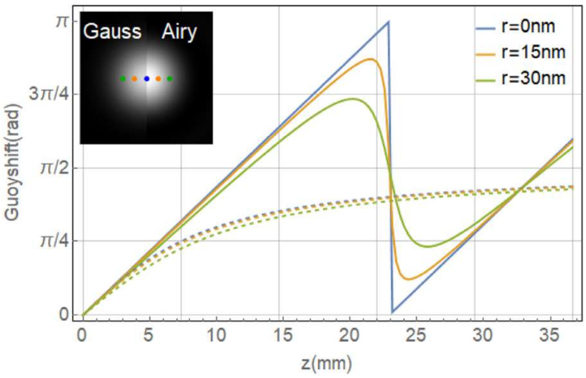

Fig. 4. Gouy phase of a spherical wave (full lines) and an HG_{00} beam (dashed) at different radii. A lens with a focal length of 120 mm is positioned at $z = -119.4$ mm. The aperture radius and Gaussian width at the lens are $w = r/\sqrt{2} = 1250$ nm. Acceleration voltage $U_a = 200$ kV. The inset shows the Gaussian waist and Airy disk formed at $z = 0$, the dots correspond to the different radii. Horizontal gridlines are at π/4, π/2 and 3π/4, vertical gridlines count Rayleigh ranges $z_r = 7.3$ mm of the Gaussian beam.

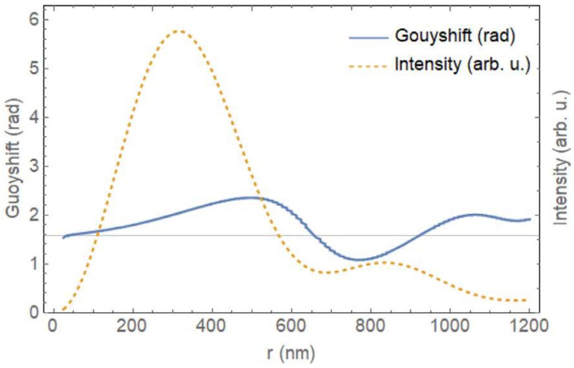

Fig. 5. Solid: numerical Gouy shift for a split Hilbert beam (see Fig. 1) after a π/2 MC. The horizontal grid line marks the targeted phase shift of π/2. The shared dashed radial intensity profile is taken along the mirror axis.

3.2. Hilbert beams

A feasible approach to produce an electron beam similar to a HG is a Hilbert plate that induces a phase shift of π between the two halfs of a round aperture. One may also use a magnetic bar to this aim [21,22]. In the following, we shall refer to such a phase shifter as a Hilbert device, independent of the principle used. Beams produced with such a device are henceforth called spherical Hilbert beams.

The Gouy shift of HG beams in the mode converter can be calculated analytically with Eq. (19). For spherical Hilbert beams we have to resort to wave optical simulations. To this aim we performed two independent simulations of an asymmetric QP π/2 setup for the horizontal and vertical components as suggested in Fig. 1. The magnification is the same as in Figs. 6 and 9 with $r_i = 357$ nm, $d = 120$ mm and quadrupole focal lengths of $f_i = 80$ mm and $f_o = 360$ mm. The acceleration voltage is $U_a = 200$ kV.

The propagated components were rotated so that their symmetry axis coincide. The difference in Gouy phase is traced in the direction of the aligned symmetry axis. The Gouy shift obtained in that way oscillates around the ideal value of π/2 that would be the outcome for an

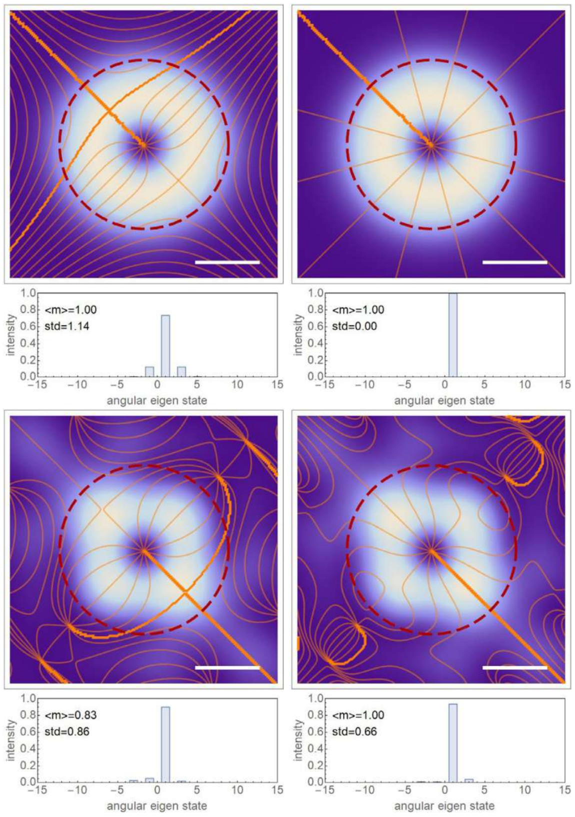

Fig. 6. Vortex beams produced by a $\pi/2$ MC. Isophasal lines are superimposed on the intensities and angular spectra immediately before (left) and after (right) QP2 in the same setup as in Fig. 5. Upper row: HG beam with width $w_o = 537$ nm, Lower row: spherical Hilbert beam with radius $r_o = 759$ nm. Scale bar: 500 nm. The dashed circle ($r = 650$ nm) marks the area selected for decomposition into azimuthal eigenmodes.

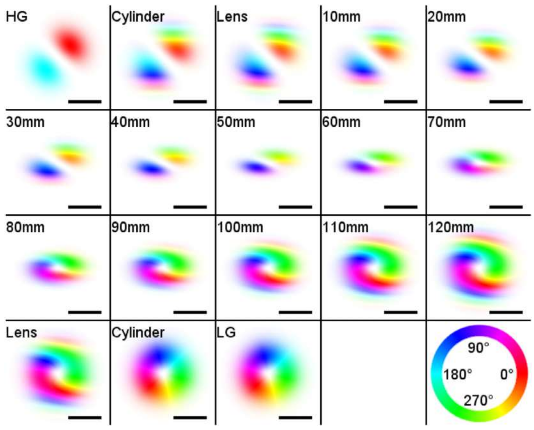

Fig. 7. Propagation of an incident rotated $HG_{0,1}$ with width $w = 367$ nm and $U_a = 200$ kV through cylinder lenses with $f = 84.9$ mm and round lenses with $f = 409.7$ mm. The last frame is a Laguerre Gaussian (LG) with the same w. The scalebar is 500 nm. The wavefront is shown for every 10 mm.

ideal HG input. The radial intensity profile shows that an acceptable average Gouy shift can be achieved at the most relevant radius.

3.3. Orbital angular momentum

When expanding the wave function of the propagating beam ψ in a given plane into $\hat{L}_z$ eigenfunctions

$$\psi(r, \phi) = \sum_m c_m(r) e^{im\phi}, \tag{20}$$

the expectation value of the OAM can be calculated as

$$\langle \hat{L}_z \rangle = \frac{\langle \psi \rangle \hat{L}_z | \psi \rangle}{\langle \psi | \psi \rangle} = \hbar \frac{\sum_m m \int |c_m(r)|^2 \, r \, dr}{\sum_m \int |c_m(r)|^2 \, r \, dr}. \tag{21}$$

Fig. 6 shows the phase structure before and after the second quadrupole for a $HG_{0,1}$ and a Hilbert beam. The parameters for the $\pi/2$ MC are identical to those in Figs. 5 and 9. Note that the phase structure has been compensated for the diverging curvature Eq. (15). The remaining purely azimuthal phase structure at the entrance to QP2 is visibly astigmatic for both beam profiles. Indeed, the decomposition according to Eq. (20) reveals a broadened distribution. After QP2 the astigmatism is corrected, and the $m = 1$ contribution increases. The $HG_{0,1}$ beam is transformed into a clean $m = 1$ LG state. QP1 did already exert the full torque of $\langle m \rangle = 1$, while QP2 establishes mode purity. The Hilbert beam picks up angular momentum on QP1 and QP2 and does also acquire a total of $\langle m \rangle = 1$, albeit with a slightly lower $m = 1$ mode purity. The mode purity may be further increased by another aperture, as the central region shows an ideal linear azimuthal phase spiral.

4. Numerical simulations

So far the setups for $\pi/2$ MCs were very much simplified. They were modeled by a composite input of an aperture, a Hilbert device, a lens and a QP followed by one single propagation step and a composite output of a lens and a QP. The analytic treatment of Gaussian beams passing through such stylized $\pi/2$ MCs as well as the very similar behavior of HG and Hilbert beams in test scenarios suggest that vortex generation is possible in an actual aberration corrected TEM. Numerical simulations on more realistic and complete setups are indispensable to confirm and possibly retune the parameters for real world electron optical designs. The obvious challenge of simulating an entire electron optical setup, is keeping track of multiple optical devices and propagation steps in between them.

4.1. Rescaled propagation

In an extended optical system, like an entire TEM column, different sections of the beam have very different lateral extend or magnification. One very efficient way to adapt the lateral scale to a propagating beam can be to replace the combined action of a lens with focal length f and further propagation over a distance d with the combined action of a propagation over a distance d', a lateral rescaling and a lens with focal length f'. So instead of propagating forward to the imaging plane, the incident wavefront is propagated backwards to the object plane. Then the magnification of the imaging and a new lens with focal length f' are applied. The transformed distance d does not need to be the full distance to the next lens or aperture. In fact it can be chosen freely, and the signs of the rescaled and remaining distance are arbitrary. With the introduction of s and s' for the original and the re-scaled grid resolution, the transformations can be written as:

$$\frac{1}{d'} = \frac{1}{d} - \frac{1}{f} \tag{22}$$

$$\frac{s'}{s} = 1 - \frac{d}{f} \tag{23}$$

$$f' = f - d. \tag{24}$$

Sign changes in d are equivalent to propagating backwards. Sign changes in f and s trigger a mirror inversion and a phase shift of π.

4.2. Virtual microscope

In this section, we present a detailed numerical study of the propagation behavior of HG and Hilbert beams through an ensemble of lenses and QPs. To this aim, we have developed a JAVA plugin for ImageJ. The graphical user interface represents a fully editable virtual microscope. Different setups can be stored in human readable and editable xml files which define among other parameters a unique order in which lenses, apertures and propagation distances are applied to an initial plane wave. Wavefronts of the propagated beam can be viewed as stacks of images.

Numerically, lenses $\mathcal{L}$, apertures, quadrupoles $\mathcal{QP}$ and other devices are represented as a complex map for the real and the imaginary part of their action, respectively.

$$\mathcal{L}(f, x, y) = \exp\left[i\cdot(x^2 + y^2)\cdot\frac{k}{2\cdot f}\right] \tag{25}$$

$$\mathcal{QP}(f, x, y) = \exp\left[i\cdot(x^2 - y^2)\cdot\frac{k}{2\cdot f}\right] \tag{26}$$

The simulation starts with a plane wave with phase 0 at $z = 0$. At every plane, the current cross section ψ_z is multiplied with the complex sheets at this plane. This step can account for arbitrary apertures, gratings, Hilbert devices, wavefront deformations by lenses and multipoles. It can also define for instance a Hermite Gaussian. Then the wavefront is propagated through free space to the next plane. The propagation over a distance d from ψ_z to ψ_{z+d} can be individually configured to be carried out in customizable steps. We always employ the par-axial approximation, since lateral dimensions are μm and relevant distances are at least mm. Each step can be propagated in frequency or spatial domain.

$$\psi_{z+d} = \mathcal{FT}^{-1}(\mathcal{P}(d)\cdot\mathcal{FT}(\psi_z)) \tag{27}$$

$$\psi_{z+d}(x, y) = -i\cdot\int_{x',y'}\psi_z(x', y')\cdot\exp\left[i\frac{(x-x')^2 + (y-y')^2}{2\cdot d}\right]dx'dy' \tag{28}$$

$\mathcal{FT}$ denotes Fourier transformation and the propagator $\mathcal{P}$ in Eq. (27) is defined in frequency range $\hat{x}, \hat{y}$

$$\mathcal{P}(d, \hat{x}, \hat{y}) = \exp\left[i\cdot(\hat{x}^2 + \hat{y}^2)\cdot\frac{d}{2\cdot k}\right] \tag{29}$$

Propagation steps in spatial domain (Eq. (28)) may also contain a custom zoom between the planes at z and $z + d$.

The custom splitting and scaling and per step choice between spatial and frequency domain are found to be versatile in circumventing the need for excessive oversizing or oversampling of the complex sheets and wavefronts. All simulations could be carried out on a grid of 512x512 pixels with dynamic resolution. The phase information is consistent with the Gouy shift, but there is an arbitrary global phase factor for different planes. The first test case for the virtual microscope is the symmetric cylinder lens setup. Fig. 7 illustrates the propagation of the phase colored wavefronts through a basic symmetric π/2 MC setup. The incoming rotated $\mathrm{HG}_{1,0}$ ($U_a = 200$ kV) has a width $w_i = 367$ nm. The round lenses with $f_L = 409.7$ mm are on the inside but share the same plane with the cylinder lenses with $f_c = 84.9$ mm which are 120 mm apart. In this ordering the effects of the first and second cylinder lens are not obscured by the isotropic curvature. The first cylinder lens introduces horizontal bands and a vertical phase curvature. The following intermediate wave fronts visualize the continuous mode conversion. And finally the second cylinder transforms the asymmetric phase pattern after the second lens into the exact LG pattern for $m = 1$.

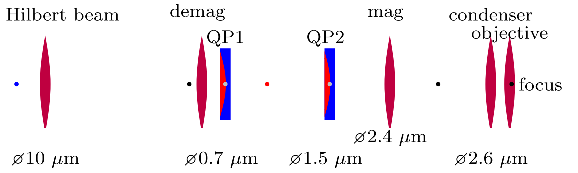

Fig. 8. Complete optical setup for vortex generation. This setup is used in Fig. 9. Lenses (purple) and quadrupoles (red/blue) focus an incoming Hilbert beam. Black and gray dots mark real images, the red/blue dot mark the real/virtual astigmatic line focus of the first quadrupole. The given diameters ⌀; are according to geometric optics. (For interpretation of the references to colour in this figure legend, the reader is referred to the web version of this article.)

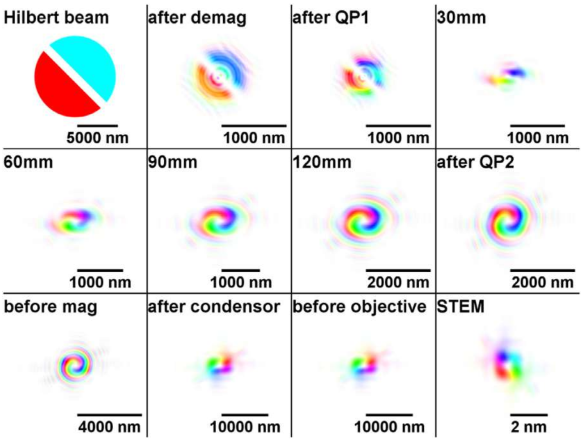

Fig. 9. Propagation from a Hilbert device in the condenser to a STEM probe with orbital angular momentum ± ħ. Captions are explained in the text. The hue coloring is identical to Fig. 7.

4.3. Spherical waves and multi-scale simulation

Moving towards a more realistic virtual setup necessitates to include round apertures and spherical waves as well as the condenser and the objective lens systems.

The full asymmetric π/2 MC setup is sketched in Fig. 8. The Hilbert device is assumed to be mounted in the condenser system and has a diameter of 10 µm. The black dots mark actual images. The lens labeled ”demag” would form another image (gray dot) at the principal plane of the second QP (QP2). The first QP (QP1) introduces astigmatism and forms one real line focus (red dot). The corresponding perpendicular line focus is virtual (blue dot). After the second QP (QP2) the beam is mode matched and appears as if emanating from an image (gray dot) in the principal plane of QP1. It is refocused in another real image in front of the condenser/objective system. The last black dot is in the focus of the objective.

The full wave optical simulation for the extended asymmetric π/2 MC setup in Fig. 8 is shown in Fig. 9. The simulation takes advantage of variable resolution on a fixed size grid. It starts from a Hilbert device in an aperture with a diameter of 10 µm. A 1 μm wide magnetic bar induces a phaseshift of π between the two sides. Similar devices have been demonstrated [21,22]. At the exit of the lens ”demag” the wavefront is demagnified and rather reminiscent of a HG beam. The demagnification at QP1 is 14.0 fold and the center of the converging curvature is at QP2 (Eq. (15)). The distance d between the QPs is 120 mm. The quadrupoles are excited asymmetrically with $f_i = 80$ mm and $f_o = 360$ mm to match the incoming width (Eq. (18)) and to provide the correct Gouy shift (Eq. (16)). The output of the π/2 MC is clearly a vortex beam and the spiraling phase pattern has a diverging

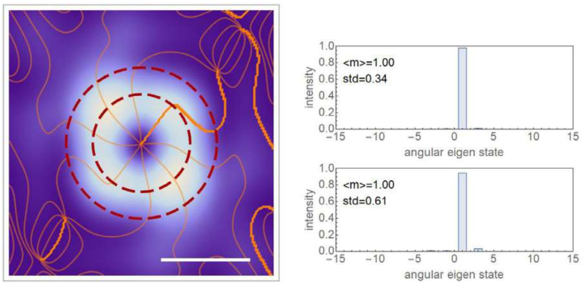

Fig. 10. Isophasal contours and angular mode distribution of the same STEM probe as in Fig. 9. The scalebar is 1 nm. The upper spectrum is for the beam inside the smaller circle ($r = 0.55$ nm) and the lower spectrum is for the beam inside the bigger circle ($r = 0.85$ nm).

curvature centered at QP1. The magnification inside the $\pi/2$ MC is $w_o/w_i = 2.12$. The next frames are before the "mag" lens and after the condenser. The magnified beam is focused by the objective lens to form a donut shaped STEM probe. Changing the helicity of the STEM probe is as straight forward and reproducible as rotating the QPs by 90°, which is an crucial aspect for measuring dichroism [23].

Notably the central bar in the Hilbert device and its diffractive blurring upon propagation to the first QP contribute to the resemblance of a $HG_{1,0}$ beam. Except for the magnification the cross sections from the interior of the $\pi/2$ MC closely resemble the internal cross sections shown in Fig. 7. The differences in the spiraling phase pattern before (120 mm) and after QP2 might seem subtle in direct phase coloring, but they are the same as in the isophasal representation shown in Fig. 6. The second QP is crucial for canceling the astigmatism introduced by QP1 and hence stabilizing the vortex state. The donut profile is then magnified and focused by the objective lens. This is very well demonstrated by the collection of vortex profiles at various magnifications in Fig. 9.

The resulting STEM probe is shown in more detail in Fig. 10. Its azimuthal spectra show a very similar mode distribution for the two selected different radii. More importantly, both spectra clearly show that the vortex beam is stable and can be projected all the way from the second QP to the focus of the objective lens.

We assumed realistic distances and respected minimum focal lengths for the simulation in Fig. 9. So the predicted donut diameter of ~ 1 nm at ~ 2 mrad should be achievable in existing electron microscopes. We confirmed numerically that the effects of spherical aberrations C_s with a typical value of a few mm and a finite source size of 50 nm are not detrimental to the predicted donut probe.

5. Conclusion

We have explored the realm of possible designs for $\pi/2$ MCs in electron optics based on reconfiguring well established and relatively wide spread probe correctors. Using already existing quadrupoles is an appealing aspect, because there is no need for mechanical modifications of the TEM column and helicity switching would be straight forward. The most relevant parameters are the distance between the two quadrupoles d, the possible excitations of the quadrupoles or minimal f_i and f_o, as well as the incident virtual aperture size. Allowing for asymmetry in the quadrupole excitations introduces a magnification or de-magnification and leads to an effective decoupling of the constraints on achieving isotropic width and curvature as well as $\pi/2$ mode conversion at the exit plane. We propose that a $\pi/2$ MC can be used to generate a very pure, and switchable $m = \pm1$ vortex beam. The design of the Hilbert device we have considered here numerically is minimalistic, and there are conceivable aperture designs that could mimic a $HG_{0,1}$ input beam even more closely. Significantly smaller probe diameters could be envisaged in dedicated setups with intermediate magnification stages and additional apertures.

Acknowledgements

CK & PS acknowledge financial support of the Austrian Science Fund (FWF): P29687-N36. TS acknowledges financial support of the Austrian Academy of Sciences: DOC-scholarship.

Supplementary material

Supplementary material associated with this article can be found, in the online version, at 10.1016/j.ultramic.2019.05.003.

References

[1] R. Juchtmans, A. Béché, A. Abakumov, M. Batuk, J. Verbeeck, Using electron vortex beams to determine chirality of crystals in transmission electron microscopy, Phys. Rev. B 91 (2015) 094112, https://doi.org/10.1103/PhysRevB.91.094112.
[2] R. Juchtmans, J. Verbeeck, Orbital angular momentum in electron diffraction and its use to determine chiral crystal symmetries, Phys. Rev. B 92 (2015) 134108, https://doi.org/10.1103/PhysRevB.92.134108.
[3] J.C. Idrobo, J. Rusz, J. Spiegelberg, M.A. McGuire, C.T. Symons, R.R. Vatsavai, C. Cantoni, A.R. Lupini, Detecting magnetic ordering with atomic size electron probes, Adv. Struct. Chem. Imaging 2 (1) (2016) 5, https://doi.org/10.1186/s40679-016-0019-9.
[4] K.Y. Bliokh, I.P. Ivanov, G. Guzzinati, L. Clark, R.V. Boxem, A. Beche, R. Juchtmans, M.A. Alonso, P. Schattschneider, F. Nori, J. Verbeeck, Theory and applications of free-electron vortex states, Phys. Rep.-Rev. Sect. Phys. Lett. 690 (2017) 1–70, https://doi.org/10.1016/j.physrep.2017.05.006.
[5] S.M. Lloyd, M. Babiker, G. Thirunavukkarasu, J. Yuan, Electron vortices: beams with orbital angular momentum, Rev. Mod. Phys. 89 (3) (2017) 035004, https://doi.org/10.1103/RevModPhys.89.035004.
[6] H. Larocque, I. Kaminer, V. Grillo, G. Leuchs, M.J. Padgett, R.W. Boyd, M. Segev, E. Karimi, "twisted' electrons, Contemp. Phys. 59 (2) (2018) 126–144, https://doi.org/10.1080/00107514.2017.1418046.
[7] P. Schattschneider, S. Rubino, C. Hebert, J. Rusz, J. Kunes, P. Novak, E. Carlino, M. Fabrizioli, G. Panaccione, G. Rossi, Detection of magnetic circular dichroism using a transmission electron microscope, Nature 441 (7092) (2006) 486–488, https://doi.org/10.1038/nature04778.
[8] P. Schattschneider, S. Loeffler, M. Stoeger-Pollach, J. Verbeeck, Is magnetic chiral dichroism feasible with electron vortices? Ultramicroscopy 136 (2014) 81–85, https://doi.org/10.1016/j.ultramic.2013.07.012.
[9] D. Pohl, S. Schneider, P. Zeiger, J. Rusz, P. Tiemeijer, S. Lazar, K. Nielsch, B. Rellinghaus, Atom size electron vortex beams with selectable orbital angular momentum, Sci. Rep. 7 (2017), https://doi.org/10.1038/s41598-017-01077-9.
[10] M. Uchida, A. Tonomura, Generation of electron beams carrying orbital angular momentum, Nature 464 (7289) (2010) 737–739, https://doi.org/10.1038/nature08904.
[11] J. Verbeeck, H. Tian, P. Schattschneider, Production and application of electron vortex beams, Nature 467 (7313) (2010) 301–304, https://doi.org/10.1038/nature09366.
[12] V. Grillo, G.C. Gazzadi, E. Karimi, E. Mafakheri, R.W. Boyd, S. Frabboni, Highly efficient electron vortex beams generated by nanofabricated phase holograms, Appl. Phys. Lett. 104 (4) (2014) 043109, https://doi.org/10.1063/1.4863564.
[13] L. Clark, A. Beche, G. Guzzinati, A. Lubk, M. Mazilu, R.V. Boxem, J. Verbeeck, Exploiting lens aberrations to create electron-vortex beams, Phys. Rev. Lett. 111 (6) (2013) 064801, https://doi.org/10.1103/PhysRevLett.111.064801.
[14] A. Beche, R.V. Boxem, G.V. Tendeloo, J. Verbeeck, Magnetic monopole field exposed by electrons, Nat. Phys. 10 (1) (2014) 26–29, https://doi.org/10.1038/NPHYS2816.
[15] A.H. Tavabi, M. Beleggia, V. Migunov, A. Savenko, O. Oktem, R.E. Dunin-Borkowski, G. Pozzi, Tunable ampere phase plate for low dose imaging of biomolecular complexes, Sci. Rep. 8 (2018) 5592, https://doi.org/10.1038/s41598-018-23100-3.
[16] M. Beijersbergen, l. Allen, H. Vanderveen, J. Woerdman, Astigmatic laser mode converters and transfer of orbital angular-momentum, Opt. Commun. 96 (1–3) (1993) 123–132, https://doi.org/10.1016/0030-4018(93)90535-D.
[17] P. Schattschneider, M. Stoeger-Pollach, J. Verbeeck, Novel vortex generator and mode converter for electron beams, Phys. Rev. Lett. 109 (8) (2012) 084801, https://doi.org/10.1103/PhysRevLett.109.084801.
[18] V. Grillo, A.H. Tavabi, F. Venturi, H. Larocque, R. Balboni, G.C. Gazzadi, S. Frabboni, P.H. Lu, E. Mafakheri, F. Bouchard, R.E. Dunin-Borkowski, R.W. Boyd, M.P.J. Lavery, M.J. Padgett, E. Karimi, Measuring the orbital angular momentum spectrum of an electron beam, Nat. Commun. 8 (2017) 15536, https://doi.org/10.1038/ncomms15536.
[19] J. Verbeeck, A. Beche, K. Muller-Caspary, G. Guzzinati, M.A. Luong, M.D. Hertog, Demonstration of a 2 × 2 programmable phase plate for electrons, Ultramicroscopy 190 (2018) 58–65, https://doi.org/10.1016/j.ultramic.2018.03.017.
[20] M. Born, E. Wolf, A.B. Bhatia, P.C. Clemmow, D. Gabor, A.R. Stokes, A.M. Taylor, P.A. Wayman, W.L. Wilcock, Principles of optics: Electromagnetic theory of

propagation, Interference and Diffraction of Light, 7th ed., Cambridge University Press, 1999. doi:10.1017/CBO9781139644181

[21] T. Tanji, H. Niimi, J. Usukura, Y. Yamamoto, S. Ohta, Electron differential phase microscopy with an a-b effect phase plate, Microsc. Microanal. 21 (S3) (2015) 1945–1946, https://doi.org/10.1017/S1431927615010508.

[22] G. Guzzinati, A. Beche, H. Lourenco-Martins, J. Martin, M. Kociak, J. Verbeeck, Probing the symmetry of the potential of localized surface plasmon resonances with phase-shaped electron beams, Nat. Commun. 8 (2017) 14999, https://doi.org/10.1038/ncomms14999.

[23] P. Schattschneider, Linear and Chiral Dichroism in the Electron Microscope, Pan Stanford, 2012. http://www.panstanford.com/books/9789814267489

Chapter 10

Elastic propagation of fast electron vortices through amorphous materials

S. Löffler, S. Sack, and T. Schachinger

Acta Crystallographica Section A 75 (2019) 902–910
10.1107/S2053273319012889

Acta Cryst A
FOUNDATIONS
ADVANCES

ISSN 2053-2733

Elastic propagation of fast electron vortices through amorphous materials

Stefan Löffler,[a]* Stefan Sack[b] and Thomas Schachinger[a,b]

[a]University Service Centre for Transmission Electron Microscopy, TU Wien, Wiedner Hauptstraße 8-10/E057-02, Wien, Austria, and [b]Institute of Solid State Physics, TU Wien, Wiedner Hauptstraße 8-10/E138-03, Wien, Austria.
*Correspondence e-mail: stefan.loeffler@tuwien.ac.at

Received 12 June 2019
Accepted 17 September 2019

Edited by L. D. Marks, Northwestern University, USA

Keywords: electron vortex beams; amorphous materials; elastic scattering.

This work studies the elastic scattering behavior of electron vortices when propagating through amorphous samples. A formulation of the multislice approach in cylindrical coordinates is used to theoretically investigate the redistribution of intensity between different angular momentum components due to scattering. To corroborate and elaborate on our theoretical results, extensive numerical simulations are performed on three model systems (Si_3N_4, $Fe_{0.8}B_{0.2}$, Pt) for a wide variety of experimental parameters to quantify the purity of the vortices, the net angular momentum transfer, and the variability of the results with respect to the random relative position between the electron beam and the scattering atoms. These results will help scientists to further improve the creation of electron vortices and enhance applications involving them.

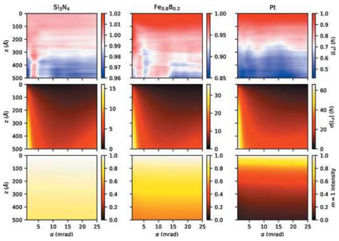

1. Introduction

The study of electron vortex beams (EVBs) is a highly active field of research in the context of transmission electron microscopy (TEM). Pure EVBs are characterized by a phase distribution proportional to the azimuthal angle and can thus be written in the form $\psi(r,\varphi) = f(r)\exp(im\varphi)$, where (r,φ) are polar coordinates, f is the radial amplitude function and m is the so-called topological charge. It can directly be verified that EVBs are eigenfunctions of the orbital angular momentum (OAM) operator $\hat{L}_z$ with $\hat{L}_z\psi = \hbar m\psi$, which implies that EVBs carry angular momentum and, by extension, a magnetic moment of $m\mu_B$ (Bliokh *et al.*, 2011).

The fact that these EVBs carry OAM has led to the proposition and demonstration of many applications ranging from the measurement of magnetic properties with atomic resolution (Verbeeck *et al.*, 2010; Rusz *et al.*, 2014; Schattschneider, Löffler *et al.*, 2014; Idrobo *et al.*, 2016; Schachinger *et al.*, 2017), the study of the dynamics of Landau states (Schattschneider, Schchinger *et al.*, 2014; Schachinger *et al.*, 2015), sample chirality (Juchtmans *et al.*, 2015) and symmetry properties of plasmon resonances (Guzzinati *et al.*, 2017), to the manipulation of nanoparticles (Verbeeck *et al.*, 2013). Despite the huge potential of EVBs and the fact that their creation and propagation through vacuum are well understood (Schattschneider & Verbeeck, 2011; Schattschneider *et al.*, 2012; Schachinger *et al.*, 2015), knowledge of their propagation through matter is still somewhat lacking. This is especially surprising since earlier studies showed that elastic scattering in crystals can drastically change the OAM of the beam (Löffler & Schattschneider, 2012; Xin & Zheng, 2012; Lubk *et al.*, 2013).

Particularly important – and little investigated – is the propagation of EVBs through amorphous materials. Firstly, such materials are used increasingly often for producing EVBs by means of specially designed phase masks (Harvey *et al.*, 2014; Shiloh *et al.*, 2014; Grillo *et al.*, 2014). Secondly, they are a common support, *e.g.* for nanoparticles. Thirdly, EVBs would allow techniques such as energy-loss magnetic chiral dichroism (EMCD) for measuring magnetic properties down to the nanoscale in crystalline samples to be applied also to amorphous materials (Schachinger *et al.*, 2017). However, it is usually assumed that an as-produced, ideal vortex beam stays that way and propagates practically unperturbed through the sample. Whether or not that is the case and, if so, to what extent is studied in this work.

This paper is structured as follows: first, we give a brief overview of the theory in Section 2. To that end, we rewrite the multislice approach used throughout this work in a cylindrical coordinate system suitable for the analysis of EVBs. From that, we deduce some general statements about the propagation behavior of EVBs. In Section 3, we give a detailed account of the numerical simulations performed in this work. In Section 4, the results of the numerical simulations are presented, which are subsequently discussed in Section 5.

2. Theory

The starting point for describing the propagation of electrons through matter is Schrödinger's equation. Throughout this work, we will adopt a paraxial multislice approach (Kirkland, 1998). In this approach, the sample is cut into thin slices and the propagation of an electron wavefunction through slice n is given by

$$\psi_n(\mathbf{r}_\perp) = \exp\left(\frac{it_n}{2k_z}\hat{\Delta}\right)\exp[-i\sigma v_{z,n}(\mathbf{r}_\perp)]\psi_{n-1}(\mathbf{r}_\perp) \qquad (1)$$

where $\mathbf{r}_\perp$ is the 2D coordinate vector in the x–y plane perpendicular to the main propagation direction z, $\psi_{n-1}(\mathbf{r}_\perp)$ is the wavefunction incident on the nth slice, $\psi_n(\mathbf{r}_\perp)$ is the wavefunction exiting the nth slice, k_z is the z component of the wavevector, t_n is the thickness of the nth slice, $\hat{\Delta}$ is the Laplace operator, σ is the so-called interaction parameter and $v_{z,n}(\mathbf{r}_\perp)$ is the electrostatic potential of the slice projected along the z direction. In equation (1), the $\exp[-i\sigma v_{z,n}(\mathbf{r}_\perp)]$ term describes (instantaneous) elastic scattering, while the $\exp[(it_n/2k_z)\hat{\Delta}]$ term describes the free-space Fresnel propagation through the slice. To propagate the electron beam through the entire sample, many such individual propagation steps have to be performed. Note that $\hat{\Delta}$ and $v_{z,n}(\mathbf{r}_\perp)$ do not generally commute, so the exponentials cannot easily be reordered.

Here, we are primarily interested in the evolution of the different OAM components, so we expand the terms in equation (1) into the eigenstates $\exp(im\varphi)$ of the OAM operator $\hat{L}_z = -i\hbar\,\partial/\partial\varphi$:

$$\psi_n(\mathbf{r}_\perp) = \sum_m f_{n,m}(r)\exp(im\varphi)$$

$$\exp[-i\sigma v_{z,n}(\mathbf{r}_\perp)] = \sum_\mu V_{n,\mu}(r)\exp(i\mu\varphi),$$

with

$$f_{n,m}(r) = \frac{1}{2\pi}\int_0^{2\pi}\psi_n(r,\varphi)\exp(-im\varphi)\,\mathrm{d}\varphi$$

$$V_{n,\mu}(r) = \frac{1}{2\pi}\int_0^{2\pi}\exp[-i\sigma v_{z,n}(r,\varphi)]\exp(-i\mu\varphi)\,\mathrm{d}\varphi, \qquad (2)$$

where (r,φ) denote the polar components of $\mathbf{r}_\perp$. In physical terms, m denotes the topological charge of a vortex component with an OAM of $m\hbar$. With these definitions, equation (1) reduces to

$$\begin{aligned}
&\sum_m f_{n,m}(r)\exp(im\varphi)\\
&= \exp\left(\frac{it_n}{2k_z}\hat{\Delta}\right)\sum_{m,\mu}V_{n,\mu}(r)f_{n-1,m}(r)\exp[i(m+\mu)\varphi]\\
&= \exp\left(\frac{it_n}{2k_z}\hat{\Delta}\right)\sum_m\left[\sum_\mu V_{n,m-\mu}(r)f_{n-1,\mu}(r)\right]\exp(im\varphi)\\
&= \exp\left(\frac{it_n}{2k_z}\hat{\Delta}\right)\sum_m g_{n,m}(r)\exp(im\varphi), \qquad (3)
\end{aligned}$$

i.e. the elastic scattering transforms the set of radial components $\{f_{n-1,m}(r)\}_m \mapsto \{g_{n,m}(r)\}_m$.

The action of the Laplacian operator, *i.e.* the Fresnel propagation between the slices, is best viewed in reciprocal space. There, the 2D Laplacian reduces to $|\mathbf{k}_\perp|^2$ and the OAM distribution is maintained (Schattschneider *et al.*, 2012), giving

$$\begin{aligned}
&\sum_m f_{n,m}(r)\exp(im\varphi)\\
&= \mathcal{F}_{\mathbf{k}_\perp\to\mathbf{r}_\perp}\left[\exp\left(\frac{it_nk^2}{2k_z}\right)\sum_m g_{n,m}(k)\exp(im\varphi_k)\right]
\end{aligned}$$

with the Hankel transforms

$$g_{n,m}(k) = i^m\int_0^\infty g_{n,m}(r)J_m(kr)r\,\mathrm{d}r$$

$$f_{n,m}(r) = \frac{1}{i^m}\int_0^\infty\exp\left(\frac{it_nk^2}{2k_z}\right)g_{n,m}(k)J_m(kr)k\,\mathrm{d}k \qquad (4)$$

where (k,φ_k) are the polar coordinates of the vector $\mathbf{k}_\perp$, $\mathcal{F}_{\mathbf{k}_\perp\to\mathbf{r}_\perp}$ denotes the 2D Fourier transform from reciprocal to real space and J_m is the Bessel function of the first kind of order m.

It can be seen that the redistribution of intensity between different OAM components happens due to the elastic scattering in the electrostatic potential v_z [see equation (3)], while during the Fresnel propagation, only the radial distributions evolve but no intensity is transferred between different OAM components. The potential scattering term can also be written in vector form as

$$\mathbf{g}_n(r) = \mathbf{V}_n(r) \cdot \mathbf{f}_{n-1}(r),$$

where

$$[\mathbf{V}_n(r)]_{m,m'} = V_{n,m-m'}(r)$$

is a Toeplitz matrix, *i.e.* a matrix in which the values along each diagonal are constant, or, equivalently, where adjacent columns (and rows) are identical apart from a shift by one element.

There are several noteworthy points here. First of all, scattering from a component m to a component $m + \delta m$ takes place only if there exists some r for which $V_{n,\delta m}(r)$ and $f_{n-1,m}(r)$ are both non-negligible. On the one hand, this reflects the obvious fact that only those areas of the potential affect the beam in which the beam intensity is non-vanishing. On the other hand, it also implies certain symmetry properties (see Section 2.1).

Secondly, one can expect $\delta m = 0$ to be the dominant term for thin slices. This results from the fact that, for thin slices, v_z is small. Thus, the potential can be written in weak-phase-object approximation as

$$\exp[-i\sigma v_{z,n}(\mathbf{r}_\perp)] \simeq 1 - i\sigma v_{z,n}(\mathbf{r}_\perp),$$

showing that there is a large constant term, which results in a large $\delta m = 0$ contribution.

2.1. Symmetry constraints

Symmetry plays an important role in the scattering behavior of electron beams, especially in crystalline specimens. Even though the potential typically does not exhibit strict symmetries in amorphous materials, it can still show certain 'approximate' symmetries, *i.e.* atomic arrangements that deviate only slightly from a symmetric case. In fact, while in crystalline samples symmetries typically only hold for certain special, high-symmetry points such as atomic columns and are severely broken if the electron beam is positioned off-column, the random distribution of atoms in amorphous systems means that the same symmetry properties hold in an approximate sense fairly independently of the beam position. Thus, a closer investigation of the symmetry constraints for OAM transfer seems worthwhile. We want to emphasize that this subsection does not only pertain to amorphous materials but also to crystalline ones.

Here, we consider the inherently 2D case in the plane perpendicular to the beam axis (*i.e.* in a slice). More precisely, we study the transformation properties of the potential scattering term $\exp[-i\sigma v_{z,n}(r, \varphi)]$ under the point group $O(2)$, which contains rotations and reflections (as well as arbitrary combinations of them).

For the case of rotations, we assume that the potential has a ν-fold rotational symmetry, *i.e.* $v_{z,n}(r, \varphi + 2\pi/\nu) = v_{z,n}(r, \varphi)$. Inserting this into equation (2) yields

$$\begin{aligned}
&\int\limits_0^{2\pi} \exp[-i\sigma v_{z,n}(r, \varphi)] \exp(-i\mu\varphi) \, \mathrm{d}\varphi \\
&= \sum_{j=0}^{\nu-1} \int\limits_{\frac{2\pi j}{\nu}}^{\frac{2\pi(j+1)}{\nu}} \exp[-i\sigma v_{z,n}(r, \varphi)] \exp(-i\mu\varphi) \, \mathrm{d}\varphi \\
&= \int\limits_0^{\frac{2\pi}{\nu}} \exp[-i\sigma v_{z,n}(r, \varphi)] \exp(-i\mu\varphi) \, \mathrm{d}\varphi \sum_{j=0}^{\nu-1} \exp\left(-2\pi i \frac{\mu}{\nu} j\right) \\
&= \begin{cases} 0 & \mu/\nu \notin \mathbb{Z} \\ \nu \int\limits_0^{\frac{2\pi}{\nu}} \exp[-i\sigma v_{z,n}(r, \varphi)] \exp(-i\mu\varphi) \, \mathrm{d}\varphi & \mu/\nu \in \mathbb{Z} \end{cases}
\end{aligned}$$

using the summation formula for finite geometric series. Therefore, in the case of a ν-fold rotational symmetry of the potential around the beam axis, $V_{n,\mu} \equiv 0 \; \forall \mu \notin \nu\mathbb{Z}$, *i.e.* intensity can only be redistributed between OAM components which differ by an integer multiple of $\nu\hbar$.

For the case of reflections, we assume that the potential is symmetric with respect to a mirror line inclined by an angle φ_0 with respect to the x axis, *i.e.* $v_{z,n}(r, \varphi_0 - \varphi) = v_{z,n}(r, \varphi_0 + \varphi)$. Inserting this into equation (2) yields

$$\begin{aligned}
&\int\limits_{\varphi_0-\pi}^{\varphi_0+\pi} \exp[-i\sigma v_{z,n}(r, \varphi)] \exp(-i\mu\varphi) \, \mathrm{d}\varphi \\
&= \int\limits_0^{\pi} \exp[-i\sigma v_{z,n}(r, \varphi_0 - \varphi)] \exp[-i\mu(\varphi_0 - \varphi)] \, \mathrm{d}\varphi \\
&\quad + \int\limits_0^{\pi} \exp[-i\sigma v_{z,n}(r, \varphi_0 + \varphi)] \exp[-i\mu(\varphi_0 + \varphi)] \, \mathrm{d}\varphi \\
&= 2 \exp(-i\mu\varphi_0) \int\limits_0^{\pi} \exp[-i\sigma v_{z,n}(r, \varphi_0 + \varphi)] \cos(\mu\varphi) \, \mathrm{d}\varphi.
\end{aligned}$$

Since the cosine is a symmetric function, it follows that, in the presence of a reflection, $V_{n,\mu}(r) = \exp(-2i\mu\varphi_0) V_{n,-\mu}(r)$, *i.e.* the $+\mu$ and $-\mu$ components differ only by a phase factor.

The case in which the scattering coefficients for $+\mu$ and $-\mu$ components have the same absolute value may lead to the hypothesis that, in such a case, no net OAM can be transferred as both scattering events happen with the same probability. However, this hypothesis clearly cannot be true as an arbitrary potential exhibiting only a mirror symmetry is not circularly symmetric and hence does not commute with the Hamiltonian. Therefore, Heisenberg's equation of motion together with Ehrenfest's theorem dictate that the net OAM has to change over time. The solution to this conundrum lies in interference effects.

While the train of thought of equal probabilities is correct for single scattering, it breaks down when considering multiple scattering as depicted in Fig. 1 (for $\mu = \pm 1$). There, it is clearly visible that, after a single potential scattering event in the first slice, the $m - 1$ and the $m + 1$ components have the same total intensity even though their phase structure is obviously different. The propagation behavior of the two components is also different, owing to the different orders of Bessel functions in equation (4). However, as the Fresnel operator is unitary, the total intensity does not change during propagation.

The situation is different after the second slice, though. After the second potential scattering event, the $m+1$ component is given by the coherent superposition of two contributions. The first one stems from the portion of the beam that was first scattered with $\delta m = 1$, then propagated as $m+1$, and then scattered again with $\delta m = 0$. The second one stems from the portion that was first scattered with $\delta m = 0$, then propagated as m, and then scattered with $\delta m = 1$. The situation for the $m-1$ component is analogous, but not identical. Since propagation and potential scattering do not commute and the propagation is dependent on m, the interference patterns emerging from the coherent superpositions can be different for the $m-1$ and the $m+1$ components, thus leading to different intensities of the two components as indicated in Fig. 1. This, in turn, leads to a change of the OAM expectation value and, hence, to a net transfer of OAM, even though each individual potential scattering event is (quasi-)symmetric in amplitude for positive and negative δm.

2.2. Radial dependence

Another interesting question is how the OAM transfer depends on the radius, which translates into the question of how the behaviors of smaller and larger beams differ. For increasing r, larger and larger OAM transfers will become important. In fact, it is reasonable to assume that the dominant OAM transfer $\delta m\hbar \neq 0$ should scale proportionally to r. This can be deduced by comparing the mean atomic distance a with the circumference of a circle with radius r. Since the mean distance is constant throughout the sample but the circumference scales linearly with r, the ratio of the two scales as $1/r$. For large r, this can be seen in a very crude approximation as the average period $p \sim a/(2\pi r)$ of a periodic oscillation of the potential as a function of φ. Thus, the frequency of this oscillation (which corresponds to the OAM transfer) is proportional to $1/p \propto r$. Consequently, one can expect that larger OAM transfers become more important with increasing beam size.

Obviously, for large r, there is also more room for variations, *i.e.* deviations from a perfect periodic oscillation with period p. Therefore, it can also be expected that the spread of possible OAM transfers should increase with increasing r. As an alternative argument leading to the same conclusion, one can invoke the uncertainty principle $\sigma[\varphi]\sigma[L_z] \sim$ const. (Franke-Arnold *et al.*, 2004): since angle and OAM are complementary variables, any localization in angle has to lead to a delocalization in OAM. Scattering on an atom produces a localized disturbance in the wavefunction with an initial

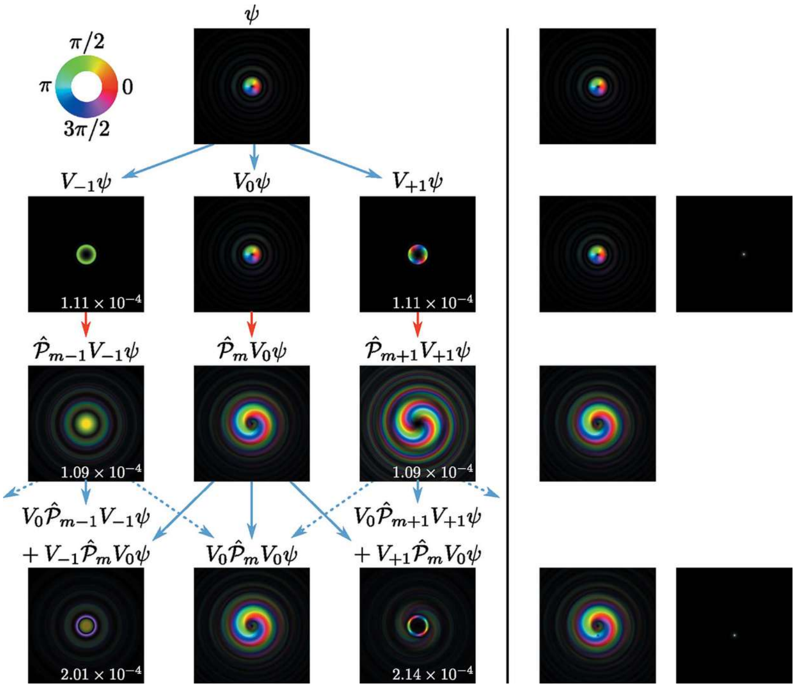

Figure 1
Schematic of the evolution of different OAM components upon transmission through two slices. The second column represents the (intially pure) vortex of order m (the images show $m = 1$), the first column shows the $m-1$ component, the third column shows the $m+1$ component, the fourth column shows the total wavefunction for reference, and the fifth column shows the scattering potential (where applicable). Blue arrows depict potential scattering while red arrows indicate Fresnel propagation ($\hat{\mathcal{P}}$). For clarity, propagation distances are exaggerated and simple single-atom model potentials are used. Dashed arrows symbolize additional scattering contributions that are omitted here. The numbers in the first and third columns give the components' intensities (with the total wavefunction normalized to 1). The index for the slice number n and the coordinates r, φ were omitted. Brightness signifies amplitude, color signifies phase as depicted in the inset in the top left.

Table 1
Densities of the materials and number of random configurations used in the simulations.

The mass densities were used as reference. The atom densities were the ones used in the simulations.

	Mass density (g cm^{-3})	Atom density (1×10^{22} cm^{-3})	Configurations
Si_3N_4	3.17	9.5	40
$Fe_{0.8}B_{0.2}$	7.18	9.0	40
Pt	21.5	6.5	60

angular extent of the order of $\sigma[\varphi] \sim a/r$. Thus, one can expect the standard deviation of the OAM, $\sigma[L_z]$, to scale roughly proportionally to r as well.

2.3. Expectation value

For some applications such as nanoparticle manipulation, the individual components of the OAM play only a secondary role compared with the expectation value of the OAM operator $\hat{L}_z$, which corresponds to the total, net OAM of the beam. Directly in front of the nth slice, this expectation value is given by

$$\langle \hat{L}_z \rangle_{n-1} = \hbar \sum_m m \int_0^\infty |f_{n-1,m}(r)|^2 r \, \mathrm{d}r,$$

while behind the slice it is given by

$$\langle \hat{L}_z \rangle_n = \hbar \sum_m m \int_0^\infty |f_{n,m}(r)|^2 r \, \mathrm{d}r = \hbar \sum_m m \int_0^\infty |g_{n,m}(r)|^2 r \, \mathrm{d}r$$

where the last equality holds due to Parseval's theorem (namely that the integrals over the absolute value squared of a function and its Fourier transform are identical), or, equivalently, due to the closure relationship of Bessel functions.

Clearly, $\langle \hat{L}_z \rangle$ is affected by asymmetries in the OAM component intensity distribution. From the derivations above, one can therefore expect that $\langle \hat{L}_z \rangle$ changes more for larger beams (which produce a wider spread of OAM component intensities) as well as for strongly scattering materials (for which $|V_{n,\mu}|$ is relatively large for $\mu \neq 0$).

3. Numerical simulations

We performed extensive numerical simulations for three amorphous model systems: Si_3N_4, which is commonly used as support material and for phase masks; Pt, which is commonly used as a focused ion beam (FIB) protection layer and in absorption masks; and $Fe_{0.8}B_{0.2}$, a magnetic material used, *e.g.*, in transformers, which could be interesting for EMCD. All simulations were carried out multiple times (see Table 1) for randomly different atom arrangements to get an idea of the variations of the various results. The simulations were performed in Cartesian coordinates using a multislice code based on the one described by Kirkland (1998). Likewise, the atomic potentials were also taken from Kirkland (1998).

For all samples, a 100 × 100 Å area was simulated with 512 × 512 pixels using thicknesses in the range of 0 to 500 Å with a slice thickness of 2 Å. All simulations were performed with a 200 keV incident beam which initially was in an OAM eigenstate with $L_z = \hbar$. The convergence angles were in the range of 1 to 25 mrad, corresponding to waist radii in the range of approximately 10 Å to 0.4 Å (see Fig. 2). For the sake of straightforward interpretation, the experimental conditions were assumed to be ideal, *i.e.* the microscope lenses were assumed to be perfectly aberration-corrected and no broadening due to a partially incoherent source or motion of the atoms was included.

The atomic positions were generated at random, taking care that the overlap between adjacent atoms was as small as possible (*i.e.* rejecting atoms that were too close to already placed atoms). The used densities are summarized in Table 1.

All simulations were carried out using an in-house multislice code (Löffler & Schattschneider, 2012; Löffler *et al.*, 2013) based on the work by Kirkland (1998).

To evaluate the OAM components, the resulting wavefunctions $\psi_n(\mathbf{r}_\perp)$ after each slice were first transformed to a polar representation $\psi_n(r, \varphi)$ using a fixed (r, φ) grid with 256 × 1024 pixels. Then, the transformation $\varphi \mapsto m$ was carried out by separately Fourier-transforming each line of constant r, yielding $\psi_n(r, m)$. Finally, the result was summed over the radius to obtain the total intensities

$$I_{m,n} = \int |\psi_n(r, m)|^2 r \, \mathrm{d}r$$

of each OAM component, which span the range from $m = -511$ to $m = 512$. From these intensities, one can in turn calculate several physically relevant parameters such as the OAM expectation value

$$\langle \hat{L}_z \rangle_n = \hbar \sum_m m I_{m,n}$$

and the OAM variance

$$\sigma^2[\hat{L}_z]_n = \langle \hat{L}_z^2 \rangle_n - \langle \hat{L}_z \rangle_n^2 = \hbar^2 \left[\sum_m m^2 I_{m,n} - \left(\sum_m m I_{m,n} \right)^2 \right],$$

i.e. the squared standard deviation. Since all calculations were carried out for several randomly generated amorphous structures, we can also estimate the 'error bars' associated with

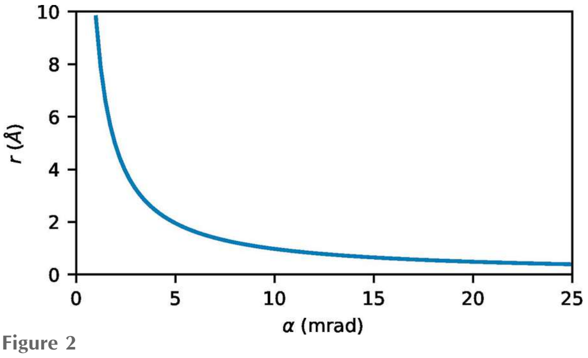

Figure 2
Dependence of the $m = 1$ beam waist radius r on the convergence semi-angle α for 200 keV electrons (Löffler, 2013).

the physical quantities due to the fact that no two samples and no two positions on a sample are identical.

4. Results

Fig. 3 shows some examples of the data produced by the simulations and during the analysis. In particular, it shows that, as predicted, the redistribution of intensity between different OAM components produced by the scattering potential is approximately symmetric but the resulting wavefunction has a distinctly non-symmetric OAM component distribution around the initial $m = 1$ component. Under the given conditions, the $m = 1$ component still exhibits the highest intensity $I_{1,n} \simeq 0.15$, but the components $m \in \{-2, -1, 0, 2, 3\}$ have considerable intensities of the order of $I_{1,n}/2$. Therefore, their sum greatly exceeds $I_{1,n}$. Even higher orders in the range $-20 \lesssim m \lesssim 20$ also have sizable intensities, and even higher orders (not depicted) still have tiny contributions, further emphasizing the broadness of the m distribution. Interestingly, though not surprisingly, different m components contribute strongly at different radii. In addition, the theoretically predicted linear increase of both the dominant $m \neq 0$ contributions as well as the m spread in the scattering potential are clearly visible.

Fig. 4 shows the dependence of several key quantities on the convergence semi-angle α (which is related to the beam size, see Fig. 2) of the incident beam as well as the thickness of the sample for the three simulated systems.

The most striking property is that while the overall features of the graphs are comparable between the three different systems, the numerical values differ greatly. Taking the maximum $\sigma[\hat{L}_z]$ as an example, it changes from $\simeq$16 for Si_3N_4 to $\simeq$36 for $Fe_{0.8}B_{0.2}$ to $\simeq$66 for Pt. A similar trend is visible for $\langle \hat{L}_z \rangle$. This phenomenon correlates nicely with the mass density of the three systems. Even though the atom density is comparable for $Si_3N_4$and $Fe_{0.8}B_{0.2}$ and is *lower* for Pt, the mass density *increases* from Si_3N_4 to $Fe_{0.8}B_{0.2}$ to Pt (see Table 1), owing to the fact that Pt atoms are much heavier than, *e.g.*, Fe atoms. Since heavier atoms generally scatter more strongly, it is logical that such systems produce stronger OAM deviations.

With respect to the changes of the expectation value $\langle \hat{L}_z \rangle$, Fig. 4 shows that the largest net OAM transfers occur for small and large convergence angles and the smallest deviations occur typically around the range 5–10 mrad, especially for

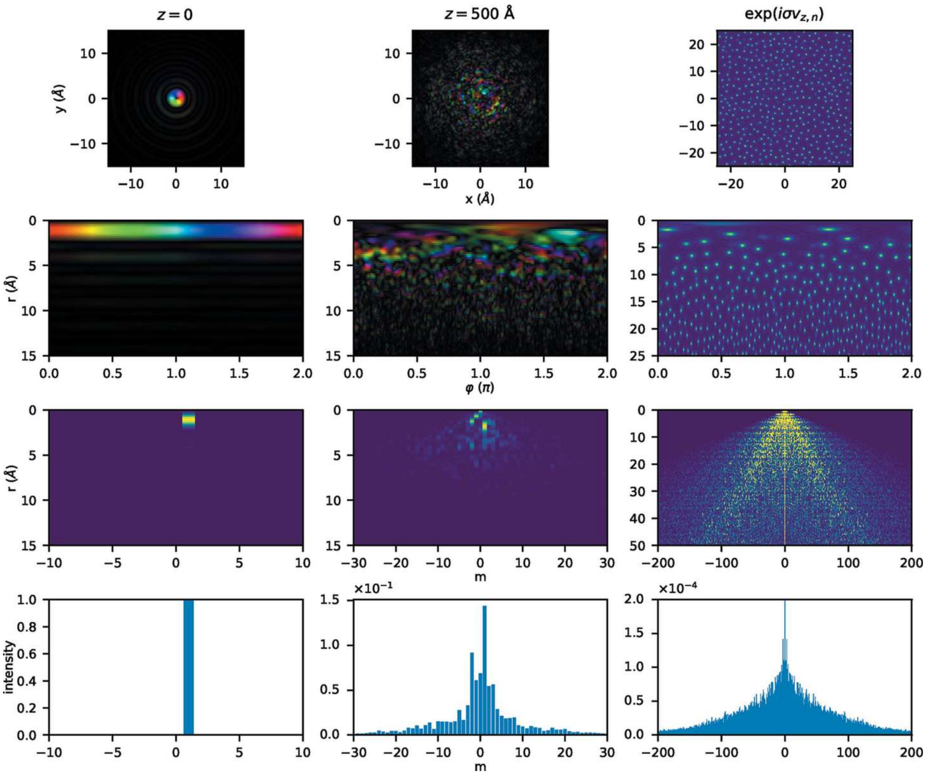

Figure 3
Some examples of the data produced by the simulations and during the analysis. Left: wavefunction at the incident plane of the sample, $z = 0$; center: wavefunction at the depth of $z = 500$ Å; right: scattering potential $\exp(i\sigma v_{z,n})$ of one slice. First row: data in Cartesian coordinates; second row: data in polar coordinates; third row: intensity of the $\exp(im\varphi)$ components as a function of m and r; fourth row: total OAM intensities integrated over r. For the wavefunctions shown in the first two rows, the phase is displayed as color (see Fig. 1) and the amplitude is displayed as brightness. For the scattering potential in the first two rows of the right column, the argument of the complex exponential is shown. The incident beam was a pure $m = 1$ vortex with a convergence semi-angle $\alpha = 10$ mrad incident on the amorphous Pt sample. In all cases, only a subset of the entire data set is shown and the contrast was enhanced to improve visibility.

small to medium thicknesses. This can be related to the size of the beam as it propagates through the sample. For small α, already the incident beam is large compared with interatomic distances and it stays that way all throughout the sample. Thus, large δm are possible from the very beginning of the propagation. For large α, the diameter of the incident beam is small, but the beam size increases considerably during propagation. Thus, although initially only small δm are viable, larger and larger δm become dominant as the beam propagates further through the sample. Conversely, a beam with a mid-range α represents a good compromise between small initial size and small growth during propagation, thereby restricting the maximal significant δm and, consequently, the variation of $\langle \hat{L}_z \rangle$. A similar result was also found for classical EMCD (where vortex beams are generated during inelastic scattering and subsequently analyzed interferometrically) in crystalline samples (Löffler & Hetaba, 2018).

For $\sigma[\hat{L}_z]$, *i.e.* the OAM uncertainty or, equivalently, the spread of the m distribution, the picture is very similar. Small α lead to a very large increase in σ with thickness. For medium α in the range of 7 to 13 mrad, σ is smallest, while it increases again for large α.

Interestingly, the α dependence is different for the $m = 1$ intensity, which gives an indication of 'how much' of the original, incident-beam structure actually is present at a given thickness. Fig. 4 shows that $I_{1,n}$ obviously decreases with thickness, but is mostly independent of α. In other words: even though the net OAM and the m distribution depend strongly on the beam size through the convergence angle and although there is complex multiple scattering going on back and forth between different m components at different radii (as visible from Fig. 3), the *overall* intensity of the $m = 1$ component seems to be fairly predictable.

To investigate the intensity of different m components as well as the expectation value in more detail, Fig. 5 shows graphs of the intensity of $m = 1$ as well as the adjacent components $m = 0, 2$ and $\langle \hat{L}_z \rangle$ for different convergence semi-angles α as a function of thickness. The adjacent components were selected because, for applications that depend on the fact that the beam is in an $m = 1$ eigenstate (such as, *e.g.*, EMCD), typically close-lying other components are more difficult to separate than far-removed ones. As an example, an $m = 100$ vortex would have practically zero intensity everywhere where an $m = 1$ vortex is strong, thus making it easy to separate and block, *e.g.*, by an aperture.

As before, the overall behavior of the curves is roughly similar for the m components of all three studied systems, except for the scale of the thickness dependence, which, again, is more dramatic for heavier specimens. Nevertheless, there are several noteworthy aspects visible in the graphs. In the first several ångströms, the decay of the $m = 1$ intensity as well as the increase of the adjacent components are practically linear. This is to be expected as, for a dominant $m = 1$ component, the transitions $1 \mapsto 0$ and $1 \mapsto 2$ will be much more probable than the scattering $0 \mapsto 1$, $0 \mapsto -1$ *etc.* However, after several ångströms, all depicted components start to deviate from their linear behavior. The $m = 1$ intensity decrease starts to slow down as soon as it reaches $\simeq$70% of

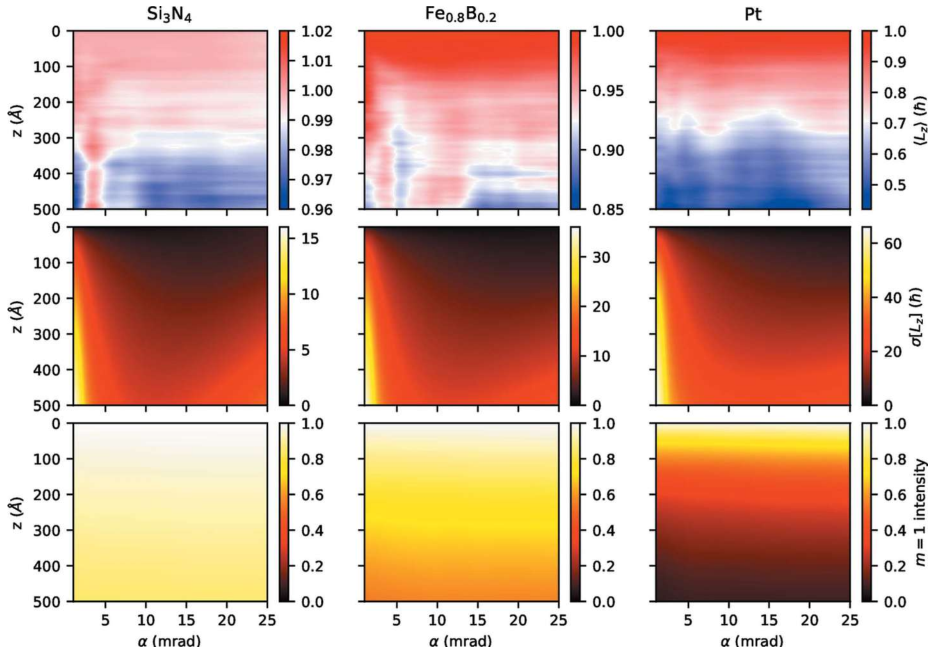

Figure 4
Behavior of the OAM as a function of thickness z and convergence semi-angle α for an incident $m = 1$ vortex beam for three different samples. Left: Si_3N_4, center: $Fe_{0.8}B_{0.2}$, right: Pt. Top: OAM expectation value $\langle \hat{L}_z \rangle$, middle: standard deviation of the OAM $\sigma[\hat{L}_z]$, bottom: intensity of the $m = 1$ component. Note the different color bar ranges. All data were averaged over multiple simulation runs.

the initial intensity, while the $m = 0, 2$ intensities become almost constant somewhere in the range of 10–30%. As the thickness increases, the $m = 0, 2$ components seem to asymptotically tend towards a similar behavior as the $m = 1$ component, as is visible for Pt at α = 25 mrad and, to some degree, already at α = 10 mrad. Note that, in all cases, the variation over several runs clearly indicates that the results are statistically significant, although the variability naturally is larger for larger mass density.

As already shown in Fig. 4, the decrease in $m = 1$ intensity does not depend strongly on the convergence angle. However, the increase of the adjacent components is influenced by the convergence angle. At the same time, the statistical uncertainty increases for increasing convergence angles (*i.e.* smaller beam waists). This can be attributed to the fact that for sufficiently small beams (*i.e.* smaller than the interatomic distance), the propagation behavior is crucially dependent on the (random) relative position of the beam with respect to close-by atoms, whereas for large beams, the effect is averaged over many atoms.

Another interesting result can be found in the behavior and statistical variation of the expectation value $\langle \hat{L}_z \rangle$. For Si_3N_4, the deviation from $\hbar$ is marginal and fairly well contained in the statistical error. For heavier systems, the deviation from $\hbar$ becomes much stronger – with a general trend towards decreasing $\langle \hat{L}_z \rangle$ – but also the statistical variation between different simulations increases dramatically.

5. Discussion

Whether the results presented here are encouraging or discouraging depends on the application at hand, the system under investigation, and the chosen experimental parameters.

If pure vortex beams are required, low mass densities as in the case of Si_3N_4 and low thicknesses are definitely preferable in order to retain a high intensity in the m component of the incident beam as well as little variation for different atom configurations. This also implies that holographic phase masks fabricated on a thick Si_3N_4 membrane can be subject to a considerable loss of mode purity.

If a high net OAM transfer is sought (*e.g.* in the case of nanoparticle manipulation), high mass densities as in the case of Pt as well as thick samples and medium convergence angles should be used. This ensures a large OAM transfer while retaining moderate statistical variations for different atom positions.

It should be noted that real sample densities, interatomic bond lengths and scattering strengths may differ from the ones presented here, *e.g.* due to the use of different materials. In addition, the sample density is influenced by deposition and

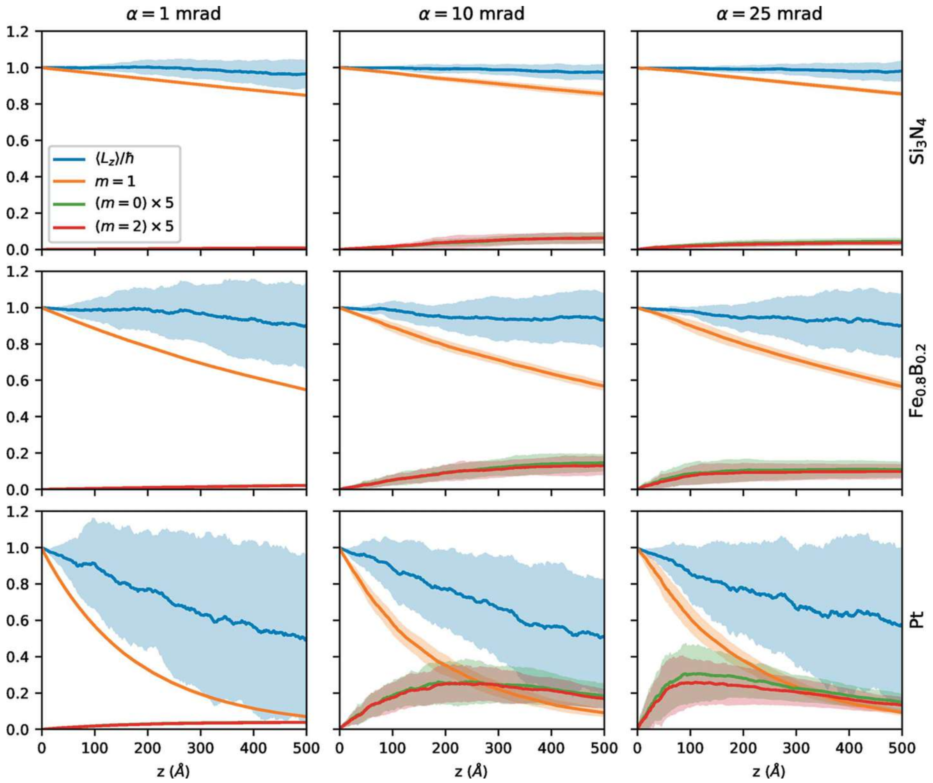

Figure 5
Expectation value $\langle \hat{L}_z \rangle$ and total intensities of the $m = 0, 1, 2$ components for Si_3N_4 (top), $Fe_{0.8}B_{0.2}$ (middle) and Pt (bottom) for α = 1 mrad (left), α = 10 mrad (center) and α = 25 mrad (right) as a function of thickness z. The intensities of the $m = 0$ and the $m = 2$ components have been magnified by a factor of 5 as indicated in the legend to improve visibility. The shaded areas indicate one standard deviation as derived from multiple simulations.

preparation parameters. However, the simulations presented in this work span from fairly low to quite high mass densities and scattering strengths, thus giving a general insight into how other samples will behave in general.

All the simulations presented in this work were performed under ideal conditions, including no incoherent source size broadening (ISSB), no atom movement and no lens aberrations. Both ISSB and atom movement would lead to an effectively different relative position between the beam and the atoms for each electron in the beam. This is conceptionally equivalent to the averaging over several random atom configurations as done in this study. Lens aberrations generally lead to a coherent broadening of the beam compared with the ideal case. While in such a situation the details of the amplitude and phase of the beam change, the overall results should be the same as those presented here when considering the appropriate beam size (see Fig. 2).

6. Conclusion and outlook

In this work, we presented extensive simulations of the propagation of electron vortex beams through amorphous materials. To that end, we have rewritten the multislice approach in cylindrical coordinates to get some theoretical insight into the vortex propagation, such as the beam-size dependence of the redistribution of intensity between different m components and the possibility of net OAM transfer despite the fact that the probabilities for transferring $\pm\delta m\hbar$ are (approximately) equal. In addition, we have also described the influence of the point-group symmetry on the vortex propagation.

The numerical simulations were performed for the three amorphous model systems Si_3N_4, $Fe_{0.8}B_{0.2}$ and Pt for a wide range of convergence semi-angles and thicknesses. Besides corroborating the theoretical results, the numerical data allowed us to quantify the net OAM transfer, the spread of vortex components that is related to the uncertainty principle and, thus, the purity of a vortex state, as well as the intensity behavior of the most important vortex components. The results showed that in order to retain high purity upon propagation, low-mass-density samples with small thickness should be chosen, while large net OAM transfers can best be achieved in heavy, thick samples. In both cases, intermediate convergence semi-angles around $\alpha \sim 10$ mrad proved beneficial.

The results presented in this work will allow theoreticians and experimentalists alike to choose the material for their studies with electron vortices more efficiently. Although this work does not completely replace full simulations for future studies, it does give some general insight into the propagation behavior of EVBs and makes predictions for a large range of systems and experimental parameters. As such, it promises to contribute to future enhancements not only of the fabrication but also of the applications of EVBs.

Funding information

TS acknowledges financial support by the Austrian Academy of Science (ÖAW) for the DOC scholarship and the 'Hochschuljubiläumsstiftung der Stadt Wien' (project H-294689/2016). The authors acknowledge TU Wien University Library for financial support through its Open Access Funding Programme.

References

Bliokh, K. Y., Dennis, M. R. & Nori, F. (2011). *Phys. Rev. Lett.* **107**, 174802.

Franke-Arnold, S., Barnett, S. M., Yao, E., Leach, J., Courtial, J. & Padgett, M. (2004). *New J. Phys.* **6**, 103.

Grillo, V., Carlo Gazzadi, G., Karimi, E., Mafakheri, E., Boyd, R. W. & Frabboni, S. (2014). *Appl. Phys. Lett.* **104**, 043109.

Guzzinati, G., Béché, A., Lourenço-Martins, H., Martin, J., Kociak, M. & Verbeeck, J. (2017). *Nat. Commun.* **8**, 14999.

Harvey, T. R., Pierce, J. S., Agrawal, A. K., Ercius, P., Linck, M. & McMorran, B. J. (2014). *New J. Phys.* **16**, 093039.

Idrobo, J. C., Rusz, J., Spiegelberg, J., McGuire, M. A., Symons, C. T., Vatsavai, R. R., Cantoni, C. & Lupini, A. R. (2016). *Adv. Struct. Chem. Imag.* **2**, 5.

Juchtmans, R., Béché, A., Abakumov, A., Batuk, M. & Verbeeck, J. (2015). *Phys. Rev. B*, **91**, 094112.

Kirkland, E. J. (1998). *Advanced Computing in Electron Microscopy*. New York: Plenum Press.

Löffler, S. (2013). PhD thesis, Vienna University of Technology. http://permalink.obvsg.at/AC11224780.

Löffler, S. & Hetaba, W. (2018). *Microscopy*, **67**(1), i60–i71.

Löffler, S., Motsch, V. & Schattschneider, P. (2013). *Ultramicroscopy*, **131**, 39–45.

Löffler, S. & Schattschneider, P. (2012). *Acta Cryst.* A**68**, 443–447.

Lubk, A., Clark, L., Guzzinati, G. & Verbeeck, J. (2013). *Phys. Rev. A*, **87**, 033834.

Rusz, J., Bhowmick, S., Eriksson, M. & Karlsson, N. (2014). *Phys. Rev. B*, **89**, 134428.

Schachinger, T., Löffler, S., Steiger-Thirsfeld, A., Stöger-Pollach, M., Schneider, S., Pohl, D., Rellinghaus, B. & Schattschneider, P. (2017). *Ultramicroscopy*, **179**, 15–23.

Schachinger, T., Löffler, S., Stöger-Pollach, M. & Schattschneider, P. (2015). *Ultramicroscopy*, **158**, 17–25.

Schattschneider, P., Löffler, S., Stöger-Pollach, M. & Verbeeck, J. (2014). *Ultramicroscopy*, **136**, 81–85.

Schattschneider, P., Schachinger, T., Stöger-Pollach, M., Löffler, S., Steiger-Thirsfeld, A., Bliokh, K. Y. & Nori, F. (2014). *Nat. Commun.* **5**, 4586.

Schattschneider, P., Stöger-Pollach, M., Löffler, S., Steiger-Thirsfeld, A., Hell, J. & Verbeeck, J. (2012). *Ultramicroscopy*, **115**, 21–25.

Schattschneider, P. & Verbeeck, J. (2011). *Ultramicroscopy*, **111**, 1461–1468.

Shiloh, R., Lereah, Y., Lilach, Y. & Arie, A. (2014). *Ultramicroscopy*, **144**, 26–31.

Verbeeck, J., Tian, H. & Schattschneider, P. (2010). *Nature*, **467**, 301–304.

Verbeeck, J., Tian, H. & Van Tendeloo, G. (2013). *Adv. Mater.* **25**, 1114–1117.

Xin, H. L. & Zheng, H. (2012). *Microsc. Microanal.* **18**, 711–719.

Part IV

Quantum Microscopy

Advanced TEM characterization techniques come in many shapes, forms, and fashions, all with their unique benefits and drawbacks. At the same time, all such techniques have a few things in common. Most noteworthy in the context of this work are the following two fundamental aspects: first, novel methods need to be based on a thorough theoretical foundation to be reliable, quantifiable, and reproducible. Second, the experimentally achievable SNR needs to be good enough to distinguish the signal of interest — which is often faint — from any background and artifacts.

In light of the necessity of a solid theoretical foundation, it may be surprising that a process as fundamental and ubiquitous as the deflection of an electron beam in a magnetic lens is typically not modeled fully quantum-mechanically. In most cases, either the trajectory of a classical, point-like particle is used, or the action of the lens is replaced by a Fourier transform (to map the incident wavefunction to the back-focal plane) with any small deviations from perfect focus subsequently being realized by short-range Fresnel propagation. While this has worked well for "classical TEM", it is not at all guaranteed to work in general, especially with modern peculiarly shaped beams (such as EVBs), or with spin-polarized beams [65].

In chapter 11, a full quantum-mechanical simulation of a magnetic lens based on a Landau-state expansion is described. Landau states are non-diffracting Laguerre-Gauss states, which form an orthonormal basis and are eigenfunctions of the Hamiltonian with a homogeneous magnetic field. For an inhomogeneous magnetic field (as present in a lens), time-dependent scattering needs to be introduced between different Landau states. The numerical treatment is still quite challenging due to the large number of Landau components that need to be considered. However, the results of this new method agree well with existing calculations (e.g. based on particle trajectories or Fourier transforms) for conventional beams, while also predicting interesting new behavior for "unusual" beams to be experimentally observed in the future. Hence, my work paves the way for a full quantum-mechanical treatment of the electron beam all the way from its source through the microscope and sample to the detector.

The second aspect — the need to improve the achievable SNR — is ubiquitous in TEM and EELS. Especially for any kind of atomic resolution work, regardless of whether one employs well-established, "classical" techniques or novel methods, the achievable signal is limited by instrument and sample stability in the broadest sense. For instance, drift and beam jitter limit the maximum effective exposure time per data point. To increase the signal (and therefore the SNR), one could increase the beam current, but only up to the point where the sample is significantly damaged by the beam in a time frame comparable to the measurement duration. With the high currents and small foci available nowadays, this limit — which has long been a major hurdle when investigating beam-sensitive materials and biological samples — can even be reached in routine experiments on resilient material science samples such as $SrTiO_3$.

It is worth noting that there are ways to reduce or even eliminate certain damage mechanisms (e.g., by reducing the acceleration voltage [22] or working in aloof mode [13]), but usually at the cost of worse spatial resolution. Recent advancements in detector instrumentation, most notably the development and increasing adoption of direct electron detection to avoid read-out noise, have improved matters. Of course, this is most beneficial when measuring with an overall low dose per data point in which case the read-out noise with conventional detectors is significant. Especially in cases in which (drastic) oversampling can be employed[1], having a purely shot-noise limited dataset enables the efficient use of all sorts of post-processing techniques such as principle component analysis (PCA). However, in cases in which oversampling is not possible or not desirable and in which the measured signal needs to be large (and, therefore, the shot-noise is the dominant noise contribution anyway), the benefits of direct detection are far less obvious. One example of such a case is the real-space mapping of orbital information (see part I), which naturally operates at the limit of the current instrumental spatial resolution, thereby preventing oversampling while still requiring sufficient signal to distinguish (potentially small) fine structure variations. Another example is EMCD (see part II), which also requires the identification of small changes in the fine structure and, thus, large signals. As EMCD is generally recorded at high energy-losses and at at least two different places (far) away from the diffraction spots, long exposure times are necessary which preclude useful oversampling.

Apart from increasing the incident dose, using better detectors, and employing post-processing on oversampled data, there is another way to improve the SNR that is largely unused in electron microscopy so far: using a better measurement basis. All quantum mechanical measurement processes project the beam's state onto a specific basis — the measurement basis — determined by the detector as well as any post-specimen lenses. Typical examples include the real space basis $|\boldsymbol{r}\rangle$ in imaging mode or the reciprocal space basis (momentum basis) $|\boldsymbol{k}\rangle$ in diffraction mode. To understand how powerful the correct basis is, consider the toy example of determining the lattice spacing of a single crystal (fig. 4). When measuring in a real-space basis (e.g., using high-resolution TEM (HRTEM)), the resulting signal can be a small oscillation on a large background signal, especially when facing low stability without aberration correction. Hence, shot-noise is dominantly caused by the large background signal and can easily eclipse the small signal of interest. Conversely, switching just a single lens in this setup is enough to measure in a reciprocal space basis, where clearly visible, distinct diffraction spots are present. These diffraction spots rise well above the noise level and enable an easy determination of the lattice spacing. This simple example shows how powerful the choice of measurement basis can be: if the basis is chosen poorly, electrons are distributed more or less evenly over the entire field of view and the signal of interest is hidden in minute variations that are often at or below the noise threshold. Conversely, choosing a good basis results in all electrons that carry the information of interest to be focused in (ideally) a single measurement channel, with all other electrons being recorded in other channel(s). With such a correlation

---

[1] Typical examples include mapping a property such as chemical composition at a spatial resolution significantly better than the length scale at which the investigated property varies and fitting a well-established model with few free parameters such as an EELS power-law background to many (energy) channels. As oversampling generally implies redundancy, it allows to spread a given number of electrons over many channels. This may lead to, e.g., reducing beam-induced damage to the sample.

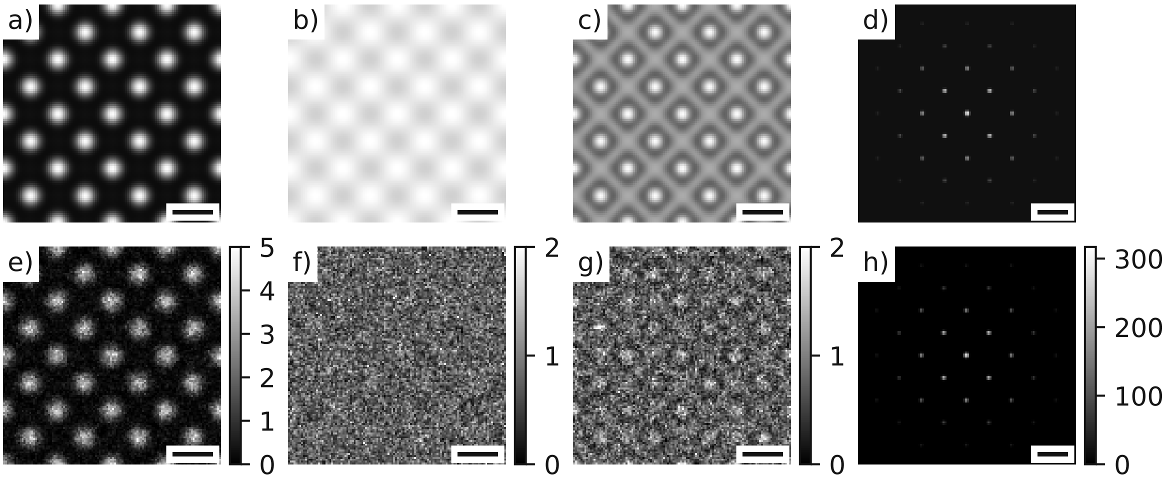

Figure 4.: Simulation of HRTEM images and diffraction patterns of Si with 300 keV electrons. a) Ideal HRTEM (without aberrations, instabilities, decoherence, etc.). b) HRTEM image simulated for an uncorrected ThermoFisher Tecnai microscope. c) HRTEM image for a C_s-corrected ThermoFisher Titan microscope. d) Diffraction pattern. a–d were simulated for infinite incident dose using the program JEMS [87]. The scale bars in a–c denote 2 Å, the scale bar in d denotes 5/nm. e–h) Same as a–d but with shotnoise corresponding to $5 \times 10^4\,\mathrm{e}^-$ in the image (for e–g, this corresponds to a dose of roughly $100\,\mathrm{e}^-/\text{Å}^2$). Colorbar values indicate e^-/px; all images have 256 px × 256 px.

between the measurement channel and the property of interest, determining the value of the property comes down to the relatively trivial task of identifying how many electrons were recorded in which channel.

In general, the solution is not as simple as switching a lens as in the example outlined above. But the key requirement to optimal measurements fundamentally is the same: one needs a suitable unitary transformation that transforms the beam's quantum state in such a way that the detector channels correspond to the chosen measurement basis. In the example above, switching the lens effectively resulted in performing a Fourier transformation of the wave function, resulting in the detector measuring the wave's different Fourier components (i.e., its momentum distribution). An example of a less-commonly used unitary transformation is the log-polar transformation for measuring the OAM distribution of EVBs [49]. However, for arbitrary wave functions (and possibly density matrices in the case of inelastic scattering), no general unitary transformation formalism is known, yet.

In chapter 12, I take a first step towards the development of general unitary transformations by describing a way of implementing arbitrary unitary transformations for the special case of a two-state quantum system. My approach builds on and generalizes the method described in chapter 9 for creating EVBs, but allows for arbitrary mappings of states on the Bloch sphere. It is noteworthy that the described method works in commercially available TEMs without any modification or addition of custom elements. As such, my work paves the way for the future development of more general unitary transformations on higher-dimensional quantum systems that may one day lead to vastly improved SNR as well as emerging new characterization techniques.

In summary, my work presented in this part significantly advanced the quantum mechanical understanding of how electron beams propagate through the microscope and how quantum-mechanical transformations can be used to optimize measurements. This paves the way for improving the efficiency and SNR of all advanced characterization techniques and for designing custom quantum scattering experiments in the future.

Chapter 11

A quantum propagator for electrons in a round magnetic lens

S. Löffler, A.-L. Hamon, D. Aubry, and P. Schattschneider

Advances in Imaging and Electron Physics 215 (2020) 89–105
10.1016/bs.aiep.2020.06.003

CHAPTER THREE

A quantum propagator for electrons in a round magnetic lens

Stefan Löffler[a,*], **Ann-Lenaig Hamon**[b], **Denis Aubry**[b], **Peter Schattschneider**[c]
[a]University Service Centre for Transmission Electron Microscopy, TU Wien, Wien, Austria
[b]Centralesupelec, Université Paris-Saclay, Gif-sur-Yvette Cedex, France
[c]Institute of Solid State Physics, TU Wien, Wien, Austria
*Corresponding author. e-mail address: stefan.loeffler@tuwien.ac.at

Contents

1. Introduction

Lens designers generally rely on classical approaches assuming point like electrons, implicitly neglecting diffraction effects. On the other hand, in almost all applications of electron microscopy, diffraction effects are central to many questions and problems. The "missing link" is normally filled by invoking Fourier transforms between object and image or diffraction planes, including defocus, astigmatism and other lens aberrations as phase factors. This thinking inherently takes for granted that electrons in a magnetic field behave as light does in an optical lens. In the classical geometric-optical limit this has been demonstrated many times (e.g. Glaser, 1952; Hawkes & Kasper, 2017; Pozzi, 2016; Reimer, 2008; Rose, 2009). Although the formal similarity of the Schrödinger equation with the Helmholtz equation in paraxial approximation suggests the applicability of

Advances in Imaging and Electron Physics, Volume 215
ISSN 1076-5670
https://doi.org/10.1016/bs.aiep.2020.06.003

classical wave optics for electrons, this is less evident for the non-paraxial case or for thick lenses where the object might be situated in the lens field. Apart of some formal solutions (Dattoli, Di Lazzaro, & Torre, 1990; Jagannathan & Khan, 1996; Khan & Jagannathan, 1995) of the general case of an electron in magnetic and electric lens fields, explicit formulations of the electron propagator in round lenses (e.g. Hawkes & Kasper, 2017; Pozzi, 1995) are still based on the work of Glaser (1952) and Glaser and Schiske (1953), published in 1952 and 1953, using a Fresnel propagator ensuing from a spherical basis.

An obstacle to this approach of using a Fresnel propagator is the need to rescale the propagation distances. To this aim, two particular solutions of the Schrödinger equation must be found. They correspond exactly to the field and axial rays in the geometric-optic description which are calculated classically beforehand.

The Glaser-Schiske solution was published in German and went largely unnoticed in the field. Thanks to a profound review of the multislice approach as compared to Glaser's work by Pozzi (1995, 2016), many details and subtle differences between electrons in a lens field and the wave optical approach were revealed.

The increasing importance of phase shaping in electron microscopy (Grillo et al., 2014; McMorran et al., 2011; Uchida & Tonomura, 2010; Verbeeck, Tian, & Schattschneider, 2010) necessitates a rethinking of how electrons can be described better than in a spherical wave basis. For instance, the peculiar rotation characteristics of electrons with quantized angular momentum was explained assuming propagation in a constant magnetic field (Bliokh, Schattschneider, Verbeeck, & Nori, 2012; Guzzinati, Schattschneider, Bliokh, Nori, & Verbeeck, 2013; Schachinger, Löffler, Stöger-Pollach, & Schattschneider, 2015; Schattschneider et al., 2014) whereas in reality, the experiments were performed in the approximately bell-shaped magnetic field of an objective lens in a transmission electron microscope (TEM). It is not known so far to which extent the non-constant field changes the predictions. Another problem is the accumulation of the Gouy phase in a convergent beam, important for vortex generation with quadrupole lenses (Kramberger et al., 2019; Schattschneider, Stöger-Pollach, & Verbeeck, 2012). An exact solution is only known for Laguerre-Gauss beams in free space or in a constant magnetic field. As a third example, we mention a recent proposal suggesting the use of electron vortices in a two-state Landau basis for the manipulation of qubits in the electron microscope (Löffler, 2020). Almost a century after the birth of electron microscopy, such questions revitalize the search for an alternative quantum description of the electron propagator in magnetic lenses.

A first clue in this quest is the realization that spherical waves and the Fresnel propagator are both good for describing electron propagation in free space but not necessarily for modeling propagation in the presence of a magnetic field where a rescaling of the propagation distances in terms of field and axial rays is mandatory. An obvious approach is to attack the problem numerically with a finite element code, feeding in the 3D- (or 2D-, in case of cylindrical symmetry) magnetic field of the lens. First trials were promising, but severe failure was observed close to focal points, without any doubt caused by the breakdown of the WKB approximation. (A prerequisite of the WKB approximation is that the amplitude varies slowly relative to the phase which is not the case close to a focal point.) Looking for an alternative, it is not too far fetched to choose a Landau state basis set. Already in 1983, Howie (1983) advertised this idea but to our knowledge it was not followed any further. Indeed, in a Landau basis, solutions are harmonic oscillators, and many features such as the well known oscillations of an electron wave packet in a constant magnetic field are easily derived.

The difficulty lies in the field variation along the electron trajectory in a TEM, a fact that renders the basis functions time dependent as the wave packet passes the lens. To our surprise, we find that even in this case, the Hamilton operator remains simple, allowing rapid diagonalization.

In order to demonstrate the method, we choose a condensor-objective — a typical thick lens — which is important from a practical point of view in electron microscopy, and is at the same time sufficiently clear to show the salient features of the present approach. It should be stressed that we do not pretend to solve the general case of a round lens numerically in this work. Questions of numerical stability, higher order relativistic corrections, as well as the inclusion of spin and aberrations go beyond the scope of this paper.

2. Theory

The classical Hamilton operator in the presence of an electromagnetic field reads

$$\hat{H} = \frac{\hat{\mathbf{p}}^2}{2m} + eV \tag{1}$$

where $\hat{\vec{\mathfrak{p}}} = \hat{\vec{p}} - e\vec{A}$ is the covariant or mechanical momentum operator, m is the electron *rest* mass, and $e = |e|$ is the elementary charge. We note for later use that in real space, $\hat{\vec{p}} = -i\hbar\nabla$.

The Schrödinger equation is not Lorentz invariant. The Dirac equation gives a fully relativistic account of charged particles in a field. Expansion of the small component of the Dirac spinor ("χ") up to $\beta = v/c$ yields the Pauli equation. Expansion up to β^3 yields (Schiff, 1999)

$$\hat{H} \doteq \frac{\hat{\vec{\mathfrak{p}}}^{\,2}}{2m} - \frac{\hat{\vec{\mathfrak{p}}}^{\,4}}{8m^3c^2} + eV + \mathrm{LS} + \mathrm{D}.$$

The second term is the relativistic correction to the kinetic energy, V is the electrostatic potential, LS is the spin-orbit coupling term, and D is the Darwin term. The 3 last terms are absent in our problem. (We assume a vanishing electrostatic field and deal with scalar electrons without spin. Note that this is the relativistically corrected Pauli equation (Schiff, 1999).) We can write

$$\hat{H} \doteq \frac{\hat{\vec{\mathfrak{p}}}^{\,2}}{2m}\left(1 - \frac{\hat{\vec{\mathfrak{p}}}^{\,2}}{4m^2c^2}\right).$$

For narrow wave packets of well defined kinetic energy E_{kin} — which we will use here —, the bracket can be approximated as

$$1 - \frac{\hat{\vec{\mathfrak{p}}}^{\,2}}{4m^2c^2} \approx 1 - \frac{E_{\mathrm{kin}}}{2E_0} = \frac{3E_0 - E}{2E_0} = \frac{3-\gamma}{2},$$

and so

$$\hat{H} \approx \frac{\hat{\vec{\mathfrak{p}}}^{\,2}}{2m^*}$$

with

$$m^* = m \cdot \frac{2}{3-\gamma}.$$

(Note that $\lim_{\gamma\to 1} 2/(3-\gamma) = 1 + E_{\mathrm{kin}}/(2E_0)$ which is Reimer's relativistic correction factor (Reimer, 2008).) Separating the in-plane components, the Hamiltonian can be written as

$$\hat{H} \approx \hat{H}_\perp + \frac{1}{2m^*}\hat{p}_z^2,$$

with

$$\hat{H}_\perp = \frac{1}{2m^*}(\hat{\vec{p}}_\perp - e\vec{A})^2. \tag{2}$$

(Here, we assume that z variations of the magnetic field are small compared to those of the (narrow) electron wave packet and can therefore be neglected.) The Hamiltonian in turn gives rise to the propagator

$$\hat{P}(t) = e^{i\hat{\Phi}}$$

with

$$\hat{\Phi} = \frac{1}{\hbar}\int \hat{H}dt \tag{3}$$

which will be the central quantity in this paper as it allows to obtain the time dependent wave function

$$|\psi(t)\rangle = \hat{P}(t)\,|\psi_0\rangle$$

from an initial condition ψ_0.

Assuming that the magnetic field is uniform within the narrow wave packet and the paraxial region, the vector potential in Coulomb gauge takes the form

$$\vec{A} = \frac{rB_z}{2}\vec{e}_\varphi. \tag{4}$$

Thus, Eq. (2) transformed into a co-rotating coordinate system can be rewritten in paraxial approximation as (Howie, 1983)

$$\hat{H}_\perp = \frac{1}{2m^*}\left(\hat{p}_x^2 + \frac{e^2B_z^2}{4}\hat{x}^2 + \hat{p}_y^2 + \frac{e^2B_z^2}{4}\hat{y}^2\right). \tag{5}$$

This is the Hamilton operator of a harmonic oscillator, the solution of which are Hermite-Gauss functions (or Landau states). Whereas Cartesian coordinates are appropriate for objects with translational symmetry such as crystals, we prefer to use cylindrical coordinates for obvious reasons. The solutions are now Laguerre-Gauss functions (Bliokh et al., 2017), characterized by two discrete quantum numbers n, l:

$$LG_{n,l} = \left(\frac{r}{w}\right)^{|l|} L_n^{|l|}\left(\frac{2r^2}{w^2}\right)\exp\left(-\frac{r^2}{w^2}\right)e^{il\phi}. \tag{6}$$

Here, $L_n^{|l|}$ are generalized Laguerre functions, and the magnetic waist is

$$w = \sqrt{\frac{4\hbar}{eB}}. \tag{7}$$

The eigenvalue of the canonical angular momentum is $\hbar l$, and $N = n + |l| + l + 1$ denotes the Nth Landau energy level.

The structure of $\hat{H}$ suggests a basis system consisting of Landau states $|nl\rangle$ in the plane perpendicular to the cylinder axis z and plane waves $|k\rangle$ propagating along z. In the $|k\rangle$ subspace, $\hat{H}$ is diagonal:

$$\langle nlk|\hat{H}|n'l'k'\rangle = \delta_{kk'}\left(\langle nl|\hat{H}_\perp|n'l'\rangle + \delta_{nn'}\delta_{ll'}\frac{\hbar^2k^2}{2m^*}\right).$$

With the vector potential Eq. (4) and squaring the momentum operator,

$$(-i\hbar\nabla_\perp - e\vec{A})^2 = -\hbar^2\nabla_\perp^2 + i\hbar e(\underbrace{(\nabla_\perp\cdot\vec{A})}_{0} + \vec{A}\cdot\nabla_\perp + \vec{A}\cdot\nabla_\perp) + e^2\vec{A}\cdot\vec{A}, \quad (8)$$

the in-plane Hamiltonian (in cylindrical coordinates (r,φ)) takes the form

$$\hat{H}_\perp = \frac{1}{2m^*}\left(-\hbar^2\nabla_\perp^2 + \frac{e^2r^2B_z^2}{4} + 2i\hbar e\frac{rB_z}{2r}\partial_\varphi\right). \quad (9)$$

With the Larmor frequency (the relativistic correction replaces m by m^*)

$$\Omega_L = \frac{eB_z}{2m^*}, \quad (10)$$

this can be written as

$$\hat{H}_\perp = -\frac{\hbar^2}{2m^*}\nabla_\perp^2 + \frac{m^*\Omega_L^2r^2}{2} + i\hbar\Omega_L\partial_\varphi. \quad (11)$$

As stated above, we observe a narrow wave packet, initially prepared at $z = 0$, propagating with velocity v along z in a magnetic field slowly varying with z. According to Ehrenfest's theorem (Ehrenfest, 1927), at time t, the packet arrives at $z = vt$, with an intensity that is essentially zero outside a narrow z range — see the subsection below. This means that in order to propagate the electron from $z_0 = 0$ to z_1, we need the propagator $P(t = z_1/v)$.

2.1 Wave packet

To get a general feeling for the possible dispersion of a narrow electron wave packet, we consider a Gaussian wave packet traveling through free space. Such a Gaussian wave packet in one dimension (z),

$$|Z(z, t=0)|^2 = e^{-z^2/(2\sigma^2)}$$

with variance σ^2, remains Gaussian, dispersing with time giving a probability distribution (Wikipedia contributors, 2020)

$$|Z(z,t)|^2 = e^{-(z-vt)^2/(2\sigma(t)^2)} \tag{12}$$

with

$$\sigma(t)^2 = \sigma^2\left(1+\left(\frac{\hbar t}{2m_0\sigma^2}\right)^2\right).$$

At 200 keV, the time to pass the column of a TEM is ca. 1×10^{-8} s. A wave packet of initially 0.1 μm extension (after the anode) spreads to ~ 1 μm at the objective lens, which is still a very small value compared to the extension of the lens field of some mm.

2.2 Time dependent Hamilton operator

As stated above, in order to describe the electron at any position z, one needs the time evolution from $t=0$ to $t=z/v$. Thus, $\hat{H}_\perp$ becomes implicitly time dependent because $B_z(z)=B_z(vt)$:

$$\hat{H}_\perp(t) = \frac{1}{2m^*}\left(-i\hbar\nabla_\perp - \frac{erB_z(vt)}{2}\vec{e}_\varphi\right)^2. \tag{13}$$

With the definition of the Larmor frequency (Eq. (10)) and the magnetic waist (Eq. (7)) at $z=0$,

$$w=\sqrt{\frac{4\hbar}{eB_0}}=\sqrt{\frac{2\hbar}{m^*\Omega_L(B_0)}}, \tag{14}$$

we may transform to the dimensionless variable $\rho = r/w$:

$$\hat{H}_\perp(t) = \frac{1}{2m^*}\left(-\frac{\hbar^2}{w^2}\nabla_\rho^2 + \frac{w^2e^2B_z(vt)^2}{4}\rho^2\right) + i\hbar\Omega_L(B_z(vt))\partial_\varphi. \tag{15}$$

With a little algebra

$$\hat{H}_\perp(t) = \hbar\Omega_L(B_0)\left(-\frac{\nabla_\rho^2}{4} + g(t)^2\hat{\rho}^2 + ig(t)\partial_\varphi\right) \tag{16}$$

where

$$g(t) = \frac{\Omega_L(B_z(vt))}{\Omega_L(B_0)} \approx \frac{B_z(vt)}{B_0} \tag{17}$$

and $B_z(0) = B_0$. Note that for $t = 0$, Eq. (16) is identical to Eq. (11). From here on, we assume that the electron wave is independent of φ, i.e., $l = l' = 0$, because we are dealing with electrons of vanishing topological charge. Therefore, the last term on the right hand side of Eq. (16) disappears.

2.3 Electron propagator

The phase factor (Eq. (3)) in the electron propagator can be evaluated as

$$\hat{\Phi} = \frac{1}{\hbar}\int_0^t \hat{H}_\perp(\tau)\,d\tau = \Omega_L(B_0)\,t\left(\hat{\rho}^2\,G(t) - \frac{1}{4}\nabla_\rho^2\right) \tag{18}$$

with

$$G(t) = \frac{1}{t}\int_0^t g^2(\tau)\,d\tau. \tag{19}$$

In the Landau basis $\{|n0\rangle\}$, the operators ∇_ρ^2 and $\hat{\rho}^2$ are both tridiagonal:

$$\nabla_\rho^2 := \langle n0|\nabla_\rho^2|m0\rangle = -\begin{bmatrix} 2 & 2 & 0 & 0 & \cdots \\ 2 & 6 & 4 & 0 & \\ 0 & 4 & 10 & 6 & \\ 0 & 0 & 6 & 14 & \\ \vdots & & & & \ddots \end{bmatrix}$$

$$\rho^2 := \langle n0|\hat{\rho}^2|m0\rangle = \frac{1}{2}\begin{bmatrix} 1 & -1 & 0 & 0 & \cdots \\ -1 & 3 & -2 & 0 & \\ 0 & -2 & 5 & -3 & \\ 0 & 0 & -3 & 7 & \\ \vdots & & & & \ddots \end{bmatrix}.$$

It is at once evident that $\hat{H}_\perp(t=0) = \hbar\Omega_L(B_0)(\hat{\rho}^2 - \frac{1}{4}\nabla_\rho^2)$ is diagonal with matrix elements

$$\langle n0|\hat{H}_\perp(t=0)|m0\rangle = E_{n0}\delta_{nm}$$

and eigenenergies

$$E_{n0} = \hbar\Omega_L(B_0)(2n+1)$$

which are a special case of the general expression (Bliokh et al., 2017)

$$E_{nl} = \hbar\Omega_L(B_0)\left(2n + \frac{|l|+l}{2} + 1\right).$$

For $t \neq 0$, $\hat{H}_\perp$ (as well as $\hat{\Phi}$) is no longer diagonal because of the factor $G(t)$. However, since $\hat{\Phi}$ is tridiagonal, the time evolution operator $\hat{P} = \exp(-i\hat{\Phi}(t))$ can easily be diagonalized. A unitary transform $\hat{U}$ that diagonalizes $\hat{\Phi}$

$$\mathrm{Diag}[\hat{\tilde{\Phi}}(t)] = \hat{U}\hat{\Phi}(t)\hat{U}^\dagger$$

also diagonalizes $\hat{P}$, such that

$$|\psi(t)\rangle = \hat{U}^\dagger \, e^{-i\,\mathrm{Diag}\left[\hat{\tilde{\Phi}}(t)\right]} \, \hat{U} \, |\psi_0\rangle \,. \tag{20}$$

For a Glaser field with half width at half maximum (HWHM) d and

$$B_z(z) = \frac{B_0}{1 + (z/d)^2}, \tag{21}$$

the time integral in Eq. (19) can be evaluated analytically, yielding

$$G(t) = \frac{1}{2}\left(\frac{1}{1 + (vt/d)^2} + \frac{d}{vt}\arctan(vt/d)\right). \tag{22}$$

(The Gouy phase $\arctan(vt/d)$ appears here intrinsically.)

3. Results

As a demonstration example, we choose a condensor-objective lens (lens parameter $k^2 = 3$) at 200 kV and $B_0 = 1.9$ T, a typical value for modern minilens-objective combinations. This case is of particular interest in the present context because it resembles a thick lens, *i.e.* the focal point is situated in a strong magnetic field, and we expect deviations from a wave optical approach that is based on thin lenses with constant refractive index. For the chosen parameters, the half width of the magnetic field Eq. (21) is calculated to (Glaser, 1952) $d = 3.0065$ mm. We assume a microprobe setup, i.e., parallel illumination at $z = 0$, where the object is normally situated. In this case, the geometric focal point is at $z = d$. The initial wave with an aperture of 300 nm radius is expanded into a Landau basis up to 42 coefficients, shown as dots in Fig. 1. Since sharp rims cause very slow convergence, the wave has been constructed with a slight apodization to suppress high orders (Fig. 2).

Evidently, the series expansion has a cutoff at coefficient number ~ 35. The wave is propagated to the focus via Eq. (20). The resulting radial probability distribution is shown in Fig. 3.

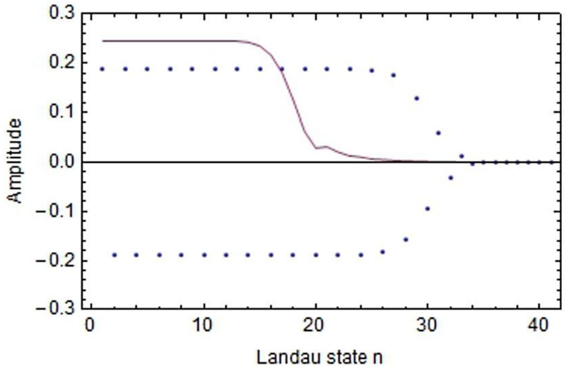

Figure 1 Expansion coefficients of the input wave (dots) and of the propagated wave at the focus (full curve).

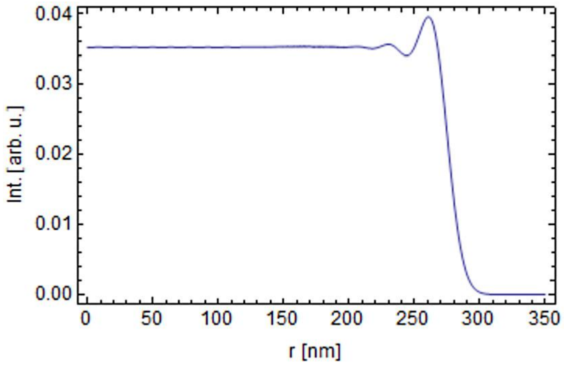

Figure 2 Input wave for an aperture with a 300 nm radius and with an apodized rim.

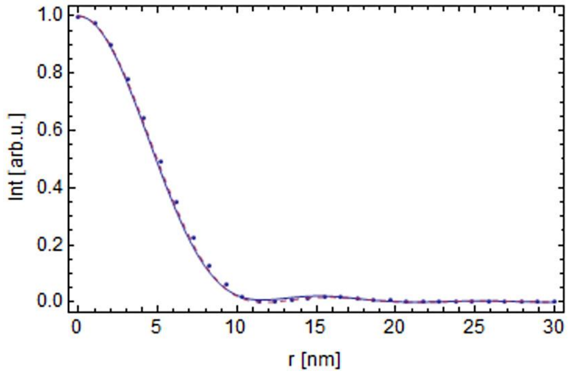

Figure 3 Input wave of Fig. 2, propagated to the focus (full line). Dots mark the wave optical Airy disk.

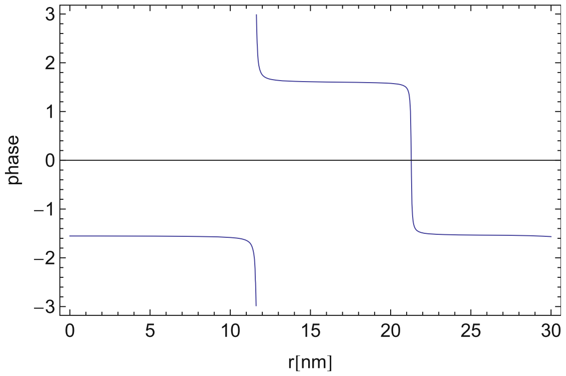

Figure 4 Radial phase structure at $z = 1.015\,d$.

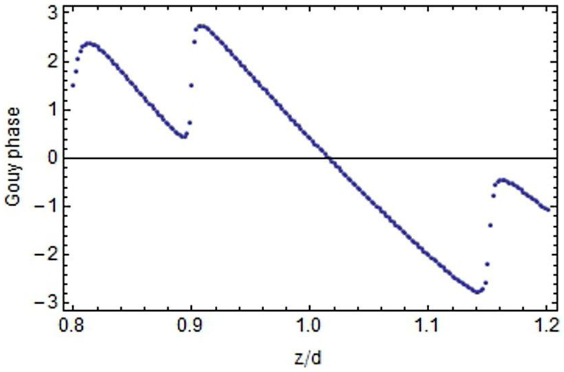

Figure 5 Gouy phase, linear in z as expected for a spherical wave close to the cross over (Born & Wolf, 1999).

The focus, found by inspection of the flat radial phase structure shown in Fig. 4, is at $1.017\,d$, confirming the expected phase jumps of π at the wave function nodes. The profile agrees well with the Airy disk computed from the wave optical convergence angle. The small deviations are caused by numerical problems with the high order Landau functions, evidenced by the kink at $n = 20$ in the otherwise smooth decay of the coefficients in Fig. 1.

The Gouy phase in the vicinity of the focus is linear in z as expected for a convergent spherical wave (Born & Wolf, 1999), see Fig. 5.

Our main result is Fig. 6, showing the evolution of the beam from the input plane to the focus and beyond. The geometric-optical ray starting at the beam radius (taking into account the apodized rim) is shown in red for comparison. The classical result is very close to the envelope of the prop-

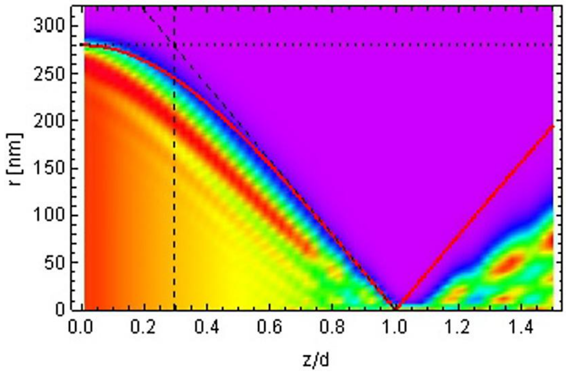

Figure 6 Convergent beam from the aperture (at $z = 0$) to the focus (at $z = d$) and beyond. The red line is the Glaser trajectory for the effective beam radius, taking into account the apodizing effect. The tangent defining the geometric convergence angle is dashed. The vertical line shows the principal plane for the exit wave in the geometric-optical approach.

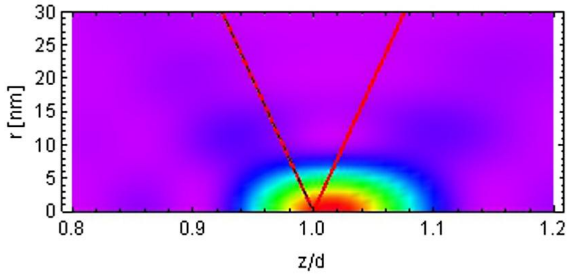

Figure 7 Zoom into the focal point of the coherent electron at 1.017 *d*. The deviation from the classical trajectory (red line) is clearly visible.

agating coherent electron. The bending of the beam in the Glaser field is clearly seen. However, the classical trajectory has a higher curvature in the left part, then becoming almost straight whereas the envelope homes in on the focus with slightly negative bending. This causes a flatter tangent at the focus and explains the smaller divergence thereafter. The wave packet is in focus shortly after the classical focal length. This can be better visualized when zooming in (Fig. 7). The effective focal width is 1.7% longer than the classical focus indicated by the red trajectory. The reason is probably twofold: numerical due to the limited number of the Landau expansion coefficients, and caused by the slightly different approximations for the relativistically corrected Schrödinger equation and for the classical trajectory which inevitably yields a point focus.

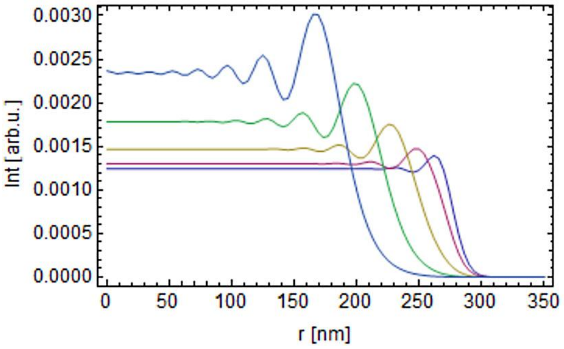

Figure 8 Radial intensity profiles at $z = 0, 0.1, 0.2, 0.3, 0.4\,d$. Note the Fresnel fringes at the rim.

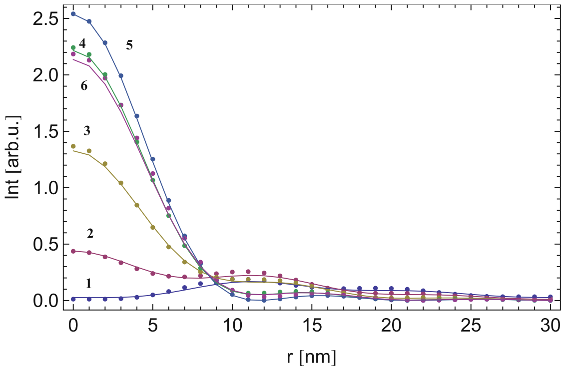

Figure 9 Radial intensity profiles close to the focus, at distances of $z = 0.92\,d$ to $1.02\,d$, numbered from 1 to 6. The dots are the results of the wave optical simulation, the full lines are cuts through Fig. 7 at the respective distances, squeezed by a factor of 1.33.

For completeness, we show some intensity profiles shortly after the initial plane (Fig. 8) and close to the focus (full lines in Fig. 9). For comparison, the dotted curves in Fig. 9 were obtained from a wave optical software based on the Fresnel propagator, developed in our group (Kramberger et al., 2019). The radial profile in focus — an Airy disk — is exactly recovered. However, it turned out that the decrease of the central maximum when withdrawing from the focus is steeper in the wave optical simulation. We found almost perfect agreement after rescaling the z values by a factor of 1.33. The reason for this discrepancy is not known. An indication is the flatter tangent of the convergent bundle seen in Fig. 6, a typical characteristic of Gaussian beams close to focus. It might also be that the weaker

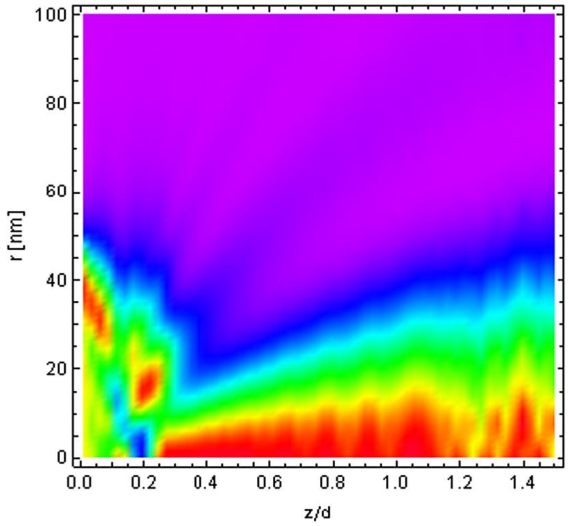

Figure 10 Evolution of the electron wave with an input aperture with 50 nm radius.

magnetic field at $z = d$ demands an expansion into a new Landau basis for better numerical stability.

Finally, we present the propagation with an aperture of 50 nm radius where diffraction effects should be strong, completely invalidating the geometric-optic interpretation. Indeed, Fig. 10 shows a completely different evolution of the beam. The envelope is drastically different from the geometric-optic prediction, with the narrowest waist at $\sim 0.3\,d$.

4. Conclusion

We have shown that a full quantum-mechanical treatment of the coherent propagation of an electron in a round lens field is surprisingly simple in a Landau basis. The envelope of the beam during propagation follows very accurately the geometric optic result, but shows differences that can be traced back to diffraction. The shift of the narrowest beam profile — a consequence of diffraction not present in ray optics — is clearly seen. The Airy disk expected from the Fourier transform of an aperture-limited plane wave is retrieved with high precision. We do not observe singularity problems as encountered within the WKB approximation, but small focus differences hinting towards different relativistic corrections. The steeper decrease of the axial maximum when withdrawing from the focus, seen in the wave optical simulation, is surprising. It might be related to higher order expansion coefficients, or to the fact that Fresnel propagation after the principal plane of a lens implicitly assumes a refractive index of 1 (vacuum) whereas the present approach works also for thick lenses, which is a condition deliberately defined for the chosen microprobe mode in a condensor-objective. Higher order approximations may shed light on this interesting finding.

It might be argued that an experiment to find the focus can clearly tell which of the two approaches is correct. Curiously, such an experiment is not as evident as it seems, for the simple reason that real lenses do not have the idealized bell-shaped magnetic field. In addition, the post-specimen optic shifts the real focal point to a virtual one. Finally, lens aberrations and the difficulty to measure the absolute position of the focal plane to an accuracy of 50 μm create prohibitive experimental conditions.

The calculations were carried out on a standard PC; diagonalization and propagation of the wave takes less than a second. However, numerical problems are encountered with Landau basis functions of order higher than about 30–40 due to the large magnitude of the competing r^{2n} and $\exp(-r^2)$ terms, limiting the present implementation to simple cases for didactic presentations of the principle.

The salient feature of the present approach is the simple form of the Hamiltonian (Eq. (16)) and the propagator phase (Eq. (18)) in a Landau basis. It is at once evident that the varying magnetic field induces transitions between the basis states. This is of interest for some recent suggestions, e.g. when the electron is to interact with microwave radiation (Poppe & Dunin-Borkowski, 2020), or the question whether or not cyclotron electrons can decay by spontaneous or induced emission of photons (Gabrielse & Dehmelt, 1985; Kaminer et al., 2016). An extension to realistic fields including lens aberrations, and to electrons with topological charge will be treated in a follow-up paper.

Acknowledgments

We thank G. Pozzi, P. Hawkes, and H. Kohl for most valuable discussions. Financial support by the Austrian Science Fund under projects P29687-N36 and I4309-N36 is gratefully acknowledged.

References

Bliokh, K., Ivanov, I., Guzzinati, G., Clark, L., Van Boxem, R., Béché, A., . . . Verbeeck, J. (2017). Theory and applications of free-electron vortex states. *Physics Reports*, *690*, 1–70. https://doi.org/10.1016/j.physrep.2017.05.006.

Bliokh, K., Schattschneider, P., Verbeeck, J., & Nori, F. (2012). Electron vortex beams in a magnetic field: A new twist on Landau levels and Aharonov-Bohm states. *Physical Review X*, *2*(4). https://doi.org/10.1103/PhysRevX.2.041011.

Born, M., & Wolf, E. (1999). *Principles of optics*. Cambridge University Press.

Dattoli, G., Di Lazzaro, P., & Torre, A. (1990). A spinor approach to the propagation in self-focusing fibers. *Il Nuovo Cimento B*, *105*(2), 165–178. https://doi.org/10.1007/BF02723075.

Ehrenfest, P. (1927). Bemerkung über die angenäherte gültigkeit der klassischen mechanik innerhalb der quantenmechanik. *Zeitschrift für Physik*, *45*(7–8), 455–457. https://doi.org/10.1007/BF01329203.

Gabrielse, G., & Dehmelt, H. (1985). Observation of inhibited spontaneous emission. *Physical Review Letters*, *55*(1), 67–70. https://doi.org/10.1103/PhysRevLett.55.67.

Glaser, W. (1952). *Grundlagen der Elektronenoptik*. Berlin, Göttingen, Heidelberg: Springer.

Glaser, W., & Schiske, P. (1953). Elektronenoptische Abbildung aufgrund der Wellenmechanik I. *Annalen der Physik*, *12*(3), 240. https://doi.org/10.1002/andp.19534470408.

Grillo, V., Gazzadi, G. C., Karimi, E., Mafakheri, E., Boyd, R. W., & Frabboni, S. (2014). Highly efficient electron vortex beams generated by nanofabricated phase holograms. *Applied Physics Letters*, *104*(4), 043109. https://doi.org/10.1063/1.4863564.

Guzzinati, G., Schattschneider, P., Bliokh, K., Nori, F., & Verbeeck, J. (2013). Observation of the Larmor and Gouy rotations with electron vortex beams. *Physical Review Letters*, *110*(9). https://doi.org/10.1103/PhysRevLett.110.093601.

Hawkes, P. W., & Kasper, E. (2017). *Principles of electron optics* (second edition). Academic Press.

Howie, A. (1983). Problems of interpretation in high resolution electron microscopy. *Journal of Microscopy*, *129*, 239–251. https://doi.org/10.1111/j.1365-2818.1983.tb04181.x.

Jagannathan, R., & Khan, S. A. (1996). *Quantum theory of the optics of charged particles*. *Advances in imaging and electron physics: Vol. 97* (pp. 257–358).

Kaminer, I., Mutzafi, M., Levy, A., Harari, G., Sheinfux, H. H., Skirlo, S., ... Soljacic, M. (2016). Quantum Cerenkov radiation: Spectral cutoffs and the role of spin and orbital angular momentum. *Physical Review X*, *6*(1). https://doi.org/10.1103/PhysRevX.6.011006.

Khan, S. A., & Jagannathan, R. (1995). Quantum mechanics of charged-particle beam transport through magnetic lenses. *Physical Review E*, *51*(3), 2510–2515. https://doi.org/10.1103/PhysRevE.51.2510.

Kramberger, C., Löffler, S., Schachinger, T., Hartel, P., Zach, J., & Schattschneider, P. (2019). $\pi/2$ mode converters and vortex generators for electrons. *Ultramicroscopy*, *204*, 27–33. https://doi.org/10.1016/j.ultramic.2019.05.003.

Löffler, S. (2020). Unitary two-state quantum operators realized by quadrupole fields in the electron microscope. Submitted for publication. Retrieved from arXiv:1907.06493.

McMorran, B., Agrawal, A., Anderson, I., Herzing, A., Lezec, H., McClelland, J., & Unguris, J. (2011). Electron vortex beams with high quanta of orbital angular momentum. *Science*, *331*, 192–195. https://doi.org/10.1126/science.1198804.

Poppe, U., & Dunin-Borkowski, R. (2020). Private communication.

Pozzi, G. (1995). *Multislice approach to lens analysis*. *Advances in imaging and electron physics: Vol. 93* (pp. 173–218).

Pozzi, G. (2016). *Particles and waves in electron optics and microscopy*. *Advances in imaging and electron physics: Vol. 194*. Academic Press.

Reimer, L. (2008). *Transmission electron microscopy*. Springer.

Rose, H. (2009). *Geometrical charged-particle optics*. Springer.

Schachinger, T., Löffler, S., Stöger-Pollach, M., & Schattschneider, P. (2015). Peculiar rotation of electron vortex beams. *Ultramicroscopy*, *158*, 17–25. https://doi.org/10.1016/j.ultramic.2015.06.004.

Schattschneider, P., Schachinger, T., Stöger-Pollach, M., Löffler, S., Steiger-Thirsfeld, A., Bliokh, K., & Nori, F. (2014). Imaging the dynamics of free-electron Landau states. *Nature Communications*, *5*. https://doi.org/10.1038/ncomms5586.

Schattschneider, P., Stöger-Pollach, M., & Verbeeck, J. (2012). Novel vortex generator and mode converter for electron beams. *Physical Review Letters*, *109*(8). https://doi.org/10.1103/PhysRevLett.109.084801.

Schiff, L. (1999). *Quantum mechanics*. McGraw-Hill.

Uchida, M., & Tonomura, A. (2010). Generation of electron beams carrying orbital angular momentum. *Nature*, *464*(7289), 737–739. https://doi.org/10.1038/nature08904.

Verbeeck, J., Tian, H., & Schattschneider, P. (2010). Production and application of electron vortex beams. *Nature*, *467*(7313), 301–304. https://doi.org/10.1038/nature09366.

Wikipedia contributors (2020). Wave packet — Wikipedia, the free encyclopedia. Online. Retrieved from https://en.wikipedia.org/w/index.php?title=Wave_packet&oldid=943842438. (Accessed 11 March 2020).

Chapter 12

Unitary Two-State Quantum Operators Realized By Quadrupole Fields in the Electron Microscope

S. Löffler

Ultramicroscopy 234 (2022) 113456
10.1016/j.ultramic.2021.113456

Ultramicroscopy 234 (2022) 113456

Contents lists available at ScienceDirect

Ultramicroscopy

journal homepage: www.elsevier.com/locate/ultramic

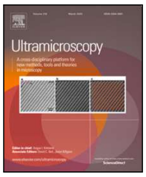

Unitary two-state quantum operators realized by quadrupole fields in the electron microscope

Stefan Löffler

University Service Centre for Transmission Electron Microscopy, TU Wien, Wiedner Hauptstraße 8-10/E057-02, 1040, Wien, Austria

ARTICLE INFO

Keywords:
Electron microscopy
Unitary operator
Qubit
Vortex beam

ABSTRACT

In this work, a novel method for using a set of electromagnetic quadrupole fields is presented to implement arbitrary unitary operators on a two-state quantum system of electrons. In addition to analytical derivations of the required quadrupole and beam settings which allow an easy direct implementation, numerical simulations of realistic scenarios show the feasibility of the proposed setup. This is expected to pave the way not only for new measurement schemes in electron microscopy and related fields but even one day for the implementation of quantum computing in the electron microscope.

1. Introduction

Unitary operators play a vital role across quantum mechanics and related fields as they model transformations between orthonormal bases. In transmission electron microscopy (TEM), the best-known such transformation is the Fourier transform which relates position space and reciprocal space and can be realized easily using a standard, round lens [1]. Going from position space representation into reciprocal space representation allows the efficient determination of crystal structures and orientations with better accuracy and signal-to-noise ratio (SNR) than, e.g., when using high-resolution TEM images acquired in imaging mode. One primary reason for this is the fact that all electrons carrying a certain information — e.g., about the lattice plane distance — are focused in one spot in reciprocal space, while being distributed over the whole micrograph in position space. Thus, measuring a few electrons in a specific reciprocal space point already gives quantifiable information about the lattice plane spacing, whereas measuring the same (low) number of electrons in a position space image will just give a few counts scattered over the entire field of view.

Another example of a unitary transformation is the use of a quadratic phase plate for measuring the orbital angular momentum (OAM) of a pure electron vortex beam [2]. Recently, an effective basis transformation was also employed to measure the OAM spectrum of an electron beam by means of a log-polar transformation [3]. In that instance, too, a setup was found that transformed different OAM components in such a way that they showed up in unique measurement channels — similar to diffraction spots —, rather than producing small variations on an otherwise fairly large signal.

The idea of having a direct one-to-one correspondence between the intensity in a channel and the sought information is closely related to the concept of sparsity commonly found in compressed sensing applications (see, e.g., [4–6] and references therein) and blind source separation (see, e.g., [7]). These methods, however, are post-processing techniques that in many cases require prior knowledge about the measured quantity. Above all else, however, their outcome strongly depends on the quality of the measured data, which in turn is heavily influenced by various noise sources, including shot noise and different electronic noise contributions in the read-out and processing components. However, unitary operators do not suffer from this problem.

Unitary operators can be applied directly to a (quantum) system *before* a measurement, thus allowing the measurement to be performed in a basis with optimal signal sparsity and SNR. The key requirement for this, however, is to find a way to perform the necessary unitary transformations directly in the instrument.

It must be emphasized that the use of unitary operators is not limited to the measurement process. It can also be used for shaping the beam. For example, a specific transformation has been used for producing electron vortex beams [8–10].

In this work, a setup is described that allows to realize arbitrary unitary operators on a two-state quantum system in a TEM. Two-state quantum systems are of particular importance as they model qubits, the building blocks of quantum computers. Such free electron qubits [11] would have many beneficial properties, from easy manipulation down to the sub-Ångstrom regime in a TEM to well-established measurement devices to very weak interaction with the environment to (in principle) easy storage, e.g. in a magnetic storage ring. Additionally, interactions

---

E-mail address: stefan.loeffler@tuwien.ac.at.

https://doi.org/10.1016/j.ultramic.2021.113456
Received 10 September 2021; Received in revised form 26 November 2021; Accepted 5 December 2021

with photons or quantum dots or other physical qubit implementations can be triggered easily [12]. Moreover, recent advances also outline potential roads towards scaling this from one to several qubits [13–16].

Apart from the fundamental research aspects, the two-state system acts as an important model for the future development of setups for unitary operators on higher-dimensional systems. Such developments could give rise to new optimized measuring schemes with improved SNR as outlined above which would be of great practical importance in electron microscopy.

2. Theory

Here, we use the vector space $\mathcal{V}$ spanned by the two orthonormal states $|0\rangle, |1\rangle$ given in position representation as

$$\begin{aligned} \langle\vec{r}|0\rangle &= HG_{1,0}(\vec{r}) \propto x \cdot \mathrm{e}^{-\frac{r^2}{w(z)^2}} \cdot \mathrm{e}^{-\frac{\mathrm{i}kr^2}{2R(z)}} \cdot \mathrm{e}^{\mathrm{i}\gamma(z)} \\ \langle\vec{r}|1\rangle &= HG_{0,1}(\vec{r}) \propto y \cdot \mathrm{e}^{-\frac{r^2}{w(z)^2}} \cdot \mathrm{e}^{-\frac{\mathrm{i}kr^2}{2R(z)}} \cdot \mathrm{e}^{\mathrm{i}\gamma(z)}, \end{aligned} \tag{1}$$

where $HG_{n,m}$ denotes the Hermite-Gaussian mode of order (n,m) [9,17,18], $w(z) = w_0\sqrt{1+(z/z_R)^2}$ is the propagation-dependent beam size with the minimal beam waist $w_0 = \sqrt{2z_R/k}$ and the Rayleigh range z_R, k is the wave number, $R(z) = z(1+(z_R/z)^2)$ is the curvature radius, and $\gamma(z) = \arctan(z/z_R)$ is the Gouy phase. Due to their primary orientation, $|0\rangle$ will be referred to as "horizontal" and $|1\rangle$ will be referred to as "vertical" in the following.

Apart from a global phase factor, all normalized states $|\psi\rangle \in \mathcal{V}$ can be written as

$$|\psi\rangle = \cos(\theta/2)|0\rangle + \sin(\theta/2)\mathrm{e}^{\mathrm{i}\varphi}|1\rangle \tag{2}$$

with $\theta \in [0,\pi], \varphi \in [0,2\pi)$. Thus, all such states lie on the Bloch sphere (with the polar angle θ and the azimuthal angle φ) as depicted in Fig. 1. Unitary operators are simply those changing θ and φ, i.e. rotations on the sphere. Following the scheme of (extrinsic) Euler angles, it is well-known that any arbitrary rotation can be decomposed into three successive rotations around cardinal axes, e.g. in the order x–z–x.

From Fig. 1 it can be seen that rotations around x correspond to changing θ. As is evident from Eqs. (1) and (2), such an operation in the chosen basis corresponds to a rotation of the coordinate system in the plane perpendicular to the optical axis by an angle of $\delta\theta/2$, i.e. $\vec{r} \mapsto \hat{R}\vec{r}$, which can be realized in two ways: either one rotates the experimental setup (electro-magnetic fields, image, sample, etc.), which may even be achievable in post-processing in some cases, or one uses the well-known Larmor rotation [19–23] in the magnetic field of round lenses ubiquitous in electron microscopy. Note that the first approach, i.e., rotating the electro-magnetic fields, is easy in the case of quadrupole fields as those can be rotated simply by changing the excitation of the four poles.

The second ingredient to realizing arbitrary unitary operators on $\mathcal{V}$ is the ability to change φ, i.e., rotations around z in Fig. 1. From Eq. (2), it is evident that this corresponds to a relative phase shift between the two basis states. Here, a scheme for creating electron vortex beams (EVB) can be extended upon: the so-called "mode conversion" [8–10], which is based on the idea of the optical mode converter [17] and uses a set of two quadrupole lenses to convert a $HG_{1,1}$ beam into a $LG_{0,\pm1}$ beam by means of the specific phase shift of $\delta\varphi = \pm\pi/2$. Here, this approach will be generalized to arbitrary phase shifts.

Fig. 2 shows the principle setup of a relative phase shifter, consisting of two quadrupole lenses. The first quadrupole (QP1) produces an astigmatic beam from an incident round beam. The beam is focused in one direction (say, horizontally) before the second quadrupole (QP2), while it is defocused in the orthogonal direction. Due to this difference, the horizontal and vertical components (corresponding to the basis states $|0\rangle$ and $|1\rangle$, respectively) acquire different Gouy phase shifts, thus resulting in a relative phase shift by the time they reach QP2. QP2 then has to be set up to compensate the action of QP1 and produce a non-astigmatic beam again.

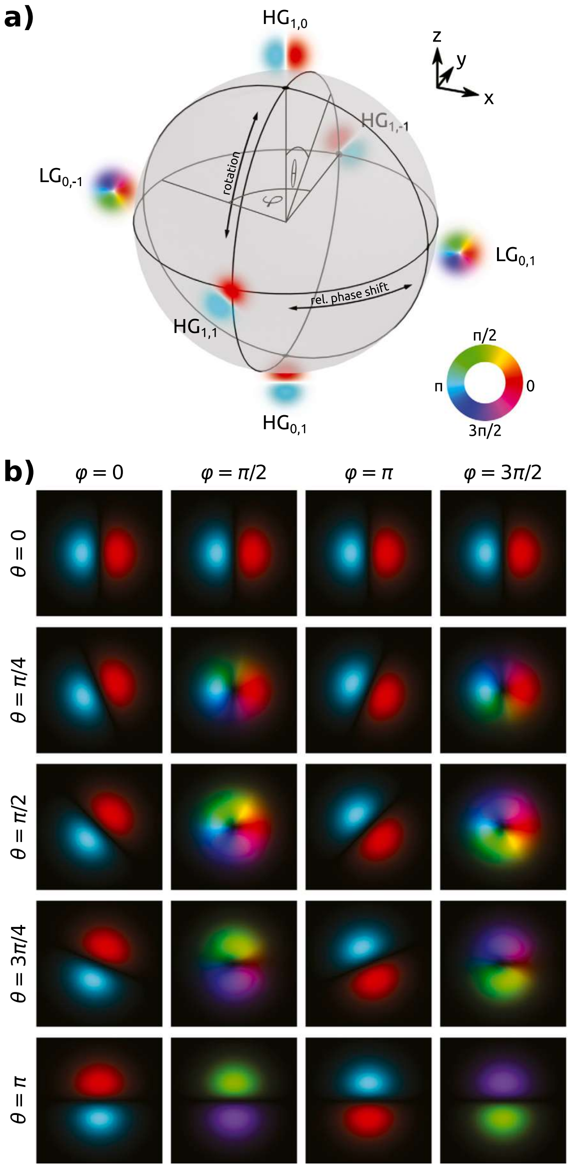

Fig. 1. (a) Schematic of the Bloch sphere for the vector space described in the text. (b) Selected states for various values of θ,φ according to Eq. (2). For all depicted states, intensity represents amplitude and color represents phase as indicated in the color wheel inset.

To model the propagation of the beam through the QP lens setup, it is beneficial to introduce the complex beam parameter $q(z) = z - z_0 + \mathrm{i}z_R$ for the two components, where z_0 is the position of the component's focus [18]. Without loss of generality, $z_0 = 0$ will be assumed in the following. The complex beam parameter completely defines a Gaussian beam and allows to calculate all its properties such as

$$w(z) = \sqrt{\frac{2|q|^2}{k\Im[q]}} \qquad R(z) = \frac{|q|^2}{\Re[q]} \qquad \gamma(z) = -\arg[\mathrm{i}q]\,. \tag{3}$$

Additionally, both the propagation and the action of a lens can be modeled easily. Propagation over a distance δz transforms $q \mapsto q + \delta z$,

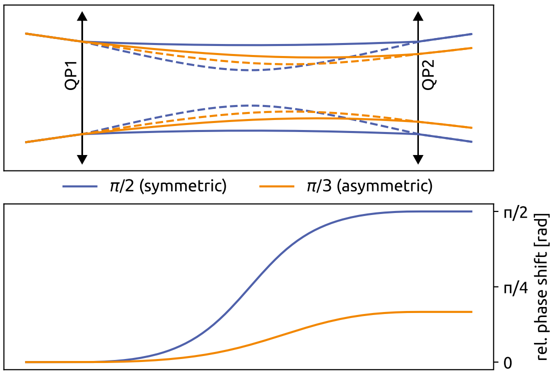

Fig. 2. Sketch of a relative phase shifter consisting of two quadrupoles (QP1, QP2). Two different settings leading to different phase shifts are shown (blue and orange). The top panel shows the horizontal (full lines) and vertical (dashed lines) beam diameters. The bottom panel shows the relative phase shift. In the shown scenario, the incident beam size was fixed.

while a lens with focal length f transforms $q \mapsto 1/(1/q - 1/f)$. A QP can then be modeled as a lens with focal length f for one component (e.g., the horizontal one) and $-f$ for the other component (e.g., the vertical one) [24].

The mode matching condition, i.e., the condition that the beam is round and non-astigmatic after QP2, results in the two conditions $w_h(z_2) = w_v(z_2)$ and $R_h(z_2) = R_v(z_2)$, where the subscripts h, v denote the horizontal and vertical components, respectively, and z_2 is the position of QP2. The first of the two conditions ensures that the beam is round at QP2, while the second condition ensures that it stays round even when propagating further after QP2 (i.e, it is non-astigmatic). It is easily seen that mode matching is achieved if $q_h(z_2) = q_v(z_2)$ [9]. A lengthy but straight-forward calculation (see Appendix) shows that for two quadrupoles with focal lengths f_1, f_2 at a distance d, this can be achieved for an incident beam with

$$q_{\mathrm{in}} = -d f_1 \frac{f_1 + \mathrm{i} d u}{f_1^2 + d^2 u^2} \quad \text{with} \quad u = -\operatorname{sgn}[f_1] \sqrt{\frac{f_1 f_2}{d^2} - 1}, \tag{4}$$

with a relative phase shift of

$$\delta\varphi = \arctan\left[\frac{2u}{u^2 - 1}\right]. \tag{5}$$

Solving for u gives

$$u = \frac{1 \pm \sqrt{1 + \tan^2 \delta\varphi}}{\tan \delta\varphi}. \tag{6}$$

This allows to calculate u for any given relative phase shift $\delta\varphi$, where the sign has to be chosen appropriately for the quadrant in the x-y-plane in which points with polar angle $\delta\varphi$ lie (corresponding to the normalized point $\frac{1}{u^2+1}(u^2 - 1, 2u)$ according to Eq. (5); see also Appendix). As shown in Fig. 3, for $\delta\varphi \in [0, \pi/2] \cup [3\pi/2, 2\pi]$ the + branch of Eq. (6) has to be taken whereas for $\delta\varphi \in (\pi/2, 3\pi/2)$ the − branch has to be taken. Knowing u in turn fixes the relation between f_1 and f_2 according to Eq. (4).

As a first example, consider $\delta\varphi = \pi/6$. $\tan\delta\varphi = 1/\sqrt{3} \approx 0.577$, resulting in the two solutions $u = \sqrt{3} + 2 \approx 3.732$ and $u = \sqrt{3} - 2 \approx -0.268$. The first solution corresponds to the (correct) point $(0.866, 0.5)$ in the first quadrant, while the second solution corresponds to the (incorrect) point $(-0.866, -0.5)$ in the third quadrant. Therefore, in this case, $u = \sqrt{3} + 2$ is the correct solution. Since u is positive, f_1 must be negative (diverging the horizontal component). This is also seen in Fig. 2.

As a second example, consider the phase shift $\delta\varphi = -2\pi/3$. $\tan\delta\varphi = \sqrt{3} \approx 1.732$, resulting in the two solutions $u = \sqrt{3} \approx 1.732$ and $u = -1/\sqrt{3} \approx -0.577$. The first solution corresponds to the (incorrect) point $(0.5, 0.866)$ in the first quadrant, while the second solution corresponds to the (correct) point $(-0.5, -0.866)$ in the third quadrant. Therefore, in this case, $u = -1/\sqrt{3}$ is the correct solution. Since u is negative, f_1 must be positive (converging the horizontal component).

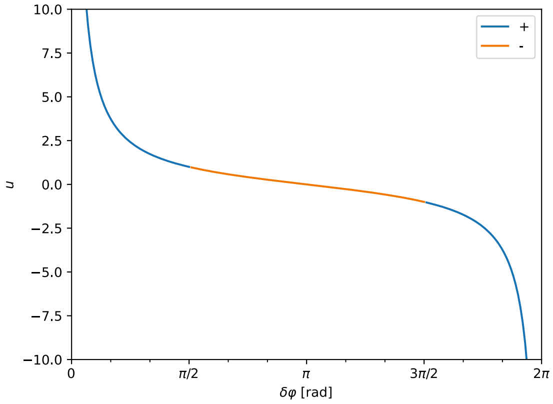

Fig. 3. Plot of u over $\delta\varphi$. The color represents the branch (the + or − variant of Eq. (6)) that produces the correct result.

Several distinct values require special attention. These are $\delta\varphi \in \{0, \pm\pi/2, \pi\}$. For 0 and π, Eq. (6) is indeterminate. Taking the limits of $\delta\varphi \to 0$ and $\delta\varphi \to \pi$, gives the values 0 and $\pm\infty$. For $u = 0$, Eq. (4) gives $f_1 f_2 = d^2$ and $q_{\mathrm{in}} = -d$, meaning a negligible small Rayleigh range and diverging beam size. This corresponds to the geometrical limit, i.e. a very large beam (compared to its waist size) far from its focus (compared to the Rayleigh range). One component goes through focus while the other one does not, resulting in a relative phase shift of π in the far field. $u = \pm\infty$, on the other hand, corresponds to infinite focal lengths, i.e., switched off quadrupoles and no relative phase shift.

$\delta\varphi = \pm\pi/2$ is the special case used for vortex creation. For these values, Eq. (6) is also indeterminate. Taking the limits results in the values $u = \pm 1$. Taking the corresponding limits in Eq. (5) shows that $u = 1$ corresponds to $\delta\varphi = \pi/2$ and $u = -1$ corresponds to $\delta\varphi = -\pi/2$. In both cases, Eq. (4) gives the well-known condition $f_1 f_2 = 2d^2$ for vortex creation [9].

Another lengthy but straight-forward calculations shows that the beam parameter of the outgoing beam (directly after QP2) reads

$$q_{\mathrm{out}} = -d f_2 \frac{-f_2 + \mathrm{i} d u}{f_2^2 + d^2 u^2}. \tag{7}$$

Noteworthy properties of the incident and the outgoing beam are

$$\begin{aligned} |q_{\mathrm{in}}|^2 &= \frac{d^2 f_1^2}{f_1^2 + d^2 u^2} & w_{\mathrm{in}} &= \sqrt{-\frac{2 f_1}{k u}} & R_{\mathrm{in}} &= -d \\ |q_{\mathrm{out}}|^2 &= \frac{d^2 f_2^2}{f_2^2 + d^2 u^2} & w_{\mathrm{out}} &= \sqrt{-\frac{2 f_2}{k u}} & R_{\mathrm{out}} &= d. \end{aligned} \tag{8}$$

With these values, it is possible to express f_1 as a function of w_{in} and u, thus yielding the following alternative form of the incident beam parameter

$$q_{\mathrm{in}} = \frac{-d k^2 w_{\mathrm{in}}^4 + 2\mathrm{i} d^2 k w_{\mathrm{in}}^2}{k^2 w_{\mathrm{in}}^4 + 4 d^2} \tag{9}$$

with

$$f_1 = -\frac{k u w_{\mathrm{in}}^2}{2} \quad \text{and} \quad f_2 = \frac{d^2}{f_1}(u^2 + 1) \tag{10}$$

To sum up, for given $\delta\varphi$, the dimensionless parameter u is uniquely determined and Eq. (10) gives the QP settings required to obtain $\delta\varphi$ for a given incident beam (with size w_{in} and curvature $-d$).

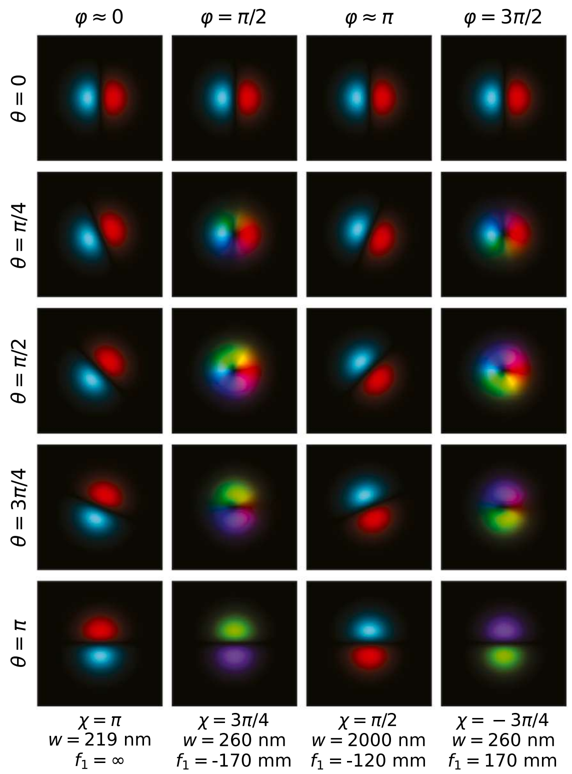

Fig. 4. Simulations of the phase shifter setup for the same values of θ, φ as in Fig. 1. In all cases, the incident beam was a $HG_{1,0}$ beam rotated by $\theta/2$. For each φ, the incident beam size w, the QP1 focal length f_1, and the global phase compensation χ are indicated. For illustration purposes, a symmetric setup with $w_{\text{in}} = w_{\text{out}}$ and $f_1 = f_2$ was used. For $f_1 = \infty$, a numerical value of 1 km was used. Amplitude and phase are shown as in Fig. 1.

3. Simulations

To corroborate the theoretical results, numerical simulations were performed using the ***virTUal TEM*** software package [9]. All optical elements were modeled as effective phase plates (i.e., thin elements) and the propagation was performed in paraxial approximation using a Fourier-space Fresnel propagator (owing to the small beam diameters and convergence angles). All simulations were performed for an incident $HG_{1,0}$ beam rotated by $\theta/2$ with an energy of 200 keV using a setup as shown in Fig. 2. For simulation simplicity, a symmetric setup (i.e., $f_1 = f_2$) was chosen in all cases. To achieve the required curvature radius of the incident beam, an initially non-diffracting beam was transformed into a convergent beam using a round transfer lens before QP1. For clarity, a matching round lens after QP2 was included to flatten the phase front to ease comparability. The two QPs had a spacing of $d = 120$ mm.

For numerical reasons, both the focal lengths and the beam sizes were bounded. The focal length was limited to $|f_1| \leq 1$ km, resulting in a minimal achievable phase shift of $\delta\varphi \approx 0.24$ mrad, while the beam size was limited to $w_{\text{in}} \leq 2$ μm resulting in phase shifts between 3.09 rad and 3.19 rad being unachievable with a single phase shifter setup.

The results are summarized in Fig. 4. A comparison to Fig. 1 shows perfect agreement. It should be noted that in all cases except $\varphi = 0$, the beam acquired a global phase χ as indicated in the figure. This stems from the propagation distance between the QPs, similar to the optical path length in light optics. As the global phase is inconsequential in this work (and can be compensated for by physical flight paths, lens systems, or temporarily changing the speed of the electrons), it is removed from the images in Fig. 4 for better comparability.

In terms of practical applicability, the chosen parameters, while not specific to any particular instrument, are in a realistic order of magnitude range. Also the beam sizes of a few hundred nanometers are readily achievable in a TEM. As far as the incident beam is concerned, no perfect Gaussian beams have been produced to date, but sufficiently close approximations are possible [2,8,9,21].

4. Discussion & outlook

Some properties of this setup are worth emphasizing. First, in order to achieve mode matching, the incident beam must have a curvature at QP1 of $-d$, meaning that in the geometric limit (for large beams), it is focused at QP2 (although for small beams, the focus will be in front of QP2). This can easily be achieved by a transfer lens before the quadrupoles.

Second, focal lengths f_1, f_2 (and therefore the beam sizes $w_{\text{in}}, w_{\text{out}}$) are coupled by the phase shift. Thus, while it is possible for a given phase shift to choose either the incident or the outgoing beam size, it is not possible to choose both at the same time. Again, this can be compensated if needed by a transfer lens system.

Third, phase shifts close to 0 lead to a very large magnitude of u and, hence, of the focal lengths. Such long focal lengths typically require very small excitations of the QPs which may not be controllable with suitable accuracy. This can be worked around by a two-step process: to achieve a small relative phase shift ε, first shift by a large α and then by $-\alpha + \varepsilon$. Similarly, phase shifts around π lead to very small u and therefore require very short focal lengths (or very large beam sizes). This, too, can be worked around by a two-step process: to achieve a phase shift of $\alpha \sim \pi$, one can instead perform two shifts by $\alpha/2$.

The setup in this work, i.e. two quadrupoles acting on a specific two-state quantum system, is, of course, a simple model system for studying unitary transformations. One big advantage of this system is that it can readily be investigated in existing TEMs [10] without the need for any changes to the instrument or the development of custom electron-optical elements. In the future, however, it will certainly be beneficial to expand this concept to other systems, in particular higher-dimensional quantum systems. On the one hand, this will facilitate enhanced measurement schemes with improved SNR for common microscopy tasks (which are usually not confined to a two-state quantum system). On the other hand, this will allow for the handling of n-state qudits (as opposed to 2-state qubits). Such a system will likely have to rely on advanced — and probably adaptive — methods for phase manipulation, such as programmable phase manipulators [13,25,26] akin to spatial light modulators (SLMs) in optics.

Performing quantum computations in an electron microscope in the future will require the realization of so-called universal quantum gates [27] — similar to universal logic gates such as NAND in conventional computing. One key ingredient to this is unitary transformations (or so-called one-qubit gates) which can arbitrarily change the state of a single qubit as presented in this paper. The other ingredient is at least one two-qubit gate such as CNOT. It can be shown that such a gate is entangling [27], i.e. it creates entanglement between previously unentangled systems. One common way this is achieved in electron microscopy is scattering [28,29]. However, it is still an open question how scattering experiments could be designed — e.g. using wave front shaping of the electron beams before and after scattering — such that most electrons scatter into an (entangled) state inside the vector space spanned by the chosen basis vectors ($HG_{1,0}$ and $HG_{0,1}$ in the case discussed in this work).

Additionally, in a quantum computing scheme, one will eventually want to increase the number of quantum gates. As far as pairs of quadrupoles (and higher-order multipoles that can be driven to act as quadrupoles) are concerned, current TEMs are limited to at most a handful, spread between the condensor/probe corrector system, the imaging lenses/image corrector system, and potentially an imaging filter. Similarly, there is a very limited number of (aperture) planes in which programmable phase manipulators could be inserted by default. Thus, large-scale quantum computation applications will require additional custom elements added to a TEM or even a complete custom instrument. However, for the time being, many open questions and tasks remain that can easily be investigated with the handful of elements at our disposal in a general-purpose TEM.

5. Conclusions

In this work, a novel concept for using mode converters in the TEM was presented that allows the realization of arbitrary unitary operators on a two-state quantum system. This paves the way for the realization of higher-dimensional unitary operators, which in turn will open entirely new possibilities for electron microscopy and all fields it is applied in, from physics to material science and chemistry to biology. Instead of post-processing data and looking for tiny signals in a huge, noisy background, the realization of unitary operators will allow much more efficient experiments by enabling scientists to devise measurement schemes where the electron beam is quantum-mechanically transformed into a basis in which the sought information can be read out directly. Moreover, together with the recent progress in understanding entanglement of free electrons, this work may well contribute one day to performing quantum computations in the electron microscope.

Declaration of competing interest

The authors declare that they have no known competing financial interests or personal relationships that could have appeared to influence the work reported in this paper.

Acknowledgments

S.L. acknowledges fruitful discussions with Peter Schattschneider and financial support by the Austrian Science Fund (FWF) under grant nrs. I4309-N36 and P29687-N36 and by TU Wien Bibliothek through its Open Access Funding Programme.

Appendix. Derivation of the mode matching condition and the phase shift

In this section, the matrix transfer method [18,24] is heavily used to derive the general mode-matching criteria for Hermite-Gaussian waves in a two-quadrupole setup. For a closely related treatment in a charged-particle formalism, see e.g. [24].

The effect of lenses ($\boldsymbol{L}$) and free space ($\boldsymbol{T}$) is modeled by matrices

$$\boldsymbol{L}(f) = \begin{pmatrix} 1 & 0 \\ -\frac{1}{f} & 1 \end{pmatrix} \qquad \boldsymbol{T}(d) = \begin{pmatrix} 1 & d \\ 0 & 1 \end{pmatrix} \tag{A.1}$$

where f is the lens' focal length and d is the distance the beam propagates through free space. An optical system of several components can be described by the product of the individual component matrices. Assuming a system described by

$$\boldsymbol{M} = \begin{pmatrix} A & B \\ C & D \end{pmatrix}, \tag{A.2}$$

a complex beam parameter q_{in} is transformed according to

$$q_{\text{out}} = \frac{Aq_{\text{in}} + B}{Cq_{\text{in}} + D}. \tag{A.3}$$

Mathematically, this corresponds to a projective transform which can be modeled in matrix notation by

$$\vec{q}_{\text{out}} = \boldsymbol{M} \cdot \begin{pmatrix} q_{\text{in}} \\ 1 \end{pmatrix} = \boldsymbol{M} \cdot \vec{q}_{\text{in}} \tag{A.4}$$

if all vectors that only differ by a non-zero scalar factor are treated as equivalent.

The two quadrupole setup discussed in this work can therefore be modeled by two matrices

$$\begin{aligned} \boldsymbol{M}_h &= \boldsymbol{L}(f_2) \cdot \boldsymbol{T}(d) \cdot \boldsymbol{L}(f_1) \\ \boldsymbol{M}_v &= \boldsymbol{L}(-f_2) \cdot \boldsymbol{T}(d) \cdot \boldsymbol{L}(-f_1) \end{aligned} \tag{A.5}$$

owing to the fact that quadrupoles act differently on horizontal and vertical components. The mode matching condition thus becomes

$$\boldsymbol{M}_h \vec{q}_{\text{in}} \propto \boldsymbol{M}_v \vec{q}_{\text{in}} \tag{A.6}$$

or, equivalently,

$$\boldsymbol{M}_v^{-1} \boldsymbol{M}_h \vec{q}_{\text{in}} = \lambda \vec{q}_{\text{in}} \tag{A.7}$$

where the proportionality comes from the equivalence of vectors that are scalar multiples of one another. Thus, finding an incident beam that is mode matched at the output is equivalent to finding an eigenvector of Eq. (A.7). Note that the eigenvectors of a matrix of the form given in Eq. (A.2) — given $C \neq 0$ — can be directly derived as

$$\boldsymbol{M} \begin{pmatrix} q \\ 1 \end{pmatrix} = \begin{pmatrix} Aq + B \\ Cq + D \end{pmatrix} = \begin{pmatrix} \lambda q \\ \lambda \end{pmatrix} = \lambda \begin{pmatrix} q \\ 1 \end{pmatrix} \tag{A.8}$$

$$Cq^2 + (D - A)q - B = 0 \tag{A.9}$$

$$q = \frac{A - D \pm \sqrt{(A - D)^2 + 4BC}}{2C}. \tag{A.10}$$

In the present case, the relevant matrix reads

$$\boldsymbol{M}_v^{-1} \boldsymbol{M}_h = \frac{1}{f_1^2 f_2^2} \begin{pmatrix} f_1^2 f_2^2 + 2 f_1 f_2 d(f_1 - d) & 2 f_1^2 f_2 d^2 \\ 2 f_2 d^2 - 2 f_1 f_2 (f_1 + f_2) & f_1^2 f_2^2 - 2 f_1 f_2 d(f_1 + d) \end{pmatrix} \tag{A.11}$$

and thus

$$q_{\text{in}} = \frac{f_1^2 d \pm |f_1| \operatorname{sgn}[f_2] d \sqrt{d^2 - f_1 f_2}}{d^2 - f_1^2 - f_1 f_2}. \tag{A.12}$$

Note that only one of the two solutions results in a sensible Rayleigh range (i.e. strictly positive imaginary part) and only if $f_1 f_2 > d^2$. Thus, it makes sense to rewrite the expression as

$$q_{\text{in}} = \frac{-d f_1^2 + \mathrm{i} d |f_1| \sqrt{f_1 f_2 - d^2}}{f_1^2 + f_1 f_2 - d^2}. \tag{A.13}$$

This is identical to Eq. (4). For future reference, note that

$$|q_{\text{in}}|^2 = \frac{d^2 f_1^2}{f_1^2 + f_1 f_2 - d^2}. \tag{A.14}$$

To calculate the relative phase shift, one needs to calculate the beam parameters directly after QP1 ($q_{1,h}, q_{1,v}$) at z_1 and directly before QP2 ($q_{2,h}, q_{2,v}$) at z_2. Direct calculation yields the expressions

$$\begin{aligned} q_{1,h} &= \frac{q_{\text{in}} f_1}{f_1 - q_{\text{in}}} \qquad q_{2,h} = \frac{d f_1 + (f_1 - d) q_{\text{in}}}{f_1 - q_{\text{in}}} \\ q_{1,v} &= \frac{q_{\text{in}} f_1}{f_1 + q_{\text{in}}} \qquad q_{2,v} = \frac{d f_1 + (f_1 + d) q_{\text{in}}}{f_1 + q_{\text{in}}}. \end{aligned} \tag{A.15}$$

The relative phase shift is thus

$$\begin{aligned} \delta\varphi &= -\arg[\mathrm{i} q_{2,v}] + \arg[\mathrm{i} q_{1,v}] + \arg[\mathrm{i} q_{2,h}] - \arg[\mathrm{i} q_{1,h}] \\ &= \arg\left[\frac{q_{1,v} q_{2,h}}{q_{1,h} q_{2,v}}\right] = \arg\left[q_{1,h}^* q_{1,v} q_{2,h} q_{2,v}^*\right] \\ &= \arg\left[(d f_1 + (f_1 - d) q_{\text{in}})(d f_1 + (f_1 + d) q_{\text{in}})^*\right] \\ &= \arg\left[d^2 f_1^2 + (f_1^2 - d^2)|q_{\text{in}}|^2 + 2 d f_1^2 \Re[q_{\text{in}}] - 2\mathrm{i} d^2 f_1 \Im[q_{\text{in}}]\right] \end{aligned}$$

$$= \arctan\left(\frac{-2d^2 f_1 \Im[q_{\mathrm{in}}]}{d^2 f_1^2 + (f_1^2 - d^2)|q_{\mathrm{in}}|^2 + 2d f_1^2 \Re[q_{\mathrm{in}}]}\right) \tag{A.16}$$

where the fact that a positive (real) factor does not change the argument of a complex number was used. Note that it is important to keep the minus sign in the numerator (rather than moving it to the denominator or in front of the fraction) to ensure the correct quadrant can be determined (as arctan is unique only up to an integer multiple of π). Applied to the specific case of Eq. (A.13) gives

$$\tan\delta\varphi = \frac{-2d\,\mathrm{sgn}[f_1]\sqrt{f_1 f_2 - d^2}}{f_1 f_2 - 2d^2}. \tag{A.17}$$

By the introduction of the dimensionless parameter

$$u = -\,\mathrm{sgn}[f_1]\sqrt{\frac{f_1 f_2}{d^2} - 1}, \tag{A.18}$$

the phase shift can be rewritten as

$$\tan\delta\varphi = \frac{2u}{u^2 - 1}. \tag{A.19}$$

which corresponds to Eq. (5).

References

[1] D.B. Williams, C.B. Carter, Transmission Electron Microscopy, Plenum Press, New York, 1996.

[2] G. Guzzinati, L. Clark, A. Béché, J. Verbeeck, Measuring the orbital angular momentum of electron beams, Phys. Rev. A 89 (2014) 025803, http://dx.doi.org/10.1103/PhysRevA.89.025803.

[3] V. Grillo, A.H. Tavabi, F. Venturi, H. Larocque, R. Balboni, G.C. Gazzadi, S. Frabboni, P.-H. Lu, E. Mafakheri, F. Bouchard, R.E. Dunin-Borkowski, R.W. Boyd, M.P.J. Lavery, M.J. Padgett, E. Karimi, Measuring the orbital angular momentum spectrum of an electron beam, Nature Commun. 8 (2017) 15536, http://dx.doi.org/10.1038/ncomms15536.

[4] Z. Saghi, D.J. Holland, R. Leary, A. Falqui, G. Bertoni, A.J. Sederman, L.F. Gladden, P.A. Midgley, Three-dimensional morphology of iron oxide nanoparticles with reactive concave surfaces, a compressed sensing-electron tomography (CS-ET) approach, Nano Lett. 11 (11) (2011) 4666–4673, http://dx.doi.org/10.1021/nl202253a.

[5] R. Huber, G. Haberfehlner, M. Holler, G. Kothleitner, K. Bredies, Total generalized variation regularization for multi-modal electron tomography, Nanoscale 11 (12) (2019) 5617–5632, http://dx.doi.org/10.1039/c8nr09058k.

[6] M. Rani, S.B. Dhok, R.B. Deshmukh, A systematic review of compressive sensing: Concepts, implementations and applications, IEEE Access 6 (2018) 4875–4894, http://dx.doi.org/10.1109/access.2018.2793851.

[7] P. Comon, C. Jutten (Eds.), Handbook of Blind Source Separation: Independent Component Analysis and Applications, ACADEMIC PR INC, 2010, URL https://www.ebook.de/de/product/9020313/pierre_comon_handbook_of_blind_source_separation_independent_component_analysis_and_applications.html.

[8] P. Schattschneider, M. Stöger-Pollach, J. Verbeeck, Novel vortex generator and mode converter for electron beams, Phys. Rev. Lett. 109 (8) (2012) 084801, http://dx.doi.org/10.1103/physrevlett.109.084801.

[9] C. Kramberger, S. Löffler, T. Schachinger, P. Hartel, J. Zach, P. Schattschneider, $\pi/2$ mode converters and vortex generators for electrons, Ultramicroscopy 204 (2019) 27–33, http://dx.doi.org/10.1016/j.ultramic.2019.05.003, arXiv:1902.05368.

[10] T. Schachinger, P. Hartel, P. Lu, S. Löffler, M. Obermair, M. Dries, D. Gerthsen, R.E. Dunin-Borkowski, P. Schattschneider, Experimental realisation of a $\pi/2$ vortex mode converter for electrons using a spherical aberration corrector, Ultramicroscopy 229 (2021) 113340, http://dx.doi.org/10.1016/j.ultramic.2021.113340, arXiv:2103.10899.

[11] O. Reinhardt, C. Mechel, M. Lynch, I. Kaminer, Free-electron qubits, 2019, arXiv:1907.10281.

[12] R. Ruimy, A. Gorlach, C. Mechel, N. Rivera, I. Kaminer, Toward atomic-resolution quantum measurements with coherently shaped free electrons, Phys. Rev. Lett. 126 (23) (2021) 233403, http://dx.doi.org/10.1103/physrevlett.126.233403.

[13] J. Verbeeck, A. Béché, K. Müller-Caspary, G. Guzzinati, M.A. Luong, M.D. Hertog, Demonstration of a 2×2 programmable phase plate for electrons, Ultramicroscopy 190 (2018) 58–65, http://dx.doi.org/10.1016/j.ultramic.2018.03.017.

[14] P. Thakkar, V.A. Guzenko, P.-H. Lu, R.E. Dunin-Borkowski, J.P. Abrahams, S. Tsujino, Fabrication of low aspect ratio three-element boersch phase shifters for voltage-controlled three electron beam interference, J. Appl. Phys. 128 (13) (2020) 134502, http://dx.doi.org/10.1063/5.0020383.

[15] P. Rosi, G.C. Gazzadi, S. Frabboni, V. Grillo, A.H. Tavabi, R.E. Dunin-Borkowski, G. Pozzi, Focused ion beam fabrication of janus bimetallic cylinders acting as drift tube zernike phase plates for electron microscopy, J. Appl. Phys. 130 (2) (2021) 024507, http://dx.doi.org/10.1063/5.0050055.

[16] A. Eberle, S. Mikula, R. Schalek, J. Lichtman, M.K. Tate, D. Zeidler, High-resolution, high-throughput imaging with a multibeam scanning electron microscope, J. Microsc. 259 (2) (2015) 114–120, http://dx.doi.org/10.1111/jmi.12224.

[17] M. Beijersbergen, L. Allen, H. van der Veen, J. Woerdman, Astigmatic laser mode converters and transfer of orbital angular momentum, Opt. Commun. 96 (1–3) (1993) 123–132, http://dx.doi.org/10.1016/0030-4018(93)90535-d.

[18] A. Yariv, Quantum Electronics, John Wiley & Sons, 1989, URL https://www.ebook.de/de/product/3635586/amnon_yariv_yariv_quantum_electronics.html.

[19] I. Ennen, S. Löffler, C. Kübel, D. Wang, A. Auge, A. Hütten, P. Schattschneider, Site-specific chirality in magnetic transitions, J. Magn. Magn. Mater. 324 (18) (2012) 2723–2726, http://dx.doi.org/10.1016/j.jmmm.2012.03.050.

[20] G. Guzzinati, P. Schattschneider, K.Y. Bliokh, F. Nori, J. Verbeeck, Observation of the larmor and gouy rotations with electron vortex beams, Phys. Rev. Lett. 110 (2013) 093601, http://dx.doi.org/10.1103/PhysRevLett.110.093601.

[21] P. Schattschneider, T. Schachinger, M. Stöger-Pollach, S. Löffler, A. Steiger-Thirsfeld, K.Y. Bliokh, F. Nori, Imaging the dynamics of free-electron landau states, Nature Commun. 5 (2014) 4586, http://dx.doi.org/10.1038/ncomms5586, arXiv:1408.1972.

[22] T. Schachinger, S. Löffler, M. Stöger-Pollach, P. Schattschneider, Peculiar rotation of electron vortex beams, Ultramicroscopy 158 (2015) 17–25, http://dx.doi.org/10.1016/j.ultramic.2015.06.004, arXiv:1703.10235.

[23] K.Y. Bliokh, P. Schattschneider, J. Verbeeck, F. Nori, Electron vortex beams in a magnetic field: A new twist on landau levels and aharonov-bohm states, Phys. Rev. X 2 (2012) 041011, http://dx.doi.org/10.1103/PhysRevX.2.041011.

[24] H. Rose, Geometrical Charged-Particle Optics, Springer-Verlag GmbH, 2013, URL https://www.ebook.de/de/product/25039540/harald_rose_geometrical_charged_particle_optics.html.

[25] G. Guzzinati, L. Clark, A. Béché, R. Juchtmans, R.V. Boxem, M. Mazilu, J. Verbeeck, Prospects for versatile phase manipulation in the tem: Beyond aberration correction, Ultramicroscopy 151 (2015) 85–93, http://dx.doi.org/10.1016/j.ultramic.2014.10.007, special Issue: 80th Birthday of Harald Rose; {PICO} 2015 – Third Conference on Frontiers of Aberration Corrected Electron Microscopy. URL http://www.sciencedirect.com/science/article/pii/S0304399114001995.

[26] G. Pozzi, V. Grillo, P.-H. Lu, A.H. Tavabi, E. Karimi, R.E. Dunin-Borkowski, Design of electrostatic phase elements for sorting the orbital angular momentum of electrons, Ultramicroscopy 208 (2020) 112861, http://dx.doi.org/10.1016/j.ultramic.2019.112861.

[27] C.P. Williams, Quantum gates, in: Texts in Computer Science, Springer London, 2011, pp. 51–122, http://dx.doi.org/10.1007/978-1-84628-887-6_2.

[28] P. Schattschneider, S. Löffler, Entanglement and decoherence in electron microscopy, Ultramicroscopy 190 (2018) 39–44, http://dx.doi.org/10.1016/j.ultramic.2018.04.007.

[29] P. Schattschneider, S. Löffler, H. Gollisch, R. Feder, Entanglement and entropy in electron–electron scattering, J. Electron Spectrosc. Relat. Phenom. 241 (2020) 146810, http://dx.doi.org/10.1016/j.elspec.2018.11.009, arXiv:1807.04694.

Conclusion

TEM, together with analytical tools such as EELS, is a vital instrument for sample characterization on the nanometer and the atomic scale. Therefore, it is a crucial tool for the design of novel and improved materials such as stronger and more durable steel, more efficient catalysts, and powerful energy storage approaches. In addition to its use in material science, TEM is also widely used in electrical engineering as well as in biology, to name just a few areas of application.

Apart from ever improving hardware, improvements to the existing methods as well as the development of novel characterization techniques are essential to cater for the ever-expanding applications and needs. In this thesis, several such improvements and developments are presented. These range from the first ever mapping of individual electronic states inside the sample with TEM-EELS (part I) to improvements in the understanding and the prediction of EMCD (part II) to contributions to the emerging field of EVBs and beam shaping (part III) to the exciting new possibilities of using the TEM as a toolkit for quantum-mechanical experiments, rather than a “mere sample analyzer” (part IV).

Each work presented here advances the fields of TEM and EELS and pushes the limits of what is currently possible. One noteworthy challenge throughout this thesis — and cutting-edge TEM in general — is the low SNR, particularly when employing advanced measurement schemes. Quantum microscopy, while far from commercial applicability at the moment, may pave the way to overcome or at least greatly reduce this challenge.

Acknowledgements

First of all, I want to thank all my collaborators and colleagues. This work would not have been possible without all the discussions, discourse, and cooperation within the community. Of course, as it is impossible to list all names explicitly, I want to mention the following people with whom I had particularly interesting discussions as well as fruitful cooperation over the years (in alphabetical order): Gianluigi Botton, Matthieu Bugnet, Christoph Eisenmenger-Sittner, Walid Hetaba, Thomas Schachinger, Peter Schattschneider, and Michael Stöger-Pollach. Furthermore, I want to acknowledge the Austrian Society for Electron Microscopy, which provides an excellent network of microscopists in Austria.

In addition, I want to thank the head of the University Service Centre for Transmission Electron Microscopy, Johannes Bernardi, the head of the Institute of Solid State Physics, Karsten Held, the dean of Physics, Thorsten Schumm, and the vice-rector for research and innovation, Johannes Fröhlich, for their continuing support, for maintaining a fruitful and rewarding work environment, and for providing the resources necessary for carrying out my research.

Moreover, I am very grateful to the Austrian Science Fund (FWF) for financially supporting several research projects I have been involved in, particularly the projects I 543-N20, J 3732-N27, P 29687-N36, and I 4309-N36.

Last but not least, I am very thankful for the love and support of my family and friends, without which this thesis would not have been possible.

Acronyms

CL cathodo-luminescence

EDX energy-dispersive X-ray spectroscopy

EELS electron energy-loss spectrometry

EFTEM energy-filtered TEM

EMCD energy-loss magnetic chiral dichroism

EVB electron vortex beam

HG Hermite-Gauss

HRTEM high-resolution TEM

LG Laguerre-Gauss

MDFF mixed dynamic form factor

OAM orbital angular momentum

PCA principle component analysis

SCCO $Sr_{14-x}Ca_xCu_{24}O_{41}$

SNR signal-to-noise ratio

STEM scanning transmission electron microscopy

STM scanning tunneling microscopy

TEM transmission electron microscope

Bibliography

[1] *Article Sharing*. Elsevier. accessed 2022-06-05. 2022. URL: https://www.elsevier.com/about/policies/sharing#Published-article.

[2] *Publication rights*. Oxford University Press. accessed 2022-06-05. 2022. URL: https://academic.oup.com/journals/pages/access_purchase/rights_and_permissions/publication_rights.

[3] M. Knoll and E. Ruska. “Das Elektronenmikroskop”. In: *Zeitschrift für Physik* 78.5-6 (1932), pp. 318–339. DOI: 10.1007/BF01342199.

[4] R. P. Feynman. “There’s Plenty of Room at the Bottom”. In: *Engineering and Science* 23.5 (1960), pp. 22–36. URL: https://resolver.caltech.edu/CaltechES:23.5.1960Bottom.

[5] F. Haguenau, P. Hawkes, J. Hutchison, B. Satiat–Jeunemaître, G. Simon, and D. Williams. “Key events in the history of electron microscopy”. In: *Microsc. Microanal.* 9.2 (2003), pp. 96–138. DOI: 10.1017/S1431927603030113.

[6] M. Haider, H. Rose, S. Uhlemann, E. Schwan, B. Kabius, and K. Urban. “A spherical-aberration-corrected 200 kV transmission electron microscope”. In: *Ultramicroscopy* 75.1 (1998), pp. 53–60. DOI: 10.1016/S0304-3991(98)00048-5.

[7] O. Krivanek, N. Dellby, and A. Lupini. “Towards sub-Å electron beams”. In: *Ultramicroscopy* 78.1–4 (1999), pp. 1–11. DOI: 10.1016/S0304-3991(99)00013-3.

[8] D. B. Williams and C. B. Carter. *Transmission electron microscopy*. New York: Plenum Press, 1996.

[9] M. Linck, P. Hartel, S. Uhlemann, F. Kahl, H. Müller, J. Zach, M. Haider, M. Niestadt, M. Bischoff, J. Biskupek, Z. Lee, T. Lehnert, F. Börrnert, H. Rose, and U. Kaiser. “Chromatic Aberration Correction for Atomic Resolution TEM Imaging from 20 to 80 kV”. In: *Phys. Rev. Lett.* 117 (Aug. 2016), p. 076101. DOI: 10.1103/physrevlett.117.076101.

[10] J. M. Zuo, M. Kim, M. O’Keeffe, and J. C. H. Spence. “Direct observation of d-orbital holes and Cu-Cu bonding in Cu_2O”. In: *Nat.* 401.6748 (Sept. 1999), pp. 49–52. DOI: 10.1038/43403.

[11] J. C. Meyer, S. Kurasch, H. J. Park, V. Skakalova, D. Künzel, A. Groß, A. Chuvilin, G. Algara-Siller, S. Roth, T. Iwasaki, U. Starke, J. H. Smet, and U. Kaiser. “Experimental analysis of charge redistribution due to chemical bonding by high-resolution transmission electron microscopy”. In: *Nat. Mater.* 10.3 (Mar. 2011), pp. 209–215. DOI: 10.1038/nmat2941.

[12] J. Repp, G. Meyer, S. Paavilainen, F. E. Olsson, and M. Persson. “Imaging Bond Formation Between a Gold Atom and Pentacene on an Insulating Surface”. In: *Science* 312.5777 (2006), pp. 1196–1199. DOI: 10.1126/science.1126073.

[13] R. Egerton. “Scattering delocalization and radiation damage in STEM-EELS”. In: *Ultramicroscopy* 180 (Sept. 2017), pp. 115–124. DOI: 10.1016/j.ultramic.2017.02.007.

[14] P. Schattschneider, M. Nelhiebel, and B. Jouffrey. “Density matrix of inelastically scattered fast electrons”. In: *Phys. Rev. B* 59.16 (Apr. 1999), pp. 10959–10969. DOI: 10.1103/PhysRevB.59.10959.

[15] K. Blum. *Density Matrix Theory and Applications*. 2nd. Physics of Atoms and Molecules. Springer, 1996. URL: https://books.google.at/books?id=kl-pMd9Qx04C.

[16] S. Löffler. “Study of real space wave functions with electron energy loss spectrometry”. PhD thesis. TU Wien, Dec. 2013. DOI: 10.34726/hss.2013.21487.

[17] H. Kohl and H. Rose. “Theory of Image Formation by Inelastically Scattered Electrons in the Electron Microscope”. In: *Advances in Electronics and Electron Physics*. Advances in Electronics and Electron Physics 65 (1985). Ed. by P. W. Hawkes, pp. 173–227. DOI: 10.1016/S0065-2539(08)60878-1.

[18] P. Schattschneider, M. Nelhiebel, H. Souchay, and B. Jouffrey. “The physical significance of the mixed dynamic form factor”. In: *Micron* 31.4 (2000), pp. 333–345. DOI: 10.1016/S0968-4328(99)00112-2.

[19] E. J. Kirkland. *Advanced computing in electron microscopy*. Plenum Press, 1998. DOI: 10.1007/978-1-4757-4406-4.

[20] P. Blaha, K. Schwarz, F. Tran, R. Laskowski, G. K. H. Madsen, and L. D. Marks. “WIEN2k: An APW+lo program for calculating the properties of solids”. In: *The Journal of Chemical Physics* 152.7 (Feb. 2020), p. 074101. DOI: 10.1063/1.5143061.

[21] F. Banhart. “Irradiation effects in carbon nanostructures”. In: *Reports on Progress in Physics* 62.8 (July 1999), pp. 1181–1221. DOI: 10.1088/0034-4885/62/8/201.

[22] J. C. Meyer, F. Eder, S. Kurasch, V. Skakalova, J. Kotakoski, H. J. Park, S. Roth, A. Chuvilin, S. Eyhusen, G. Benner, A. V. Krasheninnikov, and U. Kaiser. “Accurate Measurement of Electron Beam Induced Displacement Cross Sections for Single-Layer Graphene”. In: *Physical Review Letters* 108.19 (May 2012), p. 196102. DOI: 10.1103/physrevlett.108.196102.

[23] T. Susi, J. Kotakoski, R. Arenal, S. Kurasch, H. Jiang, V. Skakalova, O. Stephan, A. V. Krasheninnikov, E. I. Kauppinen, U. Kaiser, and J. C. Meyer. “Atomistic Description of Electron Beam Damage in Nitrogen-Doped Graphene and Single-Walled Carbon Nanotubes”. In: *ACS Nano* 6.10 (Oct. 2012), pp. 8837–8846. DOI: 10.1021/nn303944f.

[24] A. Messiah. *Quantum mechanics*. Mineola, N.Y: Dover Publications, 1999.

[25] C. Hébert and P. Schattschneider. “A proposal for dichroic experiments in the electron microscope”. In: *Ultramicroscopy* 96.3-4 (2003), pp. 463–468. DOI: 10.1016/S0304-3991(03)00108-6.

[26] P. Schattschneider, S. Rubino, C. Hebert, J. Rusz, J. Kunes, P. Novák, E. Carlino, M. Fabrizioli, G. Panaccione, and G. Rossi. “Detection of magnetic circular dichroism using a transmission electron microscope”. In: *Nat.* 441 (2006), pp. 486–488. DOI: 10.1038/nature04778.

[27] P. Schattschneider, I. Ennen, S. Löffler, M. Stöger-Pollach, and J. Verbeeck. “Circular dichroism in the electron microscope: Progress and applications (invited)”. In: *J. Appl. Phys.* 107.9, 09D311 (May 2010), p. 09D311. DOI: 10.1063/1.3365517.

[28] R. F. Egerton. *Electron Energy-Loss Spectroscopy in the Electron Microscope.* 2nd. New York: Plenum Press, 1996.

[29] S. Löffler, I. Ennen, F. Tian, P. Schattschneider, and N. Jaouen. “Breakdown of the Dipole Approximation in Core Losses”. In: *Ultramicroscopy* 111.8 (July 2011), pp. 1163–1167. DOI: 10.1016/j.ultramic.2011.03.006.

[30] P. Schattschneider, C. Hébert, S. Rubino, M. Stöger-Pollach, J. Rusz, and P. Novák. “Magnetic circular dichroism in EELS: Towards 10 nm resolution”. In: *Ultramicroscopy* 108.5 (2008), pp. 433–438. DOI: 10.1016/j.ultramic.2007.07.002.

[31] J. Rusz, S. Rubino, O. Eriksson, P. M. Oppeneer, and K. Leifer. “Local electronic structure information contained in energy-filtered diffraction patterns”. In: *Phys. Rev. B* 84 (6 Aug. 2011), p. 064444. DOI: 10.1103/PhysRevB.84.064444.

[32] J. Verbeeck, H. Tian, and P. Schattschneider. “Production and application of electron vortex beams”. In: *Nat.* 467.7313 (2010), pp. 301–304. DOI: 10.1038/nature09366.

[33] P. Schattschneider, M. Stöger-Pollach, S. Rubino, M. Sperl, C. Hurm, J. Zweck, and J. Rusz. “Detection of magnetic circular dichroism on the two-nanometer scale”. In: *Phys. Rev. B* 78.10, 104413 (2008), p. 104413. DOI: 10.1103/PhysRevB.78.104413.

[34] P. Schattschneider, B. Schaffer, I. Ennen, and J. Verbeeck. “Mapping spin-polarized transitions with atomic resolution”. In: *Phys. Rev. B* 85 (13 Apr. 2012), p. 134422. DOI: 10.1103/PhysRevB.85.134422.

[35] B. Warot-Fonrose, F. Houdellier, M. Hÿtch, L. Calmels, V. Serin, and E. Snoeck. “Mapping inelastic intensities in diffraction patterns of magnetic samples using the energy spectrum imaging technique”. In: *Ultramicroscopy* 108.5 (2008), pp. 393–398. DOI: 10.1016/j.ultramic.2007.05.013.

[36] J. Salafranca, J. Gazquez, N. Pérez, A. Labarta, S. T. Pantelides, S. J. Pennycook, X. Batlle, and M. Varela. “Surfactant Organic Molecules Restore Magnetism in Metal-Oxide Nanoparticle Surfaces”. In: *Nano Lett.* 12.5 (May 2012), pp. 2499–2503. DOI: 10.1021/nl300665z.

[37] T. Thersleff, J. Rusz, S. Rubino, B. Hjörvarsson, Y. Ito, N. J. Zaluzec, and K. Leifer. “Quantitative analysis of magnetic spin and orbital moments from an oxidized iron (1 1 0) surface using electron magnetic circular dichroism”. In: *Sci. Rep.* 5 (Aug. 2015), p. 13012. DOI: 10.1038/srep13012.

[38] T. Thersleff, J. Rusz, B. Hjörvarsson, and K. Leifer. “Detection of magnetic circular dichroism with subnanometer convergent electron beams”. In: *Phys. Rev. B* 94.13 (2016), p. 134430. DOI: 10.1103/PhysRevB.94.134430.

[39] W. Wallisch, M. Stöger-Pollach, and E. Navickas. “Consequences of the CMR effect on EELS in TEM”. In: *Ultramicroscopy* 179 (Aug. 2017), pp. 84–89. DOI: 10.1016/j.ultramic.2017.04.011.

[40] M. Uchida and A. Tonomura. “Generation of electron beams carrying orbital angular momentum”. In: *Nat.* 464 (Apr. 2010), pp. 737–739. DOI: 10.1038/nature08904.

[41] B. J. McMorran, A. Agrawal, I. M. Anderson, A. A. Herzing, H. J. Lezec, J. J. McClelland, and J. Unguris. “Electron Vortex Beams with High Quanta of Orbital Angular Momentum”. In: *Science* 331.6014 (2011), pp. 192–195. DOI: 10.1126/science.1198804.

[42] A. Béché, R. Van Boxem, G. Van Tendeloo, and J. Verbeeck. “Magnetic monopole field exposed by electrons”. In: *Nat. Phys.* 10.1 (Dec. 2013), pp. 26–29. DOI: 10.1038/nphys2816.

[43] J. Verbeeck, H. Tian, and A. Béché. “A new way of producing electron vortex probes for STEM”. In: *Ultramicroscopy* 113.0 (2012), pp. 83–87. DOI: 10.1016/j.ultramic.2011.10.008.

[44] L. Clark, A. Béché, G. Guzzinati, A. Lubk, M. Mazilu, R. Van Boxem, and J. Verbeeck. “Exploiting Lens Aberrations to Create Electron-Vortex Beams”. In: *Phys. Rev. Lett.* 111 (6 Aug. 2013), p. 064801. DOI: 10.1103/PhysRevLett.111.064801.

[45] G. Guzzinati, L. Clark, A. Béché, and J. Verbeeck. “Measuring the orbital angular momentum of electron beams”. In: *Phys. Rev. A* 89 (2 Feb. 2014), p. 025803. DOI: 10.1103/PhysRevA.89.025803.

[46] L. Clark, A. Béché, G. Guzzinati, and J. Verbeeck. “Quantitative measurement of orbital angular momentum in electron microscopy”. In: *Phys. Rev. A* 89 (5 May 2014), p. 053818. DOI: 10.1103/PhysRevA.89.053818.

[47] H. Larocque, F. Bouchard, V. Grillo, A. Sit, S. Frabboni, R. E. Dunin-Borkowski, M. J. Padgett, R. W. Boyd, and E. Karimi. “Nondestructive Measurement of Orbital Angular Momentum for an Electron Beam”. In: *Physical Review Letters* 117.15 (Oct. 2016), p. 154801. DOI: 10.1103/physrevlett.117.154801.

[48] T. R. Harvey, V. Grillo, and B. J. McMorran. “Stern-Gerlach-like approach to electron orbital angular momentum measurement”. In: *Physical Review A* 95.2 (Feb. 2017), p. 021801. DOI: 10.1103/physreva.95.021801.

[49] V. Grillo, A. H. Tavabi, F. Venturi, H. Larocque, R. Balboni, G. C. Gazzadi, S. Frabboni, P.-H. Lu, E. Mafakheri, F. Bouchard, R. E. Dunin-Borkowski, R. W. Boyd, M. P. J. Lavery, M. J. Padgett, and E. Karimi. “Measuring the orbital angular momentum spectrum of an electron beam”. In: *Nature Communications* 8 (May 2017), p. 15536. DOI: 10.1038/ncomms15536.

[50] T. Schachinger, S. Löffler, A. Steiger-Thirsfeld, M. Stöger-Pollach, S. Schneider, D. Pohl, B. Rellinghaus, and P. Schattschneider. “EMCD with an electron vortex filter: Limitations and possibilities”. In: *Ultramicroscopy* 179 (2017), pp. 15–23. DOI: 10.1016/j.ultramic.2017.03.019. eprint: 1703.09156.

[51] J. Rusz and S. Bhowmick. “Boundaries for Efficient Use of Electron Vortex Beams to Measure Magnetic Properties”. In: *Phys. Rev. Lett.* 111 (10 Sept. 2013), p. 105504. DOI: 10.1103/PhysRevLett.111.105504.

[52] P. Schattschneider, S. Löffler, M. Stöger-Pollach, and J. Verbeeck. “Is magnetic chiral dichroism feasible with electron vortices?” In: *Ultramicroscopy* 136 (Jan. 2014), pp. 81–85. DOI: 10.1016/j.ultramic.2013.07.012. eprint: 1304.7976.

[53] J. C. Idrobo, J. Rusz, J. Spiegelberg, M. A. McGuire, C. T. Symons, R. R. Vatsavai, C. Cantoni, and A. R. Lupini. “Detecting magnetic ordering with atomic size electron probes”. In: *Advanced Structural and Chemical Imaging* 2.1 (2016), p. 5. DOI: 10.1186/s40679-016-0019-9.

[54] D. Pohl, S. Schneider, J. Rusz, and B. Rellinghaus. “Electron vortex beams prepared by a spiral aperture with the goal to measure EMCD on ferromagnetic films via STEM”. In: *Ultramicroscopy* 150 (2015), pp. 16–22. DOI: 10.1016/j.ultramic.2014.11.025.

[55] J. Rusz, S. Bhowmick, M. Eriksson, and N. Karlsson. “Scattering of electron vortex beams on a magnetic crystal: Towards atomic-resolution magnetic measurements”. In: *Phys. Rev. B* 89 (13 Apr. 2014), p. 134428. DOI: 10.1103/PhysRevB.89.134428.

[56] K. Y. Bliokh, P. Schattschneider, J. Verbeeck, and F. Nori. “Electron Vortex Beams in a Magnetic Field: A New Twist on Landau Levels and Aharonov-Bohm States”. In: *Phys. Rev. X* 2 (4 Nov. 2012), p. 041011. DOI: 10.1103/PhysRevX.2.041011.

[57] P. Schattschneider, T. Schachinger, M. Stöger-Pollach, S. Löffler, A. Steiger-Thirsfeld, K. Y. Bliokh, and F. Nori. “Imaging the dynamics of free-electron Landau states”. In: *Nature Communications* 5, 4586 (Aug. 2014), p. 4586. DOI: 10.1038/ncomms5586. eprint: 1408.1972.

[58] T. Schachinger, S. Löffler, M. Stöger-Pollach, and P. Schattschneider. “Peculiar rotation of electron vortex beams”. In: *Ultramicroscopy* 158 (Nov. 2015), pp. 17–25. DOI: 10.1016/j.ultramic.2015.06.004. eprint: 1703.10235.

[59] G. Guzzinati, P. Schattschneider, K. Y. Bliokh, F. Nori, and J. Verbeeck. “Observation of the Larmor and Gouy Rotations with Electron Vortex Beams”. In: *Phys. Rev. Lett.* 110 (9 Feb. 2013), p. 093601. DOI: 10.1103/PhysRevLett.110.093601.

[60] J. Verbeeck, H. Tian, and G. Van Tendeloo. "How to Manipulate Nanoparticles with an Electron Beam?" In: *Adv. Mater.* 25.8 (2013), pp. 1114–1117. DOI: 10.1002/adma.201204206.

[61] R. Juchtmans, A. Béché, A. Abakumov, M. Batuk, and J. Verbeeck. "Using electron vortex beams to determine chirality of crystals in transmission electron microscopy". In: *Phys. Rev. B* 91.9 (Mar. 2015), p. 094112. DOI: 10.1103/PhysRevB.91.094112.

[62] G. Guzzinati, A. Béché, H. Lourenco-Martins, J. Martin, M. Kociak, and J. Verbeeck. "Probing the symmetry of the potential of localized surface plasmon resonances with phase-shaped electron beams". In: *Nat. Commun.* 8 (2017), p. 14999. DOI: 10.1038/ncomms14999.

[63] A. Asenjo-Garcia and F. J. García de Abajo. "Dichroism in the Interaction between Vortex Electron Beams, Plasmons, and Molecules". In: *Phys. Rev. Lett.* 113.6 (Aug. 2014), p. 066102. DOI: 10.1103/PhysRevLett.113.066102.

[64] E. Karimi, L. Marrucci, V. Grillo, and E. Santamato. "Spin-to-Orbital Angular Momentum Conversion and Spin-Polarization Filtering in Electron Beams". In: *Phys. Rev. Lett.* 108 (4 Jan. 2012), p. 044801. DOI: 10.1103/PhysRevLett.108.044801.

[65] P. Schattschneider, V. Grillo, and D. Aubry. "Spin polarisation with electron Bessel beams". In: *Ultramicroscopy* 176 (2017), pp. 188–193. DOI: 10.1016/j.ultramic.2016.11.029.

[66] R. Shiloh, P.-H. Lu, R. Remez, A. H. Tavabi, G. Pozzi, R. E. Dunin-Borkowski, and A. Arie. "Nanostructuring of electron beams". In: *Physica Scripta* 94.3 (Jan. 2019), p. 034004. DOI: 10.1088/1402-4896/aaf258.

[67] R. Shiloh, Y. Lereah, Y. Lilach, and A. Arie. "Sculpturing the electron wave function using nanoscale phase masks". In: *Ultramicroscopy* 144 (2014), pp. 26–31. DOI: 10.1016/j.ultramic.2014.04.007.

[68] J. Pierce, J. Webster, H. Larocque, E. Karimi, B. McMorran, and A. Forbes. "Coiling free electron matter waves". In: *New Journal of Physics* 21.4 (Apr. 2019), p. 043018. DOI: 10.1088/1367-2630/ab152d.

[69] I. Kaminer, J. Nemirovsky, M. Rechtsman, R. Bekenstein, and M. Segev. "Self-accelerating Dirac particles and prolonging the lifetime of relativistic fermions". In: *Nature Physics* 11.3 (Jan. 2015), pp. 261–267. DOI: 10.1038/nphys3196.

[70] N. Voloch-Bloch, Y. Lereah, Y. Lilach, A. Gover, and A. Arie. "Generation of electron Airy beams". In: *Nature* 494.7437 (Feb. 2013), pp. 331–335. DOI: 10.1038/nature11840.

[71] R. Shiloh, R. Remez, and A. Arie. "Prospects for electron beam aberration correction using sculpted phase masks". In: *Ultramicroscopy* 163 (Apr. 2016), pp. 69–74. DOI: 10.1016/j.ultramic.2016.02.002.

[72] R. Shiloh, R. Remez, P.-H. Lu, L. Jin, Y. Lereah, A. H. Tavabi, R. E. Dunin-Borkowski, and A. Arie. “Spherical aberration correction in a scanning transmission electron microscope using a sculpted thin film”. In: *Ultramicroscopy* 189 (June 2018), pp. 46–53. DOI: 10.1016/j.ultramic.2018.03.016.

[73] A. H. Tavabi, V. Migunov, C. Dwyer, R. E. Dunin-Borkowski, and G. Pozzi. “Tunable caustic phenomena in electron wavefields”. In: *Ultramicroscopy* 157 (Oct. 2015), pp. 57–64. DOI: 10.1016/j.ultramic.2015.04.003.

[74] R. Shiloh and A. Arie. “3D shaping of electron beams using amplitude masks”. In: *Ultramicroscopy* 177 (2017), pp. 30–35. DOI: 10.1016/j.ultramic.2017.02.001.

[75] J. Verbeeck, A. Béché, K. Müller-Caspary, G. Guzzinati, M. A. Luong, and M. D. Hertog. “Demonstration of a 2×2 programmable phase plate for electrons”. In: *Ultramicroscopy* 190 (July 2018), pp. 58–65. DOI: 10.1016/j.ultramic.2018.03.017.

[76] P. Thakkar, V. A. Guzenko, P.-H. Lu, R. E. Dunin-Borkowski, J. P. Abrahams, and S. Tsujino. “Fabrication of low aspect ratio three-element Boersch phase shifters for voltage-controlled three electron beam interference”. In: *Journal of Applied Physics* 128.13 (Oct. 2020), p. 134502. DOI: 10.1063/5.0020383.

[77] G. Ruffato, E. Rotunno, L. Giberti, and V. Grillo. “Arbitrary Conformal Transformations of Wave Functions”. In: *Physical Review Applied* 15.5 (May 2021), p. 054028. DOI: 10.1103/physrevapplied.15.054028.

[78] A. H. Tavabi, H. Larocque, P.-H. Lu, M. Duchamp, V. Grillo, E. Karimi, R. E. Dunin-Borkowski, and G. Pozzi. “Generation of electron vortices using nonexact electric fields”. In: *Physical Review Research* 2.1 (Feb. 2020), p. 013185. DOI: 10.1103/physrevresearch.2.013185.

[79] V. Grillo, G. Carlo Gazzadi, E. Karimi, E. Mafakheri, R. W. Boyd, and S. Frabboni. “Highly efficient electron vortex beams generated by nanofabricated phase holograms”. In: *Appl. Phys. Lett.* 104.4, 043109 (2014), p. 043109. DOI: 10.1063/1.4863564.

[80] T. R. Harvey, J. S. Pierce, A. K. Agrawal, P. Ercius, M. Linck, and B. J. McMorran. “Efficient diffractive phase optics for electrons”. In: *New Journal of Physics* 16.9 (Sept. 2014), p. 093039. DOI: 10.1088/1367-2630/16/9/093039.

[81] L. Allen, M. W. Beijersbergen, R. J. C. Spreeuw, and J. P. Woerdman. “Orbital angular momentum of light and the transformation of Laguerre-Gaussian laser modes”. In: *Phys. Rev. A* 45.11 (June 1992), pp. 8185–8189. DOI: 10.1103/PhysRevA.45.8185.

[82] M. Beijersbergen, L. Allen, H. van der Veen, and J. Woerdman. “Astigmatic laser mode converters and transfer of orbital angular momentum”. In: *Optics Communications* 96.1-3 (Feb. 1993), pp. 123–132. DOI: 10.1016/0030-4018(93)90535-d.

[83] T. Schachinger, P. Hartel, P. Lu, S. Löffler, M. Obermair, M. Dries, D. Gerthsen, R. E. Dunin-Borkowski, and P. Schattschneider. “Experimental Realisation of a $\pi/2$ Vortex Mode Converter for Electrons Using a Spherical Aberration Corrector”. In: *Ultramicroscopy* 229 (2021), p. 113340. DOI: 10.1016/j.ultramic.2021.113340. eprint: 2103.10899.

[84] P. Schattschneider, M. Stöger-Pollach, and J. Verbeeck. “Novel Vortex Generator and Mode Converter for Electron Beams”. In: *Phys. Rev. Lett.* 109.8 (Aug. 2012), p. 084801. DOI: 10.1103/PhysRevLett.109.084801.

[85] S. Löffler and P. Schattschneider. “Elastic propagation of fast electron vortices through crystals”. In: *Acta Crystallographica Section A* 68.4 (July 2012), pp. 443–447. DOI: 10.1107/S0108767312013189. eprint: 1111.6050.

[86] A. Lubk, L. Clark, G. Guzzinati, and J. Verbeeck. “Topological analysis of paraxially scattered electron vortex beams”. In: *Phys. Rev. A* 87 (3 Mar. 2013), p. 033834. DOI: 10.1103/PhysRevA.87.033834.

[87] P. Stadelmann. “EMS - a software package for electron diffraction analysis and HREM image simulation in materials science”. In: *Ultramicroscopy* 21.2 (1987), pp. 131–145. DOI: 10.1016/0304-3991(87)90080-5.